MASS TRANSFER FROM A TURBULENT IMPINGING JET WITH AND WITHOUT CHEMICAL REACTION

A thesis

presented for the

Degree of Doctor of Philosophy

of the University of London

by

GERAINT JONES DAVIES

July 1971.

John Percy Research Group in
Process Metallurgy,
Royal School of Mines,
Imperial College of Science
and Technology,
Prince Consort Road,
LONDON, S.W.7.

BIBL.
LONDIN.
UNIV.

BEST COPY

AVAILABLE

Variable print quality

ABSTRACT

Mass transfer effects between a vertical, impinging, axially symmetric, turbulent jet, produced by the discharge of fully developed tube flow, and a flat plate, are studied in three systems. The first system is that of napthalene erosion by a jet of air. The other systems include the effect of chemical reaction in the study of two vapour deposition reactions; the deposition of CoO from the hydrogen assisted thermal decomposition of Cobalt Acetylacetonate in the presence of free oxygen, and the decomposition of nickel tetracarbonyl in a nitrogen carrier gas. The mass transfer rate controlling zones are identified for each system.

The development of apparatus and experimental techniques used in investigating the relevant variables is described.

Mathematical models, which describe the observed mass transfer, are derived from heat transfer analogies, dimensional analysis, the extension of a laminar stagnation point solution, and a Von Karman integral technique, the last being specifically for the wall jet region.

Mass transfer in the three systems is correlated for various jet Reynolds numbers in terms of the stagnation point Sherwood number to include the effect of jet/plate distance, Schmidt number, and, in the case of the vapour deposition systems, the dilution effect due to entrainment.

Vapour deposition from an impinging jet is shown to produce a highly localised chemical deposit, the shape of which is partly predicted by the mass transfer analysis.

TABLE OF CONTENTS

Page No.	Section	Title
1		Title Page
2		Abstract
3		Table of Contents
8	Chapter 1	INTRODUCTION
12	Chapter 2	THEORETICAL BACKGROUND
14	2.1	Momentum Transfer
14	2.1.1	Universal Theories
15	2.1.2	Statistical Models
16	2.1.3	Mathematical Models
16	2.1.4	Prandtl's First Model
20	2.1.5	Kolmogorov-Prandtl Model
20	2.1.6	Clauser Model
21	2.1.7	Taylor Model
21	2.1.8	Laminar Stagnation Point Model
23	2.1.9	Specific Theories
23	2.1.10	Glauert's Wall Jet Model
23	2.1.11	Poreh and Cermak's Wall Jet Model
24	2.1.12	Dawson and Trass Wall Jet Model
25	2.1.13	Empirical Law Theories
25	2.1.14	Leont'ev Plane Wall Jet Model
26	2.1.15	Dimensional Analysis Theories
27	2.2	Heat and Mass Transfer
29	2.2.1	Universal Theories
30	2.2.2	Specific Theories
30	2.2.3	Empirical Law Theories

Page No.	Section	Title
30	2.2.4	Dimensional Analysis Theories
31	2.3	Discussion of the Various Approaches
33	2.4	Available Empirical Data
35	2.4.1	Heat Transfer Data
36	2.4.2	Mass Transfer Data
38	2.5	The Free Turbulent Jet
41	2.6	The Role of Turbulence in Heat and Mass Transfer
43	Chapter 3	THEORETICAL ANALYSIS
45	3.1	Extension of Frossling's Stagnation Point Solution
47	3.2	Adaption of Reshotko and Cohen's Stagnation Point Model
49	3.3	Heat Transfer Analogies
49	3.3.1	Heat Transfer Analogy from Gardon and Cobonpue Data
50	3.3.2	Heat Transfer Analogy from Perry's Data
52	3.3.3	Equivalent Stagnant Film Model
53	3.4	Prediction of Mass Transfer Rates in the Wall Jet
55	3.4.1	Assumptions
55	3.4.2	Wall Jet Theory
58	3.4.3	Prediction of Growth Rate for the Wall Jet Boundary Layer
69	3.4.4	Wall Jet Mass Transfer Prediction
71	3.5	Implications of the Theoretical Models
72	Chapter 4	EROSION OF NAPTHALENE WITH AN AIR JET
73	4.1	Napthalene Erosion Experimental Method
76	4.1.1	Calculation of the Sherwood Number
76	4.2	Experimental Results
76	4.2.1	Wall Jet Region

Page No.	Section	Title
78	4.2.2	Dimensionless Profile
78	4.2.3	Effect of Jet/Plate Distance
78	4.2.4	Stagnation Point Variation with Reynolds Number
78	4.3	Discussion of Results
78	4.3.1	Wall Jet Region
90	4.3.2	Inconsistency in the Wall Jet Mass Transfer Profile
94	4.3.3	Effect of Jet/Plate Distance
94	4.3.4	Dimensionless Profile
94	4.3.5	Stagnation Point Variation with Reynolds Number
96	4.3.6	Errors
96	4.4	Conculsions
98	Chapter 5	VAPOUR DEPOSITION
105	Chapter 6	APPLICATION OF MASS TRANSFER THEORY TO VAPOUR DEPOSITION SYSTEMS
109	Chapter 7	VAPOUR DEPOSITION OF COBALT OXIDE
112	7.1	The Cobalt Oxide Deposit
118	7.2	Preparation of CoAcAt
118	7.3	CoO Deposition Apparatus and Experimental Method
129	7.4	Description of Analysis Methods
130	7.5	Surface Temperature Measurement
131	7.6	Analysis of the CoO Deposits
133	7.6.1	Interference Theory
137	7.7	Calculation of the Sherwood Number
137	7.8	CoO Deposition Experimental Results
139	7.8.1	Temperature Conditions Under the Jet
139	7.8.2	Arhenius Plot for CoO Deposition
142	7.8.3	Reynolds Number Effect in High Temperature Region

Page No.	Section	Title
142	7.8.4	Effect of Varying Jet Plate Distance in the High Temperature Region
142	7.8.5	Radial Deposition Profile
148	7.8.6	Scanning Electron Microscopy Results
148	7.9	Discussion of Experimental Results
148	7.9.1	The Chemical and Mass Transfer Control Regions
150	7.9.2	Temperature Conditions Under the Jet
150	7.9.3	The Effect of Jet Plate Distance
150	7.9.4	The Nature of the Deposit
150	7.9.5	The Deposit Profile
151	7.9.6	Experimental Errors
151	7.10	Conculsions
152	Chapter 8	NICKEL DEPOSITION FROM THE TETRACARBONYL
154	8.1	Nickel Deposition Experimental Apparatus and Method
164	8.1.1	Calibration of the Evaporator and Analysis of the Carbonyl Concentration
168	8.1.2	Analysis of the Deposit Shape
170	8.1.3	Calculation of the Sherwood Number
170	8.1.4	Summary of Safety Precautions
171	8.2	Nickel Deposition Experimental Results
171	8.2.1	The Boudouard Reaction
172	8.2.2	Arhenius Plot
172	8.2.3	Order of Reaction
172	8.2.4	Effect of Reynolds Number Variation
175	8.2.5	Fall off in Reaction Rate with Time
175	8.2.6	Effect of Jet/Plate Distance
175	8.2.7	Thermal Effects
178	8.2.8	The Nature of the Deposits

Page No.	Section	Title
181	8.3	Discussion of Experimental Results
181	8.3.1	Chemical and Mass Transfer Control Regions
182	8.3.2	Order of Reaction
183	8.3.3	Thermal Effects
183	8.3.4	Nature of Deposits
184	8.3.5	Prediction of Varying the System
184	8.4	Conclusions
186	Chapter 9	CORRELATION OF MASS TRANSFER EFFECTS
187	9.1	Stagnation Point Mass Transfer
190	9.2	The Radial Mass Transfer Profile
	Appendices	
194	1	Calculation of Diffusion Coefficients
197	2	Decay of Reactant Concentration due to Entrainment
201	3	Computer Program
208	4	Tabulated Results
231	5	References
236	6	Nomenclature
240		Acknowledgements

C H A P T E R O N E

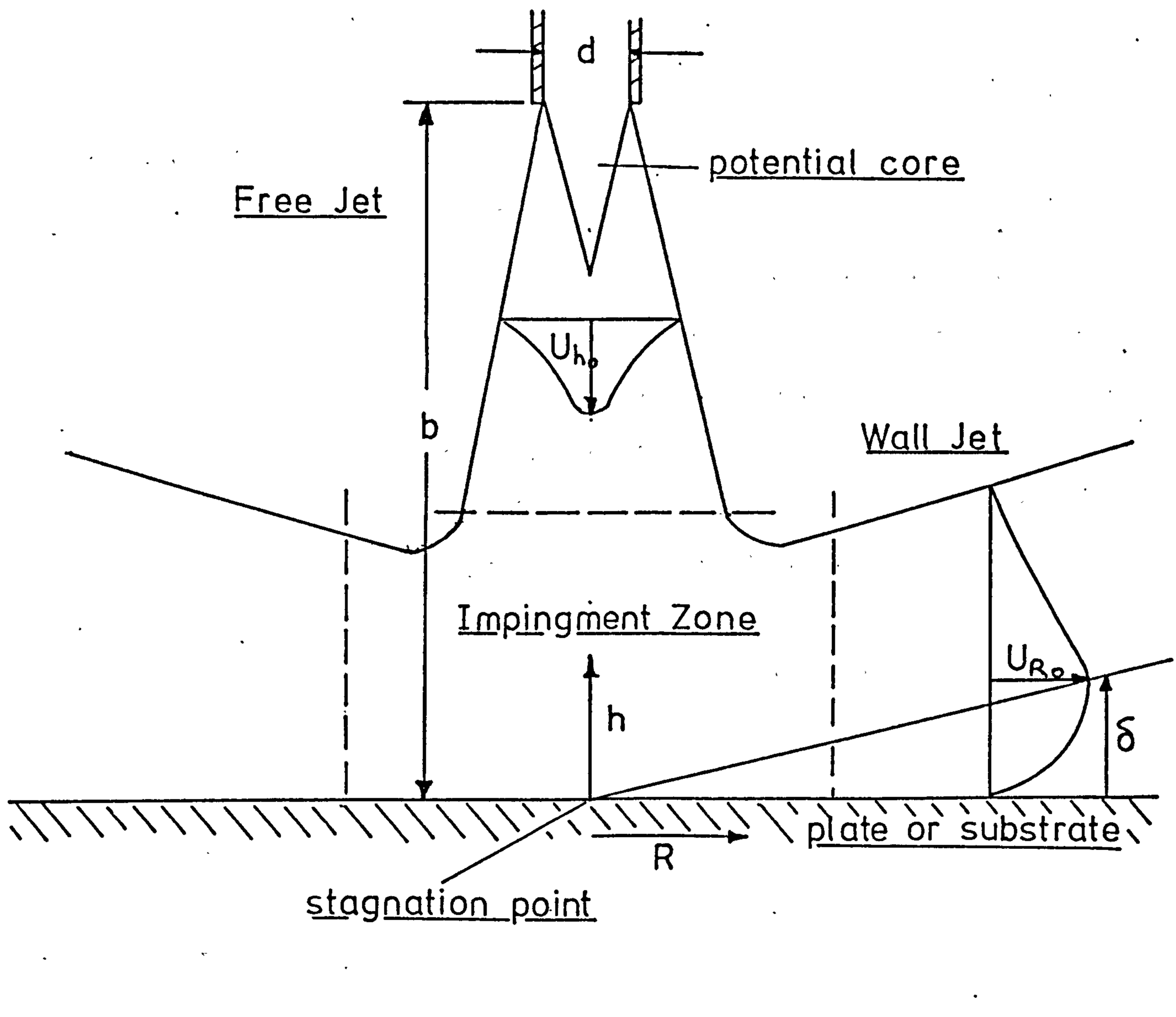
INTRODUCTION

INTRODUCTION

The study of impinging jet flow is important in the understanding of many practical phenomena, including plasma welding, VTOL aircraft, paper drying, particle sizing and jet cooling or heating. Work has been done on the fluid dynamics of all or part of the impinging jet system. Heat transfer effects have also been investigated, but little work has been done to date on mass transfer effects. The present work is concerned with the analysis of the latter in three systems. The first system is the erosion of napthalene with an impinging jet of air. The second and third systems include the effects of chemical reaction from the study of two vapour deposition reactions where thermally sensitive chemicals mixed as vapours in the jet flow react on a heated plate, onto which the jet impinges, to produce a deposit.

The work was prompted by the idea of producing localised deposits in vapour deposition systems which in future work could be further localised so as to be of importance in the production of minute electronic components.

As mass transfer rates are considerably higher in turbulent flow than in laminar flow a turbulent axially symmetric jet was employed. Turbulent flow is at present not so well understood as laminar flow and the analysis of the former is more complex than with the latter case. Various approaches to the problem of analysing the turbulent impinging jet are discussed in the second chapter together with a discussion of relevant work on the axi-symmetric system. Mathematical models describing and predicting mass transfer in the system are derived in chapter three, to enable other systems to be predicted as well as to predict variations in those studied in the present work. From the previous work on similar systems and some of the theoretical analyses, a physical model emerges of the impinging jet, fig (1.1). The system is considered to consist of three main zones linked by two transition regions. The first zone covers the freely discharging jet where it is still



fig(1.1) DIAGRAM OF THE IMPINGING JET

unaffected by the presence of the plate or substrate. This zone extends from the jet orifice to within 1 - 2 jet diameters of the plate. There follows a transition region and then the impingment zone where the flow has components in the two orthogonal directions h and R. The rapid change in the direction of the flow in this zone produces a high level of mixing which promotes rapid transfer of mass and heat between the jet and the plate. This transfer occurs across a thin sublayer in the stagnation region which limits the transfer rate. The flow passes from the impingment zone through the second transition region into the third zone of the radial wall jet where flow in the h direction is negligible.

The theoretical models are applied to the napthalene erosion work of chapter four. Certain modifications to the theoretical approach are necessary in analysing the vapour deposition systems and these are covered in chapter six and followed in chapters seven and eight by the vapour deposition work itself on Cobalt Oxide and Nickel deposition systems. An effort is made in the final chapter to correlate the mass transfer data presented in the three systems. For the sake of continuity, many calculations, tabulated results, together with references and nomenclature are contained in appendices.

C H A P T E R T W O

THEORETICAL BACKGROUND

2.0 THEORETICAL BACKGROUND

The basic problem in calculating the momentum, heat or mass transfer from the flow of a viscous fluid is the simultaneous solution of the differential conservation equations for mass, energy and momentum. These equations for incompressible flow would be of the form of the Navier-Stokes equations. In laminar flow, laws describing the viscous effects of the fluid are well known. In turbulent flow the effect of the turbulent eddies characterising this type of flow makes the solution of the relevant equations much more complex, due to the dependence of the effective viscosity, diffusion coefficient and thermal conductivity, on position in the flow field and the level of turbulence. The solution is dependent even in the most refined approaches now available on a mathematical model that attempts to describe the effects of turbulence.

The solution of mass and heat transfer is in some measure secondary to the solution of momentum transfer so the latter will be considered in isolation from the first two. There are many possible approaches to the mathematical solution of turbulent flow. They fall into four categories or different levels. The first type of method can be called the Universal theory approach where the differential conservation equations can be solved simultaneously solely from the use of a mathematical model of turbulence and the relevant boundary conditions. The model of turbulence is usually specified as an equation for calculating an effective viscosity or conductivity term. The second type of method, the Specific theory, involves the use of one or more limiting identities or equations derived from the physical nature of the system. The type of assumptions involved limit the solution to that particular system. For example, one analysis discussed later assumes that the similarity between the radial wall jet flow and a semi-section through free jet flow enables the wall jet to be treated theoretically like a free jet. The third method or Empirical law theory uses a relationship derived from

one or more other; often dissimilar, systems and applies it to another system with little or no modification. This is in effect another effort at producing a universal theory relying on any intrinsic similarity that exists between all flow systems. The approach is particularly useful in boundary layer flows, of which the wall jet region is a special example. Shear stress laws for instance can be measured in one boundary layer flow and applied to another. The final classification is the approach of dimensional analysis which, although in many cases little more than good scientific accountancy, is often useful in prediction via the use of analogies and in scaling.

2.1 Momentum Transfer

The methods and implications of those methods that are useful in the analysis of turbulent flow with especial reference to those applied to the impinging jet system are discussed in the four categories outlined above.

2.1.1 Universal Theories

The differential equation for the conservation of property ϕ in axisymmetric flow is of the form:

$$\rho U_h \frac{\partial \phi}{\partial h} + \rho U_R \frac{\partial \phi}{\partial R} - \frac{1}{R}\frac{\partial}{\partial R}\left[\frac{\mu_{eff}}{\sigma_\phi} R \frac{\partial \phi}{\partial R}\right] = S_\phi$$

Convective Term Conductive Term Source Term

The essential problem in integrating these types of equation for momentum, heat, mass, chemical species etc., is in knowing how the effective conductivity varies with the integral parameters. Universal theories then usually start with a conductivity hypothesis of the form μ_{eff} = f (some selected parameters). The selected parameters are then specified empirically as in the mixing length approach of Prandtl, discussed later, or, alternatively, specified by a conservation equation as with the turbulence energy of

Kolmogorov, also discussed later.

Once a hypothesis has been made the integration poses a complex and tedious problem. The method commonly used is a finite difference solution involving the placing of an imaginary grid over the flow field and the solution of the relevant equations for each grid element. The elements are made small enough, so that if parameters are known on one side of the element, from a boundary condition or previous calculation, they can be calculated on the other side by an approximation to the rate of change of the parameter over the width of the element. A further discussion of this technique and other computer methods can be found in Spalding (1967) and Spalding and Patankar (1967).

2.1.2 Statistical Models

The main characteristics of turbulent flow are the irregular fluctuations in velocity components at a particular point. Whereas in laminar flow, if the flow is in one dimension, velocity components in the other two can be neglected, inunidirectional turbulent flow the eddy components in the other dimensions are significant. If U and V are the instantaneous velocity components in a two dimensional flow field, they equal the sum of two components

$$U = \bar{U} + U' \quad \ldots\ldots\ldots (2.1)$$

$$V = \bar{V} + V' \quad \ldots\ldots\ldots (2.2)$$

where $\bar{U}$ and $\bar{V}$ are the time averaged velocity components and U' and V' are the turbulent fluctuating components. As these components are apparently random it is reasonable to consider a statistical approach in representing them, for if these were known an effective conductivity could be calculated. Taylor (1935) and Corrsin (1951) have applied statistical theories of turbulence to simple well defined cases but a generally applicable theory is not yet available.

2.1.3 Mathematical Models

In the absence of a statistical theory that might completely describe turbulent flow, many workers have developed mathematical models to describe the effect of turbulence, usually based on a simple physical model.

2.1.4 Prandtl's First Model

Prandtl (1925) produced a model based on the physical model of a packet of fluid travelling a length l and dissipating its momentum, heat and mass only at the end of its passage. This 'mixing' length varies with position in the flow field.

To explore the model further, it is worth returning to the original definition of turbulence by Boussinesq (1877) who defined an effective viscosity for turbulent flow by analogy with Newton's law for laminar viscous flow.

$$\tau = \mu_{eff} \frac{dU}{dy} \quad \ldots\ldots\ldots (2.3)$$

From Prandtl's model the effective viscosity is replaced by the purely viscous forces and the turbulent contribution.

$$\mu_{eff} = \mu_{visc} + \mu_{turb} = \mu_{visc} + \rho l^2 \left|\frac{d\bar{U}}{dh}\right| \quad \ldots\ldots (2.4)$$

The turbulent contribution, often referred to as the eddy viscosity, is dependent on the time smoothed velocity gradient and the mixing length l, both of which can vary across the field of flow.

Although the laminar viscous contribution μ_{visc} is still present in equation (2.4) its contribution can be neglected excepting where the flow is near a wall. The flow near a wall is dominated by the laminar contribution and account of this is necessary especially if the point of interest is transfer at the wall. Indeed, at the stagnation point of the impinging

jet, the flow in the main stream is so well mixed that transfer of heat, mass and momentum to the plate or substrate will be dominated by viscous effects in the thin boundary layer that will be set up there.

Parallel in concept to the eddy viscosity are the eddy mass and thermal diffusivities. These can be included in dimensionless numbers to allow dimensionless correlations to be made. Unfortunately not as much is known about these parameters as is known about their laminar equivalents and turbulent transfer data is often correlated in terms of laminar properties, the validity of this can be questioned.

The distribution of the mixing length l across turbulent boundary layers has been studied by several workers. The distribution used in the analyses discussed later is that recommended by Spalding (1967) fig (2.1). This is relevant to one boundary layer region of the impinging jet, the wall jet.

For the part of the flow furthest from the wall the variation of l is similar to that in free turbulent flow, uniform across the layer and proportional to the thickness of the layer. Nearer the wall, l is proportional to the distance from the wall. Next to the wall turbulence decays into the laminar sublayer and to account for this certain modifications like the one due to Van Driest (1956) can be applied.

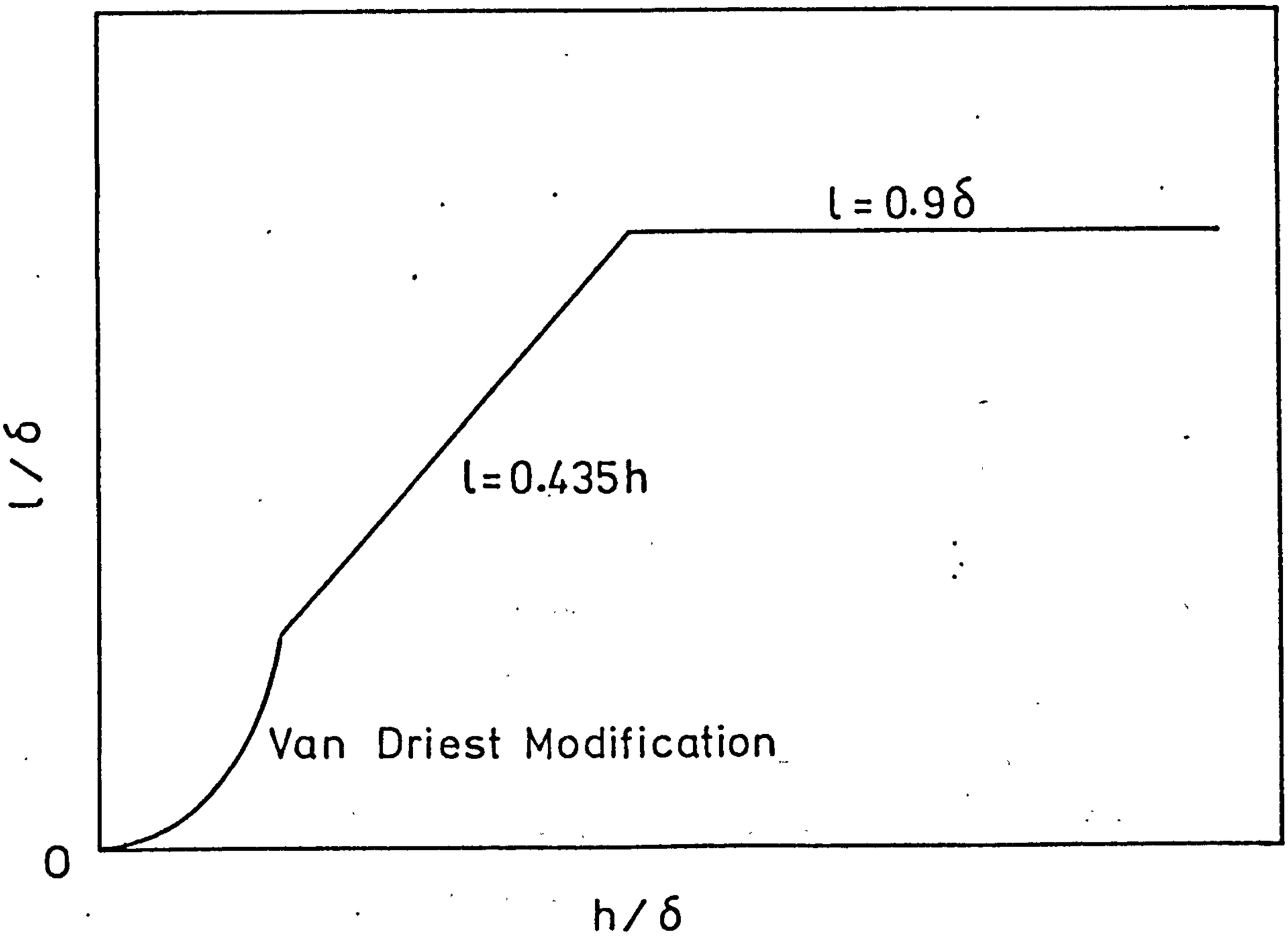
The main variation of l can be expressed as:

$$0 \leqslant y \leqslant \lambda\delta/k \; : \; l = ky \quad \ldots\ldots\ldots (2.5)$$

$$\lambda\delta/k < y \; : \; l = \lambda\delta \quad \ldots\ldots\ldots (2.6)$$

introducing two constants k and λ. Much work has been done towards finding values for these parameters that can be applied to the solution of all boundary layers.

Prandtl's theory predicts from equation (2.4) that the effective



fig(2.1) DISTRIBUTION OF THE PRANDTL MIXING LENGTH ACROSS A TURBULENT BOUNDARY LAYER NEAR A WALL AFTER SPALDING

viscosity vanishes at a point of velocity gradient, for example at the point of maximum velocity in a wall jet or free jet, implying that shear stress is zero at such positions. This has been criticised in the context of the wall jet by Bradshaw and Gee (1962) and Poreh, Cermak and Tseui (1967) who measured shear stresses on the plane of maximum velocity using hot wire anemometers. A more complex model than that of Prandtl is then necessary to explain this observation.

Spalding and Patankar (1967) evolved a method of analysing any turbulent boundary layer using values of k and λ of 0.435 and 0.09 respectively from the correlation of data by Escudier (1965). They successfully predicted the data of Myers, Shauer and Eustis (1961) for a plane wall jet, but failed to predict the data of Baker (1967) for a radial wall jet. Plane wall jets and radial wall jets are very similar. The first is produced by flow issuing from a slot near to a wall or by the impingment of a jet produced from a slot. The second is produced by flow issuing from a circular orifice either very close to, or, as in the case of the present study, some distance from the wall.

To explain the anomaly the authors claim that, as the velocity profiles and angles of spread are almost identical in plane and radial wall jets, a mass balance leads to the conclusion that the effective viscosity in a radial wall jet must be twice as large as that in a plane wall jet. This leads to the conclusion that the two constants k and λ must be increased in the case of the radial flow by a factor of $\sqrt{2}$. These revised values do not sucessfully predict the velocity profile, which depends not so much on the absolute values of k and λ but on their ratio. A ratio of k to λ of 8.0 is necessary, indicating values for the constants of 0.8 and 0.1.

In a subsequent report, Spalding (1967b) uses values for k and λ of 0.58 and 0.725 and acknowledges that probably no one combination of

values can predict all the properties of even one boundary layer accurately. Prandtl's hypothesis also cannot be used in the solution of flows exhibiting more than one flow direction, like the stagnation area of the impinging jet, since, in this example particularly, momentum is transferred by more than one velocity gradient and each gradient will interact.

2.1.5 Kolmogorov - Prandtl Model

This is an extension of Prandtl's first model by Kolmogorov (1942) and Prandtl (1945). Turbulence is described in terms of the same mixing length as before together with the level of the kinetic energy of the turbulent motion given by:

$$\text{K.E.} = \tfrac{1}{2}\,(U'^2 + V'^2 + W'^2) \quad \ldots\ldots\ldots \quad (2.7)$$

This approach enables the solution to be made of flows like that around the stagnation point and boundary layer flows involving a velocity maximum. The impingment of a slotted jet and heat transfer in the system has in fact been modelled by Wolfstein (1968). He compares his predictions with the data of Shauer and Eustis (1963), Heckested (1956) and Gardon and Akifrat (1965). In all he manages good qualitative if not quantitative agreement. He predicts a variation of heat transfer at the stagnation point proportional to the root of the jet Reynolds number, whereas the rates measured by Gardon and Akifrat indicate a higher power relationship.

2.1.6 Clauser Model

Clauser (1954) and other workers assumed that the effective viscosity is uniform across the outer part of the boundary layer, as in Spalding and Patankar's use of Prandtl's first model, and within the boundary layer, proportional to the product of stream velocity and distance from a boundary. Although this type of hypothesis is popular it breaks down for flows showing

a velocity maximum and in the region of a wall.

2.1.7 Taylor Model

It will be necessary in later stages in this work to refer to properties of the freely expanding jet and because of this it is worth considering Taylor's (1932) turbulence model as it predicts the behaviour of the turbulent jet very satisfactorily. Prandtl's early model was used by Tollmein (1926) to successfully describe the velocity profile of the free jet, but the model fails to adequately describe the temperature and concentration profiles produced in heat and mass transfer from the jet. Taylor's model is successful in the latter cases. Prandtl's physical model assumes that shear stresses in turbulent flow are caused by momentum transfer. Taylor's model assumes these stresses to be caused by transfer of vorticity. The methods are best compared as by Abramovich (1963) through the relationship of the two predicted mixing lengths.

$$1 \text{ Taylor} = 1 \text{ Prandtl} \times \sqrt{2} \qquad \ldots\ldots\ldots (2.8)$$

and the difference in the predicted properties by equations (2.9) and (2.10).

$$\frac{\Delta T}{\Delta T_o} = \sqrt{\frac{Uh}{Uh_o}} \qquad \ldots\ldots \text{Taylor model} \qquad \ldots\ldots\ldots (2.9)$$

and

$$\frac{\Delta T}{\Delta T_o} = \frac{Uh}{Uh_o} \qquad \ldots\ldots \text{Prandtl model} \qquad \ldots\ldots\ldots (2.10)$$

2.1.8 Laminar Stagnation Point Model

Although the bulk of the impinging jet system is dominated by the inertial forces of turbulent flow, near the wall viscous forces become important. Their contribution to the system is secondary in the wall jet region, but, because of the high mixing in the stagnation region, the boundary layer produced is so small that their effect becomes more important.

This leads to the approach of solving the stagnation point flow structure only in terms of the viscous effects. Schlicting (1968) presents the results of such an analysis by Frossling, although the resultant boundary layer thickness is not comparable with the data of Hrycak et al (1970).

2.1.9 Specific Theories

The approaches discussed in this section involve not only the assumption of a mixing length hypothesis but also the use of some equation or identity which can be deduced from the flow field. Most of the work in this vein is concerned only with the wall jet region.

2.1.10 Glauert's Wall Jet Model

Glauert (1956) split the wall jet into two regions. The upper region he considered as part of a free jet which is joined to the inner boundary layer on the plane of maximum radial velocity. Glauert argued from Prandlt's hypothesis that this was a plane of zero shear stress. He solved the boundary layer equations to produce the velocity profile by finding a similarity solution. This is the identity derived from a knowledge of the flow field that the radial velocity profile in the wall jet appears to be similar along its development path. Further, finding that his turbulence model gives an eroneous shape to his velocity profile near the wall he developed another model based on the empirical Blasius (1913) formula for boundary layers in pipe flow. Bakke (1957) first tested Glauert's analytical velocity profile empirically with some success. Glauert's use of the Blasius equation for wall friction has been criticised by Poreh, Tseui and Cermak (1967) who measured much higher drag forces in the wall jet. A more detailed discussion of Glaucrt's work can be found from Bradshaw and Gee (1960).

2.1.11 Poreh and Cermak's Wall Jet Model

Poreh and Cermak (1959) treat the radial wall jet as half of a free radial jet and use Goertler's (1942) turbulence model as applied to the free jet in their theoretical analysis. They derive formulae for the maximum velocity decay and the wall shear stress. Their work predicts closely

their empirical data from a water system, possibly showing in this the limited effect of the wall on the flow.

In the impingment zone they propose a region of irrotational flow where an increasing maximum radial velocity would be expected such as:

$$U_{Ro} = aR \quad \ldots\ldots\ldots \quad (2.11)$$

To support this they quote only four experimental points which could conceivably be replotted to demonstrate a wide range of models.

2.1.12 Dawson and Trass Wall Jet Model

Dawson and Trass (1966) use an approach which could well be classified with the succeeding section as, apart from the turbulence model, the Blasius friction law and a velocity profile power law are employed. The model derived is compared with the data of Poreh and Cermak (1959) but the predicted values are much higher than the empirical data for the maximum radial velocity.

2.1.13 Empirical Law Theories

This method involves the use of empirical formulae to reduce the mathematics to definite integrals. Apart from the points raised in the Dawson and Trass approach (2.1.12) this approach is often used in the preceding sections. Glauert used the Blasius friction law and Wolfstein and Spalding use 'wall functions' or simplified flow models near a boundary to increase the efficiency of their computer methods.

Whereas some workers have concentrated on the derivation of universal models of turbulence, others have tried to establish universal equations or laws that describe velocity profiles, wall shear stresses and entrainment rates and that can be applied to any boundary layer.

2.1.14 Leont'ev Plane Wall Jet Model

Although this model is applied essentially to the plane wall jet it is a good example of this type of method. Leont'ev (1966) assumes a power law velocity profile for the inner part of the wall jet of the type:

$$\frac{U_R}{U_{Ro}} = \left[\frac{h}{\delta}\right]^{1/7} \quad \ldots\ldots\ldots \quad (2.12)$$

and also a friction law for the wall using two unknown constants. Substituting these expressions into a momentum conservation equation he arrives at an expression for the drag coefficient. Choosing values for the unknown constants, he compares his analysis with the data of Myers et al (1963) to obtain a good correlation.

2.1.15 Dimensional Analysis Theories

If all the variables pertinent to a problem are known, the problem can be defined in terms of groups of these variables, so chosen that each group has no overall dimensional value. The method is so common and its merits so appreciated that dimensionless numbers Re, Pr, St, etc. are used in preference to unit variables in the display of data, even where the effect of varying some parameters, especially fluid properties such as viscosity and density, have not been studied.

The anomaly of using laminar data to correlate turbulent flow data has been mentioned, although in the impinging jet system the stagnation point can be considered in these terms. The use of this approach is most pertinent in mass and heat transfer analogies and further discussion of this approach is left for later sections.

2.2 Heat and Mass Transfer

Momentum transfer from a fluid to a surface produces a velocity gradient at right angles to that surface, the velocity increasing until it attains the velocity of the free stream or, as in the case of the wall jet, until the effect of another boundary is felt. In the latter case a velocity maximum is produced. The process of heat and mass transfer between fluid and surface produces thermal and concentration gradients in much the same way, although a maximum in them is more unusual than in the case of momentum transfer.

Prandtl's mixing length model, based on single values of k and λ, where a packet of fluid dissipates its momentum, heat and mass at the same point, predicts an identical height and shape to the velocity, thermal and concentration boundary layers and implies that the turbulent Prandtl and Schmidt numbers are equal to unity.

For complete similarity of boundary layers the laminar Prandtl and Schmidt numbers must also be equal to unity. In fact for many gaseous systems they are of that order.

With $Pr_{turb} = Pr_{lam} = 1$ an analogy between heat and momentum transfer can be proposed giving:

$$St_{turb} = \tfrac{1}{2}C_f \quad \ldots\ldots \quad (2.13)$$

This was first done by Reynolds and the analogy is known after him. This can be extended for mass transfer:

$$St_{turb} = \tfrac{1}{2}C_f = \frac{Sh_{turb}}{Re} \quad \ldots\ldots\ldots \quad (2.15)$$

The Taylor Prandtl analogy is an extension of this to include the effect of the laminar sublayer.

$$St_{turb} = \frac{\frac{1}{2}C_f}{1 + \frac{U_{lam}}{U_{eff}} (Pr_{lam} - 1)} \quad \ldots\ldots\ldots \quad (2.15)$$

where the velocities are the maximum velocities in their respective layers.

Measurements of turbulent Schmidt and Prandtl numbers indicate that they are not always equal to unity and one relationship derived for $Pr_{turb} \neq 1$ is due to Reichardt (1950):

$$Nu = \frac{\frac{1}{2}C_f \; Re \; Pr}{Pr_{turb} + \sqrt{\frac{1}{2}C_f} \left((Pr - Pr_{turb}) \, a + A \right)} \quad \ldots\ldots\ldots \quad (2.16)$$

where a is a quantity allowing for the sublayer and A is a function of Pr_{turb}.

The Chilton Colburn (1934) analogy is a popular one claimed to give a correlation of within 14%. Momentum, heat and mass transfer are correlated in terms of 'j' factors, again using only laminar parameters, such that:

$$j_M = j_H = C_f / 2 \quad \ldots\ldots\ldots \quad (2.17)$$

where
$$j_M = \frac{k \, M}{U \rho} \, Sc^{2/3} \quad \ldots\ldots\ldots \quad (2.18)$$

and
$$j_H = \frac{Nu}{Re \; Pr^{1/3}} \quad \ldots\ldots\ldots \quad (2.19)$$

It is assumed in these relationships that the mass and heat transfer rates are small enough not to affect momentum transfer. Many analytical approaches use the analogies outlined above, or other, often more complex analogies, to predict heat and mass transfer rates in a system where the momentum equations only are solved. Equation (2.17) is only applicable in two dimensional boundary layer flow. For the stagnation point, for instance, the radial shear stress plots seem to approach the region asymptotically, predicting infinite transfer of heat and mass in this area. Conversely, it may be reasoned that

at the stagnation point itself there is no drag on the fluid implying via the Reynolds analogy zero transfer of heat or mass.

2.2.1 Universal Theories

As the transfer of mass or heat occurs at the fluid/solid interface, even though the boundary layers might extend out into the flow, it is in the wall region that care has to be taken to use accurate relationships to predict these fluxes. Spalding and Patankar (1967) used the Van Driest (1956) modification to the Prandtl mixing length distribution near the wall, and the following expression for effective conductivity of heat or mass in this region.

$$\frac{\mu_{tot}}{\sigma_{tot}} = \frac{\mu_{lam}}{\sigma_{lam}} + \frac{1}{\sigma_{turb}} (\mu_{eff} - \mu_{lam}) \quad \ldots\ldots (2.17)$$

where σ is the Prandtl or Schmidt number. In the main stream of the flow the conserved property transfer across a unit of the computational grid can be calculated using the completely turbulent value for σ . In the wall layer the total values from equation (2.17) are used. Values the authors obtained via this procedure compare well with published data although they present no values specifically for the wall jet.

Wolfstein (1968) uses an almost identical relationship to (2.17).

$$\frac{\mu_{tot}}{\sigma_{tot}} = \frac{\mu_{lam}}{\sigma_{lam}} = \frac{\mu_{turb}}{\sigma_{turb}} \quad \ldots\ldots\ldots (2.18)$$

He derives a relationship between the stagnation point Stanton number and the slot Reynolds number and produces heat transfer profiles across the plate. Overlapping with this section and the Empirical Law theories is the work of Baker (1967). Working on mass transfer by transpiration across a porous wall to a wall jet he uses two solution techniques. The first is based on Prandtl's hypothesis, with modified empirical input, and the second

a 'parametric' method with an assumed velocity profile plus auxiliary empirical relationships. He finds similar problems to Spalding and Patankar (1967) in his first method in the choice of k and λ values.

2.2.2 Specific Theories

Dawson and Trass use the complex mass transfer analogy of Sherwood (1959) which is specifically for a turbulent boundary layer. The final wall jet model derived is highly dependent on the laminar Schmidt number. Correlations with work on napthalene erosion with air jets and cinnamic acid erosion with water jets over a wide range of Sc is good. Some of the napthalene data is presented with that of the present work in chapter four.

2.2.3 Empirical Law Theories

The lower the level of theoretical approach the more usual it is to find an analogy being used. Leont'ev uses the Reynolds analogy to convert his wall jet friction law to a prediction of heat transfer. He compares his work successfully to the data of Seban and Back (1961, 1962).

2.2.4 Dimensional Analysis Theories

The use of the various analogies outlined at the beginning of this section in many of the other theoretical approaches underlines the importance of this method. Much heat transfer data is correlated in expressions of the form

$$Nu = A\, Re^{B}\, Pr^{C} \quad \ldots\ldots\ldots \quad (2.19)$$

where A, B and C are constants. The choice of values for powers B and C is often made by analogy from other work. Gardon and Cobonpue (1961) correlate their heat transfer from an impinging jet data for the stagnation point using an exponent of 0.5 on Re and 0.3 on Pr. The former value comes from the type of analysis made by Frossling (2.1.8) and the latter which is

a value universally adopted is probably due to the work of Pohlhausen (1921). He found that the ratio of thermal to momentum boundary layer thicknesses was given by $Pr^{1/3}$.

A popular approach in mass transfer is the definition of an equivalent stagnant film model. Ignoring the complexities of solving a variable boundary layer thickness of unknown flow characteristics, a film providing the total resistance to mass transfer is defined by a dimensionless relationship. The film is assumed to be stagnant and Stephan-Maxwell diffusion equations are used to calculate the mass transferred.

This approach is used by Carlton and Oxley (1967b) and is especially interesting in the present context as they were predicting mass transfer in a vapour deposition system in cross flow over cylinders.

They define a mass transfer coefficient from:

$$k = D_{AB} \frac{P}{\delta_f RT} \quad \ldots\ldots\ (2.20)$$

and calculate δ_f the film thickness by using the Chilton Colburn analogy on relevant heat transfer work. This value of δ_f is then used as the diffusion path in the computer aided solution of the Stephan-Maxwell equations.

2.3 Discussion of the Various Approaches

The universal theory approach is the most desirable from an aesthetic and scientific viewpoint. The use of the Kolmogorov-Prandtl turbulence model as employed by Wolfstein, indicates that a parallel method of solution for the axially symmetric impinging jet is possible. The Specific theory approach is mainly applicable to the wall jet region and quite a number of investigations using different limiting assumptions have proved useful. The Empirical Law theory has not been directly applied to the system, although available empirical data on the impinging jet is quite comprehensive.

Dimensional analysis techniques are by far the easiest to apply, and the available heat transfer data on impinging jets could be used directly via an analogy to predict mass transfer rates. It is unfortunate that the use of laminar parameters in many analogies makes the relevance of this type of approach open to suspicion. The kind of method used by Carlton and Oxley offers the chance to concentrate on the physio-chemical aspects of mass transfer in vapour deposition systems, although the physical model of an equivalent stagnant film is not appealing.

2.4 Available Empirical Data

Most of the momentum data available is confined to the wall jet region. Poreh and Cermak (1959) have presented data on an impinging water jet. Poreh, Tsuei and Cermak (1967), Bradshaw and Love (1959), Poland (1967) and Hrycak et al (1970) have between them measured the pressure profile on the plate, wall jet velocities and velocity profiles and the effect on these of jet/plate distance. Other workers have made contributions in the field. For the wall jet velocity decay with radial distance, Poland, at distances from the stagnation point of $R/b > 0.27$, gives:

$$\frac{U_{Ro}}{U_e}\left[\frac{b}{d}\right] = 1.18\left[\frac{R}{b}\right]^{-1.05} \quad \ldots\ldots\ (2.21)$$

Poreh, Tsuei and Cermak give:

$$\frac{U_{Ro}}{U_e}\left[\frac{b}{d}\right] = 1.32\left[\frac{R}{b}\right]^{-1.1} \quad \ldots\ldots\ (2.22)$$

Bradshaw and Love's data gives:

$$\frac{U_{Ro}}{U_e}\left[\frac{b}{d}\right] = 1.10\left[\frac{R}{b}\right]^{-1.04} \quad \ldots\ldots\ (2.23)$$

and Poreh and Cermak at $R/b > 0.3$

$$\frac{U_{Ro}}{U_e}\left[\frac{b}{d}\right] = 0.835\left[\frac{R}{b}\right]^{-1.0} \quad \ldots\ldots\ (2.24)$$

the exponent of -1.0 in the last case comes from the restrictions of their theoretical model as discussed in section (2.1.11).

Although the data would seem best correlated in terms of R/d instead of R/b only Hrycak et al do this to give:

$$\frac{U_{Ro}}{U_e} = 1.4\left[\frac{d}{R}\right]^{1.12} \quad \ldots\ldots\ (2.25)$$

The rate of growth of the wall jet boundary layer in terms of $\delta_{\frac{1}{2}}$, where $\delta_{\frac{1}{2}}$ is the height of the boundary layer where $U_R = \frac{1}{2}U_{Ro}$ is also studied. Bakke (1957) gives:

$$\delta_{\frac{1}{2}} \propto R^{0.94} \quad \ldots\ldots\ldots \quad (2.26)$$

Poland gives:

$$\frac{\delta_{\frac{1}{2}}}{b} = 0.02 \left[\frac{R}{b}\right]^{1.16} \quad \ldots\ldots\ldots \quad (2.27)$$

and Poreh, Cermak and Tseui:

$$\frac{\delta_{\frac{1}{2}}}{b} = 0.098 \left[\frac{R}{b}\right]^{0.9} \quad \ldots\ldots\ldots \quad (2.28)$$

Only one wall shear stress law is available for radial wall jets from Poreh, Cermak and Tseui:

$$\frac{\tau}{\rho U_{Ro}^2} = 0.06 \left[\frac{U_{Ro}\delta}{\nu}\right]^{-0.3} \left[\frac{b}{R}\right]^{0.16} \quad \ldots\ldots \quad (2.29)$$

Although two similar, and less complex, relationships are available for plane wall jets, from Bradshaw and Gee (1962).

$$\frac{\tau}{\frac{1}{2}\rho U_{Ro}^2} = 0.0315 \left[\frac{U_{Ro}\delta}{\nu}\right]^{-0.182} \quad \ldots\ldots \quad (2.30)$$

and Sigalla (1958)

$$\frac{\tau}{\frac{1}{2}\rho U_{Ro}^2} = 0.0565 \left[\frac{U_{Ro}\delta}{\nu}\right]^{-0.25} \quad \ldots\ldots \quad (2.31)$$

although Sigalla's work has been critisised by Bradshaw and Gee.

In the region of proposed potential flow around the stagnation point equations are quoted based on limited data.

Poreh and Cermak give:

$$\frac{U_{Ro}}{U_e}\left[\frac{b}{d}\right] = 81.7\left[\frac{R}{b}\right] \quad \ldots\ldots \quad (2.32)$$

and Bradshaw and Love:

$$\frac{U_{Ro}}{U_e}\left[\frac{b}{d}\right] = 17.7\left[\frac{R}{b}\right]^{0.51} \quad \ldots\ldots\ldots \quad (2.33)$$

This type of correlation is criticised by Tani and Komatsu (1966) who fit a polynomial tc their data. Snedeker and Donaldson (1964) give graphs of the stagnation point velocity gradient. Their work is analysed in the next chapter.

The velocity profile plots of some of the workers mentioned above show that the velocity profile in the wall jet is radially similar, and that the shape is well described by Glauert's analytical profile. In addition detailed analysis of the shape of the velocity profile near to the wall has been made by Schwartz and Cosart (1961) and Dickenson (1963) who both found a fourteenth power law fitted the velocity profiles, rather than a seventh power law, which is often assumed in turbulent boundary layer flows. Their work then implies for $0 \leqslant h \leqslant \delta$:

$$\frac{U_R}{U_{Ro}} = \left[\frac{h}{\delta}\right]^{1/14} \quad \ldots\ldots\ldots \quad (2.34)$$

2.4.1 Heat Transfer Data

Many workers have studied heat transfer from an impinging jet. Much of the work is unfortunately irrelevant to the present study as the jets were placed too close to the plate for the flow to become fully developed. This is the case for the work of Huang (1964) and Sitharamayya and Subba Raju (1969). The work of Smirnov et al (1961), although using a fully developed

impinging jet, can be disregarded in the present context as the walls of the apparatus were very close to the jet in their enclosed experimental system, and wall effects will then be very important. Heat transfer in a wall jet has been investigated by Jakob et al (1950) and Zerbe and Selna (1946), both using a slotted jet to produce a plain wall jet. In the wall jet region Jakob et al found:

$$Nu \propto Re^{0.8} \left[\frac{R}{d}\right]^{-0.4} \quad \ldots\ldots\ldots \quad (2.35)$$

Zerbe and Selna found:

$$Nu \propto Re^{0.65} \quad \ldots\ldots\ldots \quad (2.36)$$

Gardon and Cobonpue (1961) and Perry (1954) have investigated heat transfer from a fully developed axially symmetric impinging jet. Gardon and Cobonpue present their data as a series of radial heat transfer profiles and a dimensionless correlation of these in the form of a scatter diagram of Nu/Nu as f (R/b), and a correlation of the stagnation point heat transfer rates to give:

$$Nu_o = 13\ Re^{0.5}\ d/b \quad \ldots\ldots\ldots \quad (2.37)$$

Perry correlates his data in terms of an overall heat transfer rate for the whole plate and presents one radial profile of Nu/Nu_o as f (R/b). His overall correlation is of the form:

$$Nu_t \propto Re^{0.7}\ Pr^{1/3} \quad \ldots\ldots\ldots \quad (2.38)$$

where a constant of proportionality is found by reference to a table.

2.4.2 Mass Transfer Data

Mass transfer processes can be of three different types, transpiration or mass injection through a porous wall into the fluid flow, evaporation or dissolution, where a solid substrate is dissolved by the passing flow as in

napthalene erosion, and finally processes like vapour deposition that involve chemical reaction at the fluid/solid boundary. Data from any of these systems will, with certain exceptions, have a basic similarity.

The work of Kumada and Mabuchi (1970) is important in considering the stagnation point mass transfer. For napthalene erosion by a slotted jet they give:

$$Sh_o = 1.42\ Re^{0.58}\ Sc^{0.43} \left[\frac{d}{b}\right]^{0.62} \quad \ldots\ldots \quad (2.39)$$

Rao and Trass (1964) and Dawson and Trass (1966) have investigated mass transfer from impinging axially symmetric jets. Rao and Trass using a water system to erode cinnamic acid produce a high Reynolds number power dependence for stagnation point mass transfer:

$$Sh_o = 0.107\ Re^{1.06} \left[\frac{d}{b}\right]^{0.54} \quad \ldots\ldots\ldots \quad (2.40)$$

Mechanical erosion is claimed by Dawson and Trass to be very important in this system. The latter workers produce data for napthalene erosion and derive an equation to predict mass transfer in the wall jet, as discussed in section (2.2.2), and apply this to their napthalene work and cinnamic acid data with corrections for mechanical erosion. Their theoretical equation is highly dependent on the Schmidt number and the relevant relationship is derived in chapter three and demonstrated in chapter four.

Baker (1967), whose theoretical approach was discussed in section (2.2.1), performed experiments on transpiration across a porous wall into a radial wall jet. The mass transfer from a laminar impinging jet has been analysed by Scholtz and Trass (1970) in the stagnation region and previously in the wall jet region (Scholtz (1963)).

2.5 The Free Turbulent Jet

A section is included on some of the work published on the free turbulent jet, as, not only is it one region of the impinging jet but certain properties of the free jet will be used in succeeding sections. The publications of Ambramovich provide a wide ranging source of technical data and analyses on most aspects of turbulent jets. A review of the general features of jets is included by Gauntner et al (1970) in the context of a general review on impinging jets.

The structure of the jet is initially that of a 'potential' core, or region of flow identical to that prevailing just inside the jet orifice. This persists for about six jet diameters downstream from the nozzle until the turbulent shear produced by the action of the issuing fluid on the surrounding fluid extends right across the section. The jet is then said to be fully developed. Different authors often give widely different values for the effective length of the potential core. Gauntner et al produce a theoretical analysis which predicts a length of 6.1d and quote various authors as having measured values from 4.7 to 7.7d. In the practical work reported in succeeding chapters, to ensure a fully developed jet was being used, the minimum jet plate distance was limited to 8d.

In the potential core the centre line maximum velocity is constant, outside this it decays as the inverse of the distance from the jet origin as for:

$$\frac{U_{ho}}{U_e} = C \frac{d}{h} \quad \ldots\ldots\ldots (2.41)$$

where C can also be taken as the length in jet diameters of the potential core. This value is thought to be a universal constant and not a function of jet Reynolds number. Hrycak et al (1970) investigated the value of C and found it to be a small function of Reynolds number (6.0 to 6.7) but

essentially constant above Re = 10,000. Wakelin (1966) reports similar findings. The variation for a fully developed turbulent jet is small enough not to be detected in the range of Reynolds numbers used in the present experiments.

The entrainment rate for a freely discharging jet is largely independent of jet conditions and Hinze (1949) has developed a mass flux relationship to predict the mass flowrates at different stations in the jet.

$$m = m_e (0.2\ b / 0.5\ d - 1) \ldots\ldots \quad (2.42)$$

The velocity profile of the fully developed jet has been predicted by various workers using a variety of turbulence models. Taylor's model as discussed in section (2.1.7) is the most successful. The profile approximates well in fact to an error curve, which is given by Poreh and Cermak (1959) as

$$\frac{U_h}{U_{ho}} = \exp(-100\ R^2 / b^2) \ldots\ldots \quad (2.43)$$

There is much conflicting data in the literature on the critical Reynolds number to produce a fully turbulent jet where the transfer mechanism is dominated by eddy diffusion. Vickers (1959) suggests a value of 1,000. Elrod (1954) suggests a value of 2,000 for jets issuing from any orifice where the significant length in the Reynolds number is the equivalent hydraulic diameter. Gardon and Cobonpue classify turbulent jets as having Reynolds numbers larger than 14,000. Other workers introduce the concept of transition or semi-turbulent jets as an intermediate state between fully laminar and fully turbulent jets. Hrycak et al, in an attempt to clarify the position performed flow visualisation experiments, using smoke injection into the flow. Their work suggests a threshold of about 4,000.

The value accepted by the different workers depends a lot on their definition of the fully turbulent jet and on whether the free jet flow in

their system had to produce its own turbulence or merely maintain the turbulence already present in the jet nozzle. For an orifice jet the flow inside the short exit section may well be smooth plug flow and the free jet turbulence will have to be produced by the shearing action of the free jet alone. A high threshold value of 14,000 is then feasible. If the jet nozzle consists of a long pipe the flow inside the pipe will be turbulent at a Reynolds number of about 2,000 depending on the internal roughness. Once this turbulence has been produced the jet has enough momentum to maintain a turbulent flow, as eddies are produced in jets issuing from orifices with Reynolds numbers as low as 1,000 as found by Hrycak et al.

For this reason the jets used in the present work were all pipe jets and the flow was assumed turbulent above a Reynolds number of 2,000.

At the higher end of the velocity scale the jet is affected by the onset of supersonic flow. Without a specially designed converging-diverging nozzle, it is thought impossible to produce velocities in the free jet above the velocity of sound in the jet fluid. For ordinary nozzles, either pipes or orifices, flows at Reynolds numbers implying supersonic velocities produce weak shock patterns on the emergence of subsonic highly compressed fluid from the nozzle. This type of jet was found by Gardon and Cobonpue to produce a periodicity in their measured stagnation point heat transfer rates as the jet/plate distance was altered. This was presumably due to the periodic nature of the shock pattern in the underexpanded free jet. No experiments in this region were attempted in the present work but some of the data of Dawson and Trass included in chapter four is within the region.

2.6 The Role of Turbulence in Heat and Mass Transfer

Increasing the frequency or magnitude of the fluctuating velocity component in turbulent flow has been seen to influence the rate of transfer of conserved properties. Gardon and Akfirat (1965) noted that heat transfer rates at the stagnation point of an impinging jet could be increased by increasing the turbulence level in the free jet. The turbulence level of a flow can be quantified most conveniently by the 'intensity' of turbulence which is the root mean squared value of the fluctuating velocity component divided by a reference velocity. This value can be raised by introducing a grid into the flow

Similar results to that of Gardon and Akfirat have been noted in stagnation flow in other systems. Gostkowski and Costello (1970) plotted $Nu/Re^{0.5}$ against intensity of turbulence for heat transfer at the stagnation point of a sphere. At low turbulence levels there was no dependence of heat transfer on turbulence level, but at higher turbulence levels, there was a significant relationship. Kestin and Maeder (1957) found that heat transfer rates were not independent of turbulence level in flow passed cylinders.

Some universal theories for turbulent flow allow the inclusion of these phenomena in their application to turbulent flow analyses. The works of Spalding and Wolfstein need the turbulence profile at the input side of the flow field for one of their initial conditions. This data must be empirical. There is no way of deriving the profile at any point in a flow field unless the profile at some earlier stage is known. The turbulence levels generated in the flow field can however be calculated. What these models fail at the moment to show is how the level of turbulence in the free stream affects stagnation flow where the controlling transfer mechanism is probably laminar diffusion. Work by Jones and Launder (1969) attempts to model this effect

by considering the penetration of the laminar sublayer, not by the turbulent eddies, but by some augmented mixing mechanism which is set up by these eddies acting above the sublayer.

As for the augmenting of turbulence levels to enhance transfer of conserved properties, this will only be effective if the amount of turbulence generated is of the same magnitude or higher than that generated by the flow itself. In this way it is possible to see how transfer rates from two identical jets will be different for the same Reynolds number and geometric conditions, if the turbulence levels in the exit plane of the two jets are different. A jet issuing from a tube jet at Re = 2500 will be fully turbulent whereas that from an orifice jet will be laminar until turbulence is set up by the shear produced between the jet and the quiescent surrounding fluid. As the same process is also occuring in the already turbulent jet from the tube, the turbulence levels for this system will always be higher than in the other. At higher Reynolds numbers the turbulence produced by the shearing mechanism will be proportionally larger and produce the bulk of the turbulence, and so turbulence levels and thus transfer rates will be similar for both systems. Even so the idea of variation in turbulence levels between seemingly identical systems goes a long way towards explaining the variation in measured heat and mass transfer rates between different workers.

Turbulence can also by augmented in the boundary layer by surface roughness, if this roughness extends above the laminar sublayer. These protrudences into the flow field act as turbulence generators by breaking up the boundary layer flow and increasing the turbulence level downstream, thus increasing the transfer of conserved properties. Because of the roughness effect care was taken in the present work to provide as smooth a surface as possible upon which the jet would impinge.

CHAPTER THREE

THEORETICAL ANALYSIS

3.0 THEORETICAL ANALYSIS

In this section an attempt will be made to predict the local mass transfer coefficient as a function of radial distance from the stagnation point, and the stagnation point value itself, as a function of jet exit properties, properties of the carrier gas and diffusing species and the geometry of the impinging jet system.

Various limiting assumptions are made, the most important of which is that of dilute solutions of diffusing species so that mass transfer effects on momentum transfer can be ignored. This assumption is valid in the three systems considered in later sections. Another important assumption is made in the ignoring of heat transfer effects. The special modifications to the theory for the vapour deposition systems are considered in a separate theoretical chapter.

A model of the type classified in the preceding section as a Universal theory will not be attempted for the entire impinging jet system but the Frossling solution of the laminar sublayer at the stagnation point, as presented by Schlicting, will be extended to predict mass transfer rates in this region. As the prediction of the stagnation point value is of special significance in determining the overall rate of deposition in the system, two other approaches are investigated. The first is by a method suggested by Reshotko and Cohen (1955) based on a dimensional analysis. The second is using a heat/mass transfer analogy on the available heat transfer data. To predict the radial mass transfer profile under the impinging jet the heat transfer analogies are extended further and a Von Karman integral technique is applied to the wall jet region.

The impinging jet consists of two established regions on the plate, the stagnation point and the wall jet. It would be convenient if the mass transfer in both regions could be described, not only in terms of the same

variables, Sh, Re, b etc., but in terms of the same power law relationship between these variables. If this were approximately true the shape of the transfer profiles produced by any jet issuing at any Reynolds number at variable jet plate distances would be similar. The heat transfer data of Gardon and Cobonpue (1961) gives a stagnation point dependence of heat transfer proportional to $Re^{0.5}$, and produces a dimensionless profile from the stagnation point to include the start of the wall jet region, albeit with considerable scatter. Perry (1954) gives a unique heat transfer profile implying no variation with system variables. Wall jet data indicates, however, a higher Reynolds number dependence implying that a good dimensionless profile is unlikely and for accurate prediction the transfer profile would have to be considered as two distinct regions joined by a transition zone.

3.1 Extension of Frossling's Stagnation Point Solution

Schlicting (1968) presents the results of a theoretical investigation by Frossling of axially symmetric stagnation flow. In the solution, potential flow is assumed in the body of the flow in this region changing to viscous flow on approaching the wall. Frossling solved the Navier-Stokes equations to give numerical values for U_R/U_{Ro}, where U_{Ro} is then the radial potential flow component.

Defining the height of the viscous boundary layer δ as the position where $U_R = 0.99U_{Ro}$, an expression for δ can be deduced from the tabulated values (Schlicting, table(5.1)) such that:

$$\delta_o = 1.969 \sqrt{\frac{\eta}{\rho a}} \quad \ldots\ldots\ldots \quad (3.1)$$

where the constant a is given by:

$$U_{Ro} = a R \quad \ldots\ldots\ldots \quad (3.2)$$

Two sets of data are considered to predict values for a, that of Poreh and Cermak (1959) and Snedeker and Donaldson (1964). The first is expressed as

$$\frac{U_{Ro}}{U_e} = 78.2 \frac{b}{d} \frac{R}{b} \quad \ldots\ldots \quad (3.3)$$

the second for free jets (see section 3.2):

$$\frac{U_{Ro}}{U_e} = 120 \frac{d^2}{b^2} \frac{1}{d} \quad \ldots\ldots \quad (3.4)$$

Poreh and Cermak's correlation would give a value of δ implying that the stagnation Sherwood number is independent of b the jet/plate distance. This is not indicated by the available heat transfer data and as the correlation comes from very limited data, only Snedeker and Donaldson's results are considered further.

Combining (3.1) and (3.4) gives:

$$\delta_o = 0.1797 \, b \, Re^{-0.5} \quad \ldots\ldots \quad (3.5)$$

δ_o is then the momentum boundary layer thickness. To deduce the mass transfer boundary layer thickness the relationship attributed to the initial work of Pohlhausen (1921) will be used, namely that the ratio of the momentum and thermal boundary layers is equal to the third root of the Prandtl number, as for:

$$\delta / \delta_{th} = Pr^{1/3} \quad \ldots\ldots \quad (3.6)$$

A similar relationship for mass transfer might be expected giving:

$$\delta / \delta_{conc} = Sc^{1/3} \quad \ldots\ldots \quad (3.7)$$

For diffusion down a concentration gradient Fick's first law gives:

$$N_A = D_{AB} \frac{d \rho_A}{d h} \quad \ldots\ldots \quad (3.8)$$

Mass transfer across a boundary layer is often described in terms of a mass transfer coefficient k and the concentration difference across the boundary layer, as for:

$$N_A = k\ (\Delta \rho_A) \quad \ldots\ldots\ (3.9)$$

If the concentration gradient can be considered linear then:

$$\frac{d\,\rho_A}{d\,h} = \frac{\Delta \rho_A}{\delta_{conc}} \quad \ldots\ldots\ (3.10)$$

Combining equations (3.8), (3.9) and (3.10) gives:

$$k = D_{AB} / \delta_{conc} \quad \ldots\ldots\ (3.11)$$

From the definition of the Sherwood number and equations (3.5) and (3.7) the stagnation Sherwood number is given by:

$$Sh_o = 5.565\ \frac{d}{b}\ Sc^{1/3}\ Re^{0.5} \quad \ldots\ldots\ (3.12)$$

The shape of the velocity profile in Frossling's solution is not linear across δ. The shape of the concentration is assumed to be similar. The profile can only be taken as linear over about one fifth of the boundary layer. This line has a gradient 1.789 times that implied by the assumptions leading to equation (3.12). Including this factor gives:

$$Sh_o = 9.956\ \frac{d}{b}\ Sc^{1/3}\ Re^{0.5} \quad \ldots\ldots\ (3.13)$$

3.2 Adaption of Reshotko and Cohen's Stagnation Point Model

Reshotko and Cohen (1955) suggest the following model for heat transfer at a stagnation point:

$$h = \frac{K}{\sqrt{V}} \left[\frac{Nu}{\sqrt{Re_W}}\right] \sqrt{a} \quad \ldots\ldots\ (3.14)$$

where K is the thermal conductivity of the gas at the solid/gas interface, Re_W the local Reynolds number and a the radial velocity gradient at the stagnation point as defined in equation (3.2)

The corresponding mass transfer relationship will be:

$$k = \frac{D_{AB}}{\sqrt{\nu}} \left[\frac{Sh}{\sqrt{Re_W}}\right] \sqrt{a} \quad \ldots\ldots\ldots \quad (3.15)$$

Reshotko and Cohen present a family of plots of Nu/Re_W against the ratio of wall to gas temperatures for various values of Pr.

For axisymmetric flow, a relationship can be derived between $Nu/Re_W^{0.5}$ and Pr for the isothermal case, where gas and solid at the wall are in equilibrium, from points taken from each curve.

This relationship is

$$\frac{Nu}{Re_W} = 0.35\ Pr + 0.41 \quad \ldots\ldots\ldots \quad (3.16)$$

The Chilton-Colburn analogy (see section 2.2) can be expressed as:

$$\frac{Sh}{Re\ Sc^{1/3}} = \frac{Nu}{Re\ Pr^{1/3}} \quad \ldots\ldots\ldots \quad (3.17)$$

Combining equations (3.17) and (3.16) gives:

$$Sh_o = (0.35Pr + 0.41) \frac{Sc^{1/3}}{Pr^{1/3}} Re_W \quad \ldots\ldots\ldots \quad (3.18)$$

The isothermal case producing equation (3.16) is equivalent to chemical equilibrium at the wall. Combining equations (3.18) and (3.15)

$$k_o = \frac{D_{AB}}{\sqrt{\nu}} (0.35Pr + 0.41) \frac{Sc^{1/3}}{Pr^{1/3}} \sqrt{a} \quad \ldots\ldots\ldots \quad (3.19)$$

The velocity gradient a is taken, as in the previous section, from the data of Snedeker and Donaldson. Their work is reported in terms of plots of

$$\frac{d}{U_{ex}} \left[\frac{dU_{Ro}}{dR}\right] R = 0 \quad \text{vs.} \quad \frac{b}{d}$$

for subsonic and underexpanded jets. Using their data for values of b/d in the fully developed impinging jet and for subsonic jets, a linear relationship can be deduced of the form:

$$\frac{d}{U_{ex}} \left[\frac{dU_{Ro}}{dR}\right] R = 0 = K \frac{d^2}{b^2} \quad \ldots\ldots\ldots (3.20)$$

The constant K varies for underexpanded and supersonic jets and for subsonic jets is found to be 120.

As $\left[\frac{dU_{Ro}}{dR}\right]_{R=0} \equiv a$, the following relationship can be derived from equations (3.20) and (3.19):

$$Sh_o = 10.95 \sqrt{Re} \frac{Sc^{1/3}}{Pr^{1/3}} (0.35Pr + 0.41) \frac{d}{b} \quad \ldots\ldots (3.21)$$

To predict the data for napthalene erosion with an air jet a value of Pr of 0.74 for air is taken giving:

$$Sh_o = 7.48 \sqrt{Re} Sc^{1/3} \frac{d}{b} \quad \ldots\ldots\ldots (3.22)$$

3.3 Heat Transfer Analogies

As discussed in section (2.4.1) a lot of heat transfer data for the impinging jet is irrelevant to the present work. The equations produced by Gardon and Cobonpue (1961) and Perry (1954) are the two chosen as the most relevant.

3.3.1 Heat Transfer Analogy from Gardon and Cobonpue Data

Gardon and Cobonpue quote a stagnation point relationship:

$$Nu_o = 13 \sqrt{Re} \frac{d}{b} \quad \ldots\ldots\ldots (3.37)$$

based on five different jet diameters but only three Reynolds numbers from 7,000 to 56,000. They give a scatter diagram of Nu/Nu_o vs. R/b. This profile can be used to predict local radial heat transfer rates between $0 \leqslant R/b \leqslant 0.8$. To facilitate this calculation a polynomial can be fitted to the mid points of the scatter band, fig (3.1). Unfortunately a fifth order polynomial is necessary to give a good correlation with these points, namely:

$$\frac{Nu}{Nu_o} \; f\left[\frac{R}{b}\right] = \frac{Nu}{Nu_o} = c_1 + c_2\left[\frac{R}{b}\right] + c_3\left[\frac{R}{b}\right]^2 + \ldots + c_6\left[\frac{R}{b}\right]^5 \quad \ldots (3.38)$$

where $c_1 = 1.00$, $c_2 = -2.115$, $c_3 = -1.546$, $c_4 = 15.617$, $c_5 = -24.153$, $c_6 = 11.743$.

From the Chilton-Colburn analogy equations, (2.37) and (2.38) predict mass transfer rates given by:

$$Sh = 13.0 \sqrt{Re} \; \frac{d}{b} \; \frac{Sc^{1/3}}{Pr^{1/3}} \; \frac{Nu}{Nu_o} \; f\left[\frac{R}{b}\right] \ldots\ldots \quad (3.39)$$

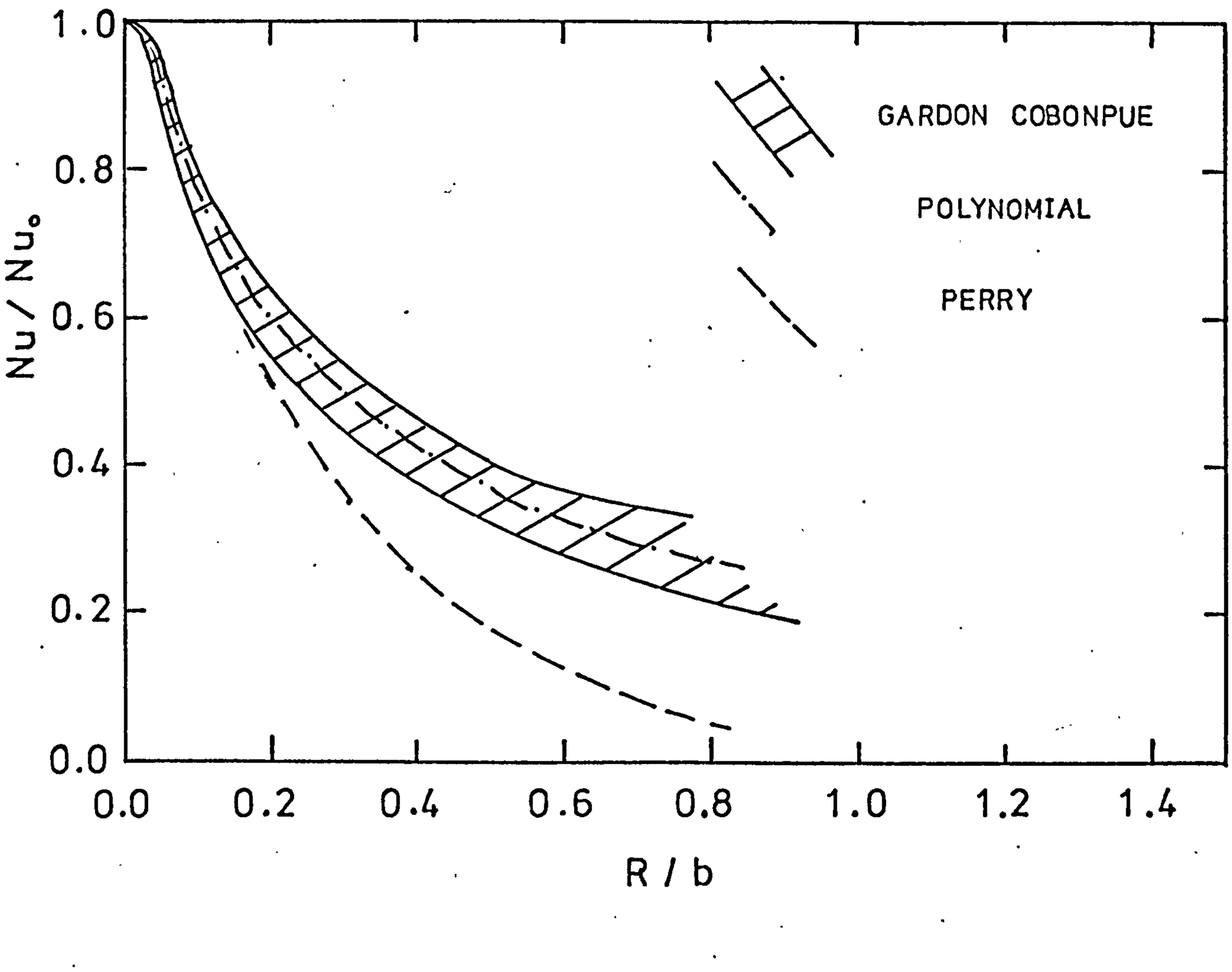
3.3.2 Heat Transfer Analogy from Perry's Data

Perry's correlation is in terms of an overall Nusselt number, averaged over the plate, of the form:

$$Nu_t = \text{Const.} \; Re^{0.7} \; Pr^{1/3} \quad \ldots\ldots\ldots (3.40)$$

The total heat transfer depends on the area considered and Perry gives a table of multiplying factors to calculate the constant in equation (3.40).

It is not clear what significant distance can be used in the Nusselt and Reynolds numbers as Perry uses the diameter of his heat detecting calorimeter, which is numerically equal to one of two jet diameters used to produce his correlation. Only one b/d distance ratio was used, producing an unique dimensionless radial profile. This profile can be conveniently fitted



fig(3.1) DIMENSIONLESS HEAT TRANSFER PROFILES

with an error curve:

$$Nu/Nu_o = \exp (-3.48\ R/b) \ldots\ldots \quad (3.41)$$

for $0 \leqslant R/b \leqslant 0.8$.

If the effective heat transmission range of the impinging jet is taken as a circle radius $R = 0.8b$, the stagnation point Nusselt number implied by equations (3.40) and (3.41) can be deduced leading to the relationship:

$$Sh = 7.83\ Re^{0.7}\ Pr^{1/3}\ \frac{d}{b}\ \exp (-3.48\ R/b) \ldots\ldots \quad (3.42)$$

3.3.3 Equivalent Stagnant Film Model

It is convenient in the section on heat transfer analogies to comment on the equivalent stagnant film model of Carlton and Oxley, discussed in section (2.2.4), as relevant heat transfer data is necessary to the method. For simple, unidirectional mass transfer of one species through another, Fick's law applies, giving:

$$N_A = D_{AB}\ \frac{\partial \rho_A}{\partial h} + \text{bulk flow term} \quad \ldots\ldots \quad (3.43)$$

It is possible to define another equation

$$\int_0^{\delta_f} dh = \int_{\rho_1}^{\rho_2} \frac{D_{AB}}{d\rho_A}$$

where the effect of bulk flow is incorporated into an equivalent stagnant film of thickness δ_f, and equation (3.43) can be rewritten in terms of this compound parameter as $N_A = D_{AB}\ \Delta \rho_A / \delta_f$. The flux N_A can also be expressed in terms of an overall mass transfer coefficient by the expression (3.9).

$$N_A = k\ \Delta \rho_A \ldots\ldots \quad (3.9)$$

giving on combination a similar expression to (3.11) where $k = D_{AB}/\delta_f$.

From the Chilton-Colburn analogy, equation (3.17) and the definition of the Sherwood number:

$$\delta_f = \frac{d\ Pr^{1/3}}{Nu\ Sc^{1/3}} \quad \ldots\ldots\ (3.44)$$

From one of the heat transfer relationships for the impinging jet, the Nusselt number in equation (3.44) can be substituted for in terms of known quantities allowing the calculation of δ_f to be made.

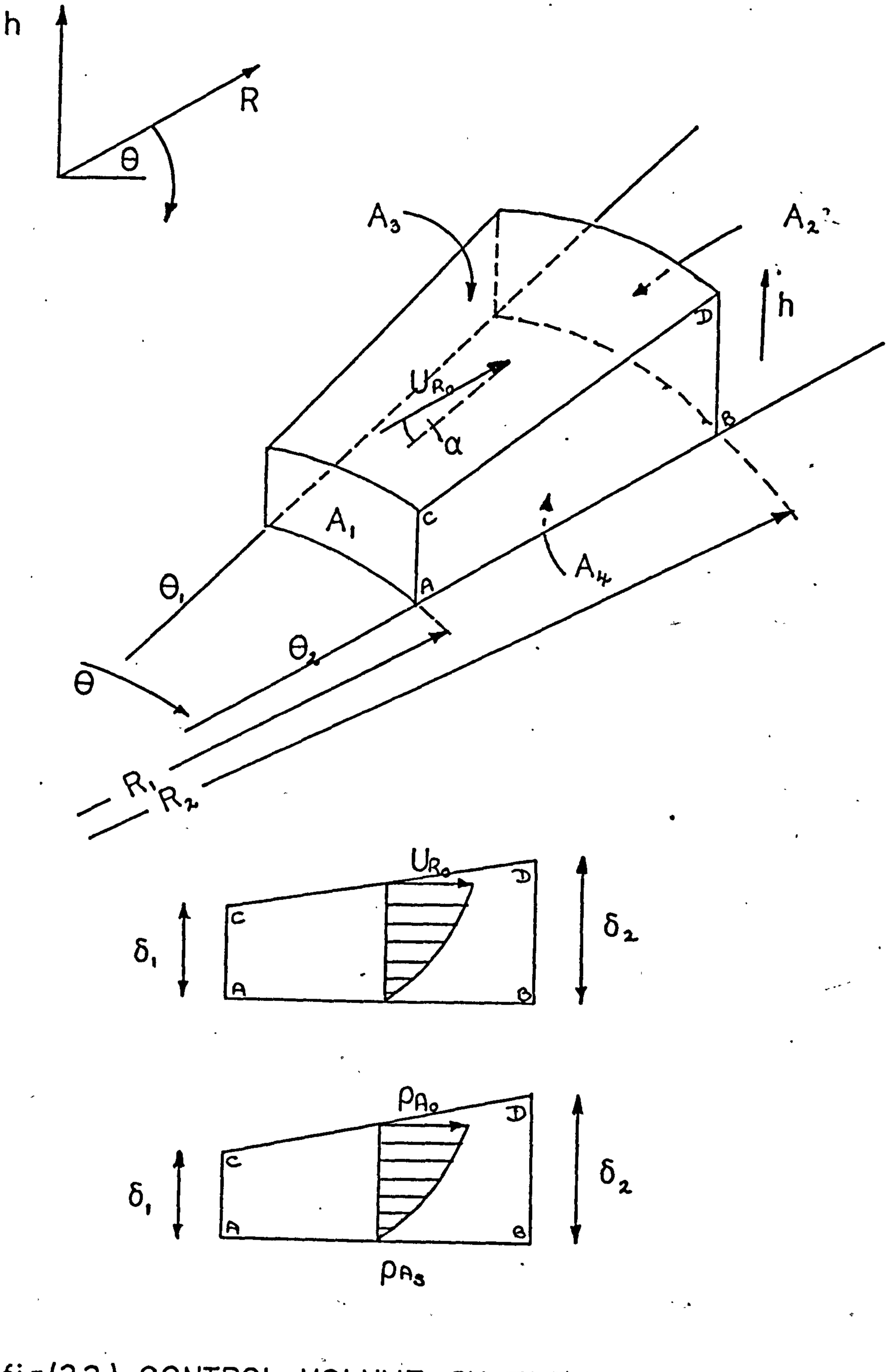
This significant distance is used in the method to solve the three dimensional multicomponent diffusion equations, called the Stephan-Maxwell equations, to produce the overall chemical model of the film. This approach is most useful where the emphasis of the work is on the chemical processes in the system. For the present work, very dilute concentrations of reactant were employed so bulk flow and the presence of reaction products could be ignored. For this case, δ_{conc} can be substituted for δ_f and equation (3.44) reduces back to the Chilton-Colburn analogy.

For the present analysis this approach is not favoured as the emphasis is on the mass transfer processes for which it is possible to derive more meaningful mathematical models as has been done elsewhere in this chapter.

3.4 Prediction of Mass Transfer Rates in the Wall Jet

Calculation is performed initially on a control volume whose upper surface is bounded by the plane of maximum radial velocity U_{Ro} at the position $h = \delta$ and by the surface of the plate $h = 0$, fig (3.2).

Mass transfer is assumed to be on the -h direction. If assumptions (3) and (4) hold, the mathematics are identical for the case of transfer from the plate to the wall jet.



fig(3.2) CONTROL VOLUME IN THE WALL JET

3.4.1 Assumptions

(1) The velocity profile in the wall jet is similar at any radial position and for h = 0 to h = δ is described by:

$$\frac{U_R}{U_{Ro}} = \left[\frac{h}{\delta}\right]^{1/x}$$

(2) The concentration profile is similar to the velocity profile and the concentration and momentum boundary layer heights are the same (Sc_{eff} = 1) therefore:

$$\frac{\rho_{As} - \rho_A}{\rho_{As} - \rho_{Ao}} = \left[\frac{h}{\delta}\right]^{1/x}$$

This follows from Prandtl's viscosity model.

(3) The concentration of the diffusing species above the boundary layer is small and constant (ρ_{Ao} = const.)

(4) Following from (3), mass transfer does not affect momentum transfer.

(5) The system can be considered of two components, products of reaction can be ignored.

(6) The mass transfer to or from the plate is given by the concentration difference across the boundary layer multiplied by a mass transfer coefficient.

(7) The wall jet flow is radially symmetrical.

(8) Heat transfer has no effect on mass or momentum transfer.

3.4.2 Wall Jet Theory

Using cylindrical co-ordinates h, R and θ, derive a Mass balance on reactant species A on the control volume shown in fig (3.2).

$$\int_{\theta_1}^{\theta_2}\int_{h=0}^{h=\delta} R_1^2\,\rho_A\,U\cos\alpha\;\,d\theta\,dh - \int_{\theta_1}^{\theta_2}\int_{h=0}^{h=\delta} R_2^2\,\rho_A\,U\cos\alpha\,d\theta\,dh$$

$$+\int_{\theta_1}^{\theta_2}\int_{R_1}^{R_2} R\,\rho_{Ao}\,U\cos\alpha\,d\theta\,dR = \int_{\theta_1}^{\theta_2}\int_{R_1}^{R_2} R\,k\;\,(\rho_{As}-\rho_{Ao})\,d\theta\,dR \;\ldots\ldots\; (3.45)$$

For the vertical faces the flow can be assumed perpendicular to the faces (the flow seems to emanate from a point source) giving:

$$U\cos\alpha = U_R \;\ldots\ldots\; (3.46)$$

This substitution cannot be made in the third term of equation (3.45), so to eliminate this, a total mass balance on the control volume is derived:

$$\int_{\theta_1}^{\theta_2}\int_{h=0}^{h=\delta} R_1^2\,\rho\,U_R\,d\theta\,dh - \int_{\theta_1}^{\theta_2}\int_{h=0}^{h=\delta} R_2^2\,\rho\,U_R\,d\theta\,dh$$

$$+\int_{\theta_1}^{\theta_2}\int_{R_1}^{R_2} R\,\rho\,U_{Ro}\cos\alpha\,d\theta\,dR = \int_{\theta_1}^{\theta_2}\int_{R_1}^{R_2} R\,k\;\,(\rho_{As}-\rho_{Ao})\,d\theta\,dR \;\ldots\ldots\; (3.47)$$

Multiplying by ρ_{Ao}/ρ :

$$\iint R_1^2\,\rho_{Ao}\,U_R\,d\theta\,dh - \iint R_2^2\,\rho_{Ao}\,U_R\,d\theta\,dh + \iint R\,k\;(\rho_{As}-\rho_{Ao})\frac{\rho_{Ao}}{\rho}\,d\theta\,dR$$

$$= \iint R\,\rho_{Ao}\,U_{Ro}\cos\alpha\,d\theta\,dR \;\ldots\ldots\; (3.48)$$

Combining, to eliminate $\cos\alpha$:

$$\int_{\theta_1}^{\theta_2}\int_{h=0}^{h=\delta} R_1^2\,U_R\,(\rho_A-\rho_{Ao})\,d\theta\,dh - \int_{\theta_1}^{\theta_2}\int_{h=0}^{h=\delta} R_2^2\,U_R\,(\rho_A-\rho_{Ao})\,d\theta\,dh$$

$$= \int_{\theta_1}^{\theta_2}\int_{R_1}^{R_2} R_{av}\;\;(k\;\;(\rho_{As}-\rho_{Ao}))\;\;(1-\frac{\rho_{Ao}}{\rho})\,d\theta\,dR \;\ldots\ldots\; (3.49)$$

Contracting the control volume so that $R_2 - R_1 = \delta R$ and $R_2 = R_1 + \delta R$

equation (3.49) becomes:

$$\frac{d}{dR} \int_{\theta_1}^{\theta_2} \int_{h=0}^{h=\delta} 2 R U_R (\rho_{As} - \rho_{Ao}) \, dh \, d\theta = \int_{\theta_1}^{\theta_2} R (k (\rho_{As} - \rho_{Ao})) (1 - \frac{\rho_{Ao}}{\rho}) \, d\theta \quad ..(3.50)$$

From assumption (7):

$$\int_{\theta_1}^{\theta_2} d\theta = 2\pi \text{ for } \theta_1 = 0^\circ, \theta_2 = 360^\circ \quad ..... (3.51)$$

and solving for k in equation (3.50):

$$k = \frac{d}{dR} \int_{h=0}^{h=\delta} 2 U_R \frac{\rho_A - \rho_{Ao}}{\rho_{As} - \rho_{Ao}} \frac{\rho}{\rho - \rho_{Ao}} \, dh \quad ..... (3.52)$$

From assumptions (1) and (2):

$$k = \frac{d}{dR} \int_{h=0}^{h=\delta} 2 U_{Ro} \left[\frac{h}{\delta}\right]^{1/x} \left[1 - \frac{h}{\delta}\right]^{1/x} \frac{\rho}{\rho - \rho_{Ao}} \, dh \quad ..... (3.53)$$

Defining $\Delta = h/\delta$ ..... (3.54)

$$dh = d\Delta \, \delta \quad ..... (3.55)$$

$$k = 2 \frac{d}{dR} \frac{\rho}{\rho - \rho_{Ao}} U_{Ro} \delta \int_0^1 (\Delta - \Delta^2)^{1/x} \, d\Delta \quad ..... (3.56)$$

The integral is now no longer a function of R and will be referred to as $\int \Delta$ where:

$$\int \Delta = \int_0^1 (\Delta - \Delta^2)^{1/x} \, d\Delta \quad ..... (3.57)$$

Two functions need to be known to evaluate equation (3.56) namely U_{Ro} and as f (R). There are many empirical equations for the former as discussed in section (2.4), from these the equation of Hrycak et al (1970) is selected:

$$\frac{U_{Ro}}{U_e} = 1.4 \left[\frac{d}{R}\right]^{1.12} \quad \ldots\ldots\ldots (2.25)$$

There are only two empirical equations for δ as f(R), due to Poland, equation (2.27), and Poreh et al, equation (2.28). Neither equation contains a Reynolds number term. Some small dependence on Re would be expected in boundary layer flow. For example for plane flow over a flat plate, Bennet and Myers (1962) derive a theoretical relationship to show that $\delta \propto Re^{-0.2}$.

In the following section an expression is derived for δ as f (R, Re) for the radial wall jet. One important assumption made initially as a consequence of Prandtl's mixing length viscosity model is that the plane of maximum radial velocity is a plane of zero shear.

From Prandtl's model

$$\mu_{eff} = \rho l^2 \left|\frac{dU_R}{dh}\right|$$

so for $h = \delta$, $U_R = U_{Ro}$ and $dU_R/dh = 0$, therefore $\mu_{eff} = 0$.

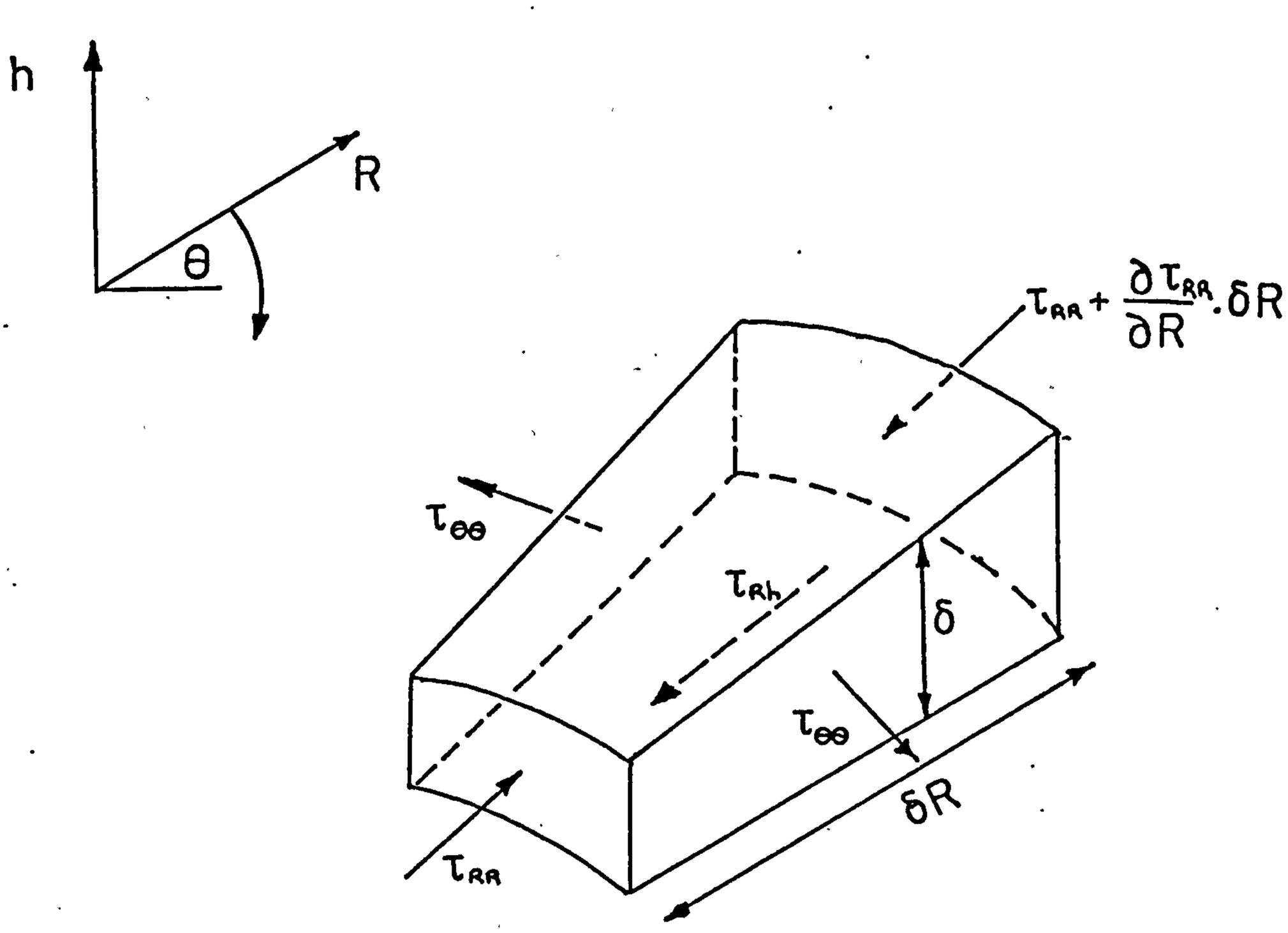
3.4.3 Prediction of Growth Rate for the Wall Jet Boundary Layer

For a differential element, fig (3.3), of width δR and height δ the shear stresses acting on the element are τ_{Rh}, τ_{RR}, $\tau_{\theta\theta}$, $\tau_{\theta R}$, $\tau_{R\theta}$, $\tau_{h\theta}$, $\tau_{\theta h}$, τ_{hR} and τ_{hh}. Expressions for these shear stresses are given by Bird, Stewart and Lightfoot (1960). As all resolution will be in the R direction, the component effects of τ_{hR} and τ_{hh} are zero.

$$\tau_{\theta R} = \tau_{R\theta} = -\mu \left[R\frac{\partial}{\partial R}\left[\frac{U_\theta}{R}\right] + \frac{1}{R}\frac{\partial U_R}{\partial \theta}\right] \quad \ldots\ldots (3.58)$$

as $$\frac{\partial U_R}{\partial \theta} = \frac{\partial U_\theta}{\partial R} = 0 \quad \ldots\ldots\ldots (3.59)$$

$$\tau_{\theta R} = \tau_{R\theta} = 0 \quad \ldots\ldots\ldots (3.60)$$



fig(3.3) DIFFERENTIAL ELEMENT IN THE WALL JET WITH THE RELEVANT SHEAR STRESSES

$$\tau_{\theta h} = \tau_{h\theta} = -\mu \left[\frac{\partial U_\theta}{\partial h} + \frac{1}{R} \frac{\partial U_h}{\partial \theta} \right] \quad \ldots\ldots\ldots (3.61)$$

$$\frac{\partial U_\theta}{\partial h} = \frac{\partial U_h}{\partial \theta} = 0 \quad \ldots\ldots\ldots (3.62)$$

therefore $$\tau_{\theta z} = \tau_{z\theta} = 0 \quad \ldots\ldots\ldots (3.63)$$

The resolved shear stresses balance the change in momentum inside the control volume.

To calculate the momentum change, consider an enlarged element in the R direction. Assuming the only fluid flow is in the R direction a momentum balance in that direction gives:

$$\iint_{A_2} U_R^2 \rho \, dA - \iint_{A_1} U_R^2 \rho \, dA + U_{Ro} \iint_{A_3} U \rho \cos\alpha \, dA$$

= resolved shear forces - F_R $\ldots\ldots\ldots (3.64)$

where α is the angle the velocity U_{Ro} makes with the R direction.

From an overall mass balance:

$$\iint_{A_2} U_R \rho \, dA - \iint_{A_1} U_R \rho \, dA = - \iint_{A_3} U \rho \cos\alpha \, dA \quad \ldots\ldots\ldots (3.65)$$

Combining equations (3.64) and (3.65)

$$\iint_{A_2} U_R (U_{Ro} - U_R) \, dA - \iint_{A_1} U_R (U_{Ro} - U_R) \, dA = F_R \quad \ldots\ldots\ldots (3.66)$$

For a cylindrical element radius R:

$$dA = 2\pi R \, dh \quad \ldots\ldots\ldots (3.66a)$$

and, shrinking the element to one of differential size in the R direction,

$$\frac{d}{dR} 2\pi R \int_0^\delta U_R (U_{Ro} - U_R) \, dh = F_R \quad \ldots\ldots\ldots (3.67)$$

For the same cylindrical element the resolved non zero shear stress components are:

$$\tau_{Rh}\, 2\pi R\, dR - \tau_{\theta\theta}\, 2\pi\, \delta\, dR - \tau_{RR}\, \delta\, 2\pi\, dR - \frac{d\tau_{RR}}{dR}\, \delta\, R\, 2\pi\, dR$$

plus a Pressure term which is neglected as there is negligible pressure drop along the boundary layer in the wall jet giving:

$$\frac{d}{dR}\int_0^{\delta} U_R\,(U_{Ro} - U_R)\, dh = +\tau_{Rh} - \tau_{\theta\theta}\frac{\delta}{R} + \tau_{RR}\frac{\delta}{R} - \frac{\partial \tau_{RR}}{\partial R}\delta \ldots\ldots \quad (3.68)$$

τ_{Rh} has been measured experimentally. Three such empirical relationships are listed in Chapter 2 and repeated here.

Sigalla:

$$\frac{\tau_{Rh}}{\frac{1}{2}\rho U_{Ro}^2} = 0.0565\left[\frac{U_{Ro}\delta}{\nu}\right]^{-0.25} \quad \ldots\ldots\ldots \quad (2.31)$$

Bradshaw & Gee:

$$\frac{\tau_{Rh}}{\frac{1}{2}\rho U_{Ro}^2} = 0.0315\left[\frac{U_{Ro}\delta}{\nu}\right]^{-0.182} \quad \ldots\ldots\ldots \quad (2.30)$$

Poreh et al:

$$\frac{\tau_{Rh}}{\rho U_{Ro}^2} = 0.06\left[\frac{U_{Ro}\delta}{\nu}\right]^{-0.3}\frac{b}{R}^{0.16} \quad \ldots\ldots \quad (2.29)$$

Sigalla's work has been criticised by Bradshaw and Gee and the equation of Poreh et al is more complex than the other two, so the equation of Bradshaw and Gee is selected for τ_{Rh} giving:

$$\tau_{Rh} = -0.01575\,\rho\, U_{Ro}^2\left[\frac{\nu}{U_{Ro}\delta}\right]^{0.182}$$

From Bird, Stewart and Lightfoot:

$$\tau_{\theta\theta} = -\mu_{eff}\left[2\left[\frac{1}{R}\frac{\partial U_\theta}{\partial \theta} + \frac{U_R}{R}\right] - \frac{2}{3}\left[\nabla.U\right]\right] \quad \ldots\ldots\ldots (3.69)$$

As $\frac{\partial U_\theta}{\partial \theta} = 0$ and $\nabla.U = 0$ for incompressible flow, equation (3.69) becomes:

$$\tau_{\theta\theta} = -2\mu_{eff}\frac{U_R}{R} \quad \ldots\ldots\ldots (3.70)$$

$$\tau_{RR} = -\mu_{eff}\left[2\frac{\partial U_R}{\partial R} - \frac{2}{3}(\nabla.U)\right] \quad \ldots\ldots\ldots (3.71)$$

giving: $$\tau_{RR} = -2\mu_{eff}\frac{\partial U_R}{\partial R} \quad \ldots\ldots\ldots (3.72)$$

but: $$\frac{\partial U_R}{\partial R} = \frac{\partial}{\partial R}\left[U_{Ro}\left[\frac{h}{\delta}\right]^{1/x}\right] \quad \ldots\ldots\ldots (3.73)$$

giving:

$$\tau_{RR} = -2\mu_{eff}\left[\frac{\partial U_{Ro}}{\partial R}\left[\frac{h}{\delta}\right]^{1/x} - U_{Ro}\,h^{1/x}\frac{\partial \delta}{\partial R}\frac{1}{x\,\delta^{(1+\frac{1}{x})}}\right] \quad \ldots\ldots (3.74)$$

$$\frac{\partial \tau_{RR}}{\partial R} = -2\mu_{eff}\left[\frac{\partial^2 U_{Ro}}{\partial R^2}\left[\frac{h}{\delta}\right]^{\frac{1}{x}} - \frac{\partial U_{Ro}}{\partial R}(h)^{\frac{1}{x}}\frac{\partial \delta}{\partial R}\frac{1}{x\,\delta^{(1+\frac{1}{x})}}\right.$$

$$- \frac{\partial^2 \delta}{\partial R^2}U_{Ro}\frac{h}{x}^{1/x}\frac{1}{\delta^{\frac{x+1}{x}}} - \frac{\partial U_{Ro}}{\partial R}\frac{\partial \delta}{\partial R}\frac{h}{x}^{1/x}\frac{1}{\delta^{(1-\frac{1}{x})}}$$

$$\left. - \frac{\partial \delta}{\partial R}U_{Ro}\frac{h}{x}^{1/x}\frac{\partial \delta}{\partial R}\frac{1}{\delta^{(2+\frac{1}{x})}}\frac{(x+1)}{x}\right] \quad \ldots\ldots\ldots (3.75)$$

The term μ_{eff} is the effective viscosity of the turbulent flow. Using Prandtl's mixing length theory

$$\mu_{eff} = \rho\, l^2\left|\frac{\partial U_R}{dh}\right|$$

where $l = l(h)$.

This latter function has been studied in the case of wall jet flow most thoroughly by Spalding and Patankar (see Chapter 2). For wall jets they recommend values for empirical constants k and λ of 0.8 and 0.1 respectively.

In the boundary layer near the wall the equation $l = kh$ is relevant (ignoring the laminar contribution) giving:

$$l = 0.8h$$

and $$\mu_{eff} = 0.64 \rho h^2 \left| \frac{dU_R}{dh} \right| \quad \ldots\ldots\ldots \quad (3.77)$$

As we are interested in the average values over the boundary layer, for any shear stress, including the effective viscosity term:

$$\tau_{xy} = \frac{1}{\delta} \int_0^{\delta} \tau_{xy} \, dh \quad \ldots\ldots\ldots \quad (3.78)$$

and from equations (3.73) and (3.77)

$$\mu_{eff} = 0.64 \rho \frac{h^2}{x} \frac{U_{Ro}}{\delta^{1/x}} h^{\left(\frac{1-x}{x}\right)} \quad \ldots\ldots\ldots \quad (3.79)$$

Examining each term of equation (3.68) individually, for the $\tau_{\theta\theta}$ term from equation (3.70):

$$\frac{1}{\delta} \int_0^{\delta} \tau_{\theta\theta} \, dh = -\frac{1}{\delta} \int_0^{\delta} 1.28 \frac{U_R}{R} \frac{\rho U_{Ro} h^2}{x \delta^{1/x}} h^{\left(\frac{1-x}{x}\right)} \, dh$$

$$= - \frac{0.64}{1 + x} U_{Ro}^2 \rho \frac{\delta}{R} \quad \ldots\ldots\ldots\ldots \quad (3.80)$$

$$- \tau_{\theta\theta} \frac{\delta}{R} = \frac{0.64}{1 + x} U_{Ro}^2 \rho \frac{\delta^2}{R^2} \quad \ldots\ldots\ldots\ldots \quad (3.81)$$

for the τ_{RR} term from equation (3.72):

$$\frac{1}{\delta}\int_0^{\delta}\tau_{RR}\,dh = \frac{-1.28\rho U_{Ro}}{\delta x}\int_0^{\delta}\left[\frac{\partial U_{Ro}}{\partial R}\frac{h^{\frac{(2+x)}{x}}}{\delta^{2/x}} - \frac{\partial\delta}{\partial R}\frac{U_{Ro}}{x}\frac{h^{\frac{(2+x)}{x}}}{\delta^{\frac{(x+2)}{x}}}\right]dh \quad \ldots(3.82)$$

giving:

$$\frac{\tau_{RR}\delta}{R} = -\frac{0.64\rho U_{Ro}}{(1+x)R}\left[\frac{\partial U_{Ro}}{\partial R}\delta^2 - \frac{\partial\delta}{\partial R}\frac{U_{Ro}\delta}{x}\right] \quad \ldots\ldots\ldots (3.83)$$

For the $\frac{\partial\tau_{RR}}{\partial R}$ term from equation (3.75):

$$\frac{1}{\delta}\int_0^{\delta}\frac{\partial\tau_{RR}}{\partial R}\,dh = -\frac{1}{\delta}\int_0^{\delta}1.28\rho\frac{h^2}{x}\frac{U_{Ro}}{\delta^{1/x}}h^{\frac{(1-x)}{x}}\left[\frac{\partial^2 U_{Ro}}{\partial R^2}\left[\frac{h}{\delta}\right]^{1/x}\right.$$

$$-\frac{\partial U_{Ro}}{\partial R}h^{1/x}\frac{\partial\delta}{\partial R}\frac{1}{x\,\delta^{\frac{(1+1)}{x}}} - \frac{\partial^2\delta}{\partial R^2}U_{Ro}\frac{h^{1/x}}{x}\frac{1}{\delta^{\frac{(1+x)}{x}}} -$$

$$\left.\frac{\partial U_{Ro}}{\partial R}\frac{\partial\delta}{\partial R}\frac{h^{1/x}}{x}\frac{1}{\delta^{\frac{(x+1)}{x}}} - \frac{\partial\delta}{\partial R}U_{Ro}\frac{h^{1/x}}{x}\frac{\partial\delta}{\partial R}\frac{1}{\delta^{\frac{(1+2x)}{x}}}\frac{(x+1)}{x}\right]dh \quad \ldots\ldots(3.84)$$

Giving:

$$-\frac{\partial\tau_{RR}}{\partial R}\delta = \frac{1.2\delta\rho U_{Ro}}{x}\left[\frac{x}{2(1+x)}\delta^2\frac{\partial^2 U_{Ro}}{\partial R^2} - \frac{1}{2(1+x)}\delta\frac{\partial U_{Ro}}{\partial R}\frac{\partial\delta}{\partial R}\right.$$

$$\left.-\frac{\partial^2\delta}{\partial R^2}\frac{U_{Ro}\delta}{2(1+x)} - \frac{\partial U_{Ro}}{\partial R}\frac{\partial\delta}{\partial R}\frac{\delta}{2(1+x)} - \left[\frac{\partial\delta}{\partial R}\right]^2 U_{Ro}\frac{(x+1)}{x^2}\right] \quad \ldots\ldots (3.85)$$

For the left hand side of equation (3.68)

$$\frac{d}{dR}\int_0^{\delta}\rho U_R\,(U_{Ro} - U_R)\,dh$$

gives on combining with assumption (1)

$$\text{Left hand side} = \frac{d}{dR}\ \delta\ U_{Ro}^{2}\ \rho\ \frac{x}{(x+1)\ (x+2)} =$$

$$\frac{\rho\ x\ U_{Ro}^{2}}{(x+1)(x+2)}\left[\frac{d\delta}{dR} - \frac{2\delta}{U_{Ro}}\ \frac{dU_{Ro}}{dR}\right] \quad \ldots\ldots\ (3.86)$$

Collecting the terms of equation (3.68) and cancelling gives:

$$\left[\frac{d\delta}{dR} + \frac{2\delta}{U_{Ro}}\ \frac{dU_{Ro}}{dR}\right]\frac{x}{x+2} = -0.01575\ (x+1)\left[\frac{\eta}{\rho\ U_{Ro}\delta}\right]^{0.182} + 0.64\ \frac{\delta^{2}}{R^{2}}$$

$$-\frac{0.64}{R\ U_{Ro}}\left[\frac{\partial U_{Ro}}{\partial R}\ \delta^{2} - \frac{\partial\delta}{\partial R}\ \frac{U_{Ro}}{x}\ \delta\right] + \frac{0.32\delta}{U_{Ro}}\left[x\delta\ \frac{\partial^{2}U_{Ro}}{\partial R^{2}} - \frac{1}{x}\ \frac{\partial U_{Ro}}{\partial R}\ \frac{\partial\delta}{\partial R}\right.$$

$$\left. - \frac{1}{x}\frac{\partial^{2}\delta}{\partial R^{2}}\ U_{Ro} - \frac{1}{x}\ \frac{\partial U_{Ro}}{\partial R}\ \frac{\partial\delta}{\partial R} - \left[\frac{\partial\delta}{\partial R}\right]^{2}\ U_{Ro}\ \frac{(x+1)^{2}}{x\delta}\right] \quad \ldots\ldots\ (3.87)$$

For U_{Ro} as f (R) the Hrycak, Lee and Gaunter equation is taken as the simplest.

$$U_{Ro} = 1.4\ U_{e}\left[\frac{d}{R}\right]^{1.12} \quad \ldots\ldots\ (2.25)$$

differentiating:

$$\frac{dU_{Ro}}{dR} = -1.568\ U_{e}\ \frac{d^{1.12}}{R^{2.12}} \quad \ldots\ldots\ (3.88)$$

Substituting equations (2.25) and (3.88) into (3.87):

$$\frac{x}{x+2}\left[\frac{d\delta}{dR}\right] - 2.24\ \frac{x}{(x+2)}\ \frac{\delta}{R} = -0.01575\ (x+1)\left[\frac{\eta\ R^{1.12}}{\delta\rho 1.4\ U_{e}\ d^{1.12}}\right]^{0.182}$$

$$+ 0.64\ \frac{\delta^2}{R^2} + 0.7167\ \frac{\delta^2}{R^2} + \frac{0.64}{x}\left[\frac{d\delta}{dR}\ \frac{\delta}{R}\right] + 0.7167x\ \frac{\delta^2}{R^2}$$

$$+ \frac{0.766}{x}\left[\frac{\delta}{R}\ \frac{d\delta}{dR}\right] - \frac{0.32}{x}\ \delta\ \frac{d^2\delta}{dR^2} - 1.4U_e\left[\frac{\delta}{R}\right]1.12\ \frac{(x+1)^2}{x}\left[\frac{d\delta}{dR}\right]^2 \quad \ldots\ldots\ (3.89)$$

The boundary layer equation of Poreh et al is useful to calculate the order of magnitude of each term. The equation:

$$\frac{\delta_{\frac{1}{2}}}{b} = 0.098\left[\frac{R}{b}\right]^{0.9} \quad \ldots\ldots\ (2.28)$$

is equivalent to:

$$\frac{\delta}{b} = 0.0205\left[\frac{R}{b}\right]^{0.9} \quad \ldots\ldots\ (3.90)$$

The orders of each term in equation (3.89) are in sequence

$$10^{-2},\ 10^{-2},\ 10^{-2},\ 10^{-4},\ 10^{-4},\ 10^{-4},\ 10^{-4},\ 10^{-4},\ 0,\ 10^{-6}.$$

As a first approximation, only the first three terms need to be considered further as the others are at least two orders of magnitude smaller. At this stage the variables are made dimentionless:

$$R^* = R/d \quad \ldots\ldots\ (3.91)$$

$$\delta^* = \delta/d \quad \ldots\ldots\ (3.92)$$

giving:

$$\frac{dU_{Ro}}{dR} = \frac{dU_{Ro}}{dR^*}\ d \qquad \text{etc.}$$

from equation (3.89) ignoring the smallest terms:

$$\frac{d\delta^*}{dR^*} = 2.24\ \frac{\delta^*}{R^*} + \frac{0.01575}{1.4^{0.182}}\ \frac{(x+1)(x+2)}{x}\ Re^{-0.182}\ \frac{R^{*0.204}}{\delta^{*0.182}} \quad \ldots\ldots\ (3.93)$$

Rewriting equation (3.93) as:

$$\frac{d\delta^*}{dR^*} = B\ \frac{\delta^*}{R^*} + C\ \frac{R^{*0.204}}{\delta^{*0.182}} \quad \ldots\ldots\ (3.94)$$

This differential equation can be solved exactly if $\delta^{*0.182} \simeq \delta^{*0.204}$ i.e. if $\delta^{*0.022} \simeq 1$. Most numbers raised to this small power will approximate to unity. The third place on the index of R* can also be ignored for simplicity.

$$\frac{d\delta^*}{dR^*} = B\ \frac{\delta^*}{R^*} + C\ \frac{R^{*0.20}}{\delta^{*0.20}} \quad \ldots\ldots\ (3.95)$$

This is now a homogeneous first order differential equation.

Substitute $\delta^* / R^* = V \quad \ldots\ldots\ (3.96)$

Differentiating: $\frac{d\delta^*}{dR^*} = V + \frac{dV}{dR^*} \quad \ldots\ldots\ (3.97)$

Substituting equation (3.97) into (3.95):

$$V + R^*\ \frac{dV}{dR^*} = \frac{C}{V^{0.2}} + BV \quad \ldots\ldots\ (3.98)$$

Rearranging and collecting terms:

$$\int \frac{V^{0.2}\ dV}{(C + (B-1)\ V^{1.2})} = \int \frac{dR^*}{R^*} \quad \ldots\ldots\ (3.99)$$

Integrating:

$$\frac{1}{B-1}\ \frac{1}{1.2}\left[\log_e\left[\frac{C}{B-1} + V^{1.2}\right]\right] = \log_e R^* \quad \ldots\ldots\ (3.100)$$

Taking antilogs and substituting from equation (3.96)

$$R^{*1.2(B-1)} = \frac{C}{B-1} + \left[\frac{\delta^*}{R^*}\right]^{1.2}$$

Rearranging and substituting for B

$$\delta^* = \left[\frac{C\ R^{*1.2}}{1.24} + R^{*2.688}\right]^{1/1.2} \quad \ldots\ldots\ldots (3.101)$$

This equation predicts a boundary layer growth dependent on R^* at low Re values but $R^{*2.24}$ at high Re values. For Poreh et al's work at high Re values they found:

$$\frac{\delta}{b} = 0.0205 \left[\frac{R}{b}\right]^{0.9}$$

equation (3.101) is not substantiated. The rate of growth of the boundary layer predicted by equation (3.101) is far too high. There must then be a restraining force on the boundary layer not considered in the force balance equation (3.68). In deriving this equation, the assumption of zero shear on the upper face of the control volume was made based on Prandtl's mixing length hypothesis. As previously discussed, two references claim measurements of shear on this plane and one, Poreh et al (1967), quotes values for this.

The shear is produced in the absence of a finite velocity gradient by the transfer of turbulent eddies. The Reynolds stresses produced in this manner can be deduced from measurements of the time smoothed eddy velocity components.

In orthogonal co-ordinates, the relevant shear stresses are given by

$$\tau_{xx} = -\rho \bar{u}_x'^2 \quad \ldots\ldots\ldots (3.102)$$

$$\tau_{yx} = -\rho u_x' u_y' \quad \ldots\ldots\ldots (3.103)$$

$$\tau_{zx} = -\rho u_x' u_z' \quad \ldots\ldots\ldots (3.104)$$

τ_{zx} is the important term, acting on the maximum velocity plane and is equivalent to τ_{Rh}. Poreh, Cermak and Tseui have correlated this stress as a ratio with the wall shear stress as a function of $h/\delta\frac{1}{2}$. At the position $h = \delta$, this ratio is about 4.

Including this factor in the force balance, makes the term producing the $R^{*2.668}$ term in the final equation an order of magnitude larger than the other relevant term which by ignoring the latter, gives from equation (3.94):

$$\frac{d\delta^*}{dR^*} = 5C \frac{R^{*0.204}}{\delta^{*0.182}} \quad \ldots\ldots\ldots (3.105)$$

Integrating:

$$\delta^* = (0.9817 \times 5C)^{0.846} \; R^{*0.948} \quad \ldots\ldots\ldots (3.106)$$

This prediction of $\delta \propto R^{0.948}$ is in good agreement with the data of Poreh, Cermak and Tseui ($\delta \propto R^{0.9}$), Bakke ($\delta \propto R^{0.94}$) and Poland ($\delta \propto R^{1.16}$). The Reynolds number dependence predicted is quite small, $\delta \propto Re^{-0.154}$. Small enough in fact not to show up among the experimental scatter in the experiments of Poreh, Cermak and Tseui.

3.4.4 Wall Jet Mass Transfer Prediction

Substituting equation (3.106) into the mass transfer equation (3.56), which was:

$$k = 2 \frac{d}{dR} \frac{\rho}{\rho - \rho_{Ao}} U_{Ro} \delta \int \Delta \quad \ldots\ldots\ldots\ldots (3.56)$$

together with the equation for the maximum velocity decay from Hrycak et al (2.25), which was:

$$\frac{U_{Ro}}{U_e} = 1.4 \left[\frac{d}{R}\right]^{1.12} \quad \ldots\ldots\ldots (2.25)$$

and expressing term C fully, the right hand side of equation (3.56) can be differentiated to give:

$$k = 0.0524 \frac{\rho}{\rho - \rho_{Ao}} U_e \int \Delta \left[\frac{(x+1)(x+2)}{x}\right]^{0.846} \frac{1}{Re^{0.154}} \frac{1}{R^{*1.172}} \quad \ldots\ldots (3.107)$$

Slightly different equations can be derived by selecting other empirical data. The equations will differ mainly in constant term, calculated above as 0.0524. This value is very sensitive to the empirical data and is subject to a large variation in value. Suitable combinations of empirical data can be selected to yield a constant to fit the empirical data in this work. However, the value will be fixed from the empirical data presented in the napthalene erosion experiments in Chapter four. The value of this constant will also depend on the exponent on the profile laws of assumptions (1) and (2). In many cases a seventh power law has been found to give a good fit to velocity profiles in boundary layer flow. Two workers (see section (2.4)) have discovered that a fourteenth power law gives a better fit in the case of the wall jet and a value of 14 is used in the later calculations for x.

Some points of note arise from equation (3.107). The most important is the overall dependence of mass transfer in the wall jet on a Reynolds number to power 0.846. The second point is the independence on b of the mass transfer. The third point is that the prediction depends on the profile exponent x.

The equation can be compared with the expression of Dawson and Trass (1966) whose analysis for the air/napthalene system gives:

$$Sh = 0.044\ Re^{0.877}\ R^{*-1.0} \quad \ldots\ldots\ldots (3.108)$$

and with the heat transfer data of Jakob et al (1950) and Zerbe and Selna (1946) discussed in section (2.4.1) which gave Reynolds number power dependences in the wall jet of 0.8 and 0.65.

Theoretical Sherwood numbers were evaluated by computer using the derived value of 0.0065 for the constant in equation (3.107). The computer program to evaluate (3.107) is listed in appendix (3). Values predicted from each of the preceding theoretical approaches are also generated by the program.

3.5 Implications of the Theoretical Models

At the stagnation point, four different models have been derived. Three, resulting in equations (3.13), (3.22) and (3.39) predict a Reynolds number power dependence of 0.5 for mass transfer while the fourth, the heat transfer analogy from Perry predicts a 0.7 power. The wall jet model predicts an overall dependence on a 0.846 power for this region. It seems unlikely therefore, that a good correlation will be obtained for a dimentionless radial mass transfer plot, and scatter similar to that found by Gardon and Cobonpue in their heat transfer work would be expected. Further to this, the wall jet rate predicted by equation (3.107) is independent of b while the stagnation point rate is dependent on b. A series of experiments in Chapter four will investigate the dependence of mass transfer on jet/plate distance in both regions.

It is significant that three stagnation point solutions should predict similar mass transfer rates. The implication of a 0.5 dependence for the Reynolds number on mass transfer is indicative in itself of the controlling step being concerned with a laminar layer. It has been discussed in Chapter two how, near the wall, laminar forces are dominant and, if the concentration gradients are confined to a region very close to a wall, the mass transfer will be described by a laminar flow solution. The high rate of mixing above the surface in the impingment zone implies that in this turbulent zone no concentration gradient will be established and the gradient will be confined to the laminar sublayer. In the turbulent wall jet, the concentration gradient extends from the sublayer into the boundary layer and turbulent transfer is then a more important mechanism and is assumed in the solution to be the dominant mechanism.

CHAPTER FOUR

EROSION OF NAPTHALENE WITH AN AIR JET

4.0 EROSION OF NAPTHALENE WITH AN AIR JET

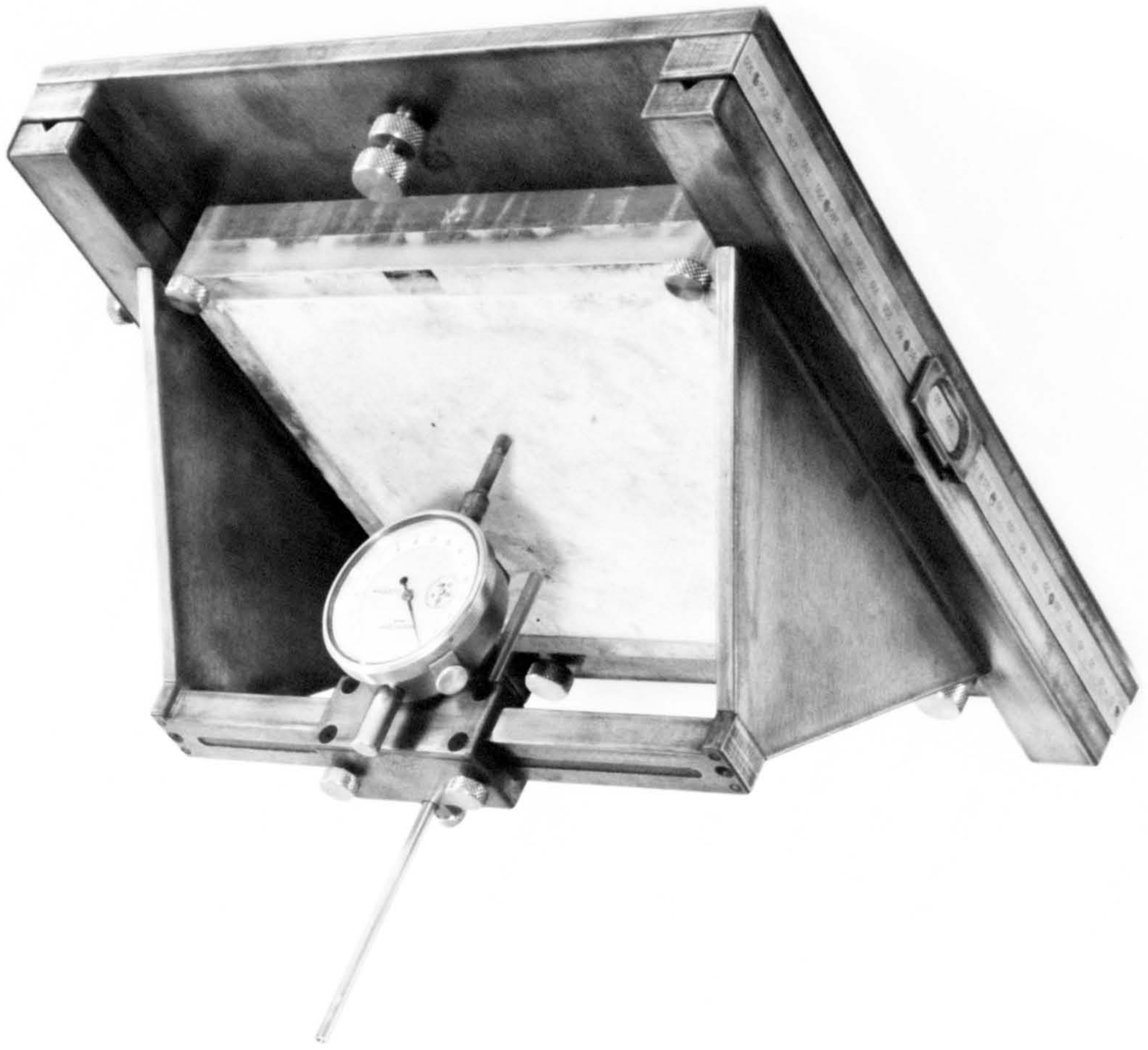
4.1 Napthalene Erosion Experimental Method

The erosion of napthalene ($C_{10}H_8$) with air is a commonly used method of assessing heat transfer relationships via a mass-heat transfer analogy and has also been used in mass transfer work including work on impinging air jets. (Dawson and Trass (1966)). The latter work was mostly concerned with the wall jet region whereas in the present study the whole profile is of interest.

The experimental apparatus is pictured in fig (4.1). A 160 mm length stainless steel tube of internal diameter 3.175 mm was used as the jet. The length was selected to ensure fully developed turbulent flow inside the pipe. It was assumed that if the Reynolds number inside the pipe exceeded the critical value of 2,100, then the exit flow was similarly turbulent in nature. The range of Reynolds numbers investigated was from 2,000 to 16,245. In the results section the data of Dawson and Trass (1966), who used a similar system but with a smaller diameter jet of 2.46 mm, is included. The range of Reynolds numbers they studied was 10,600 to 81,400.

The jet was prepared by milling the exit end and then carefully deburring it. This was found necessary in producing symmetrical erosion patterns in the napthalene.

The preparation of the napthalene surface is also critical. There is some discussion as to whether a fine or a coarse grain structure is preferable. In the present work a fine structure was produced by ironing the surface of a napthalene block cast in a perspex mould. The remelting with a domestic flat iron and controlled temperature produced a flat hard surface which was found to erode uniformly. Surfaces without this preparation were found to break up under the action of the jet and to erode preferentially around the edges of napthalene grains where shrinkage or gas cavities were present.



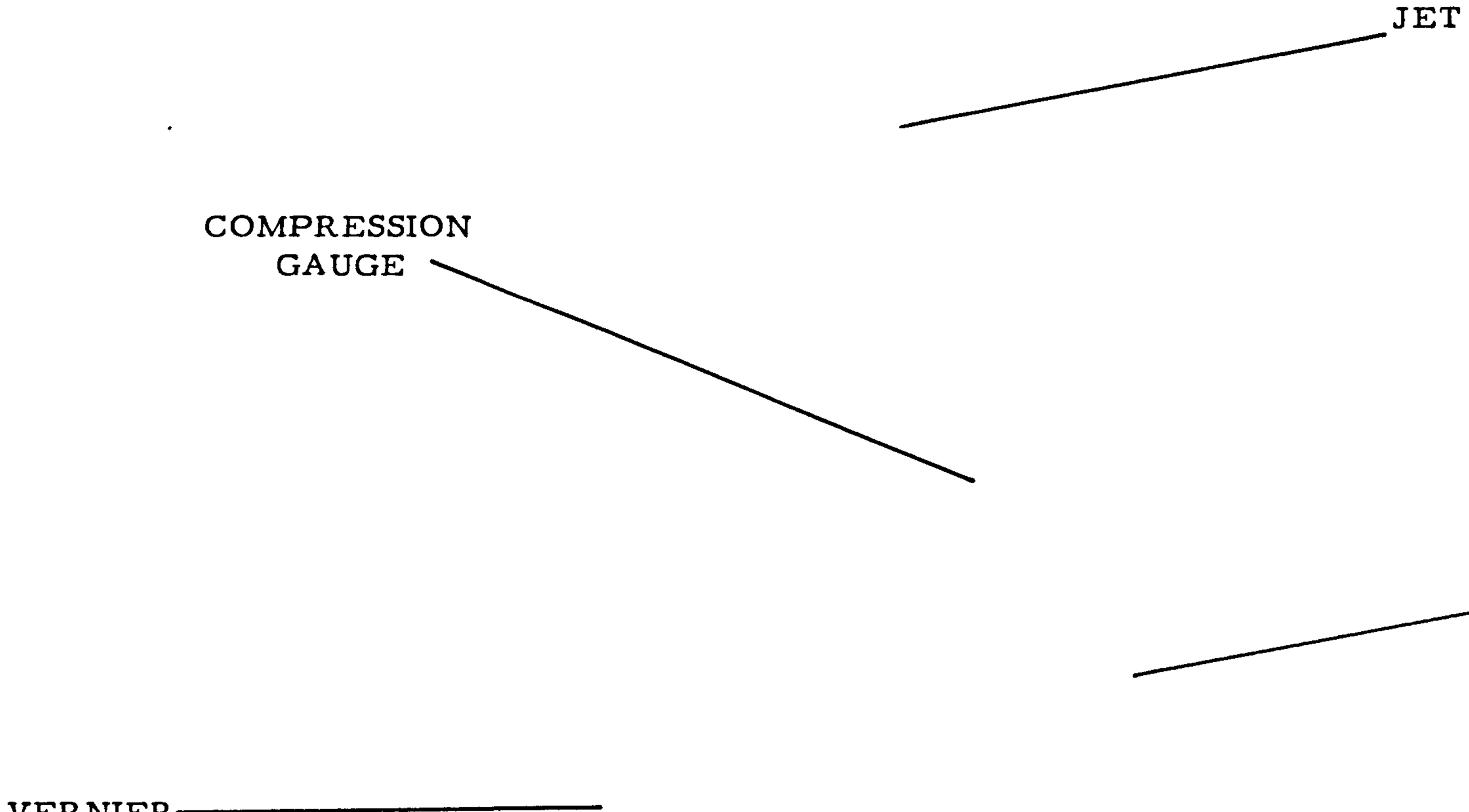


Fig (4.1) NAPTHALENE EROSION AND PROFILING APPARATUS

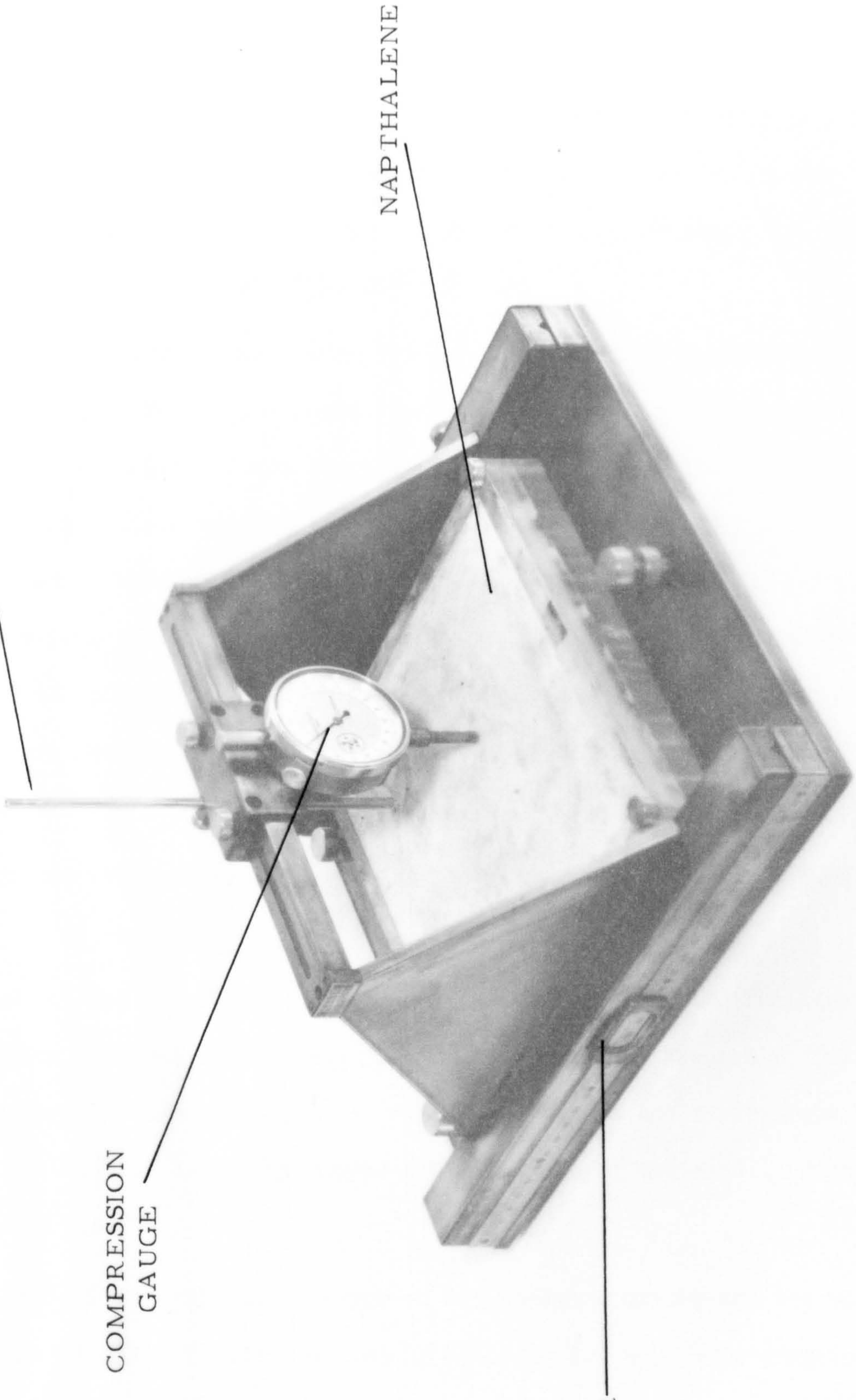


Fig (4.1) NAPTHALENE EROSION AND PROFILING APPARATUS

The temperature of the air leaving the napthalene block was monitored with a high grade mercury thermometer and the average temperature taken to calculate the surface concentration of napthalene from the vapour pressure. It was assumed that the partial pressure of napthalene adjacent to the surface was equal to its vapour pressure at the surface temperature. The vapour pressure data used was from Trass (1958).

Air was metered through a calibrated rotameter and manometer to the jet for a measured time. The profile of the napthalene was measured before and after the experiment, with the compression gauge, fig (4.1), reading to $\pm$ 0.002 mm, at various positions across the surface. The upper part of the rig moved with respect to the lower on a ball bearing assembly, which could be locked during an experiment. A reference reading was taken each time on the top of the perspex mould. The amount of napthalene eroded was found by averaging two readings made symmetrically either side of the stagnation point of the jet.

The precise position of both jet and gauge was given by the calibrated vernier.

Most of the experiments were done at constant jet/plate distance, measured with calibrated slip gauges, of twelve jet diameters (b = 12d). For one particular Re value (7,429) the jet/plate distance was varied from 8d to 24d, and for the two lowest Re values a distance of 8d was used to limit the experimental time.

Results are tabulated in terms of the Sherwood number and the corresponding dimensionless radial position in appendix (4) and shown graphically in the succeeding section. A value of 2.45 is taken for the Schmidt number of the air/napthalene system and a value of 6.11 mm^2/sec for the diffusion coefficient of napthalene in air, both from Trass (1958).

Other derived values are also tabulated in appendix (4).

4.1.1 Calculation of the Sherwood Number

The Sherwood number is defined as:

$$Sh = \frac{k\ d}{D_{AB}}$$

k is defined as:

$$k = \frac{\text{Mass Transferred}}{\rho_{Ao} - \rho_{As}}$$

ρ_{As}, the concentration in the bulk for the napthalene experiments, is small enough to be neglected for most experiments and ρ_{Ao} was calculated from the vapour pressure data of Trass via the ideal gas law.

$$\rho_{Ao} = \frac{P_{C_{10}H_8} \times \text{M.Wt.}}{R\ T} \quad \ldots\ldots\ldots (4.1)$$

This is plotted as a function of temperature in fig (4.2).

The mass transferred was calculated from the erosion depth per unit time and the density of the napthalene solid to produce the local Sherwood number from the expression:

$$Sh = \frac{t\ \rho_{C_{10}H_8} d}{s\ \rho_{Ao}\ D_{AB}} \quad \ldots\ldots\ldots\ldots (4.2)$$

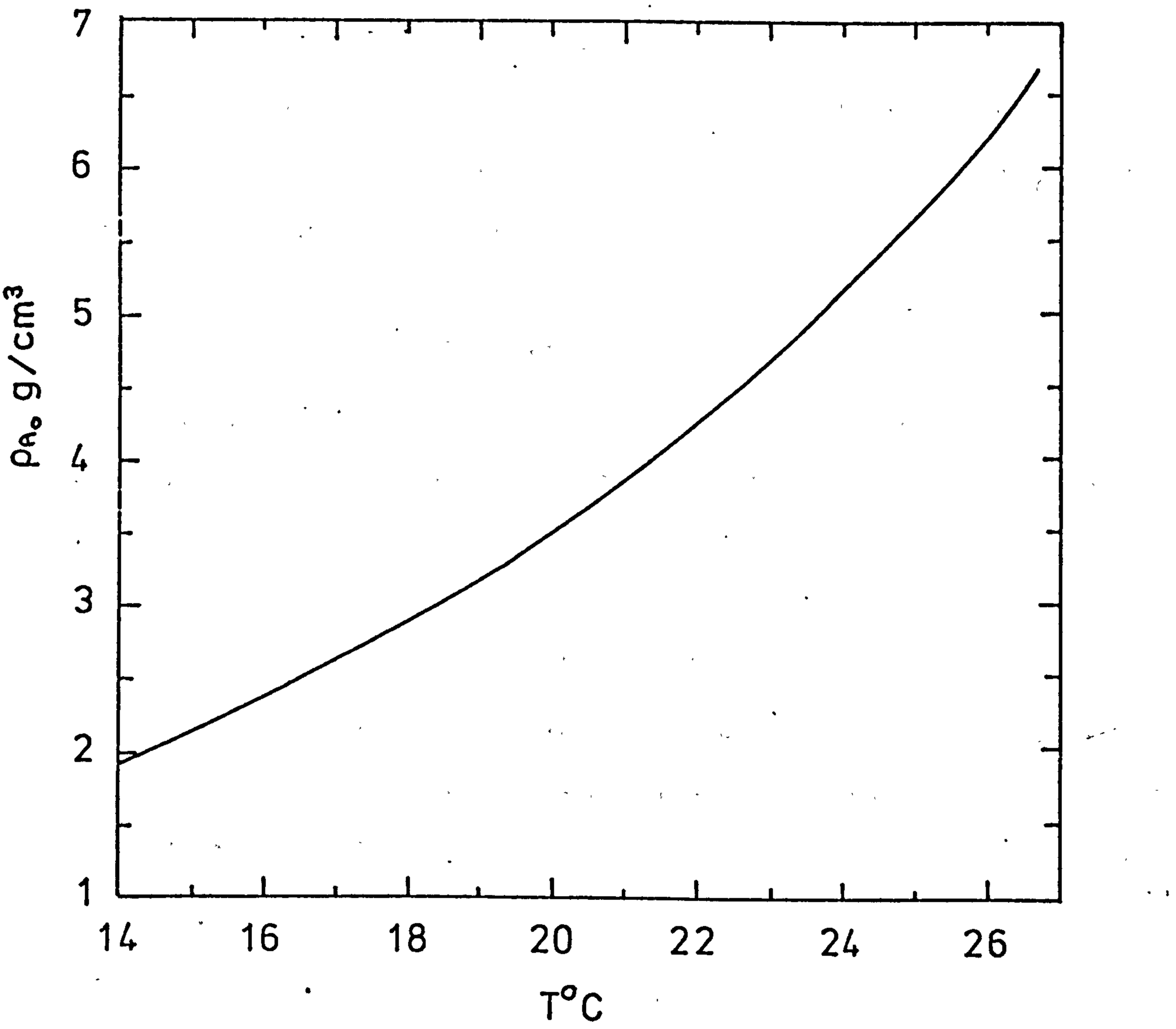
The S.G. of napthalene was taken as 1.145 (D_{AB} = 6.11 mm^2/sec from Trass).

4.2 Experimental Results

One complete duplicate was made of run 1(a), run 1(b). Other runs were duplicated only to ascertain the stagnation point value which, being the area of highest transfer, was most susceptible to error.

4.2.1 Wall Jet Region

The dimensionless profiles for the napthalene runs are plotted in



fig(4.2) SATURATION CONCENTRATION OF NAPTHALENE IN AIR AS A FUNCTION OF TEMPERATURE

figures (4.3) to (4.18) together with the data of Dawson. The theoretically predicted variation of transfer in the wall jet from equation (3.107) is plotted together with Dawsons prediction, equation (3.108), for his own work for comparison. The five runs at constant Re and varying b/d ratio are plotted together in fig (4.4). This is the graph used to fix the empirical constant in equation (3.107).

4.2.2 Dimensionless Profile

Values of Sh/Sh_o as a function of dimensionless radial position R/b were calculated for all experiments to produce the scatter band in fig (4.19) which is compared with the heat transfer profiles of Gardon and Cobonpue and Perry. Dawson's results are not included in the scatter band.

4.2.3 Effect of Jet Plate Distance

Fig (4.20) shows the dependence of stagnation Sherwood number on the jet plate distance for constant Re of 7,429. A line of best fit passing through the origin is included.

4.2.4 Stagnation Point Variation with Reynolds Number

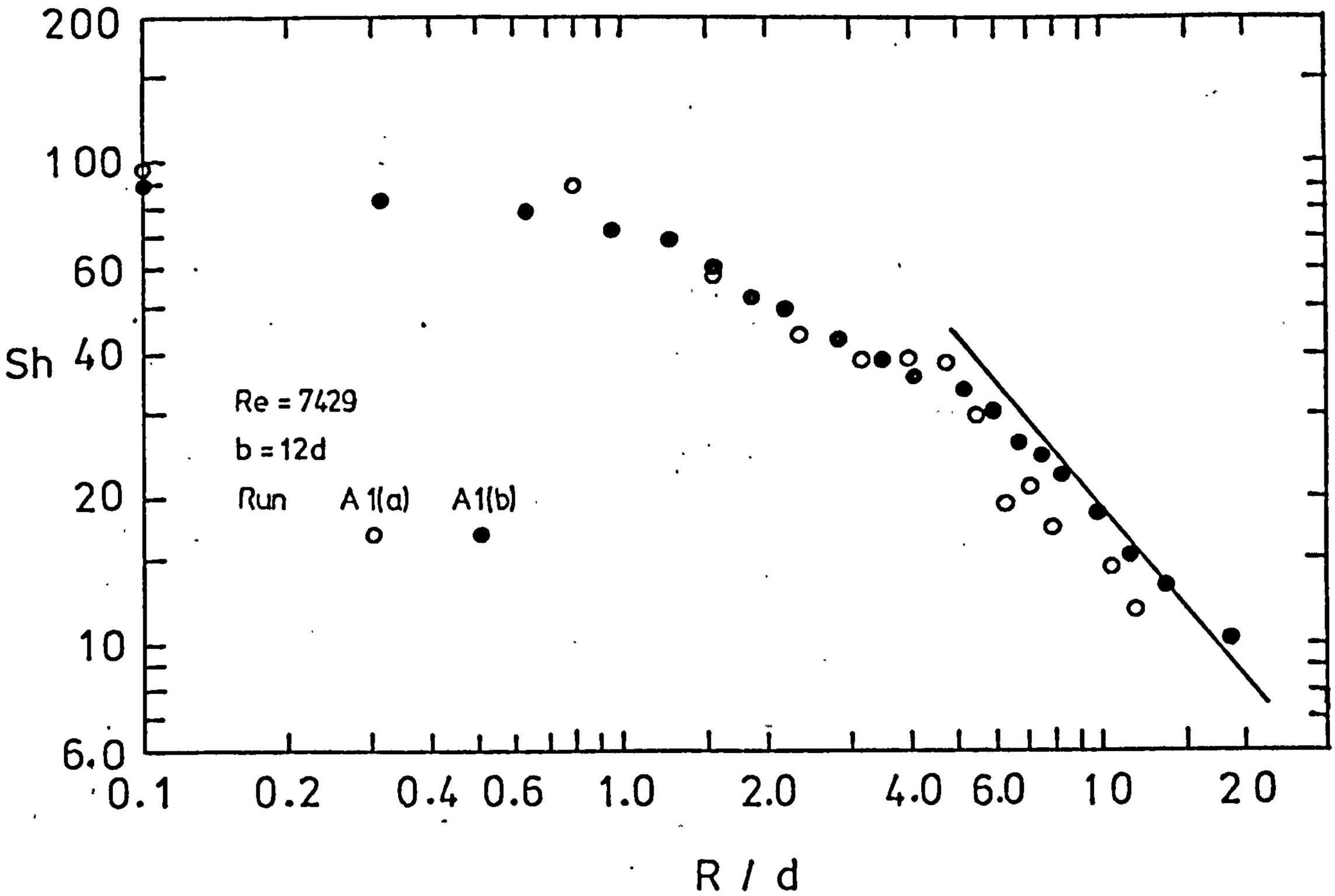
All the napthalene runs in the present series are plotted together with the results of Dawson in dimensionless groups as suggested by equations (3.13), (3.42), (3.39), (3.22). Plotted with it for comparison are these equations, fig (4.21), as derived in chapter three for the stagnation point transfer rates.

4.3 Discussion of Results

4.3.1 Wall Jet Region

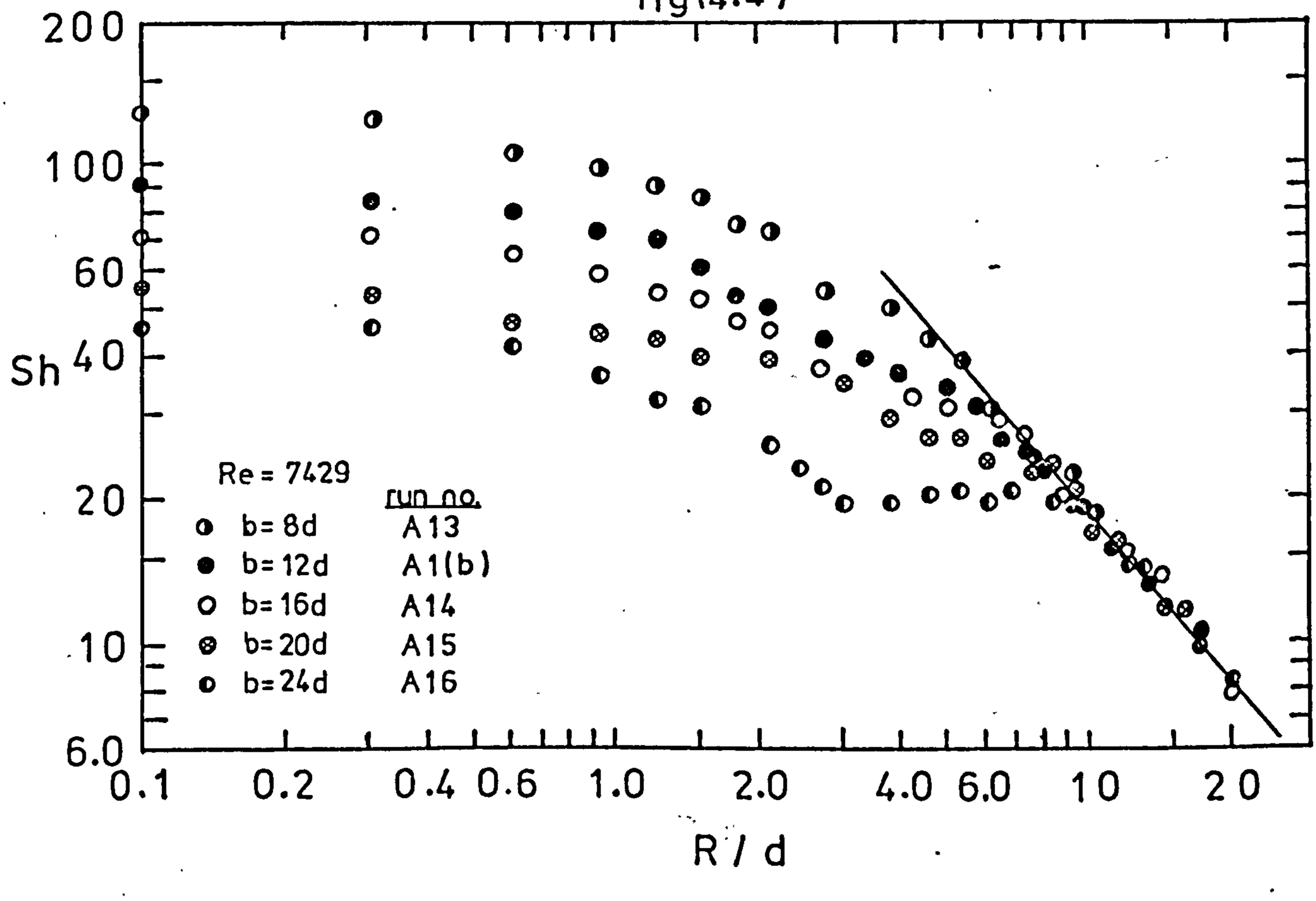
The most significant graph is shown in figure (4.13). This shows that

fig(4.3)

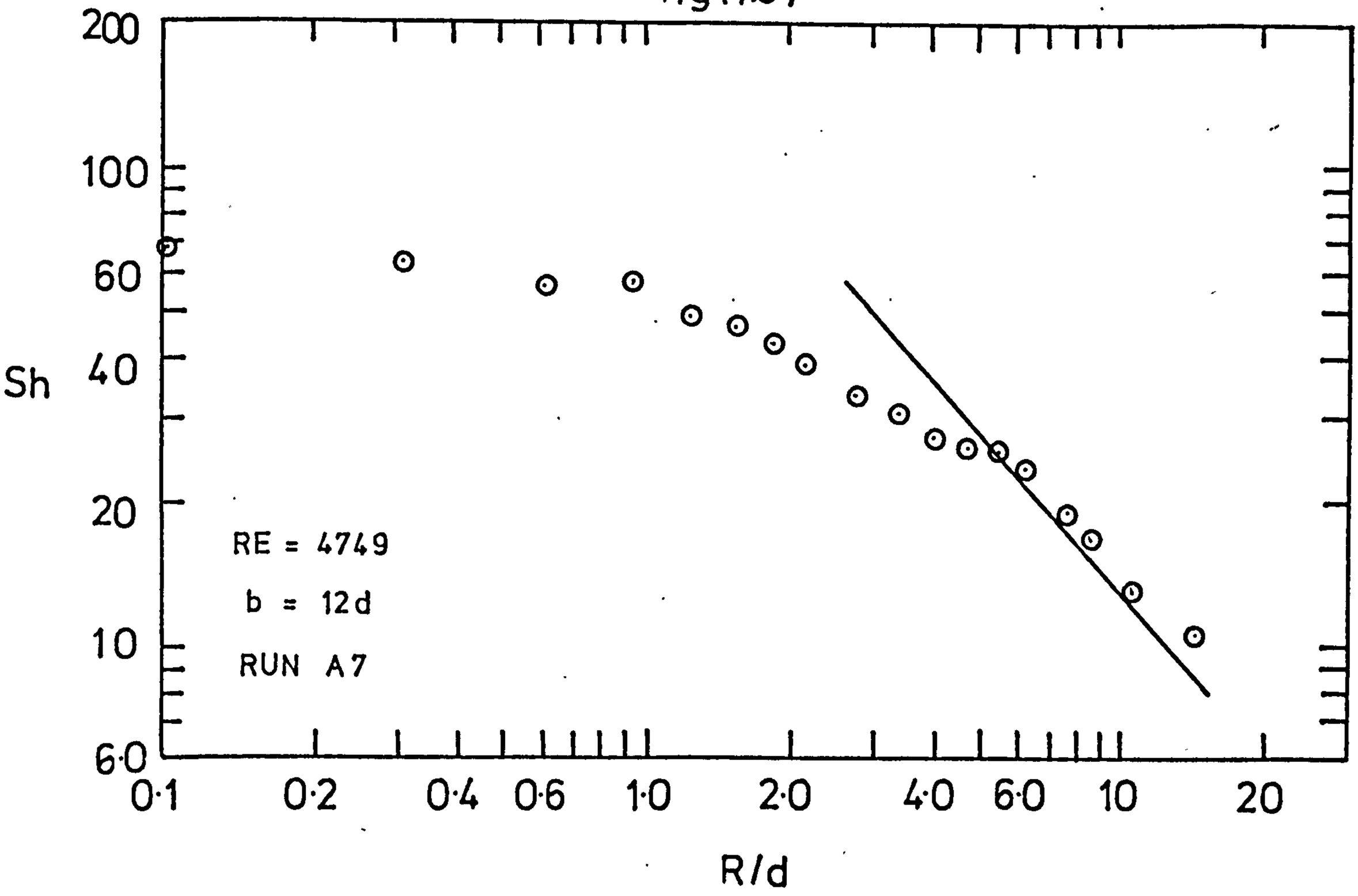


SHERWOOD NUMBER AS A FUNCTION OF RADIAL POSITION

fig(4.4)

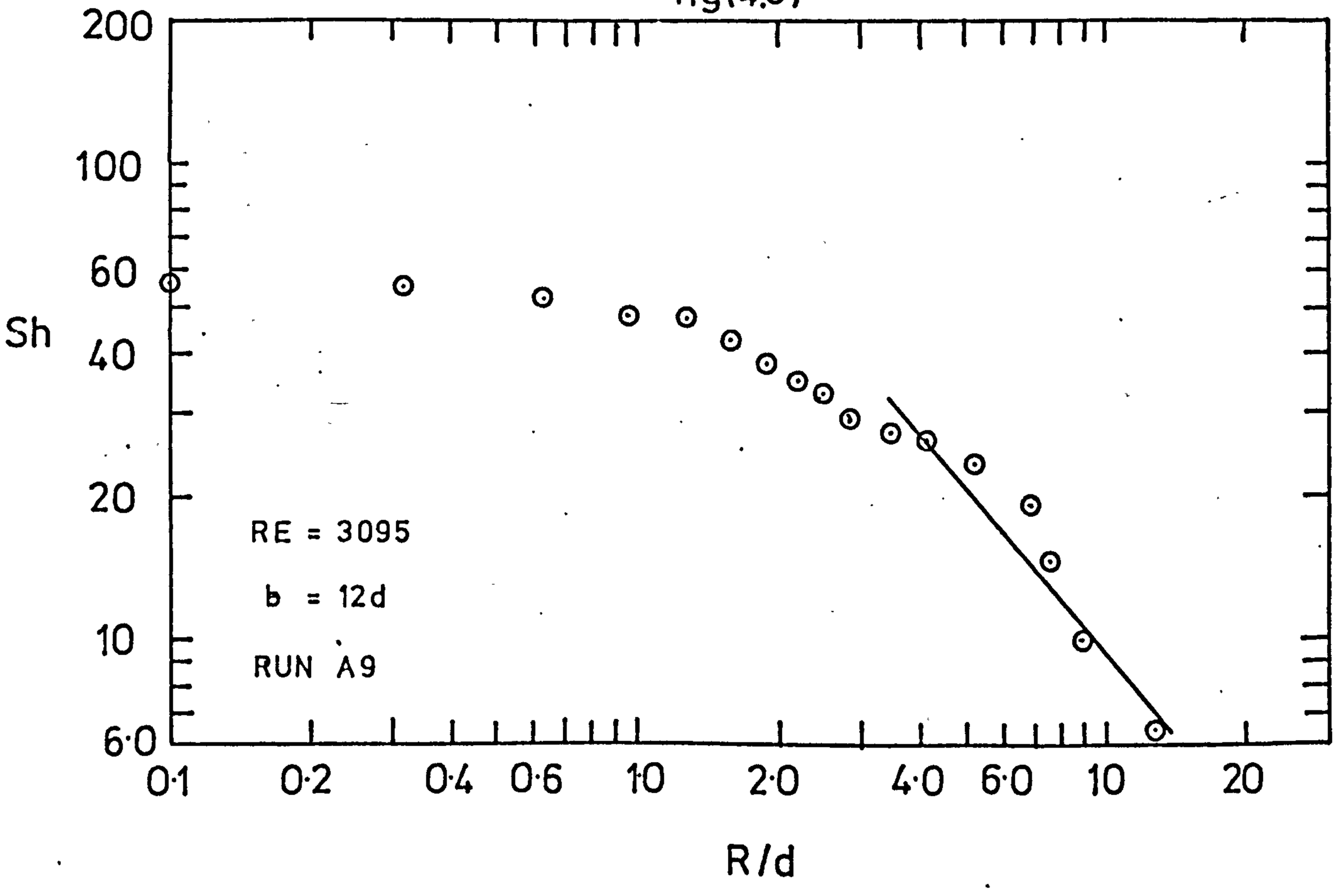


fig(4.5)

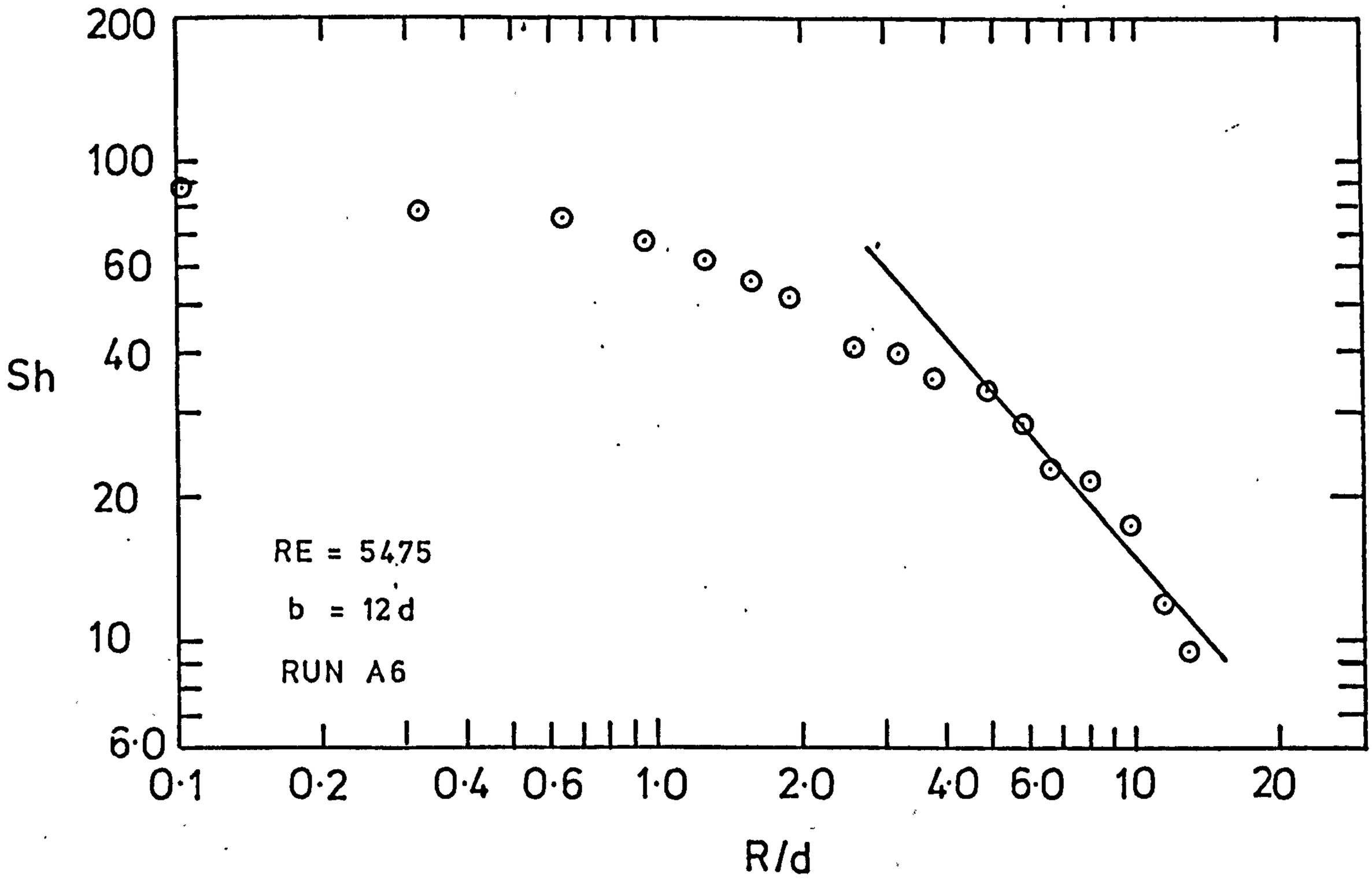


SHERWOOD NUMBER AS A FUNCTION OF RADIAL POSITION

fig(4.6)

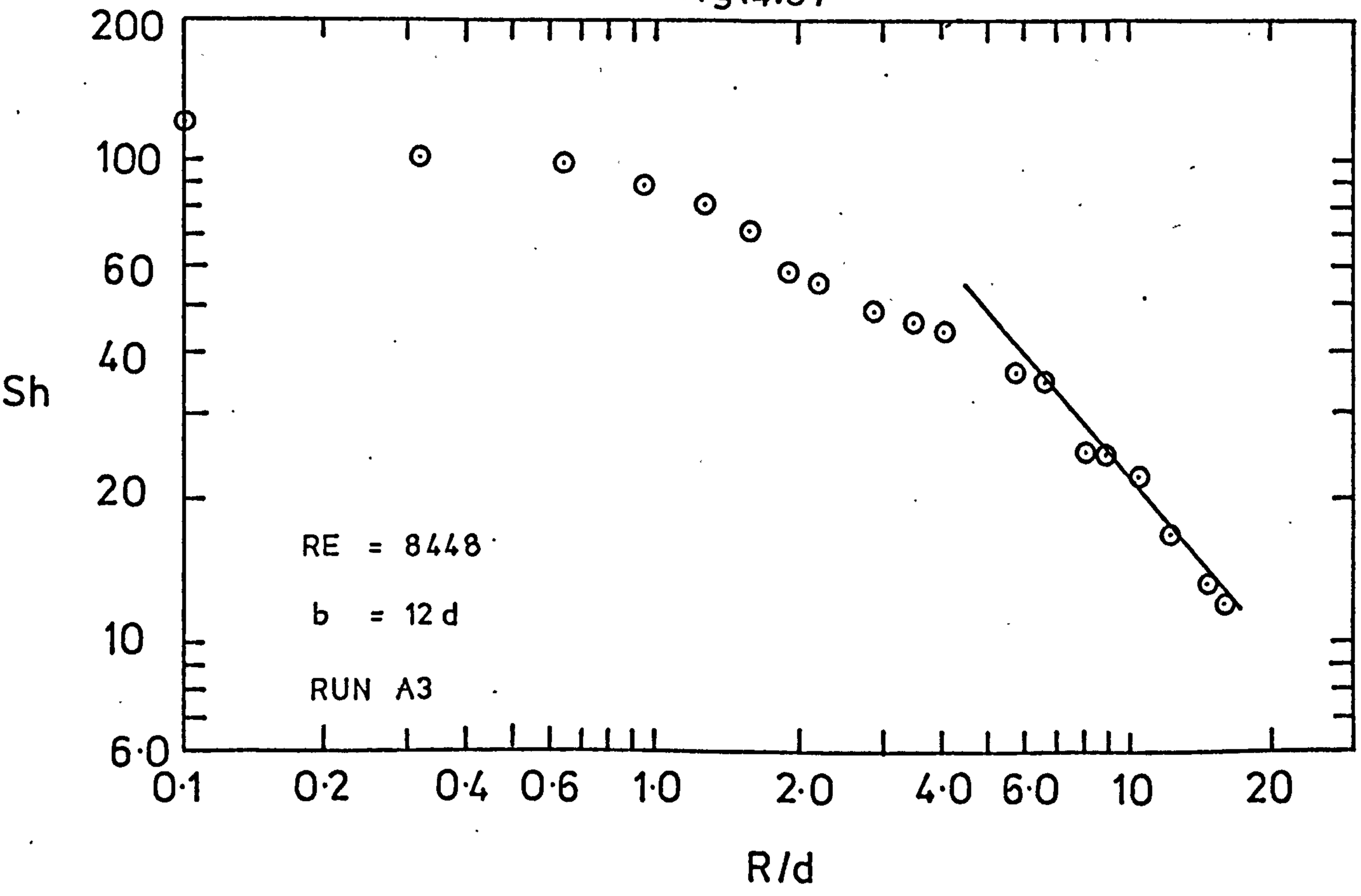


fig(4.7)

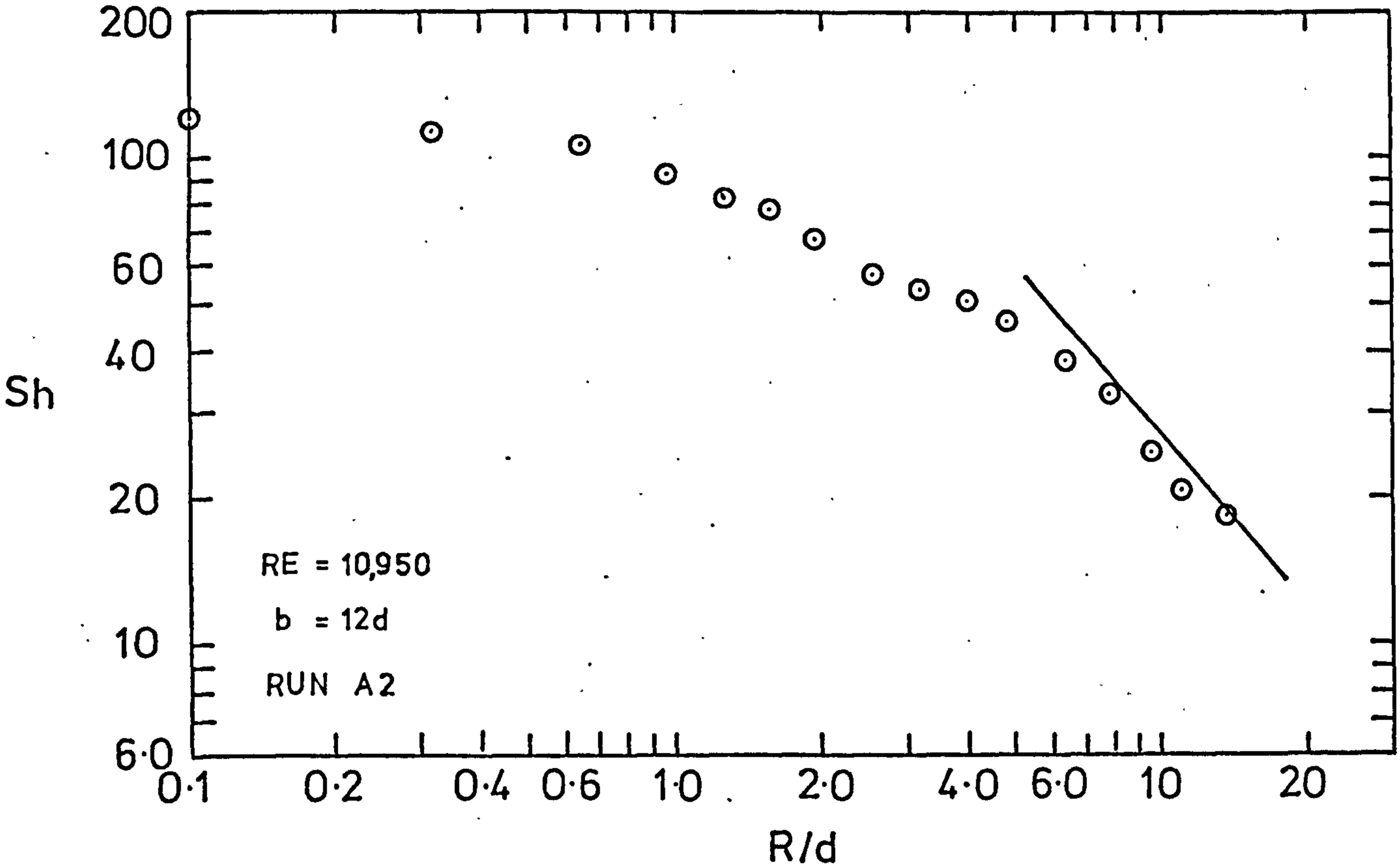


SHERWOOD NUMBER AS A FUNCTION OF RADIAL POSITION

fig(4.8)

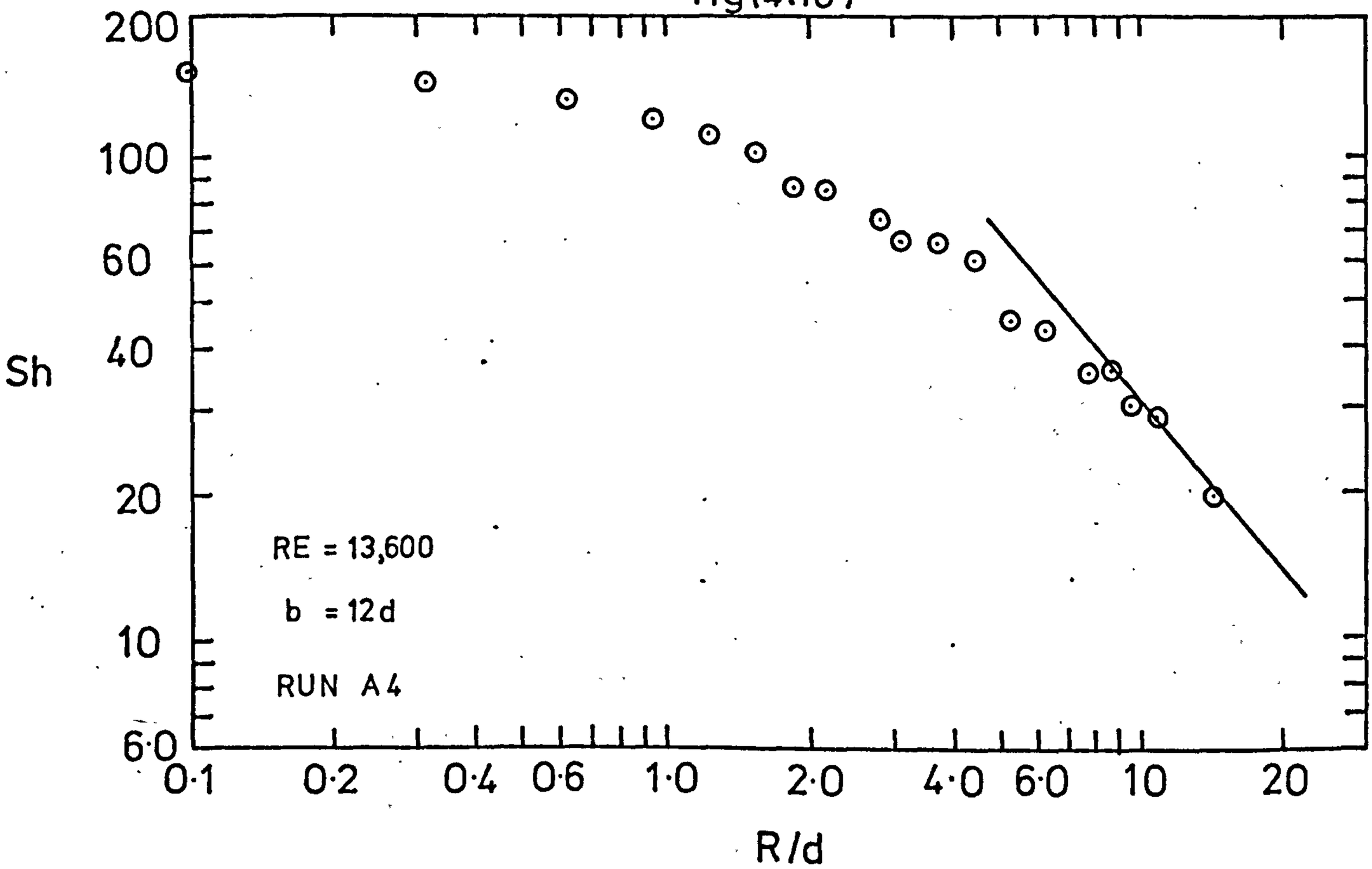


fig(4.9)

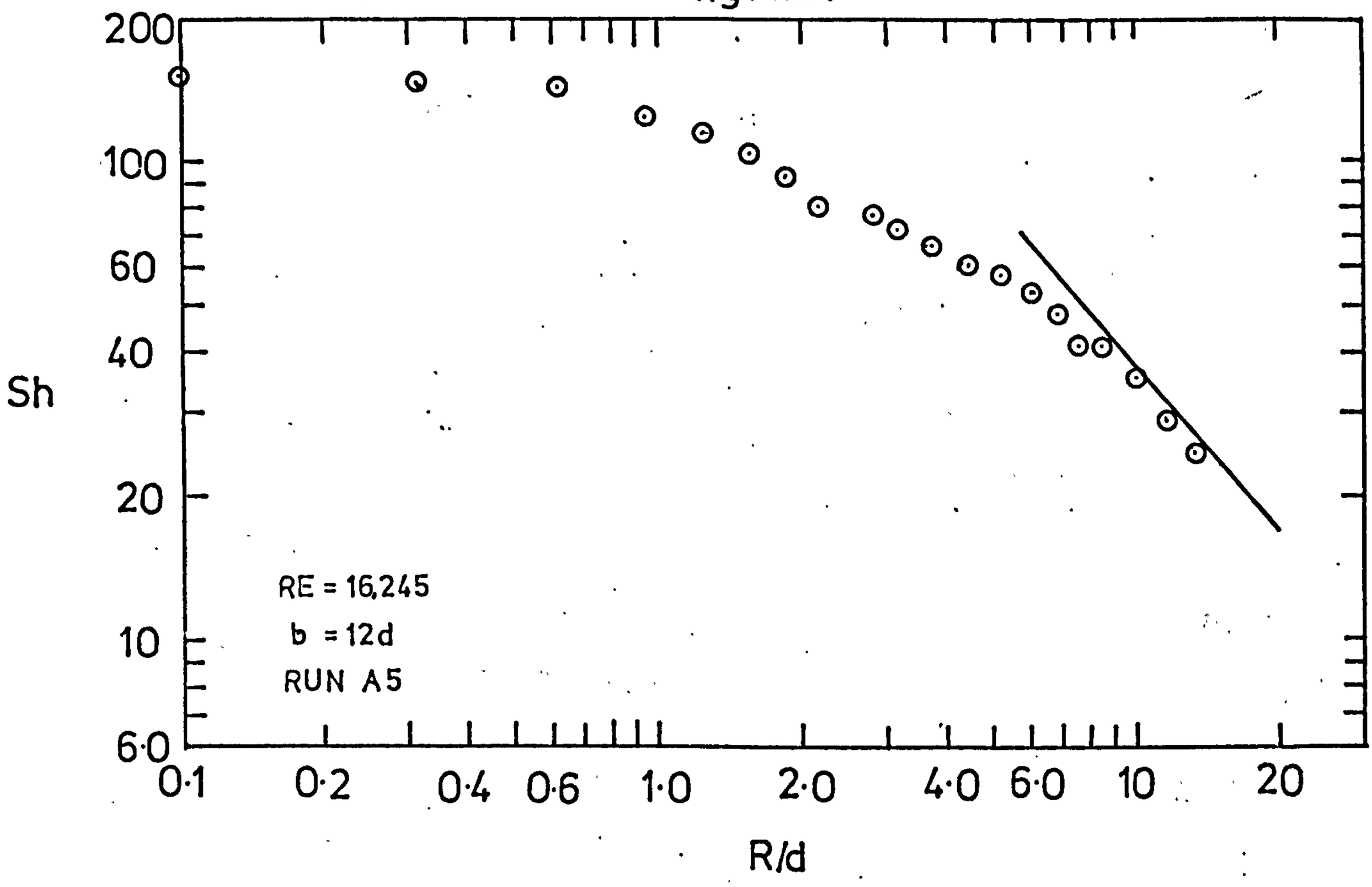


SHERWOOD NUMBER AS A FUNCTION OF RADIAL POSITION

fig(4.10)

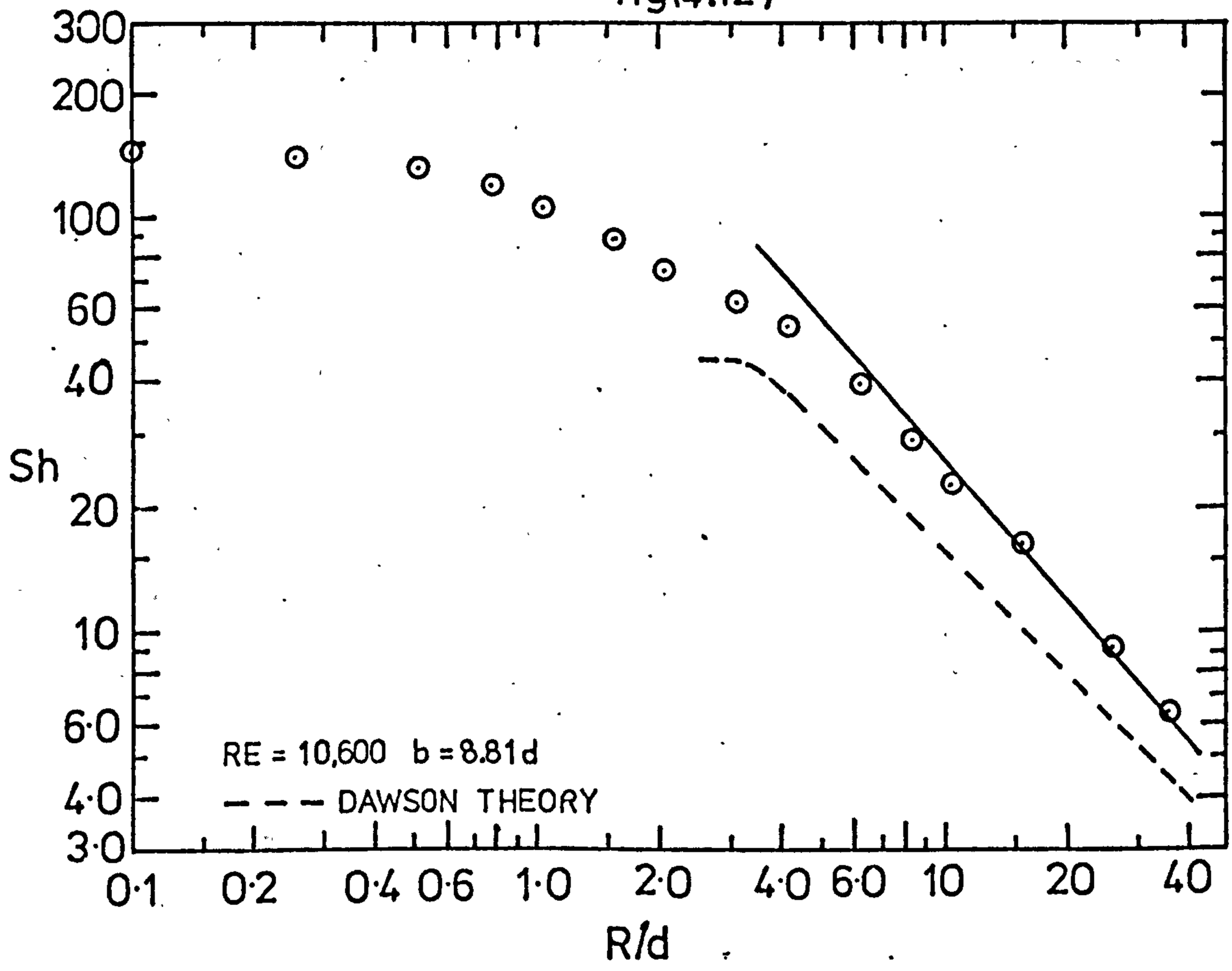


fig(4.11)

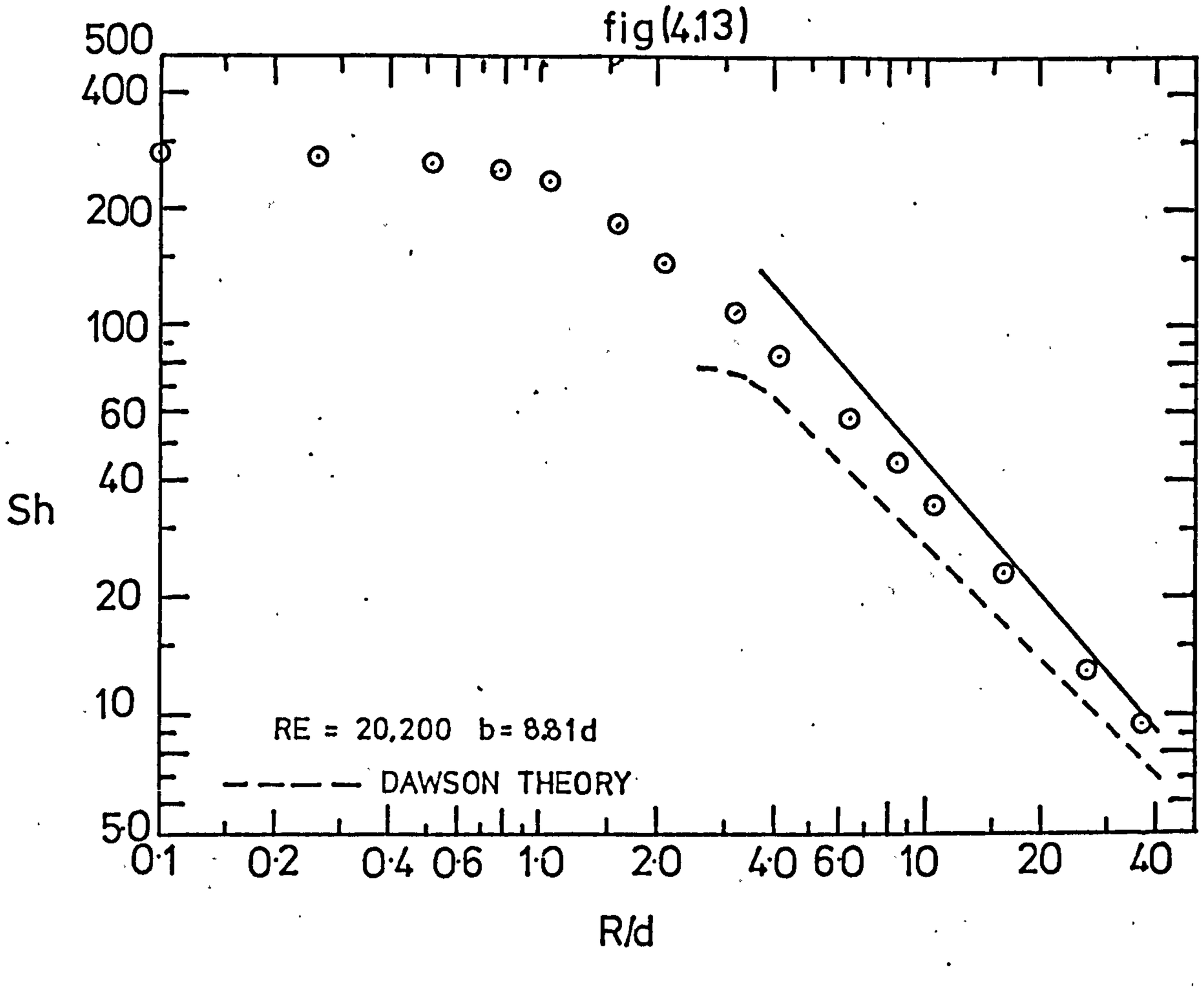


SHERWOOD NUMBER AS A FUNCTION OF RADIAL POSITION

fig(4.12)

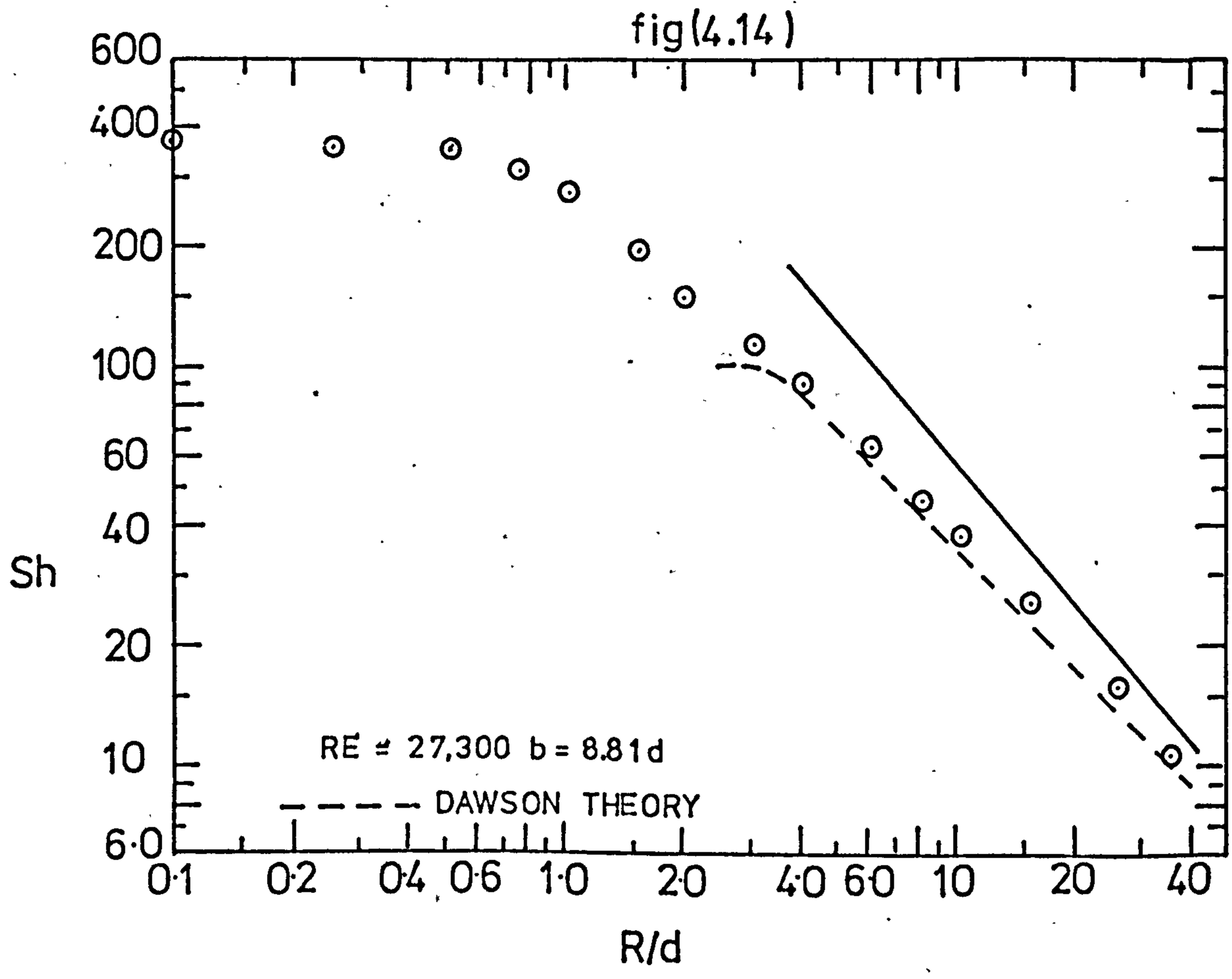


fig(4.13)

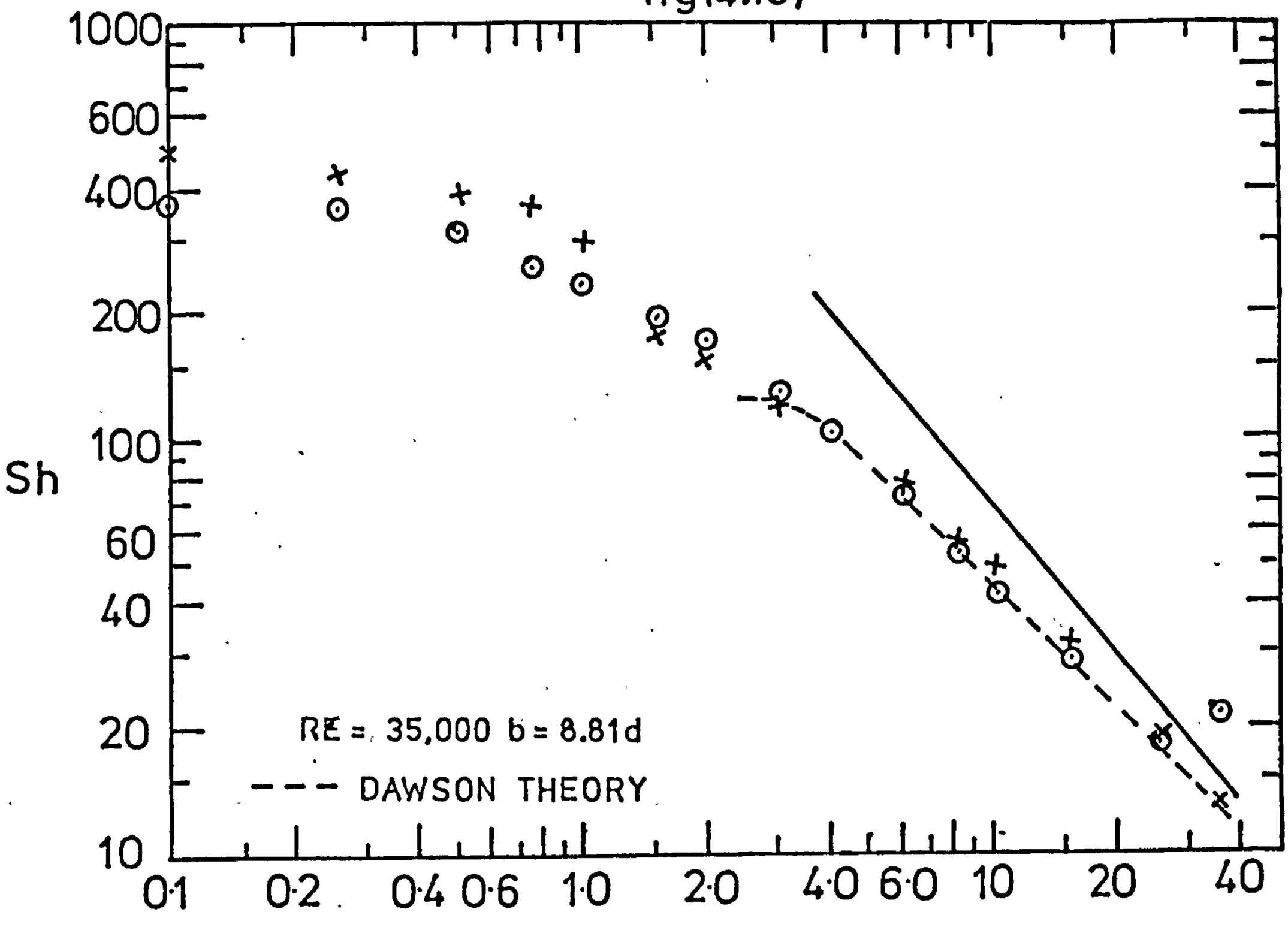


SHERWOOD NUMBER AS A FUNCTION OF RADIAL POSITION

fig(4.14)

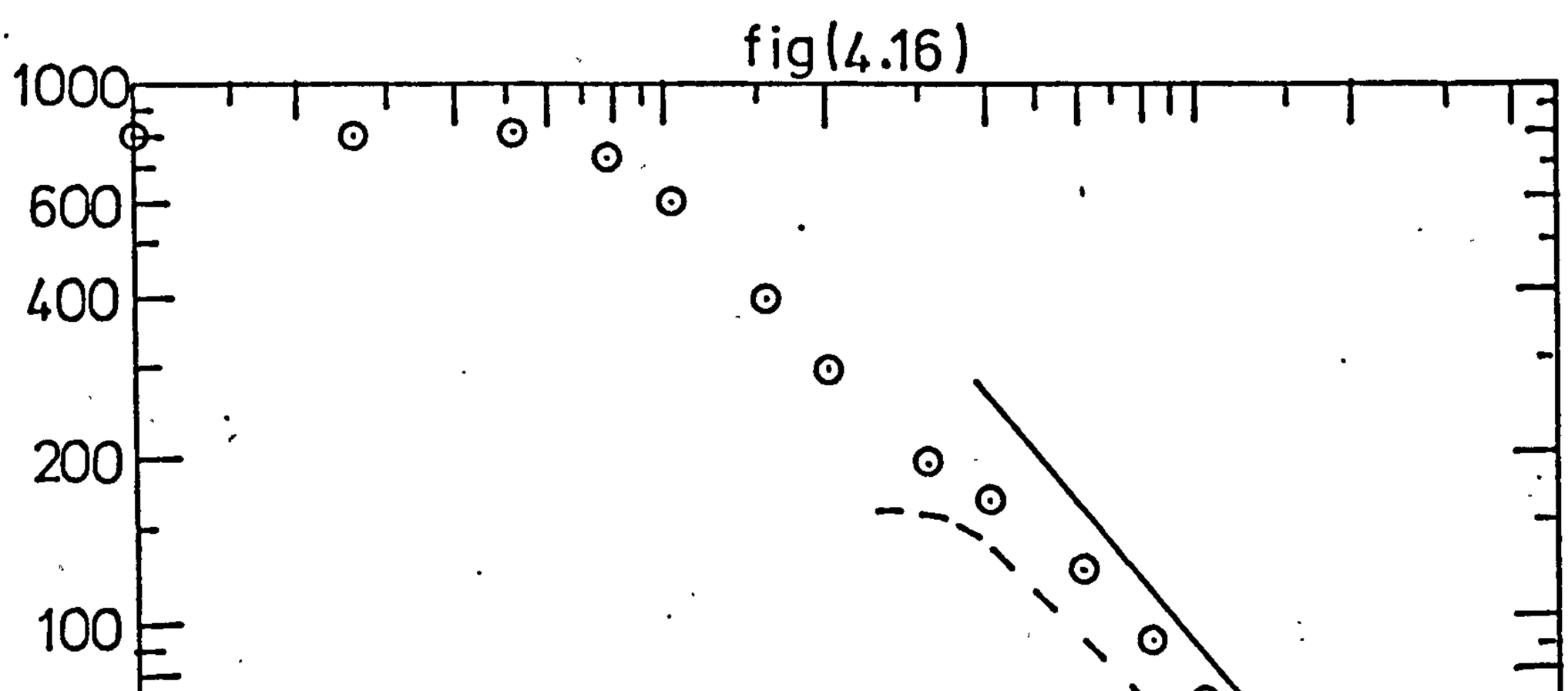


fig(4.15)

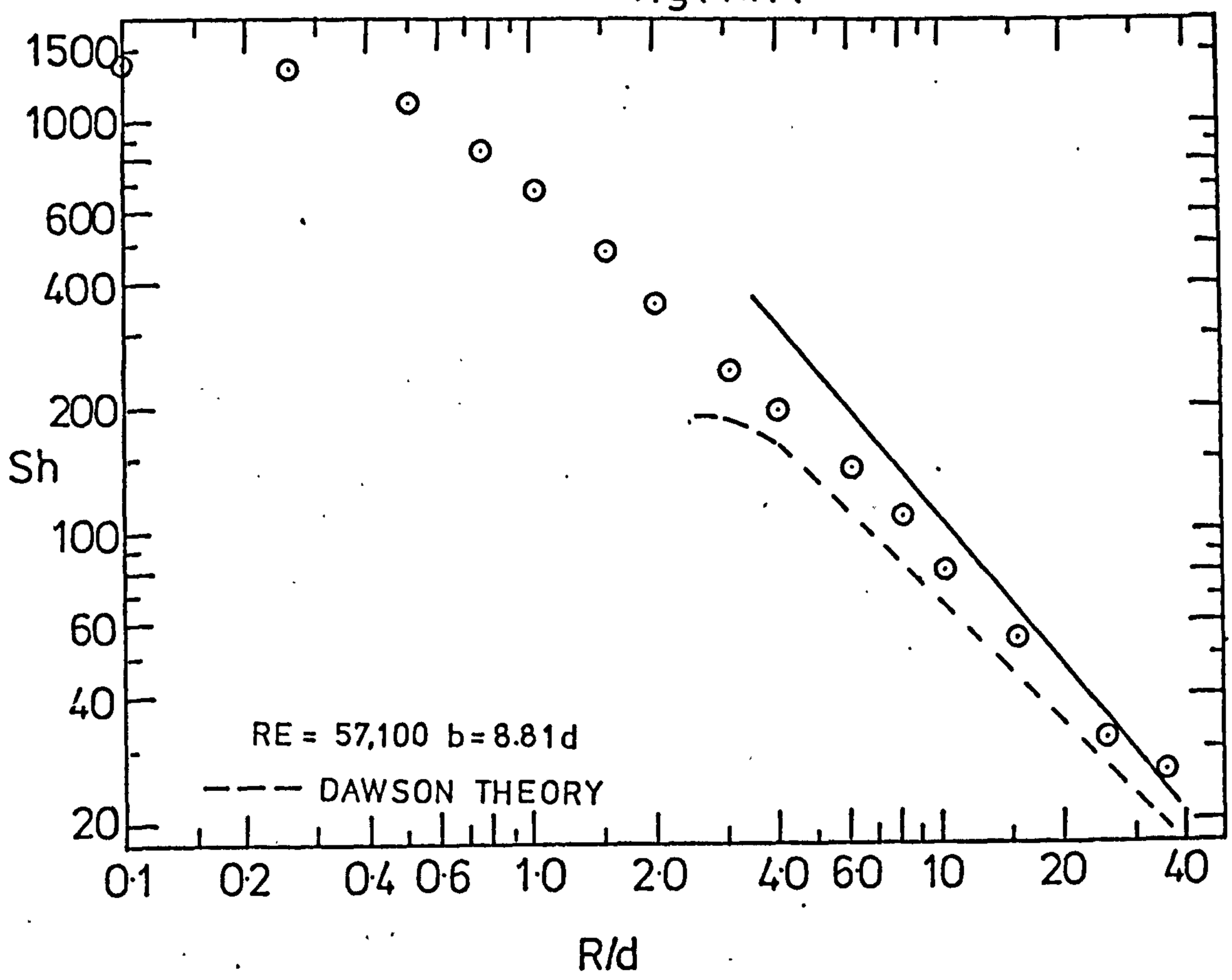


SHERWOOD NUMBER AS A FUNCTION OF RADIAL POSITION

fig(4.16)

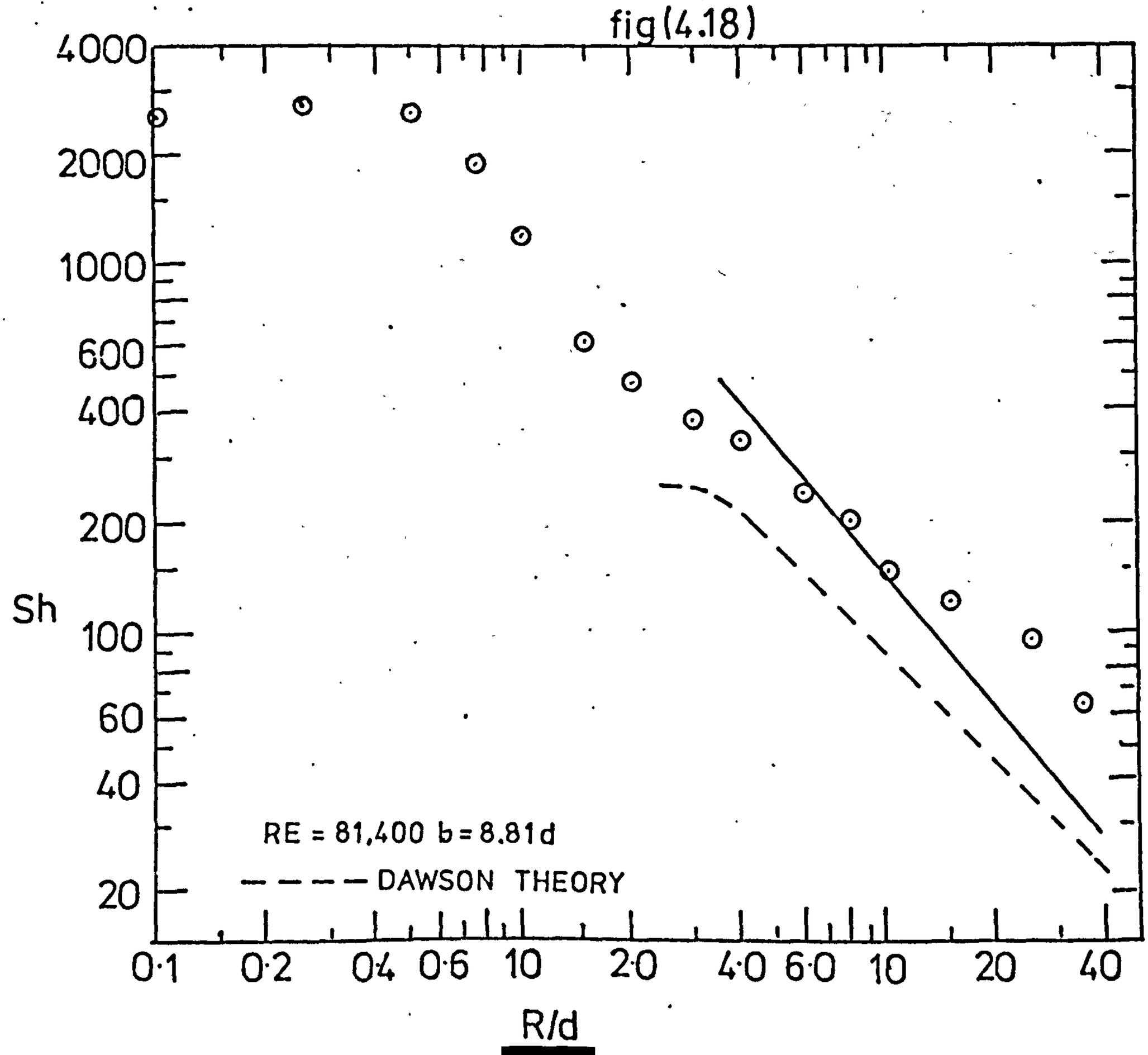


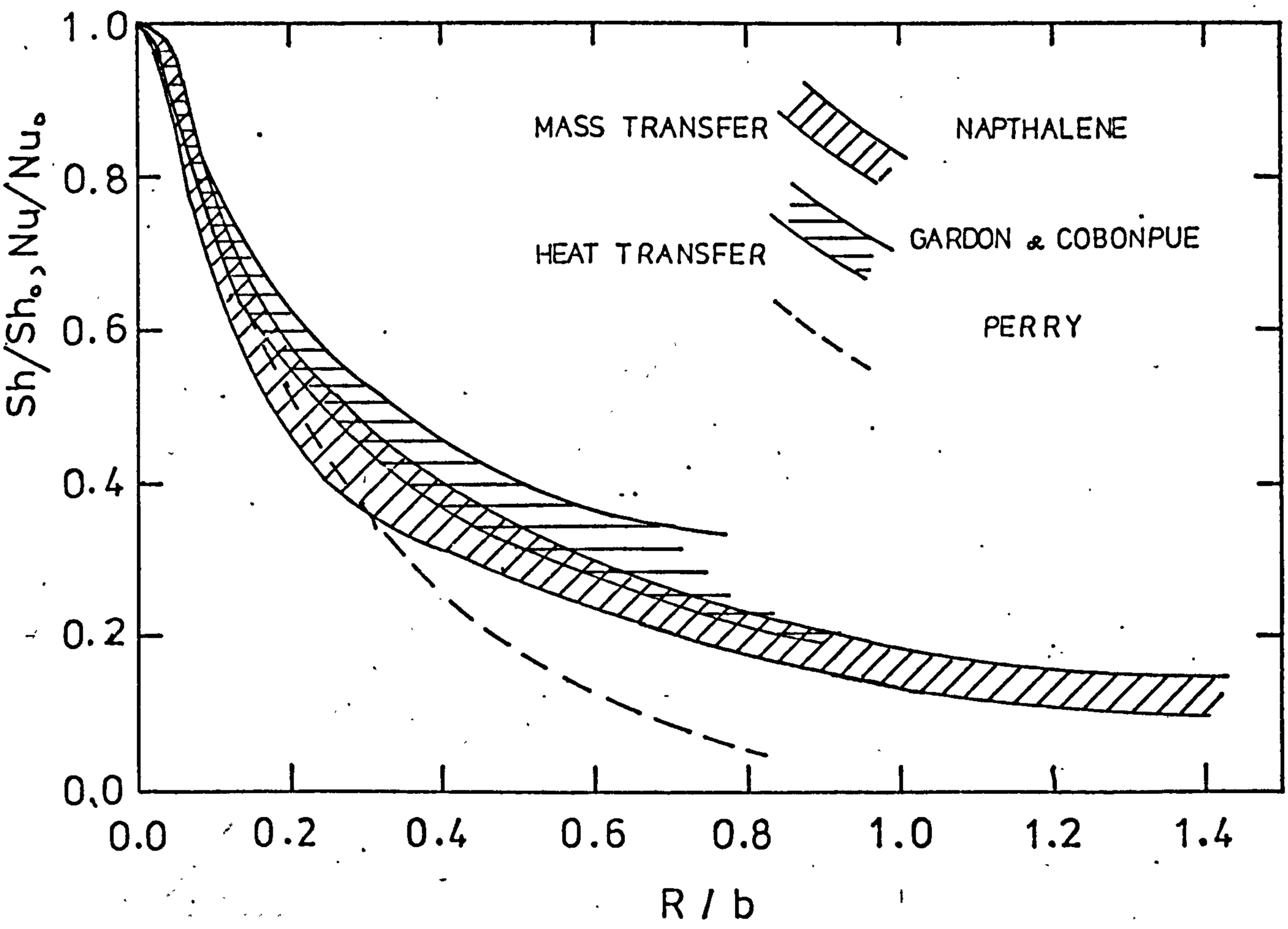
fig(4.17)



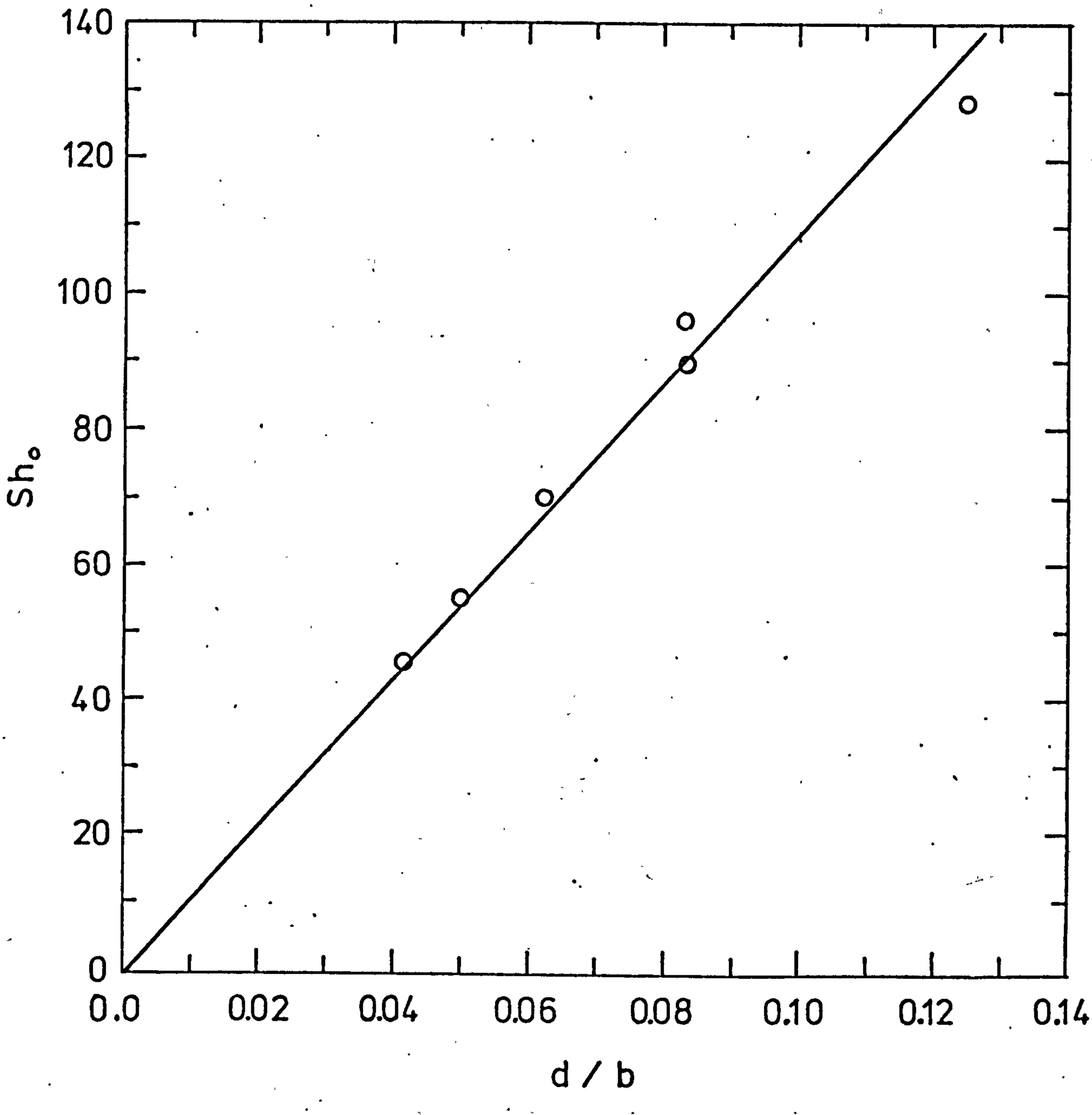
SHERWOOD NUMBER AS A FUNCTION OF RADIAL POSITION

fig(4.18)

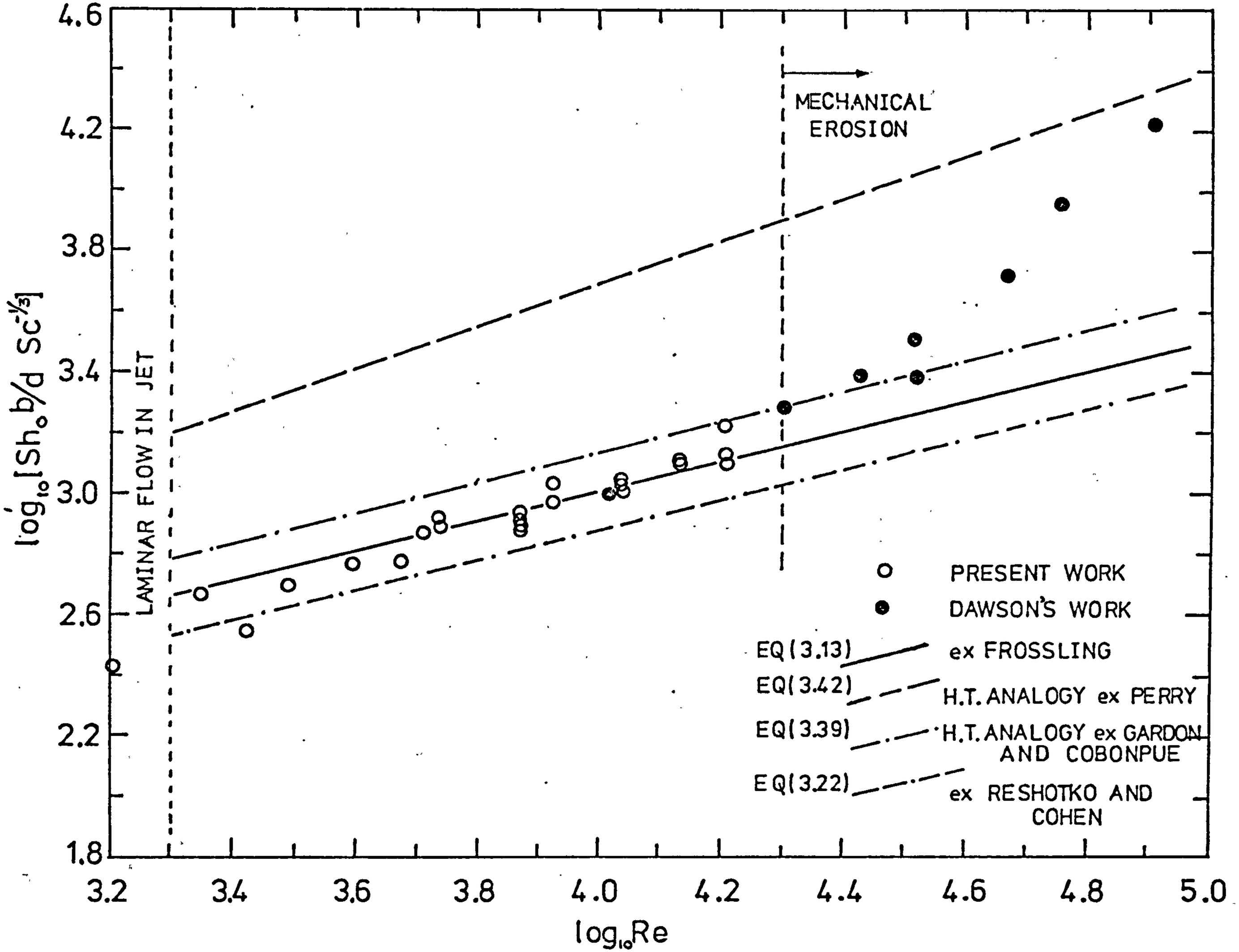




fig(4.19) DIMENSIONLESS MASS AND HEAT TRANSFER PROFILES



fig(4.20) STAGNATION POINT MASS TRANSFER DEPENDENCE ON JET-PLATE DISTANCE



fig(4.21) STAGNATION MASS TRANSFER VARIATION WITH REYNOLDS NUMBER AND COMPARISON WITH THEORY

the mass transfer coefficient becomes independent of jet plate distance in the wall jet region as might be expected by analogy with the velocity decay laws found by other workers and listed in section (2.4). The radial plots conform to the same line at different radial distances the latter being dependent on the jet plate distance. The various plots converge on the same line when $R/b = 0.4 - 0.5$. Poreh and Cermak (1959) claim their wall jet was formed at $R/b \simeq 0.3$ and other workers give similar values.

The position of the wall jet plot in this figure is taken to evaluate the constant in equation (3.107). The shape of the profile is predicted by the $R/d^{-1.172}$ relationship. The other figures (4.4) to (4.18) show how well the Reynolds number dependence fits the data of a range of experiments from Re = 3,095 to 81,400, for two jet diameters and varying jet/plate distance and how the profile compares with the model of Dawson. The latter's analysis exhibitis a curve on the stagnation point side of the wall jet because of the constraints of his model. The agreement between his results and theory is comparable with the present analysis. He predicts a flatter profile, but there is insufficient evidence to favour either. The overall Re dependence is also similar. Dawson's work gives $Re^{0.877}$ for the napthalene system whereas the present work gives $Re^{0.846}$.

4.3.2 Inconsistency in the Wall Jet Mass Transfer Profile

It is observable that in many of the napthalene erosion profiles the general smooth fall off in the radial mass transfer rate is broken between values of R/b of 0.2 - 0.3 by a decrease followed by an increase in mass transfer rate. This produces a hollow in the mass transfer profile and is best seen in run A16, fig (4.4). The magnitude of this effect seems to increase with decreasing Reynolds number and increasing jet plate distance. It is not noticable in the higher Reynolds number experiments.

The position of the hollow corresponds to the edge of the impingment

zone, a region before the start of the wall jet where little napthalene free air is entrained to dilute the air which has dissolved relatively large amounts of napthalene in the high mass transfer region of the stagnation area. Apart from the rise in napthalene concentration, the air will have undergone some cooling because of the sublimation energy needed by the napthalene to vaporise. Both these effects tend to lower the driving force until sufficient air has been entrained in the rapidly expanding wall jet to reduce these effects to negligible proportions.

Approximate calculations are now made to estimate the order of magnitude of each effect, assuming initially that complete mixing occurs in a vertical section at a given radial position in this region. This will give the minimum value for each effect, as, in reality, concentration and thermal gradients will be set up.

From the Clasius Clapyron Equation:

$$\frac{d\log_{10} P}{d(1/T)} = -\frac{\Delta H_V}{2.303R} \quad \ldots\ldots\ldots (4.3)$$

where ΔH_V is the molar heat of sublimation. In the absence of direct data for ΔH_V this equation can be used to estimate it.

From Trass (1958):

$$\log_{10} P = 11.55 - 3{,}765/T \quad \ldots\ldots\ldots (4.4)$$

differentiating (4.4):

$$\frac{d\log_{10} P}{d(1/T)} = 3{,}765 \quad \ldots\ldots\ldots (4.5)$$

From equations (4.3) and (4.5), $\Delta H_V = 17{,}229$ cal/mole.

Consider the relevant area on the napthalene surface as a circle radius 0.25b having an average Sherwood number of $2/3\ Sh_o$.

The mass of napthalene eroded in unit time is given by:

$$\frac{\pi}{d} (0.25b)^2 \rho_{Ao} D_{AB} Sh_o \frac{2}{3} \text{ grams} \ldots\ldots\ldots\ldots (4.6)$$

If Sh_o can be expressed:

$$Sh_o = 15.6 Re^{0.5} d/b \ldots\ldots\ldots\ldots (4.7)$$

From equations (4.6) and (4.7) the number of moles of napthalene eroded in unit time $\dot{M}$ is given by:

$$\dot{M} = \frac{\pi(0.25b)^2 \rho_{Ao} D_{AB} 15.6 Re^{0.5} d}{d\ 1.5\ M.Wt.\ b} \ldots\ldots\ldots\ldots (4.8)$$

Assuming the total volume of air involved per unit time is given by the equivalent volume in a free jet at the same distance from the jet, the mass of air involved per unit time from the Hinze (1949) formula is given by:

$$\dot{m} = \dot{m}_e (0.2b/0.5d - 1) \ldots\ldots\ldots\ldots (2.42)$$

where

$$\dot{m}_e = \frac{Re\, \eta\, \pi d^2 \rho}{\rho\, d\, 4.0} \ldots\ldots\ldots\ldots (4.9)$$

If all the heat to sublime the napthalene is given up by the gas the temperature drop produced ΔT is given by:

$$\Delta T = \frac{\Delta H_V \dot{M}}{\dot{m}\, Cp_{air}} \ldots\ldots\ldots\ldots (4.10)$$

For the experimental conditions of run A16 ΔT is calculated as 4.8×10^{-3} °C.

At 17°C a drop in temperature of 1°C produces a drop in saturated napthalene concentration in air of about $0.25.10^{-7}$ g/cc (fig (4.1)) which as a percentage of the value at 17°C is about 10%. Thus 10% of the driving force would be lost if the effect produced a temperature drop of 1°C. The

thermal effect then produces a percentage drop of only $5 \times 10^{-2}\%$ in the expected value.

For the concentration effect the mass of napthalene eroded and the volume of air involved are given by the above equations. The percentage reduction in the driving force is given by:

$$\% \text{ Reduction} = \frac{\text{Mass of napthalene}}{\text{Volume of air}} \frac{100}{\rho_{Ao}} \%$$

$$= \frac{\rho \pi 0.25^2 \; b \; \rho_{Ao} \; D_{AB} \; 15.6 \; Re^{0.5} \; 400}{Re \; \eta \; \pi \; d(0.4 \; b/d - 1) \; \rho_{Ao}} \%$$

which for the same experimental conditions as before gives a value of 3.4%.

From the analyses it can be seen how the effects should increase with a decrease in Re d/b. The magnitude of the temperature and concentration effects will be made larger than those calculated when the effect of the profiles of each is included. From the work of Poland (1967), especially his plot of velocity profiles in the impingment zone and outwards, the height of the maximum radial velocity is only some 0.1 to 0.2 of the total height of the flow pattern. If the conserved property gradients follow that of velocity a factor of 5 - 10 can be applied to the calculated percentage reductions.

The magnitude of the thermal effect is reduced, however, because of the eroneous assumption that all the heat is taken from the gas. The thermal loss will be shared by the napthalene block.

The dominant factor is then the build up of napthalene concentration in the impingment zone and rough calculation shows that its effect is in the same order of magnitude as that found empirically.

4.3.3 Effect of Jet Plate Distance

Plotting the stagnation point Sherwood numbers of the runs in fig (4.3) in fig (4.20) against the inverse of the dimensionless jet plate distance, d/b, shows the similarity of the correlation with the heat transfer work of Gardon and Cobonpue (1961). Thus although the wall jet region mass transfer is independent of jet plate distance and only dependent on Re, the stagnation point is dependent on both.

4.3.4. Dimensionless Profile

Although the mass transfer rates in the two discernible regions of the impinging jet, the stagnation point and the wall jet, are dependent on different functions, it is interesting to note the similarity of the profiles over the present range of experiments. The widest scatter is in fact in the region where the concentration effects are most pronounced. The profile will be expected to become much flatter with increasing Re as the wall jet region transfer increases proportionally more than the stagnation region. This explains the slight discrepancy between the mass and heat transfer profiles - the latter being for Re in the range 7,000 to 30,000 - the former 3,095 to 16,245. The profile given by Perry is not compatible with the present work excepting in the stagnation zone.

4.3.5 Stagnation Point Variation with Reynolds Number

The log plot of $Sh_o b/d\ Sc^{-1/3}$ against Reynolds number, fig (4.21) correlates the present data and that of Dawson onto one curve. The three theoretical plots derived from the stagnation model of Frossling, the heat transfer analogy from Gardon and Cobonpue's data, and the dimensional model of Reshotko and Cohen predict the trend of the data over most of the range investigated with varying success, the first mentioned being the best. The heat transfer analogy from Perry's data is totally unsuccessful in predicting

the data and because of the similar lack of success with the dimensionless radial profile, fig (4.19), the model is not considered further.

The slope of the data approximates to that of the three similar theoretical plots over most of the range covered in the present work and some of that covered by Dawson. Divergence from this slope of 0.5 is apparent at both low and high Reynolds numbers. For Reynolds numbers below 2,000 the flow inside the pipe jet would be laminar and any turbulence in the impinging jet would have to be produced by the system. The turbulence in jets in this Reynolds number region issuing from orifices, where similarly the only mode of turbulence production is in the jet system, has been found by Hrycak et al (1970) to be much lower than in higher Reynolds number jets and, as stagnation heat transfer rates have been found, as discussed in section (2.6) to depend on turbulence level, a decrease in the rate of mass transfer is expected around this critical Reynolds number value of 2,000.

The divergence in the high Reynolds number region is ascribed to mechanical erosion of the napthalene surface by the air jet, eroneously enhancing the true mass transfer rate. Scatter of results was found to increase for Reynolds numbers in the region of 16,000, some runs being disregarded because of the visible break-up of the napthalene surface. This was the major reason for limiting the experiments to a Reynolds number of 16,245.

A similar mechanical erosion mechanism has been shown to operate in cinnamic acid erosion in a water system by Dawson and Rao and Trass (1964) by the substitution of saturated cinnamic acid solutions for the water. 'Mass' transfer proportional to Reynolds number still occurred.

Trass (1970) ascribes the divergence of the stagnation point napthalene values from a Reynolds dependence of power 0.5 to a similar mechnical erosion phenomenon.

The two highest points from Dawson's data correspond to velocities

implying supersonic flow in the jet, but in the absence of a designed nozzle probably producing underexpanded flow of the type partially investigated by Gardon and Cobonpue. The latter found greatly increased heat transfer rates, although the rates exhibited a periodicity depending on jet/plate distance. This is a further reason to explain the divergence of Dawson's data from the theoretical line.

4.3.6 Errors

The most critical parameter to be assessed in napthalene erosion work is the temperature. A variation of a fraction of a degree can give inconsistent results as the vapour pressure is highly temperature sensitive, fig (4.1).

The gauge used in the measurements was calibrated in units of 0.002 mm. This is not a true measure of the accuracy of the readings as the reproducability was only within $\pm$ 0.006 mm. Measurements of the order of 0.01 mm are then liable to a large error and experiments with the smaller erosion profiles are liable to some scatter, as seen by comparing runs A1(a) and (b).

Reproducability in the stagnation point runs decreased with increasing Re due to the erosion phenomenon.

4.4 Conclusions

(1) The mass transfer model for the wall jet region successfully describes the shape and dependence on various parameters of the measured mass transfer rates.

(2) Of the stagnation point mass transfer models, the one derived from the work of Frossling is most successful in describing the variation of mass transfer with Re in the range 4,000 to 16,000. Below this range the transition between turbulent and laminar flow decreases the transfer rates.

(3) Mechanical erosion is an important phenomenon in the napthalene system above Re = 16,000.

(4) The dimensionless mass transfer profile is compatible with the heat transfer data of Gardon and Cobonpue, although the use of the Chilton Colburn analogy to predict the individual mass transfer profiles provides only a rough approximation.

(5) The heat transfer data of Perry is totally incompatible with the present work. The analysis from the work of Snedeker and Donaldson is not sufficiently accurate to be of practical importance.

C H A P T E R F I V E

VAPOUR DEPOSITION

VAPOUR DEPOSITION

Vapour deposition in the context of the present work is taken to mean the deposition of one chemical species on another by the thermally assisted reaction between one or more species.

Many coating processes are available to the technologist including electro deposition and vacuum deposition to enable one species to be coated by another. Vapour deposition can be the only practical method of producing high purity deposits, but in general the use of the method is limited by the necessity that the article to be coated must be raised to a sufficiently high temperature to activate the chemical reaction.

In a vapour deposition process the feed vapours are generated from solid, liquid or gaseous sources and transported to the reaction surface, which is at a sufficiently high temperature to promote the chemical reaction in the feed, and cover or plate the reaction surface with the product of the reaction. Sometimes, but not often, the substrate itself takes part in the chemical reaction. In some systems only one species takes part in the reaction, the species being able, for example like some metal carbonyls, to undergo thermal decomposition. In other systems a reducing agent such as hydrogen is necessary to promote the reaction or in some uses to enable a lower substrate temperature to be used than for the simpler thermal decomposition reaction systems.

In selecting a possible vapour deposition system it is then necessary to select a system where the thermally sensitive species is easily volatilised and the resulting thermal or thermochemical reaction is feasible at convenient substrate temperatures. In many cases the reaction products cause problems of contamination of the product or corrosion.

Vapour deposition reactions are by definition heterogeneous and being surface reactions are subject to a variety of possible rate controlling

chemical steps in the production of the product. If thermodynamic restraints can be ignored, i.e. the reaction at the given temperature can be considered to go to completion, then three possible steps can control the rate.

(1) Reactant adsorption on to the substrate.

(2) Chemical reaction on the surface.

(3) Deadsorption of the reaction products.

As in most cases the energy required for stage (2) is higher than for the other two stages, this is usually the rate controlling stage, where the reaction rate is dominated by a chemical mechanism.

If the chemical reaction is fast enough so that the feed gases react immediately they reach the substrate surface, the reaction rate will be controlled by the diffusion process that brings the reactant to the surface. The effective concentration of the thermally sensitive species at the surface is then zero and the deposition rate is now controlled by a mass transfer step and the rate can be predicted from mass transfer theory.

This leads to the splitting of rate controlling mechanisms into the two regions of chemical and mass transfer control. It is important in the understanding of vapour deposition reactions to determine the factors influencing the change over from a zone of chemical control to one of mass transfer control. The two regions can be most easily identified by the effect of temperature on reaction rate in each zone. In a chemically controlled region the reaction rate is given by some expression of the type

$$\text{Rate} = A\, e^{-E/RT} \quad \ldots\ldots\ (5.1)$$

where E is termed the activation energy.

An idea of temperature dependency for the mass transfer region can be gained by examining the theoretical expression for the mass transfer rate in the impingment zone of the impinging jet of the type derived in chapter three.

$$Sh = K\,Re^{0.5}\,\frac{d}{b}\,Sc^{1/3} \quad \ldots\ldots\ldots \quad (5.2)$$

Rewriting in terms of dimensionable variables.

$$\frac{k\,d}{D_{AB}} = K\left[\frac{U\,\rho\,d}{\eta}\right]^{0.5}\,\frac{d}{b}\,\left[\frac{\eta}{\rho\,D_{AB}}\right]^{1/3} \quad \ldots\ldots (5.3)$$

The mass transfer coefficient k is a measure of the reaction rate.

Molecular theories of viscosity predict $\eta \propto T^{0.5}$, $\rho \propto 1/T$ and for small ranges of temperature $D_{AB} \propto T^{3/2}$. Sc would then be expected to be fairly independent of temperature and the mass transfer rate to vary as for:

$$k \propto \left[\frac{\rho}{\eta}\right]^{0.5} D_{AB} \ldots\ldots\ldots \quad (5.4)$$

suggesting:

$$k = f\left(T^{\frac{3}{4}}\right) \quad \ldots\ldots\ldots \quad (5.5)$$

If a classical Arhenius plot of log reaction rate against the inverse temperature is made, the slope in the chemical control zone is -E/R and in the mass transfer zone -0.75. As values of E are in the order of 20 - 50 k cals per gram mole, the slope of the graph in the chemical zone can be expected to be far larger in the chemical zone than in the mass transfer zone, in fact about four orders of magnitude higher.

Mass transfer rates will then be relatively unaffected by temperature change but will depend on parameters affecting the mass transfer step, most important of all being the Reynolds number for the system. Altering the Reynolds number in the chemical zone will only alter the residence time of the chemicals above the substrate and will then have a minimal effect on deposition rates.

A useful way of classifying chemical reactions is by the 'order' of the chemical reaction. If the reaction rate is independent of reactant

concentration the reaction is said to be of zero order. If the rate is proportional to the reactant concentration then the reaction is first order, proportional to the concentration to power two, second order and so on. The position is complicated if the rate is a function of the concentration of more than one species but in the case of vapour deposition reactions it is often useful to determine the apparent order with respect to the thermally sensitive species holding the concentration of reducing agents and other species constant.

Examining, in the context of zero, first and second order reactions, the effect on reaction rates of varying concentration temperature and Reynolds number gives an insight into vapour deposition systems. The mass transfer controlled zone, where the rate is proportional to the concentration of reactant, acts as a first order system.

Zero Order Reactions

$$\frac{d\,\rho_A}{d\,t} = K$$

For zero order reactions there is a unique Arhenius plot for the chemically controlled region as the rate is only a function of temperature. The temperature dividing the mass transfer and chemical zones is a function of both concentration and Reynolds number. The mass transfer zone can be entered by decreasing the concentration or by increasing the temperature, fig (5.1).

Examples of this type of behaviour are found in the hydrogen reduction of niobium pentachloride, Babich et al (1967) and Tantalum pentachloride and pentaiodide, Valla (1971).

First Order Reactions

$$\frac{d\,\rho_A}{d\,t} = K\,\rho_A$$

For first order reactions the rate is a function of concentration producing a family of Arhenius plots in the chemical zone. The temperature dividing the mass transfer and chemical zones is not a function of concentration and the mass transfer zone can only be entered by increasing the temperature.

An example of first order reaction could be Nickel Carbonyl. Work reported by Carlton and Oxley (1967) gives the reaction as first order although their own work indicates a more complex second order mechanism.

Second Order Reaction

$$\frac{d\ \rho_A}{d\ t} = K\ \rho^2{}_A$$

A family of curves is produced in the chemical zone Arhenius plot. The zone dividing temperature is a function of concentration and temperature. The mass transfer zone can be entered by increasing either temperature or concentration.

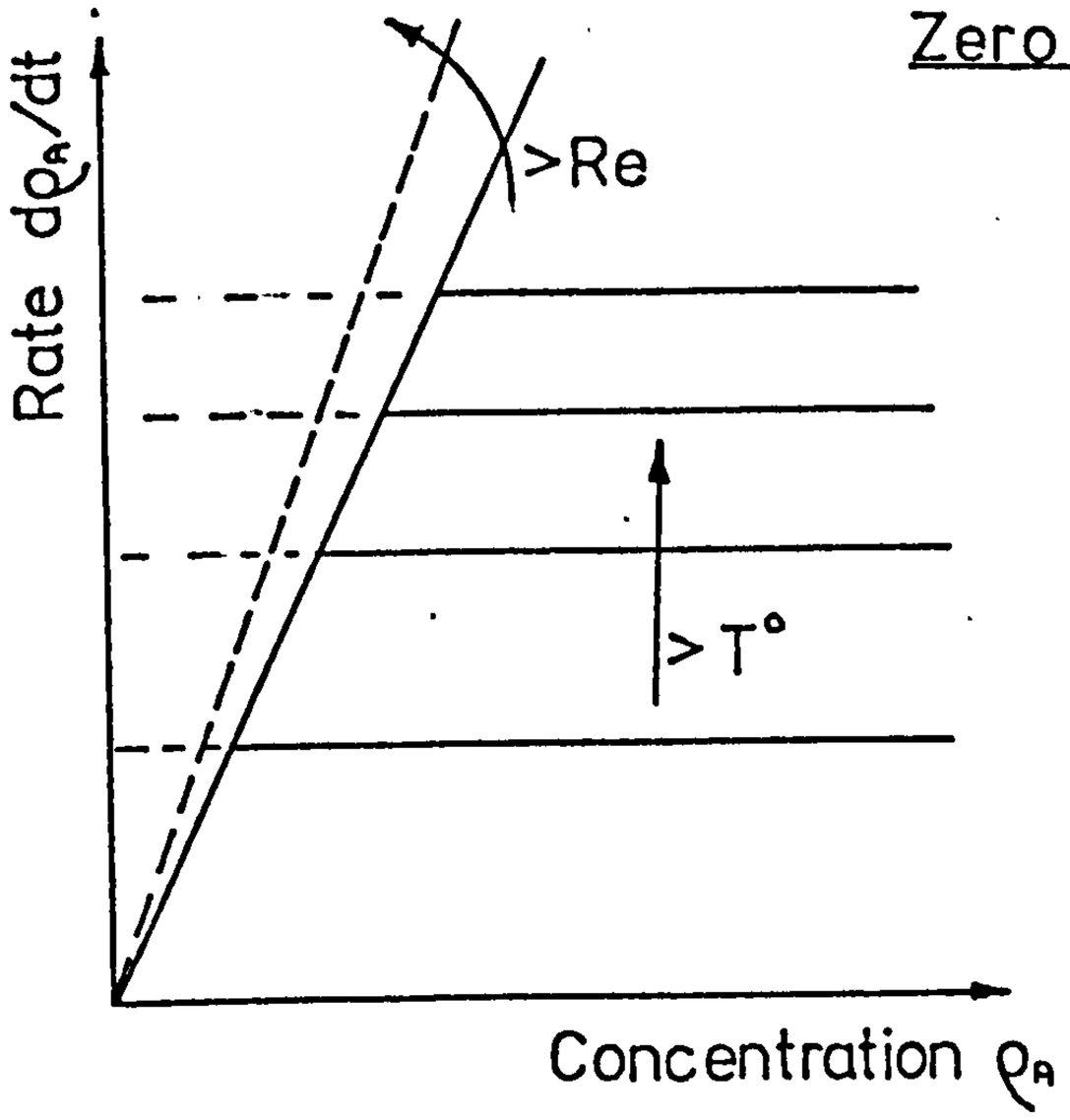
Summary

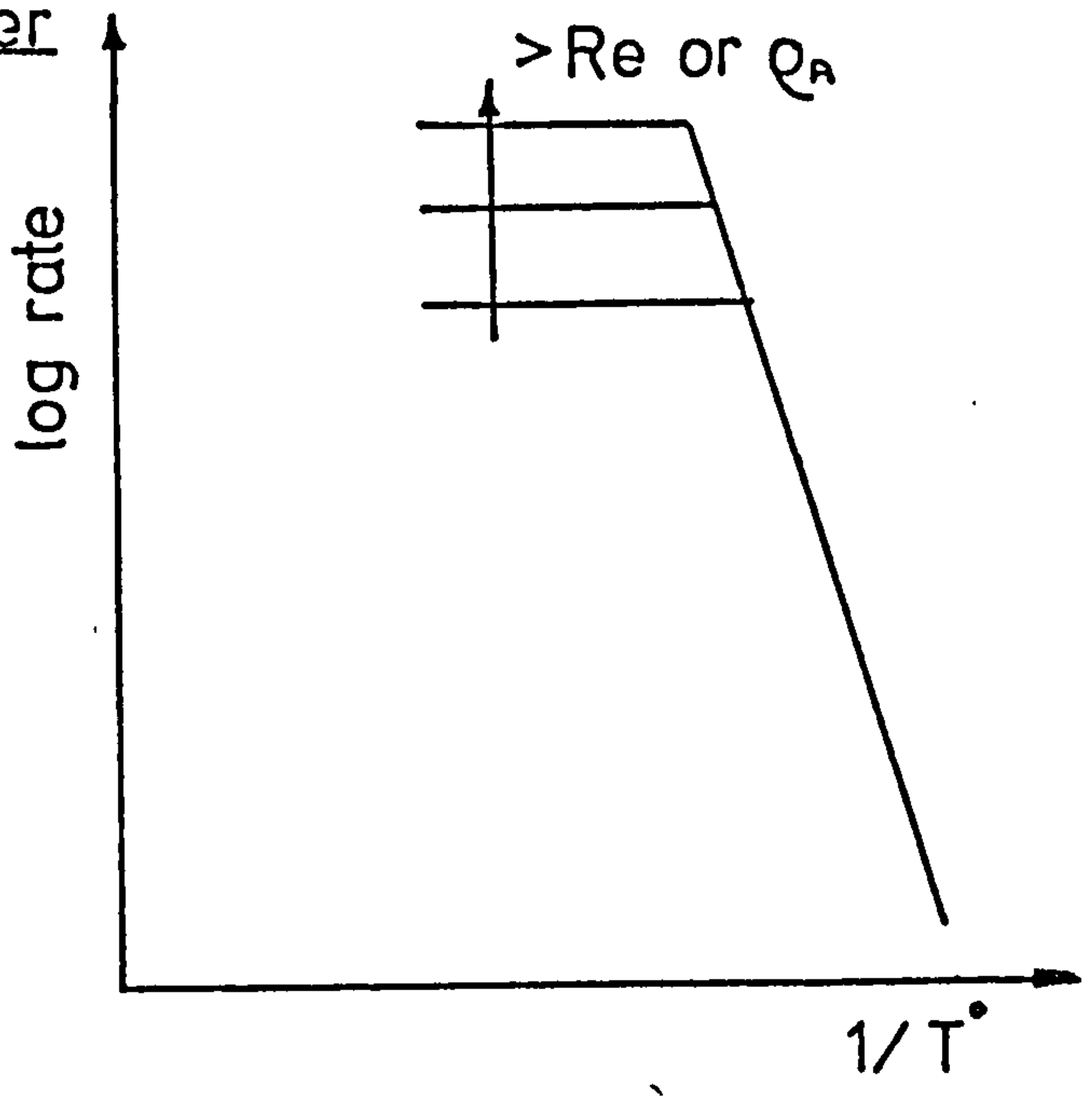
Effect on changeover temperature on increasing	Zero Order	First Order	Second Order
Re	Temp. Rises	Temp. Rises	Temp. Rises
Concentration of Reactant	Temp. Rises	Temp. Const.	Temp. falls

For further discussion of vapour deposition the work of Carlton, Oxley and Blocher (1966) is recommended as a standard text.

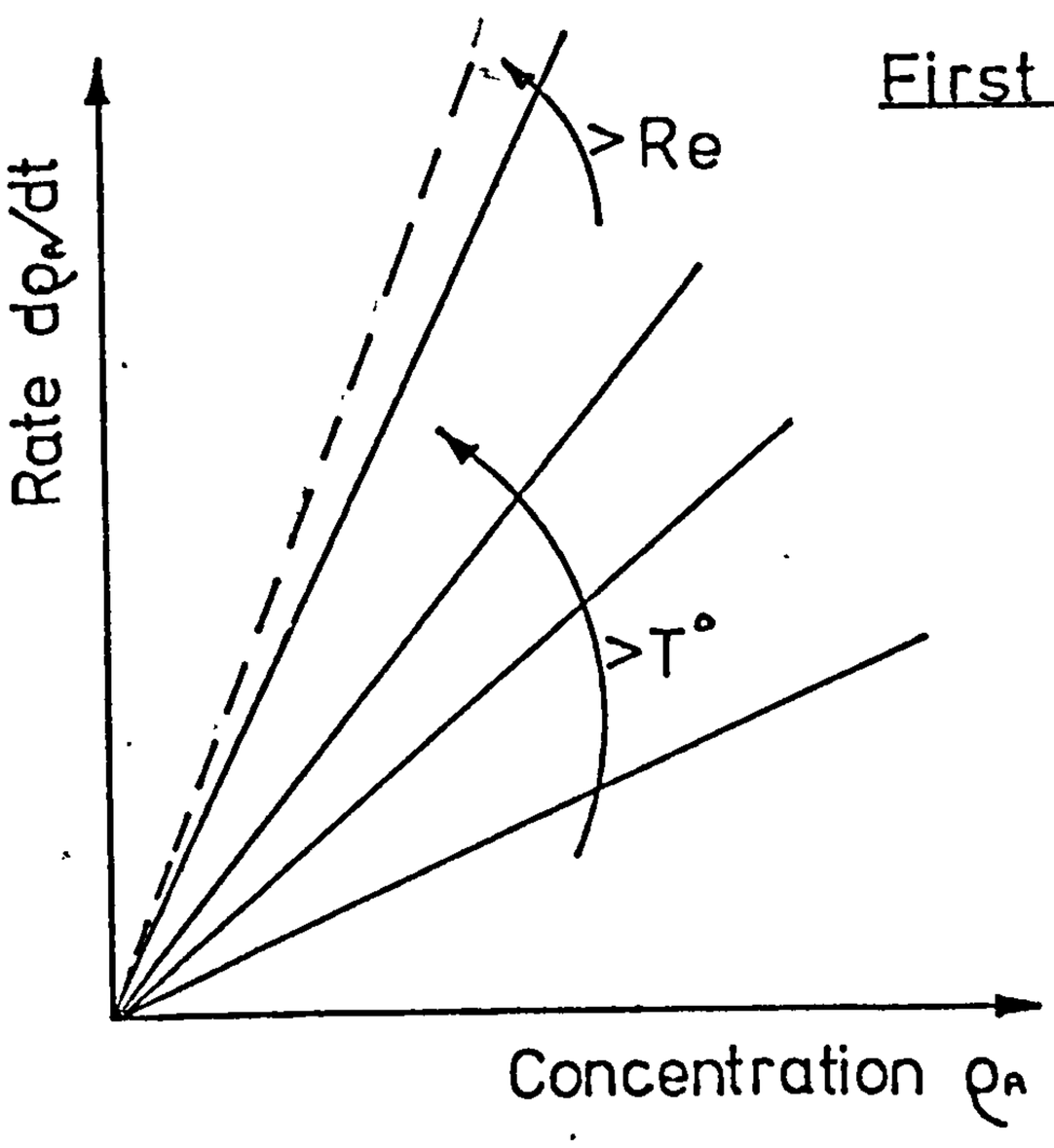
fig(5.1) VAPOUR DEPOSITION SYSTEMS

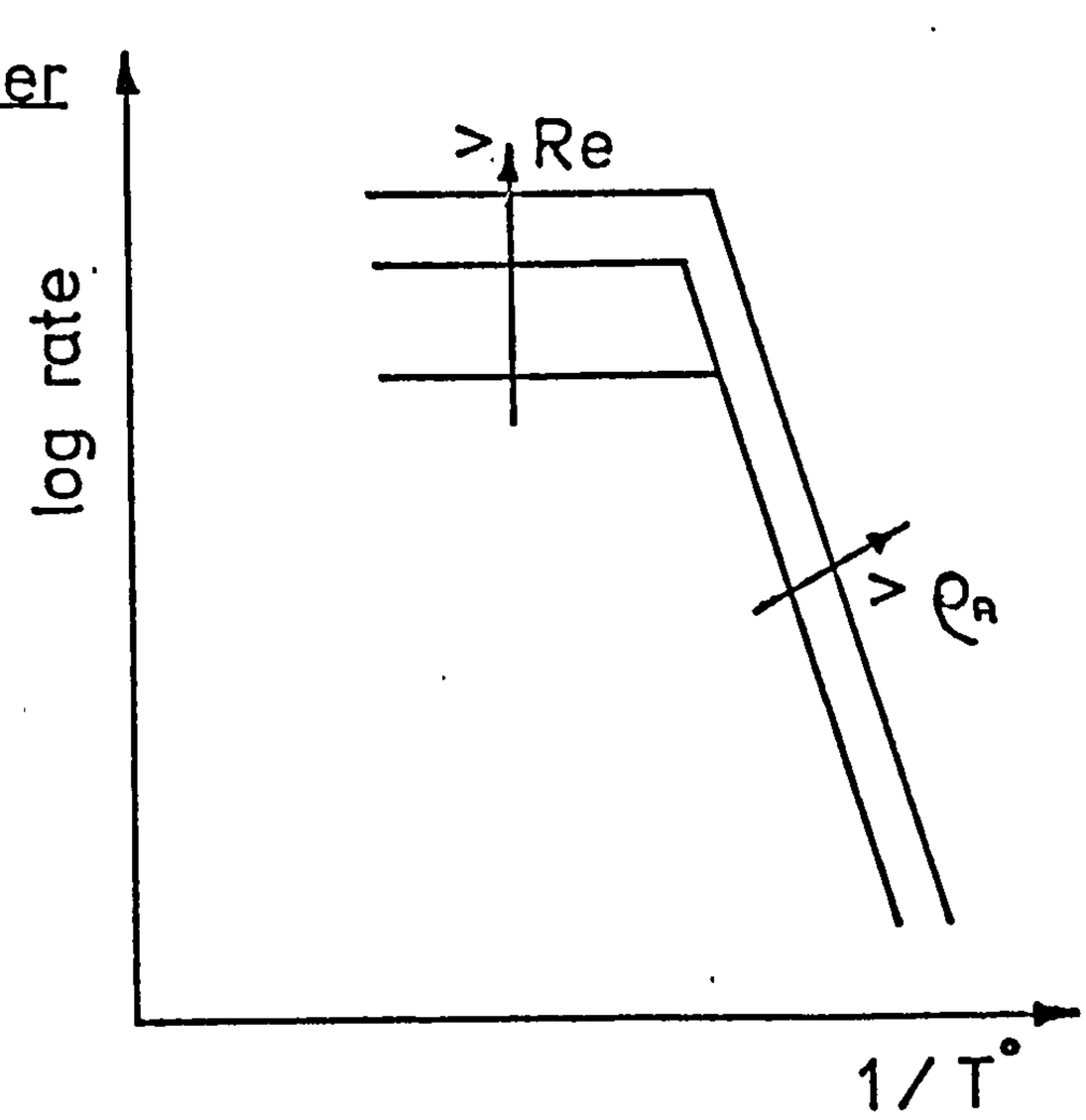
Zero Order



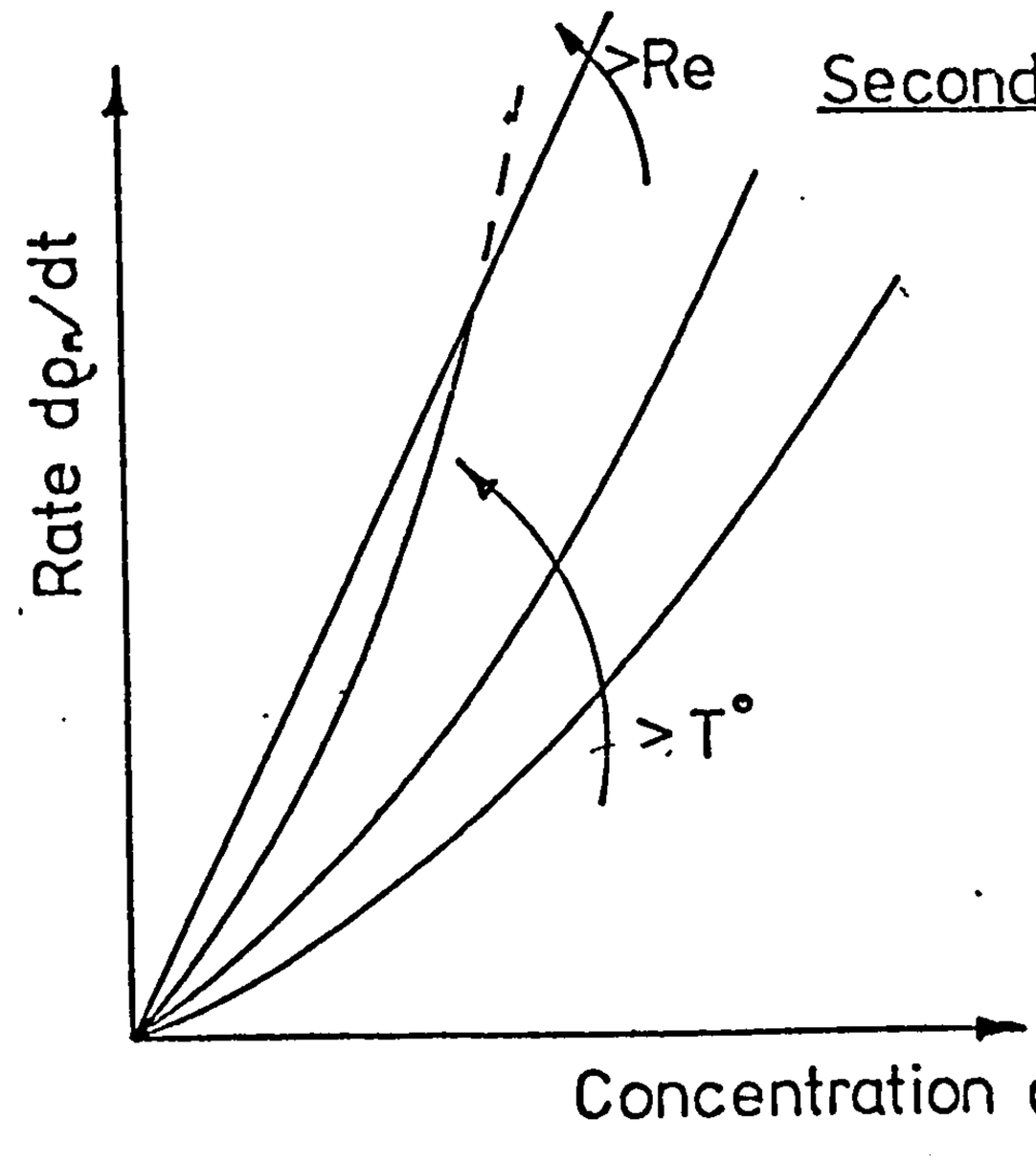


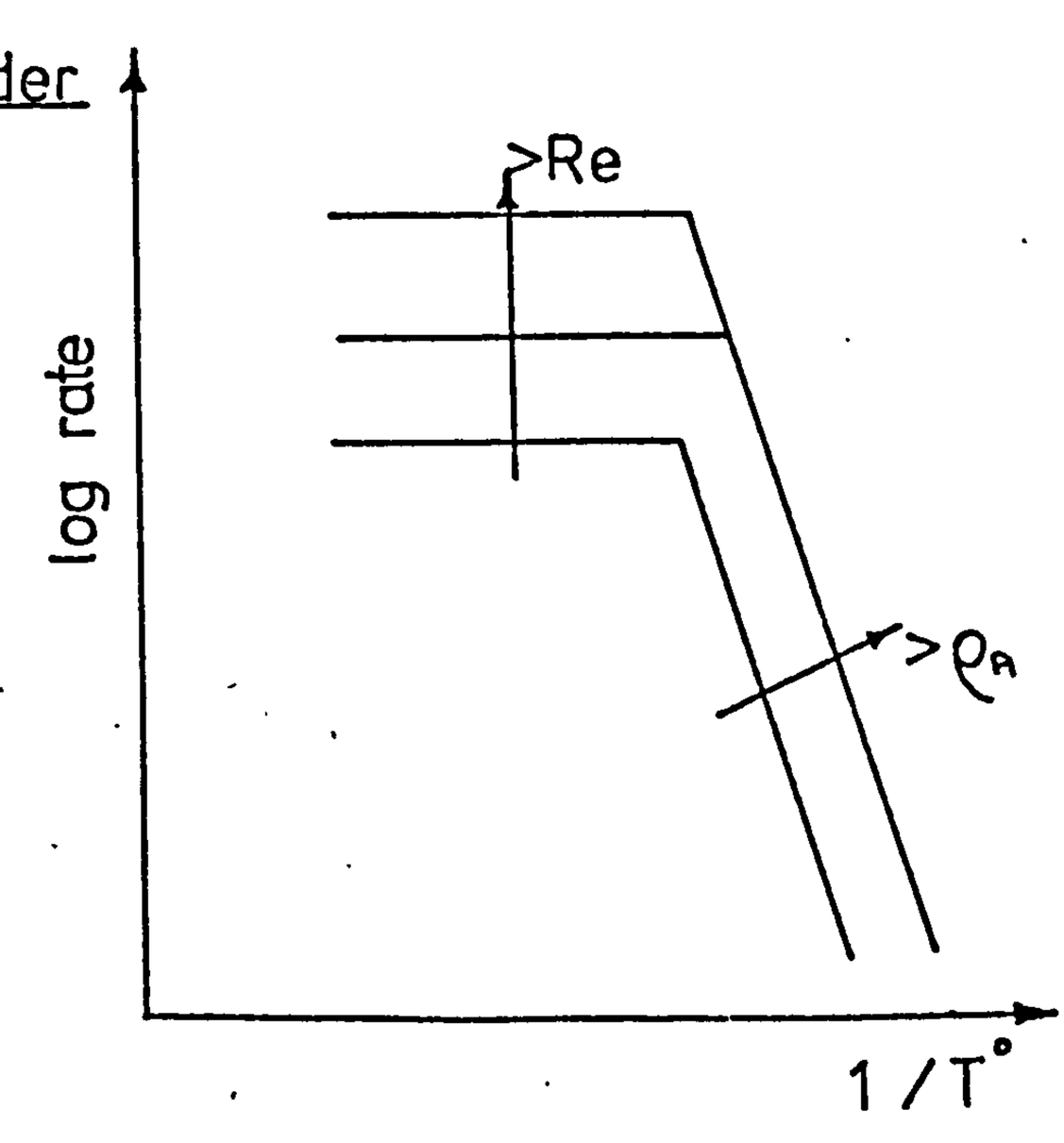
First Order





Second Order





CHAPTER SIX

APPLICATION OF MASS TRANSFER THEORY TO VAPOUR DEPOSITION SYSTEMS

APPLICATION OF MASS TRANSFER THEORY TO VAPOUR DEPOSITION SYSTEMS

The theory derived for mass transfer in the impinging jet and applied to the napthalene system is complicated by two factors when applying it to vapour deposition systems. Firstly, the driving force is reduced across the plate by the presence of a concentration profile within the jet due to the entrainment of gas containing no reactant species. Secondly, the driving force is reduced still further by depletion of the reactant by chemical reaction on the substrate. As the amounts of diffusing species used in the vapour deposition experiments are less than five mole percent, the effects on the system due to bulk flow and product evolution can be neglected. The conversion levels in the two systems are also low making dilution by entrainment the more important of the two factors.

The mass transfer profile in the stagnation region was not well predicted in the theory but has been established by the napthalene work. The mass transfer profile in the wall jet region has been established as varying approximately inversely with radial distance from the stagnation point. As the entrainment rate in the wall jet varies directly with radial distance, the reactant concentration reduces with radial distance. Because of this dilution, and, because of reaction depletion, this fall off is in fact faster. Combining the effects of both concentration fall off and mass transfer coefficient being proportional to $1/R$ the mass transfer is proportional to $1/R^2$. Compared with the deposition rates at the stagnation point the deposition rate in the wall jet region will be negligible for vapour deposition systems and further modelling is then restricted to the former region.

The simplified model for the stagnation point is to assume that the radial reactant concentration profile in the stagnation region is given by the concentration profile in the free jet. This profile is calculated from

the velocity profile as applied by Poreh and Cermak (1959)

$$\frac{U_h}{U_{ho}} = \exp\left[-100\,\frac{R^2}{b^2}\right] \quad \ldots\ldots\ldots \quad (2.43)$$

and the relationship given by Abramovich (1963) from Taylor's viscosity model applied to free jets:

$$\frac{\rho_{Ah}}{\rho_{Aho}} = \frac{T_h}{T_{ho}} = \sqrt{\frac{U_h}{U_{ho}}} \quad \ldots\ldots\ldots \quad (6.1)$$

Combining equations (2.43) and (6.1):

$$\frac{\rho_{Ah}}{\rho_{Aho}} = \exp\left[-50\,\frac{R^2}{b^2}\right] \quad \ldots\ldots \quad (6.2)$$

Table (6.1) gives the dimensionless deposition profile for vapour deposition systems, ignoring entrained reactant and reaction depletion, calculated from equation 6.2 and the mean mass transfer profile from the data in fig (4.19).

Table (6.1)

R/b	Sh/Sh_o fig (4.19)	$\exp\left[-50\,\frac{R^2}{b^2}\right]$	Sh/Sh_o Vap. Deposit
0.05	0.89	0.883	0.79
0.1	0.72	0.607	0.44
0.15	0.61	0.325	0.20

The Sherwood number for the Vapour Deposition work is then defined using a value of k, the mass transfer coefficient, in terms of the concentration ρ_{Aho}, irrespective of the true local radial value and is in this case a measure of the <u>mass</u> transferred at positions other than the stagnation point.

Estimation of the depletion effects due to reaction requiresa more

complex analysis, probably only suitable for the Universal type theories outlined in chapter two. This will have the effect of quickening the decay of the profile derived in table (6.1).

The jet axis value of the reactant species ρ_{Aho} decays with distance from the jet and in calculating the stagnation Sherwood number this relationship, and how it is affected by entrained reactant, needs to be known. An analysis of this is made for each of the two systems used in Appendix (2).

CHAPTER SEVEN

VAPOUR DEPOSITION OF COBALT OXIDE

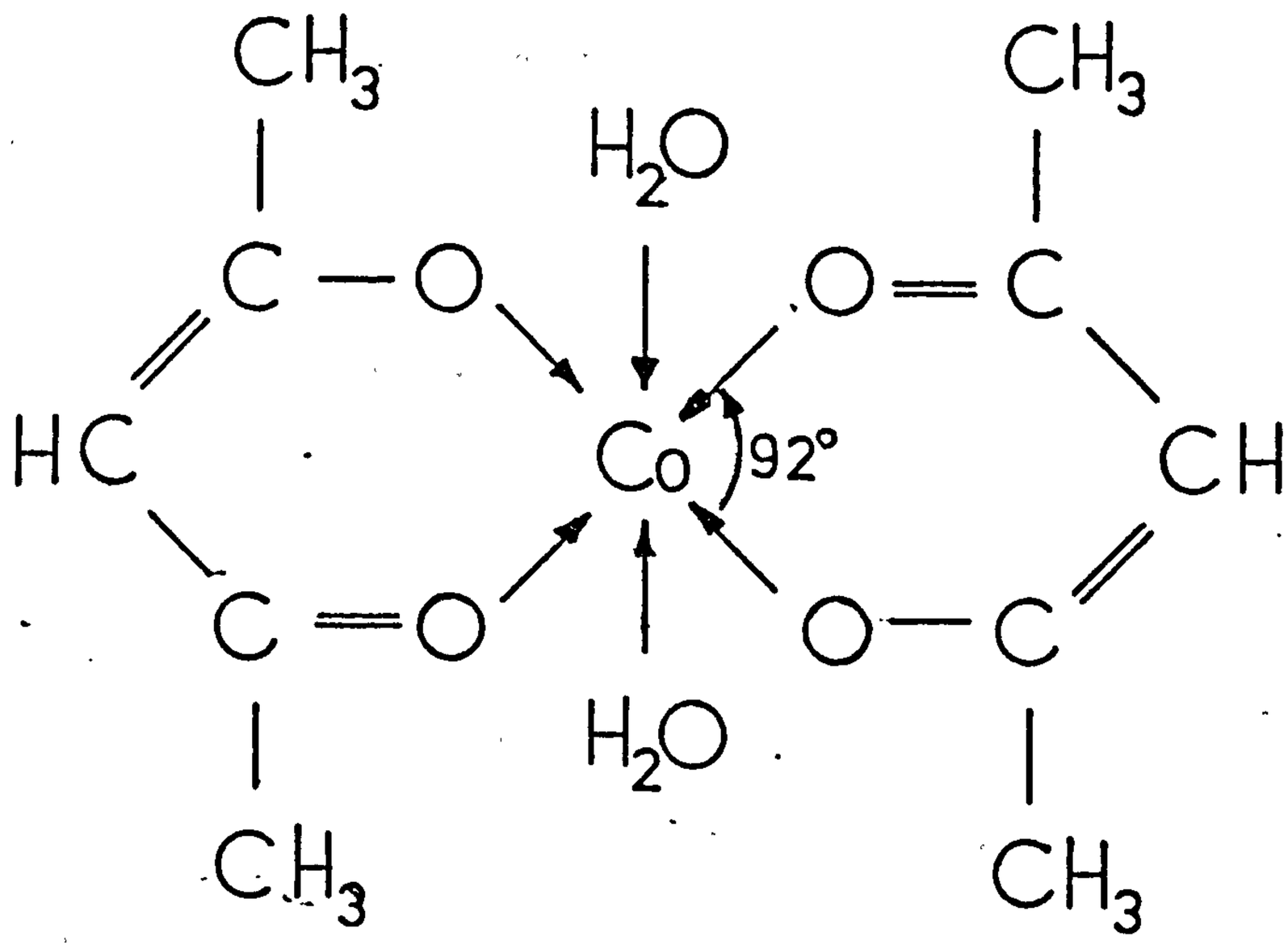
7.0 VAPOUR DEPOSITION OF COBALT OXIDE

Cobalt acetylacetonate, $Co(C_5H_7O_2)_2$ fig (7.1), is an example of a bidentate chelate. A chelate is a special example of a chemical complex, (so special in fact that there is some contention whether chelates should be classified with complexes). A metallic complex has the characteristic form of a central metal atom surrounded by chemical groups or units known as ligands. These ligands can be attached to the metal atom by a single donor atom or, as in the case of chelates, by two atoms, and further in the latter case so as to form a heterocyclic ring. The process of forming a chelate ring is called chelation and the molecule from which the ring is formed is the chelating agent. The term chelate, derived from the Greek word for a lobsters claw, was first coined to describe the calliper like mode of attachment of the ligand(s) to the metal atom. The term bidentate in the case of the duovalent cobalt compound describes the number of links from the ligand, "two teeth" in this case.

The crystal structure of this salmon pink coloured compound was analysed by Bullen (1959), with its unsaturated rings the structure would be expected to be planar which it nearly is. The cobalt atom lies about 0.4×10^{-7} mm above the plane of the two rings. Extra ligands such as water, ammonia and alcohol can be taken up to form stable octahedral complexes. In fig (7.1) water molecules are shown in this configuration. These extra ligands can be driven off by the action of heat.

No information could be found in the literature of thermodynamic properties of cobalt acetylacetonate, which in the rest of the section will be referred to as CoAcAt.

Hoene et al (1958), studying the thermal dissociation of the compound, present data that suggests that dissociation of the compound into acetone



fig(7.1)COBALTOUS ACETYLACETONATE

and CO_2 is virtually complete above 300°C. The hydrogen reduction to cobalt metal with the possible formation of acetylacetone would then be expected to be complete at a lower temperature.

Berg and Truemper (1965) measured the heat of sublimation of CoAcAt giving a value of 15.0 k cal per mole. Via the approximate Troughton's rule the entropy could be estimated. The authors also measured the vapour pressure in the range 50°C - 90°C.

The compound starts to decompose at temperatures in excess of 120°C and also exhibits sublimation. Melting point data is available for other acetylacetonates but none has been noted for CoAcAt.

The acetylacetonates are in general an area of interest to workers in the field of vapour deposition because of their high vapour pressures at low temperatures and their ability to undergo thermal or hydrogen assisted thermal decomposition at moderate temperatures. A study of films of metallic cobalt produced from the hydrogen reduction of CoAcAt on heated glass substrates has been made by Jablonowski (1962). In the present study cobalt oxide is produced by the hydrogen reduction of CoAcAt in the presence of controlled quantities of free oxygen. The substrate material used was copper and the hydrogen acted in the dual role of reducing agent and carrier gas.

7.1 The Cobalt Oxide Deposit

Ideally the hydrogen reduction of CoAcAt will produce metallic cobalt with the evolution of acetylacetone as for:

$$Co(C_5H_7O_2)_2 + H_2 = Co + 2C_5H_8O_2$$

It was found by Jablonowski (1962) that in reality, some carbonaceous deposits are co-formed, but that these can be eliminated by the controlled addition of water vapour to the hydrogen carrier gas.

In the present work, proving runs showed that good metallic films of

cobalt metal could be produced in this way. It was further found that the addition of free oxygen produced an oxidised deposit, which, being transparent, allowed the thickness of the deposit to be measured via an optical interference technique.

Electron probe analysis of the deposits indicated the presence of cobalt and oxygen, but the films were too thin to allow an accurate estimation of the cobalt /oxygen ratio and the particular oxide of cobalt being produced. Xray analysis techniques to illucidate the crystal structure also failed, any readings being masked by the presence of the copper substrate.

The deposits were too small for accurate chemical analysis. In fact any chemical analysis of the cobalt/oxygen ratio is complicated by the ability of CoO and Co_3O_4 to absorb oxygen into the lattice, even at room temperature in the former case. (Information, Cobalt Monograph (1960))

To calculate the mass transfer coefficient for the vapour deposition of the cobalt oxide it is essential to establish which of the three oxides of cobalt is produced in the system. The analysis of the gas impinging on the plate, after drying, was 95% H_2, 4.95% N_2, 0.05% O_2, with a minimal amount of CoAcAt (0.0001%). The hydrogen flow is passed through water and so entrains an amount of water vapour. The jet also entrains gas already inside the reactor vessel introducing small amounts of organic matter produced in the decomposition of the acetylacetonate.

In calculating the oxygen potential of the system we have two limiting possibilites. The highest is found by assuming the oxygen is free to exert a partial pressure of 5×10^{-4} atmos. The lowest is found by assuming all the oxygen to have reacted with the hydrogen to produce water vapour, and this, combined with the entrained water vapour, produces an oxygen potential from the equilibrium with hydrogen. The H_2/H_2O ratio was

estimated to be 600. (The minimum value is for complete saturation of the carrier gas to give a value of 60.)

Cobalt produces the oxides CoO, Co_3O_4 and $Co_2O_3.H_2O$, the latter existing only as the monohydrate which decomposes at 300°C. Thermodynamic data is available for CoO and Co_3O_4 and as $Co_2O_3.H_2O$ is unstable at the temperatures investigated,it is eliminated as a possibility.

For the oxide, metal, oxygen equilibria in the following reactions:

$$Co + \tfrac{1}{2}O_2 = 2CoO$$

$$\Delta G_T^o = -56,910 + 0.69T\log_{10}T + 16.03T \quad .....(7.1)$$

$$3CoO + 2O_2 = Co_3O_4$$

$$\Delta G_T^o = -207,300 - 2.3T\log_{10}T + 90.56T \quad .....(7.2)$$

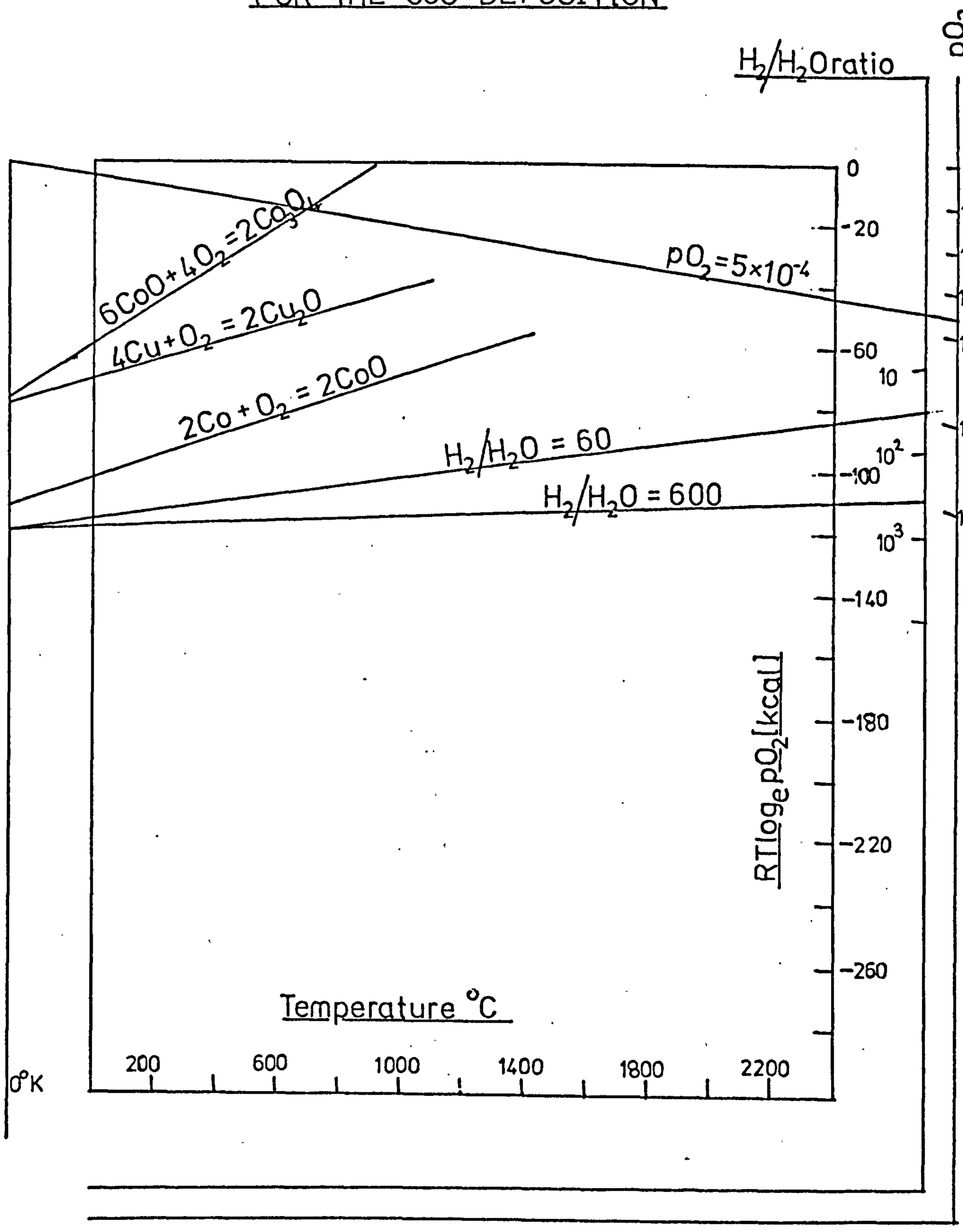
Data for the reaction

$$6CoO + O_2 = 2Co_3O_4$$

can be calculated from (7.1) and (7.2) by subtracting six times the ΔG^o value from (7.1) from twice the value from (7.2).

The equilibrium values of the free energies are plotted versus temperature on an Ellingham type diagram in fig (7.2) together with data for the oxidation of copper and the maximum and minimum oxygen potentials of the system. As the CoO/Co_3O_4 equilibrium line does not lie at any temperature below that for Co/CoO the production of Co_3O_4 directly from cobalt is not possible and Co_3O_4 is produced only via the monoxide CoO. From the Ellingham diagram it is apparent that at equilibrium with all the oxygen reduced to water no cobalt oxide at all is produced, whether the system is saturated with water vapour or not. This was confirmed experimentally using a carrier gas of pure hydrogen deliberately saturated with water and no free oxygen present.

fig(7.2) OXYGEN POTENTIAL DIAGRAM FOR THE CoO DEPOSITION



Two factors may explain the production of a cobalt oxide. Firstly the system is removed from standard state in the production of thin films of oxide which have a high surface energy contribution to total free energy, compared with bulk quantities. The surface energy of most materials is similar and although no data could be found on cobalt oxides, using values for MgO found by Gilman (1960) will allow calculation of the order of the surface energy contribution.

For a film of area 100 mm^2 and thickness 1×10^{-4} mm the calculated surface energy, from the MgO data of 1200 ergs/sq.cm., is $5.02.10^{-7}$ k cals. If the deposit is CoO this volume of oxide has a Gibbs free energy, from its $8.63.10^{-7}$ g moles, of $4.89.10^{-5}$ k cals. The surface energy contribution for films of the thickness produced in the experiments is then about two orders of magnitude smaller than that for the free chemical energy, and much too small to explain the 18 kilocalories the Co/CoO line needs to be depressed to come below even the highest possible equilibrium potential of the system.

The second, more relevant, factor is that a non-equilibrium state may well exist, with the cobalt reacting with the oxygen much faster than the hydrogen can. Hydrogen-oxygen reaction kinetics are highly complex and have received much attention (Hinshelwood and Williamson (1934)). Certain compounds and radicals catalyse the reaction, others inhibit it. At moderate temperatures, in the absence of photocatalysis, the combination of hydrogen and oxygen occurs solely on surfaces, the rate being dependent solely on the hydrogen partial pressure and the nature of the surface and almost independent of oxygen concentration. Free radicals expecially influence the reaction rate and such radicals can well be produced in the reduction of the cobalt chelate. The oxidation rate of bulk cobalt metal has been studied by Chattopadhyay and Measor (1969) and the initial rates are very high. Bearing in mind that any cobalt produced is in a finely divided and therefore highly reactive form the cobalt-oxygen reaction could

well occur more rapidly than the inhibited hydrogen-oxygen reaction.

The implication of the last paragraph is that we must be more concerned with the oxygen concentration in calculating the effective oxygen potential of the system. The value calculated from an oxygen partial pressure of 5.10^{-4} atmospheres would imply that if the further oxidation of CoO to Co_3O_4 has as high a rate as the initial oxidation, Co_3O_4 can be produced, as the CoO/Co_3O_4 line lies below the oxygen potential line up to almost 700°C, a temperature much above that used.

This further oxidation is not considered to occur and the evidence for this is that the atmosphere above the substrate is reducing to copper oxide. Substrates tarnished at the start of an experiment were in fact made bright as the oxide layer reduced. This implies that the effective oxygen potential of the system lies below the Cu/Cu_2O equilibrium line and thus well below the CoO/Co_3O_4 equilibrium line. Furthermore the cobalt oxide once formed is not attacked by the copper even after holding the system a long time at temperature.

Experiments were performed to check on the contribution, if any, of the copper substrate to the reaction and the deposits, as reported later, made onto a glass substrate were identical to those made on copper.

It could also be argued that the deposit may be chemically inhomogeneous in that the Co/O ratio may vary across the surface because of some variation in the oxygen potential above the deposit. Oxides often exhibit marked differences in optical properties and any inhomogeneity might be expected to be manifest in some variation of optical properties across the deposit. When viewed under polarised light with an analyser no variation in nature could be detected. No variation in refractive index could be found in work reported later. It is then concluded that the films produced were homogeneous.

In conclusion it is considered that the deposits produced were of CoO and that the atmosphere above the substrate is highly metastable and may well consist of a hydrogen-oxygen reaction being catalytically retarded to produce only a partial reduction in the amount of free oxygen present. Experience during this series of experiments indicates that using lower concentrations of oxygen does not result in the production of oxidised deposits, while an increase in oxygen concentration could well involve an explosion hazard and the deposits produced in experiments performed using about double the oxygen concentration normally employed, were much less well formed.

7.2 Preparation of CoAcAt

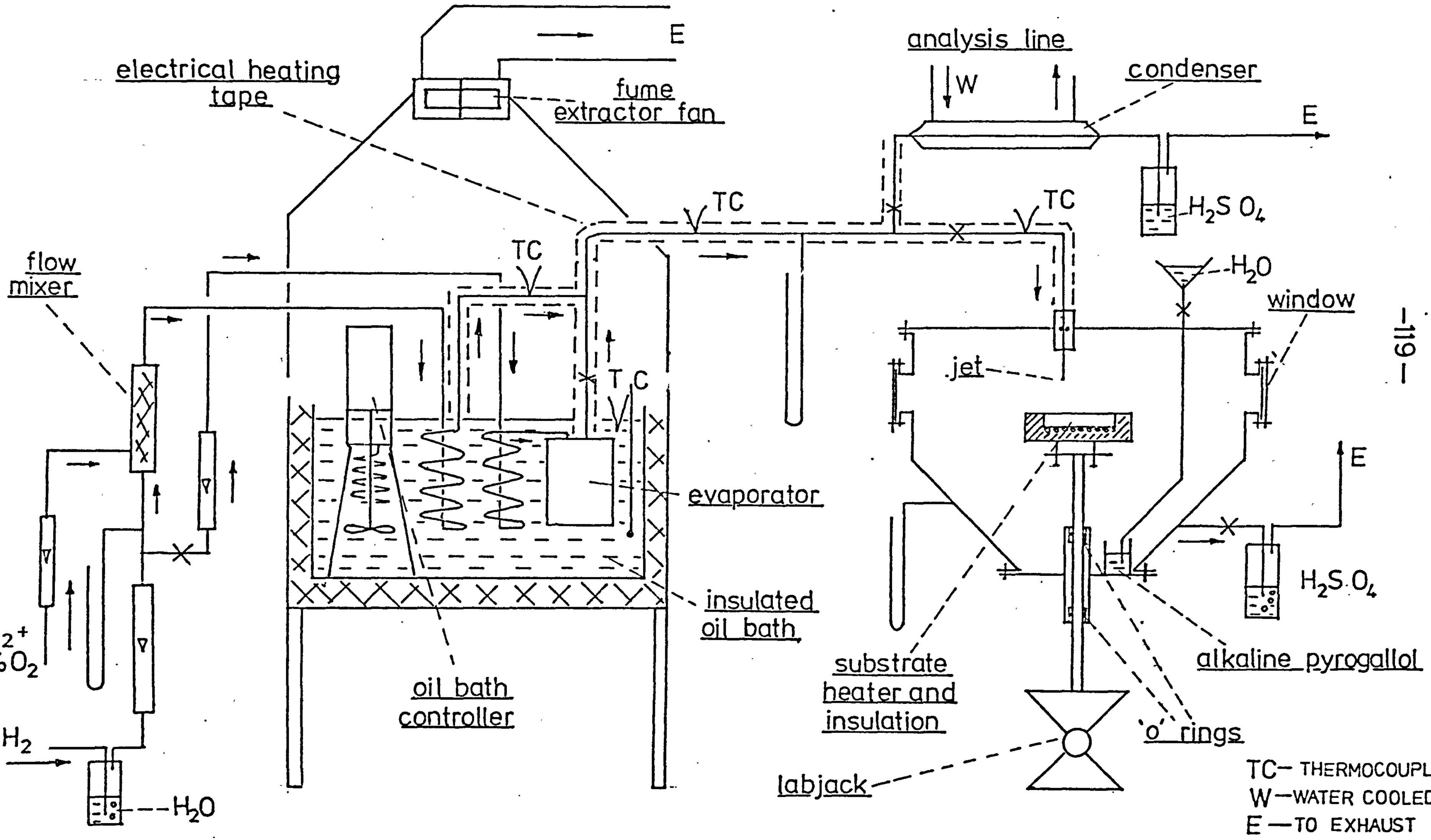
CoAcAt is not available commercially and was prepared in the following way. A mixture of 20g acetylacetone and 100 mls of 10% sodium carbonate solution was added slowly with stirring to a solution of 30g $Co(NO_3)_2.6H_2O$ in 100 ml. distilled water. A fairly violent reaction produced a froth of CoAcAt which was filtered off, washed, carefully dried and then purified by recrystallisation from a minimum of hot 100% ethanol. The compound was then fully dried and ground with a mortar and pestle to a fine powder.

7.3 CoO Deposition Apparatus and Experimental Method

The cobalt oxide deposition apparatus shown schematically in fig (7.3) consisted of a gas metering and mixing system, an evaporator to introduce CoAcAt into the flow and a delivery system to pass the heated gas mixture through a jet to impinge onto a heated copper substrate.

Hydrogen and the Nitrogen containing 1.05 mole per cent Oxygen were metered through a calibrated system by rotameters and a mercury manometer. The hydrogen passed initially through a dreschel bottle containing water.

fig(7.3) SCHEMATIC DIAGRAM OF CoO DEPOSITION APPARATUS

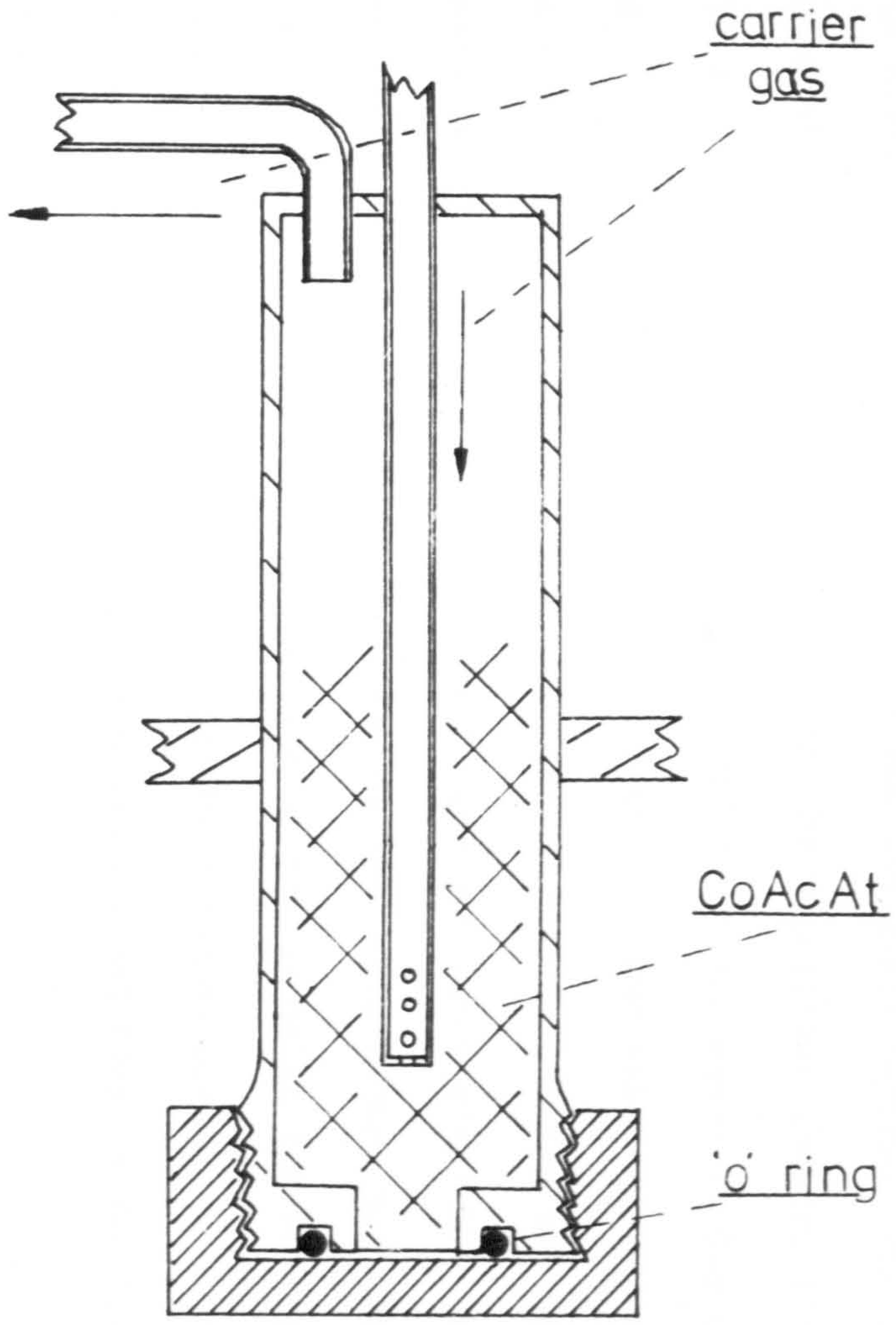


The flow was then divided, a small portion being metered into the evaporator via a heating coil, the rest entering with the Nitrogen (1% Oxygen) into a mixing chamber. The mixing chamber acted as a safety precaution to eliminate any pockets of high oxygen containing gas which might otherwise have been produced. The mixed gas flow was then passed through a heating coil and recombined with the evaporator flow.

The heating coils were flattened coils of copper tubing supported in a well mixed, insulated oil bath controlled at $142^{o}C \pm 0.1^{o}C$. The coils were flattened to increase the velocity of the gas passing through them and thus increase heat transfer rates. A special oil had to be used to withstand the high oil bath temperature. The oil, a long chain glycol, produces a toxic vapour at the temperature used and because of this an extractor system was built around the oil bath. The evaporator is detailed in fig (7.4) together with a sectional diagram of one chamber. The evaporator consisted of four such closed cylinders made of mild steel and the evaporator flow passed through each in turn. The first three cylinders in the sequence contained a measured quantity of CoAcAt in its fine powder form. The carrier gas was forced through fine holes drilled in the closed ended inlet pipe of each cylinder. This design was used in the belief that the jet action from the fine holes would agitate the CoAcAt powder and act as a fluidised bed, saturating the evaporator carrier gas stream and giving reproducible and controllable concentrations of CoAcAt in the main stream. The fourth cylinder contained a plug of glass wool to filter any powder that might be blown through the evaporator from the other chambers. The evaporator was totally submerged in the controlled temperature oil bath.

After the evaporator and main flows of Hydrogen plus Nitrogen (1% O_2) were recombined the mixture passed along the delivery system of glass tubing. The temperature of the flow was monitored by Chromel-Alumel thermocouples and its pressure with a mercury manometer. The temperature



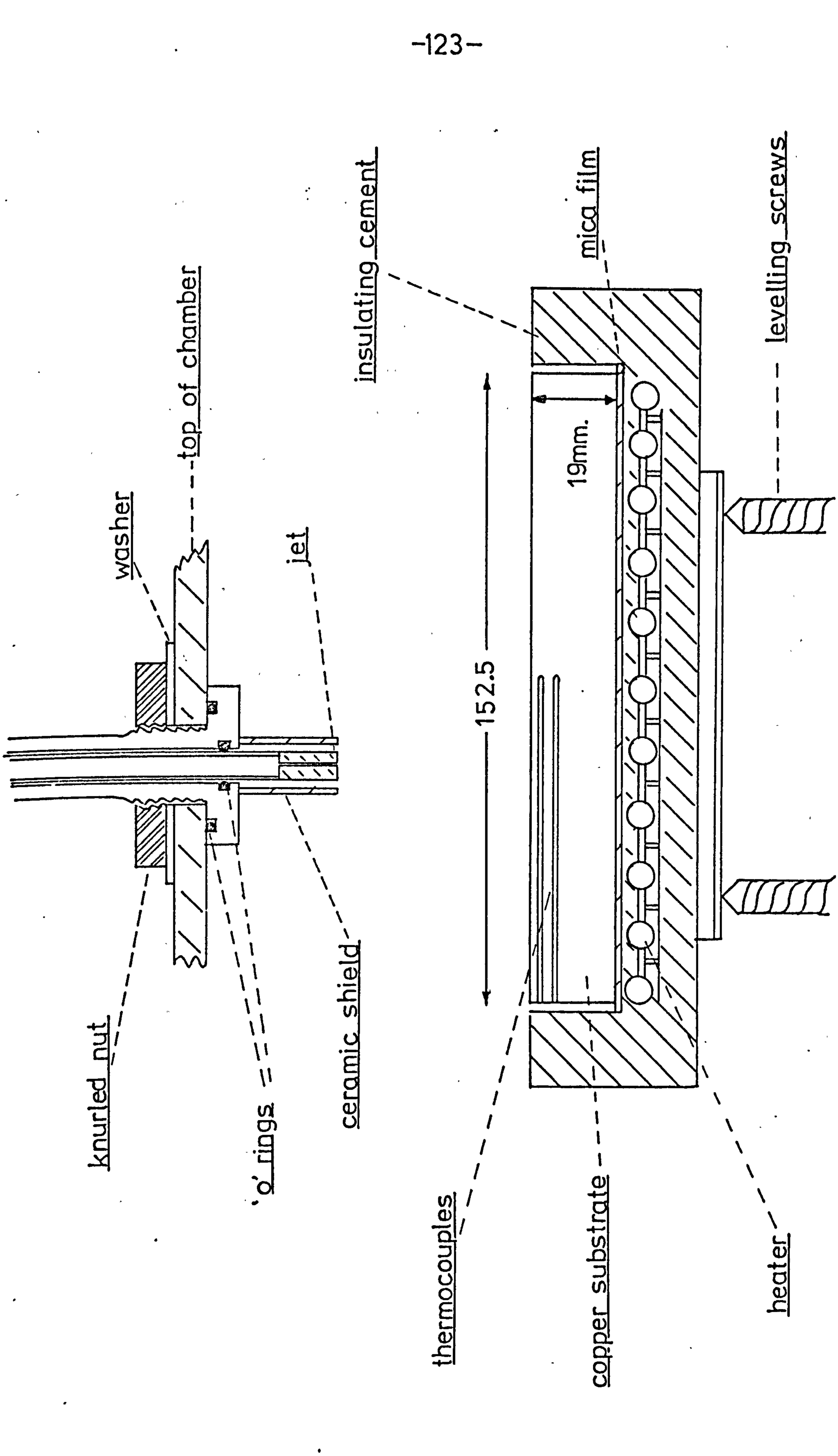


fig(7.4) PHOTOGRAPH AND SECTIONAL DIAGRAM OF CoAcAt EVAPORATOR

of the gas was maintained, to prevent possible precipitation of CoAcAt, . with electric heating tape wrapped around the glass tubing. Via the delivery system the gas flow was introduced into the deposition chamber through a 7.94 mm. I.D. stainless steel tube in an 'O' ring assembly. The assembly, fig (7.5), allowed the jet to be raised and lowered while still maintaining gas tightness. The larger steel tube had at the exit end a stainless steel insert carrying a 20 mm length of fine bore stainless steel hypodermic tubing of I.D. 0.84 mm which acted as the jet. The tubing had been milled at right angles to its axis and checked microscopically for roundness and to measure the bore. A length of hypodermic tubing more than twenty times the jet diameter was chosen to produce established flow in the tube before the jet exit.

The jet produced in this manner impinged onto a substrate of copper 19 mm thick and 152.5 mm diameter, fig (7.5). The substrate was heated by 2100 watt inconel sheathed nichrome resistance heater separated from the substrate and insulated from it by a layer of mica. The heater was adapted from a domestic 'radiant ring'. The substrate and heater were encased in an insulating cement leaving the upper surface of the copper open. The substrate was drilled radially with four nominally 1 mm diameter holes in two pairs, each pair one above the other at distances of 3.175 and 6.35 mm from the exposed surface. One pair travelled radially to the centre of the substrate, the other pair at right angles to the first to a distance of 38 mm from the centre. These holes were drilled to carry 1 mm diameter mineral insulated chromel-alumel thermocouples to provide a means of measuring the surface temperature of the substrate beneath the jet (see section 7.5), and to provide a control point for the heater.

The jet was aligned vertically by levelling the deposition chamber and the substrate aligned horizontally by means of three symmetrically placed levelling screws bearing on the heater frame. The jet was positioned



fig(7.5) SUBSTRATE AND JET ASSEMBLY

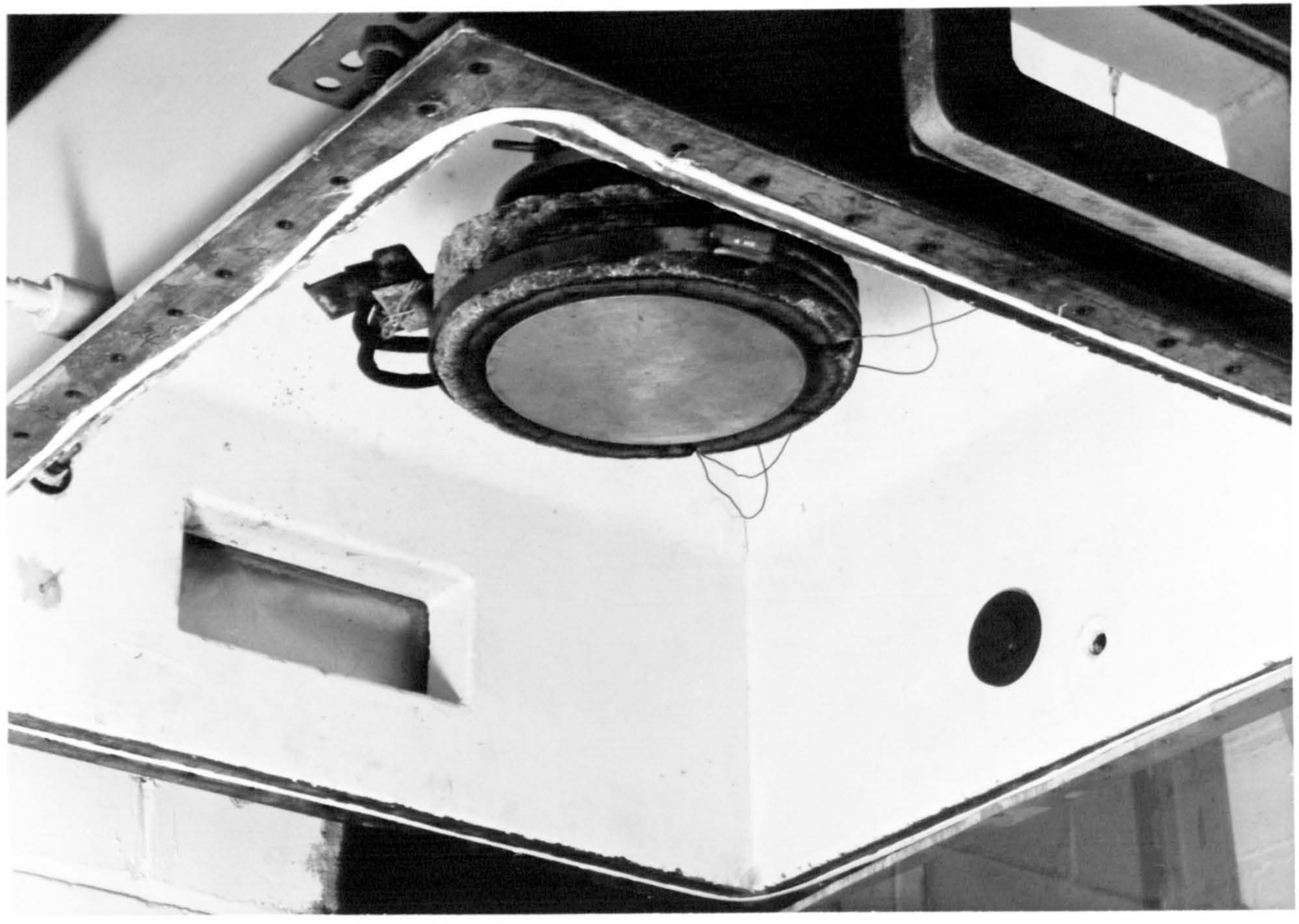
eccentrically in relation to the centre of the substrate on an axis 38 mm from the axis of the substrate. The substrate assembly was supported on a stainless steel shaft passing vertically through a double 'O' ring assembly in the base of the chamber. This allowed the shaft, and therefore the substrate, to be raised and lowered but most important to be rotated. Turning the shaft allowed a series of deposits to be made on a circle at constant radial position on the substrate. This circle passed directly over one of the thermocouple pairs. This technique produced a considerable saving in experimental time as up to sixteen separate deposits could be made on the substrate without dismantling the apparatus.

The substrate could be considered an infinite flat plate with respect to the jet as the deposits were localised to a radius of a few millimeters. The distance from the substrate to the chamber roof was sufficient so as not to interfere with the flow pattern of the impinging jet. The tube carrying the jet was protected from overheating by a ceramic shield.

As well as the four substrate thermocouples additional thermocouples monitored the heater insulation and chamber atmosphere temperatures. The output from all thermocouples was displayed on a multipoint recorder.

The deposition chamber was constructed of welded 3.175 mm mild steel plate with a 6.4mm mild steel top bolted to the body on a flange and sealed to it with a braided PTFE gland. Two pyrex glass windows were incorporated at opposite sides of the chamber allowing a clear view of the substrate surface. Fig (7.6) shows the chamber with the top removed and the substrate assembly in position. The substrate could be removed or the assembly aligned via either window opening. Major work involved unbolting the top cover and the inconvenience of this among other things resulted in the construction of another chamber for the later carbonyl work.

Metal to metal or metal to glass seals in the chamber where not



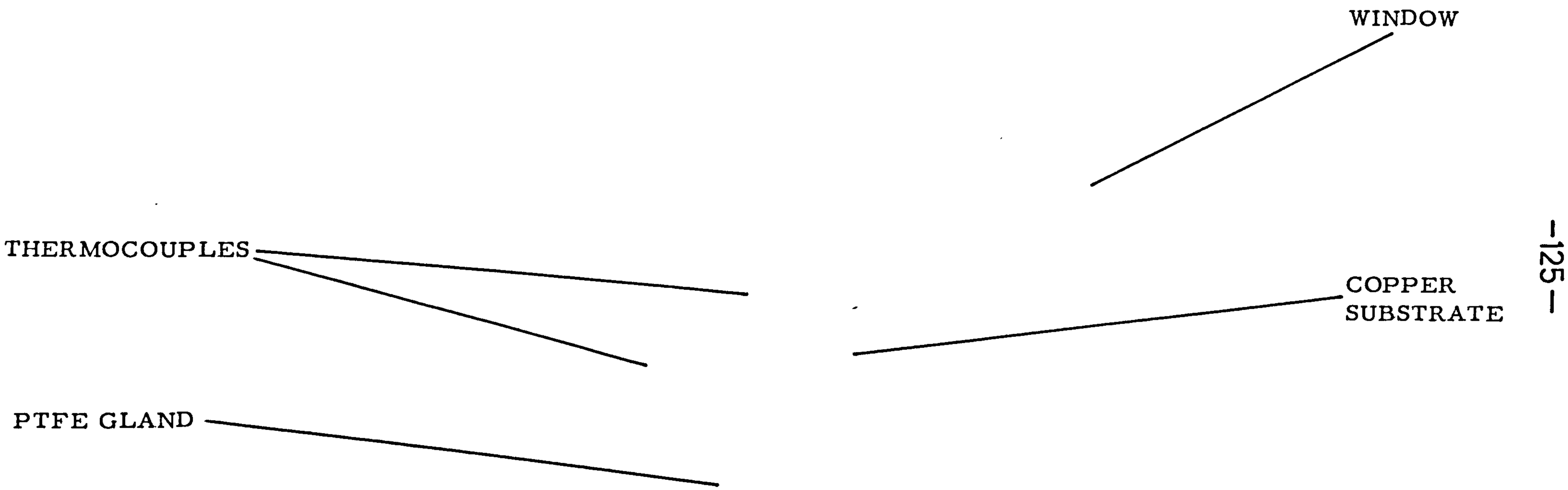


Fig (7.6) VIEW OF CoO DEPOSITION CHAMBER AND SUBSTRATE ASSEMBLY WITH CHAMBER TOP REMOVED

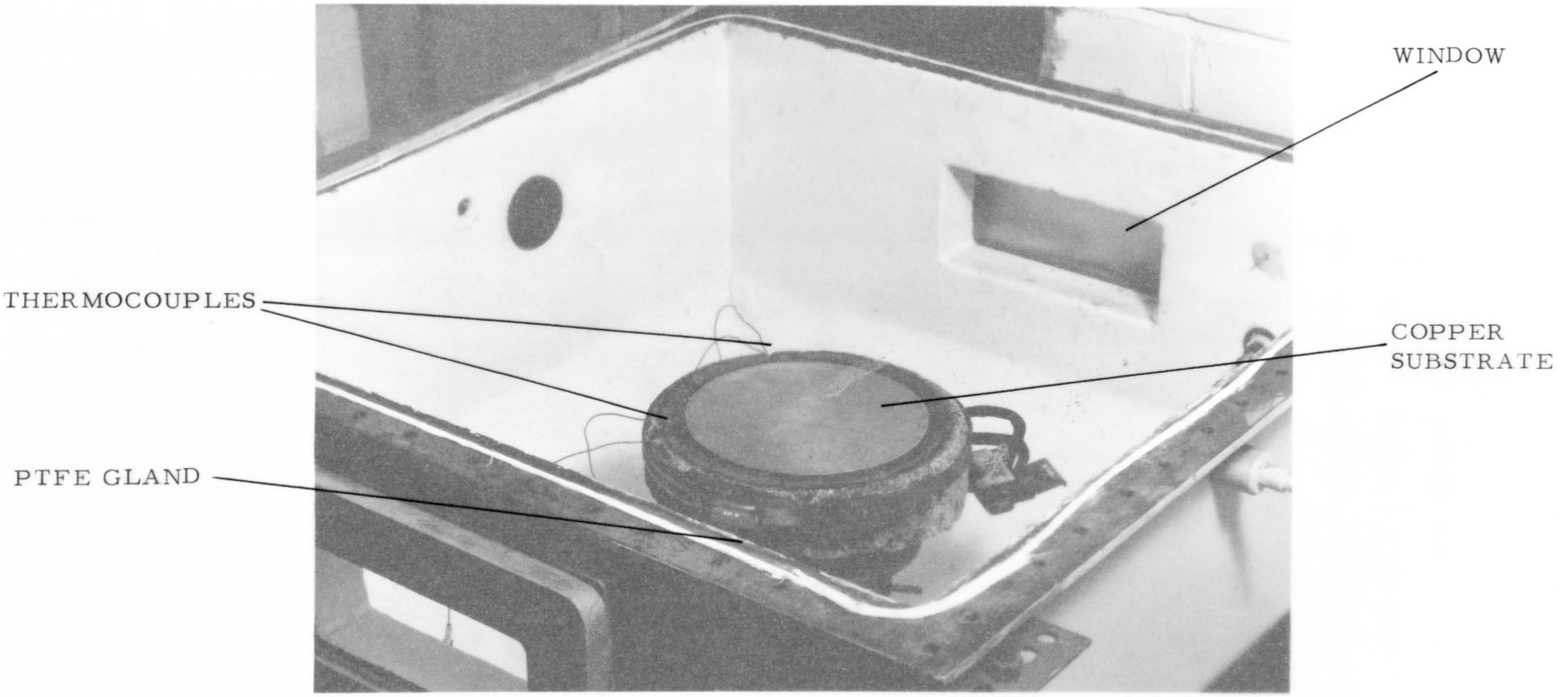


Fig (7.6) VIEW OF CoO DEPOSITION CHAMBER AND SUBSTRATE ASSEMBLY WITH CHAMBER TOP REMOVED

effected by 'O' ring seals were made with braided PTFE between bolted flanges. All connections for bringing tubes or wires into the chamber were fixed with a resin glue. The inside of the chamber was protected with chemical and temperature resisting polyurethane paint on a self etching chromate primer base.

The jet/plate distance could be set by moving either the jet or the substrate assembly and the distance was measured before an experiment using graduated slip gauges. Also before an experiment, after setting up the apparatus and sealing the system, the apparatus was purged with hydrogen. As oxygen was the gas most likely to interfere with the experiment, efforts were made to simplify this operation by removing the gas chemically with alkaline pyrogallol. This was made inside the apparatus by running water through the chamber top into a beaker containing dry, premixed pyrogallol powder and caustic soda pellets, placed inside the apparatus just before sealing.

Before each experiment the substrate was prepared by removing old deposits by grinding with successively finer grades of silicon carbide paper. The substrate was then polished with a proprietary polish and finished with fine MgO powder in a water slurry using a selvet cloth. After degreasing with alcohol and carbon tetrachloride the substrate was placed inside the chamber. When the system had been purged the substrate was heated in the hydrogen atmosphere at 300^{o}C to reduce any surface oxide present.

The substrate temperature was controlled at a preset value using a fast cycling 'Eurotherm' controller which worked off the output of the chromel alumel thermocouple nearest to the centre and surface of the substrate. Control of temperature was found to be good with a $\pm$ 1^{o}C maximum variation, and the variation of temperature across the substrate

acceptable. The even distribution of the heater output and the high conductivity of the thick copper substrate combined to give this even surface temperature.

An experiment was started when the oil bath reached temperature with no flow through the evaporator. When the system temperatures had stabalised the two PTFE taps isolating the evaporator were opened. A short induction period was noted while the flow through the evaporator built up to a value controlled by the isolating taps. During this period a little CoAcAt was delivered to the deposition chamber. The start of the effective operation of the evaporator produced a visible growth on the substrate surface. The substrate was then rotated and a series of deposits made of varying duration. Unfortunately CoAcAt reacts slowly at 140^{o}C with hydrogen and this caused a quite sudden drop in CoAcAt delivery after some 30 - 40 minutes. Total run times for the use of one charge of CoAcAt in the evaporator were then limited to 20 minutes. Deposition times for individual deposits varied from 5 seconds to over 5 minutes.

The evaporator system was found to deliver constant and reprcducable concentrations of CoAcAt. This was checked initially by a series of identical runs (constant Reynolds number, jet/plate distance and evaporator flow). An example of the good reproducability achieved is given in the results section. The overall concentration was found during selected runs by redirecting the flow from the chamber into a water cooled condenser followed by a dreshel bottle containing sulphuric acid. As the amounts of CoAcAt present were very low, titration methods to determine the cobalt recovered were not accurate enough. Two sensitive methods proved very useful and are described in the next section. Only one concentration of CoAcAt could be used as no effort was made to determine the order of the reaction because of the analysis difficulties and the complexity of the reaction. As discussed in chapter five, varying the concentration can

change the rate controlling step of the deposition rate.

The range of Reynolds numbers employed was limited at the lower end by the desire to study turbulent jets and at the upper end by the pressure build up in the apparatus, which was over half an atmosphere at the higher flowrates. This pressure level was due almost entirely to the pressure drop down the narrow jet necessary to produce the required flowrates. Higher Reynolds numbers could be produced by using a larger jet diameter but this has two undesirable effects. As the present study was limited to fully developed jets impinging on the plate the minimum approach distance was limited to the length of the potential core, which as discussed in chapter two is a function of jet diameter ($\simeq 6d$). Turbulent jets have an entrainment rate largely independent of jet diameter. The mass flux at a downstream position being equal to the exit mass flux plus the entrainment. Thus a jet having a diameter of twice that used would not only need an increased flowrate to produce similar Reynolds numbers but would have a minimum approach distance to the plate of twice the smaller jet. Over this distance the jet would entrain almost twice the quantity of unheated gas. As there is a limit to the thermal output from the heater there is a limit to the maximum temperature in the substrate that can be produced for a given quantity of gas impinging on the substrate. The facility to study a large range of Reynolds numbers was then sacrificed in these experiments by using the small diameter jet with its correspondingly small mass flowrates, in order to produce a high variation in possible substrate temperature and jet/plate separation. The range of Reynolds numbers studied was 2213 to 4637 using gas data for the jet exit temperature. The range of $^{b}/_{d}$ ratios used was 9.07d to 33.75d.

The shape of the deposits was analysed by the interference technique discussed in section (7.6) using mercury vapour light. The nature of the deposits was further investigated by other optical methods and using the

scanning electron microscope. Depositions were made at the highest Reynolds number studied over a range of temperatures from 221°C to 397°C to identify the mass transfer and chemical control regions in the system. Viscosity data for the mixture of nitrogen and hydrogen was calculated from the method recommended by Bird, Stewart and Lightfoot (1961). Diffusion coefficients are calculated in Appendix (1). All calculations other than the Reynolds number were calculated using a film temperature found by averaging the jet exit and substrate temperatures. The Reynolds number is a measure of the kinetic energy of the system and this is not then affected much by the substrate. The diffusion processes occur however near the plate, in a region of temperature change between the inlet to the substrate values. As no analysis of heat transfer effects has been attempted the effect of temperature is assumed to be accounted for by averaging the two extreme values.

The entrainment of gas which has been recycled inside the deposition chamber by the jet gives rise to some complication in calculating the concentration driving force for the relevant calculations. An analysis of this effect is contained in Appendix (2).

7.4 Description of Analysis Methods

The two analytical techniques used in assessing the concentration of CoAcAt at the jet exit were colorimetry and atomic absorption spectroscopy.

For the colorimetric technique the method used was from Sandell (1950). The condensed CoAcAt is dissolved in dilute H_2SO_4 and the volume of liquid reduced by evaporation. Standards were prepared by dissolving a known quantity of cobalt nitrate in 5N nitric acid. Aliquots were taken from this and diluted so as to give a range of standards. All solutions were made to contain 6% w/w KCNS and 50% v/v acetone. At 6% KCNS the deep blue colour from the cobalt complex (possibly $Co(CNS)_4^{=}$) is almost independent of

Co:CNS ratio. The same applies to the 50% acetone content. Test samples were made up in an identical manner and compared with a calibration curve from the standards in a colorimeter at a wavelength of 550 μm.

Atomic absorption spectroscopy proved a much more convenient method. Samples and standards are made up similarly by dissolving in 10% H_2SO_4. Small amounts were sucked into the flame of a Perkin Elmer 290B model spectro-photometer and the samples were compared with a calibration curve produced from the standards. Very little quantities of highly dilute solutions (parts per million) only are necessary and this together with the ease of operation made this a more desirable method.

Results from each method compared favourably ($\pm$ 4½%). The average of all the measurements gave a concentration of CoAcAt at the plate of $2.702.10^{-7}$ g/cc.

7.5 Surface Temperature Measurement

Surface temperatures were measured as discussed above by extrapolating two thermocouple readings to the surface. If the heat flow is effectively normal to the surface then a linear temperature gradient exists between the lower thermocouple giving a reading T_1, the upper thermocouple reading T_2 and the surface temperature T_s such that

$$\frac{T_s - T_2}{T_2 - T_1} = \frac{h_1}{h_2} \quad \ldots\ldots (7.3)$$

where h_1 and h_2 are the distances between T_2 and the surface and T_1 and T_2 respectively. As $h_1 = h_2$, from equation (7.3)

$$T_s = 2T_2 - T_1 \quad \ldots\ldots (7.4)$$

The thermal demand will be greatest underneath the jet at the stagnation point and this is why the measuring themocouples were positioned to pass

beneath the jet axis so as to measure the true value of T_s. This implies that there may be a significant initial drop in T_s as the substrate is rotated to its new position. The effects of this are discussed with the relevant results in the following sections.

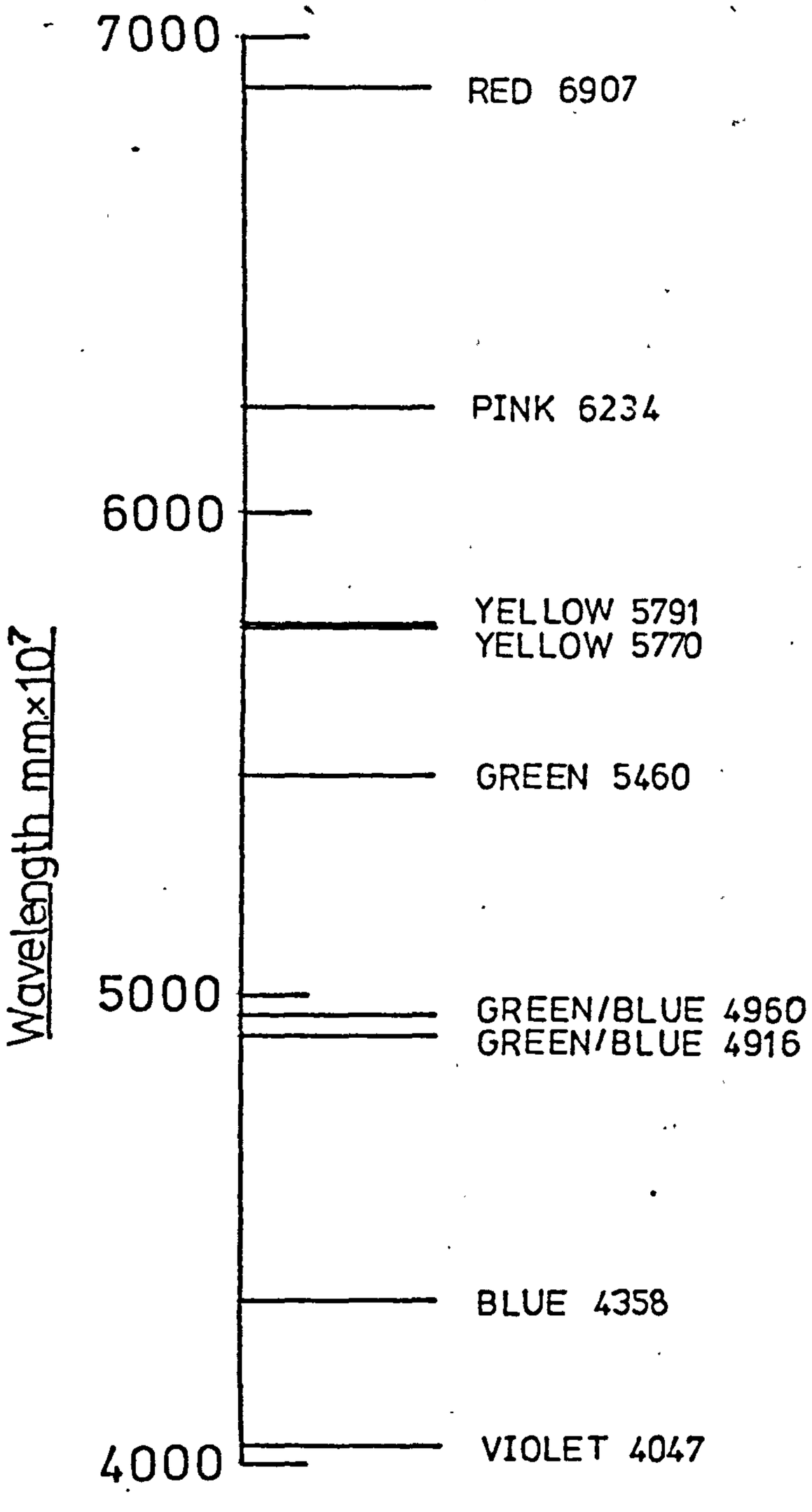
7.6 Analysis of the CoO Deposits

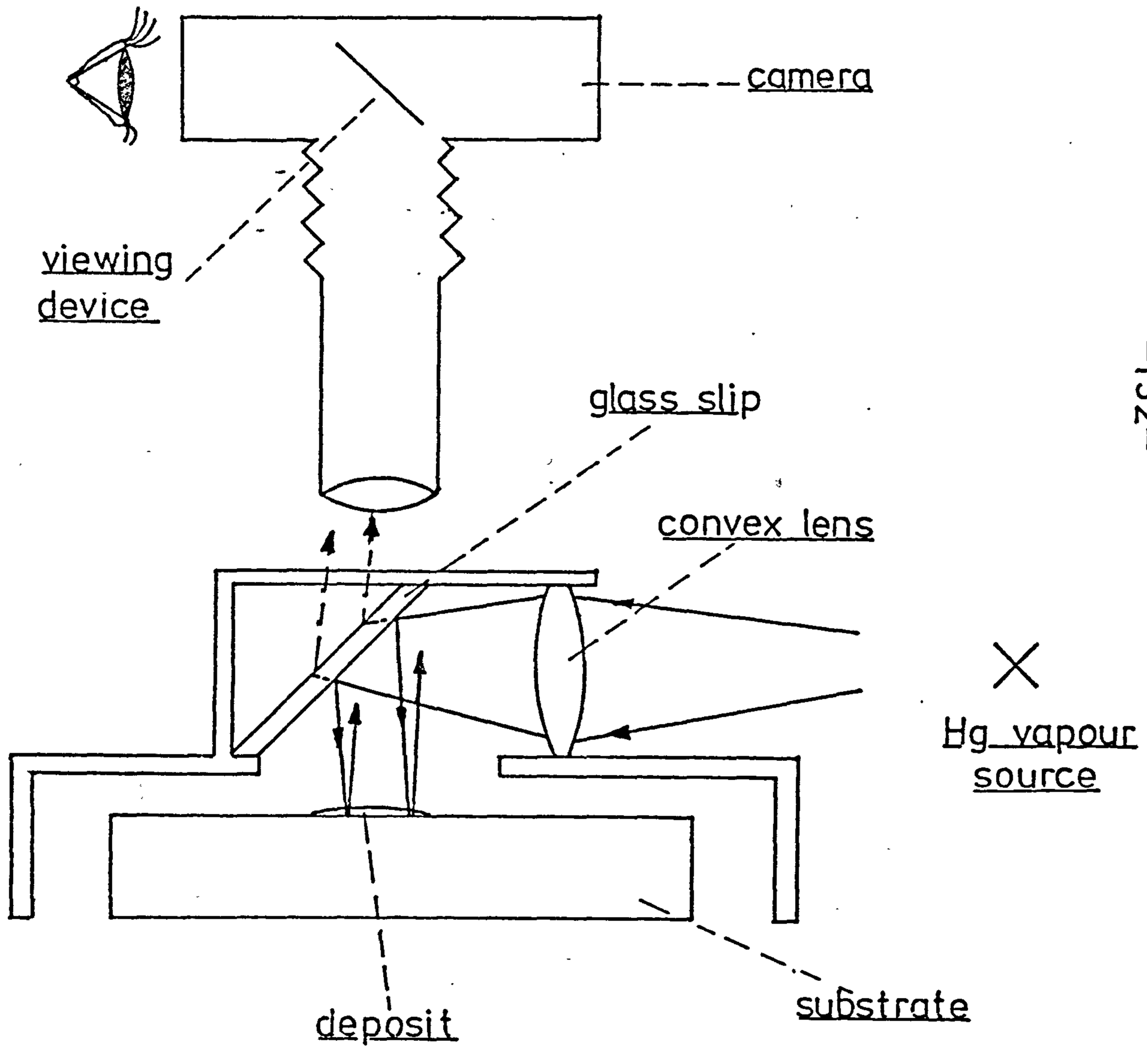
The CoO deposits on the copper substrate were viewed and photographed under mercury vapour lamp illumination using the apparatus shown schematically in fig (7.7) together with the mercury spectrum. Mercury vapour light was chosen to provide a series of monochromatic sources, the individual lines of the spectrum, allowing a further topographical analysis than that available from using a single line source. From the spectrum four convenient lines were chosen, red (6907), the yellow doublet (5770 and 5791), green (5460) and violet (4047). The units of the wavelengths in brackets are mm x 10^7.

The interference rings produced between the oxide and the substrate were photographed using Kodak Ektachrome EX135-20 film using the apparatus in fig (7.7). The objective lens was an f 4.5 80 mm lens. The film exposure time was calculated from a calibrated 'Sixtar' light meter. Calibration was necessary because of the line spectrum of the light source. The film responded well to this spectrum, the colours produced in the resulting transparencies showed little perceptible variation from those viewed on the actual deposit. Possibly because of the different intensity of each line in the spectrum underexposed films tended to display the red and violet fringes the best while overexposing the films tended to favour the yellow and green patterns.

Prints from typical transparencies are shown in figs (7.11) and (7.12), some colour definition has been lost in the printing.

fig(7.7) MERCURY SPECTRUM AND CoO DEPOSIT PHOTOGRAPHY APPARATUS





7.6.1 Interference Theory

The familiar thin film interference analysis holds for the case of transparent solid films. The optical path difference produced between ray A, in fig (7.8), which undergoes refraction through the transparent CoO and reflection from the copper surface, and ray B, which is reflected from the top of the cobalt oxide layer is equal to $2\mu t\cos\phi$. Ray A has also undergone a rare/dense/rare reflection which introduces a π phase change. The condition for constructive interference between rays A and B is then that:

$$2\mu t\cos\phi = (n+\tfrac{1}{2})\lambda \quad \ldots\ldots(7.5)$$

where n is an integer from zero.

Equation (7.5) is the commonly used thin film relationship pertaining to gas films. Allowance must be made in this case for the reflection of ray A from the copper surface as the refractive indices of the oxide and the metal will be close enough to affect the π phase change by a small phase change θ. Introducing θ into equation (7.5):

$$2\mu t\cos\phi = (n + \tfrac{1}{2} + \theta)\lambda \quad \ldots\ldots(7.6)$$

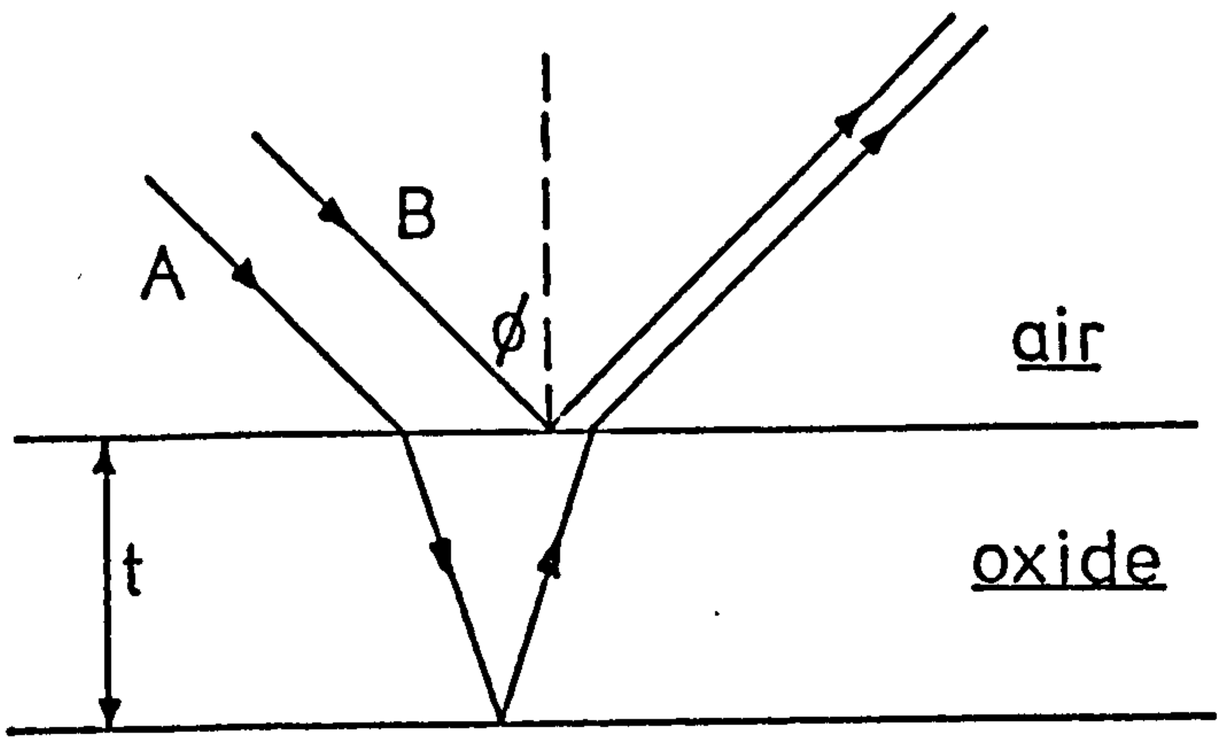
for normal incidence of rays A and B $\phi = 0$, $\cos\phi = 1$ giving:

$$2\mu t = (n + \tfrac{1}{2} + \theta)\lambda \quad \ldots\ldots(7.7)$$

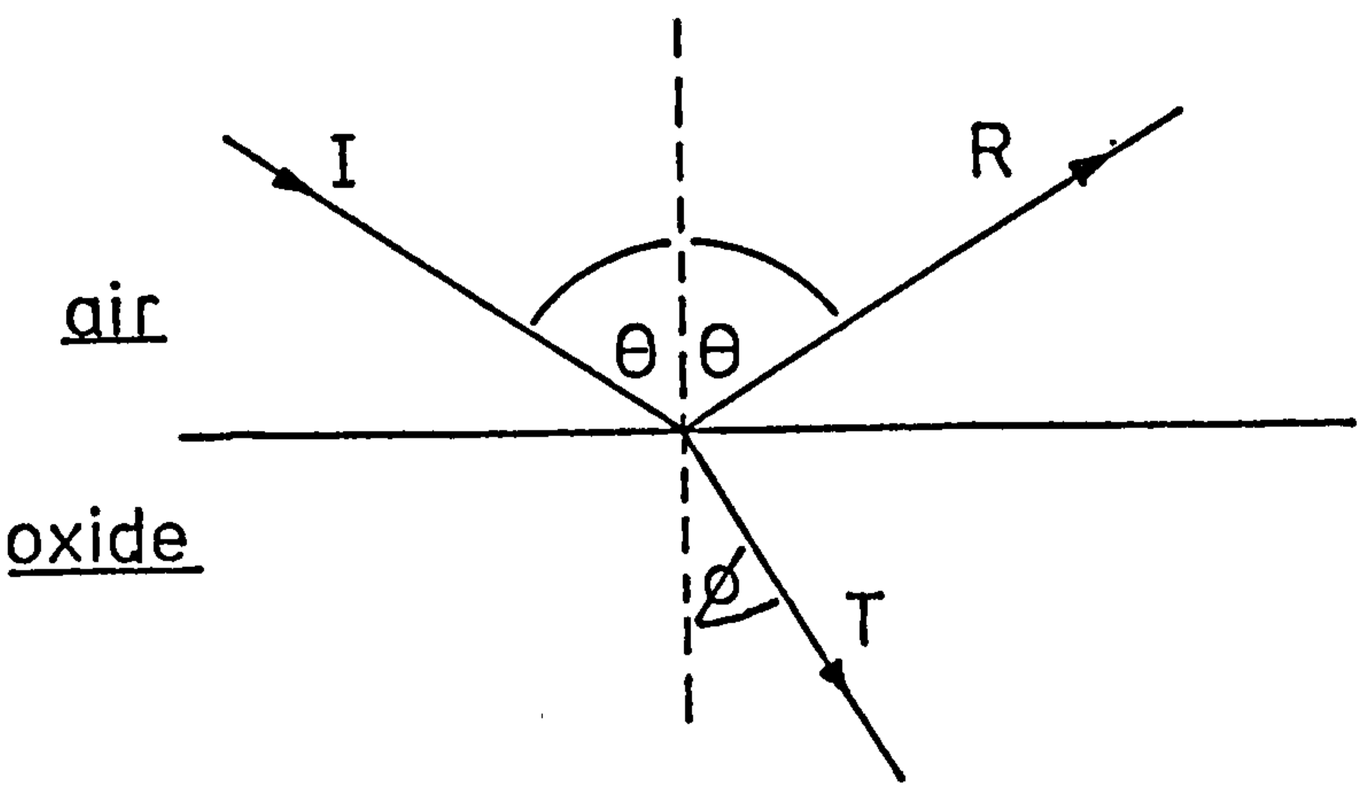
The equation still contains four unknowns μ, n, θ, λ and t which we wish to calculate. λ values can be taken from standard tables and n is deduced from the order of the ring leaving μ and θ as unknowns. The refractive index can be calculated from the Brewster angle for the film.

Light reflected from a non-metallic surface is always at least partially polarised. At a particular angle this polarisation becomes complete. Brewster was the first to show experimentally that the tangent of this angle is equal to the refractive index of the medium. From figure (7.9)

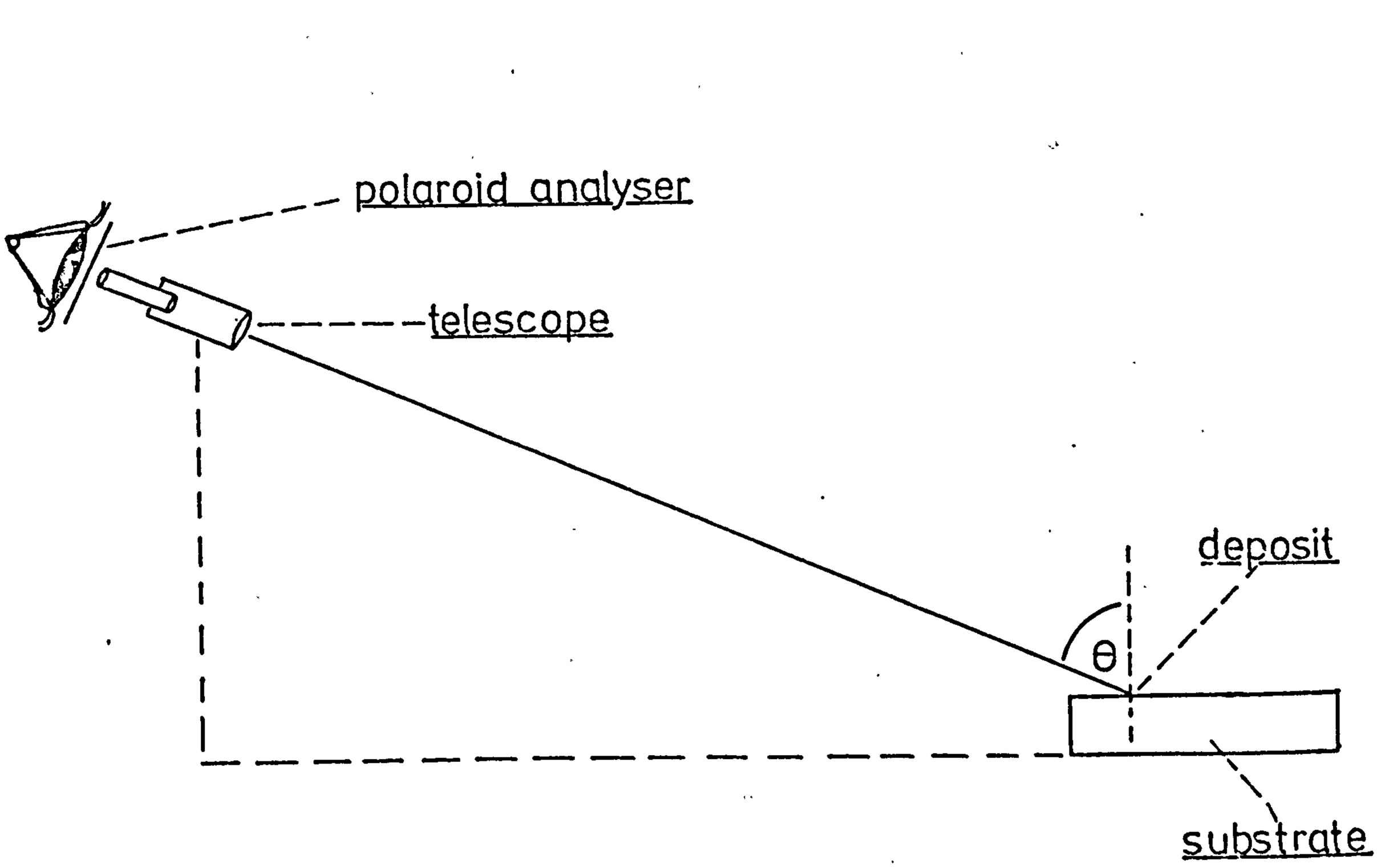
$$\mu = \tan\theta = \frac{\sin\theta}{\cos\theta} = \frac{\sin\theta}{\sin\phi} \quad \ldots\ldots(7.8)$$



fig(7.8)



fig(7.9)



fig(7.10) BREWSTER'S ANGLE MEASUREMENT

Thus sin ϕ = cos θ and so $\theta + \phi = 90^{\circ}$. The relected and refracted rays R and T are then at right angles for light incident at Brewster's angle. The phenomenum can be briefly explained by the idea of the longitudinal vibrational component (into the page) in the incident beam I being unable to enter the denser medium and undergo refraction. The reflected ray R is then polarised and the condition can be detected by a suitably rotated polaroid 'analyser'.

A formal proof of the phenomenon can be found in texts on theoretical optics derived from the electromagnetic theory of light.

The Brewster angle for the CoO deposits was measured to derive μ using the apparatus shown schematically in fig (7.10). The oxide deposit was viewed through a telescope the objective area of which had been reduced to a slit. The viewing angle was altered until Brewster's angle was detected by rotating the analyser. The deposit could then be made to disappear as the light reflected from the surface was being blocked by the analyser whereas light from the refracted ray returning from the copper surface was allowed through. The copper surface beneath the deposit could be clearly seen, suffering only a slight reduction in the intensity of light reflected from the deposit area compared with the rest of the substrate.

The method is not particularly sensitive and a series of readings gave an average value of μ of 1.73 ± 0.15. No variation in μ as a function of λ could be determined within this scatter.

The phase change θ can be obtained in a variety of ways. Using two monochromatic sources and extrapolating between two bands to deduce the thickness at a common point is a possibility. Performing two experiments varying only the length of time for the deposit and thus the thickness and comparing the stagnation point thicknesses in proportion to the experiment time is another way. The most convenient method is to use the observation that the red band of the first order spectrum coincides with the violet

band of the second order spectrum. We can then write simply

$$(n + \tfrac{1}{2} + \theta)\ \lambda \text{ red} \quad = \quad (n + 1\tfrac{1}{2} + \theta)\ \lambda \text{ violet} \ldots\ldots\ (7.9)$$

for $n = 1$, θ can be solved as equal to -0.085.

Equation (7.7.) can now be used to generate values for t the deposit thickness corresponding to the various fringe positions. These are tabulated in table (7.1) from

$$t \quad = \quad (n + 0.415)\ \lambda\ /3.46,\ n \quad = \quad 0,1,2, \ \ldots\ldots\ (7.10)$$

Table 7.1

CoO deposit thicknesses in mm x 10^7

Colour	Violet	Green	Yellow	Red
λ	4047	5460	5780	6907
n				
0	486	655	693	829
1	1655	2233	2364	2825
2	2825	3811	4034	4821
3	3994	5389	5705	6817
4	5164	6968	7375	8813
5	6334	8545	9046	10810

As the spectrum order n rises the bands tend to overlap one another. This has the effect of obscuring the less intense fringe. For example the violet line of the third order band ($n = 3$) lies within the second order band, but, as the centre of the yellow doublet fringe of the latter band is extremely close to it ($t = 3994, 4034$) and as the doublet has a high intensity the violet line is visually suppressed.

The zero order band corresponds to deposit thicknesses from 486 to 829 mm x 10^7. Local variations in deposit thickness of the order of atomic

layers in this region tend to blur the fringes together, see fig (7.12). The centre of this outer band was taken to represent the position of the yellow doublet.

7.7 Calculation of the Sherwood Number

The Sherwood number is calculated from:

$$Sh_o = \frac{t_o \ \rho \ Co \ (\text{in deposit})^{\ d}}{s \ \rho \ Co \ (\text{in gas})^{\ D} \ CoAcAt/H_2} \quad \ldots\ldots (7.11)$$

$$= \frac{t_o \ (\text{density CoO}) \ (MWtCo) \ (MWtCoAcAt) \ d}{s \ (\rho \ CoAcAt \text{ at jet}) \ (MWtCo) \ (MWtCoO) \ D_{AB}}$$

With values of CoAcAt concentration from the chemical analysis and diffusion coefficient from Appendix (1) this gives

$$Sh_o = 1.194.10^6 \ t_o/s \ \ldots\ldots (7.12)$$

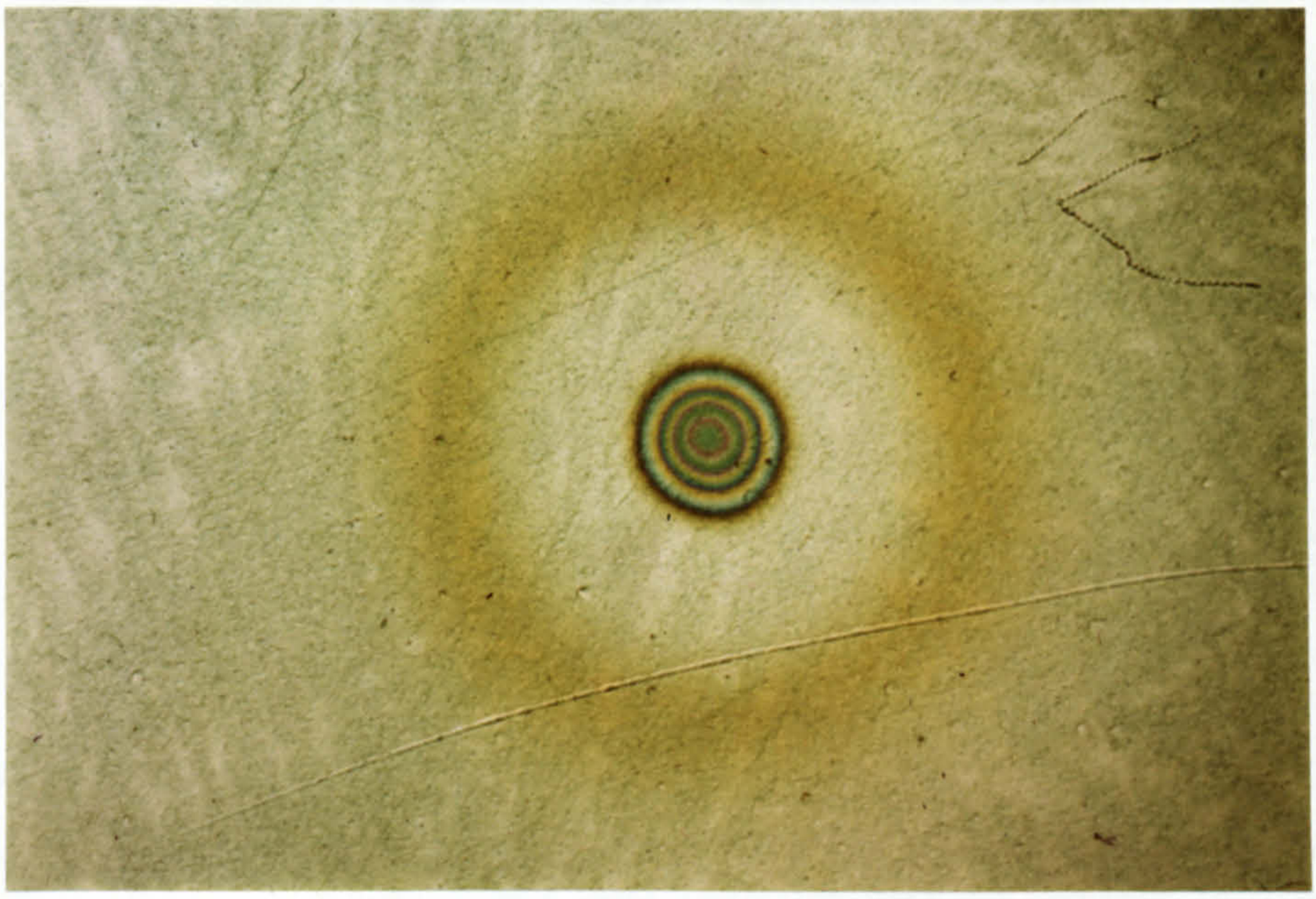
with s in seconds and t_o in mm x 10^7. This makes no allowance for entrainment, which from Appendix (2) changes equation (7.12) to

$$Sh_o = 1.194.10^6 \ \frac{t_o \ b}{s \ d}$$

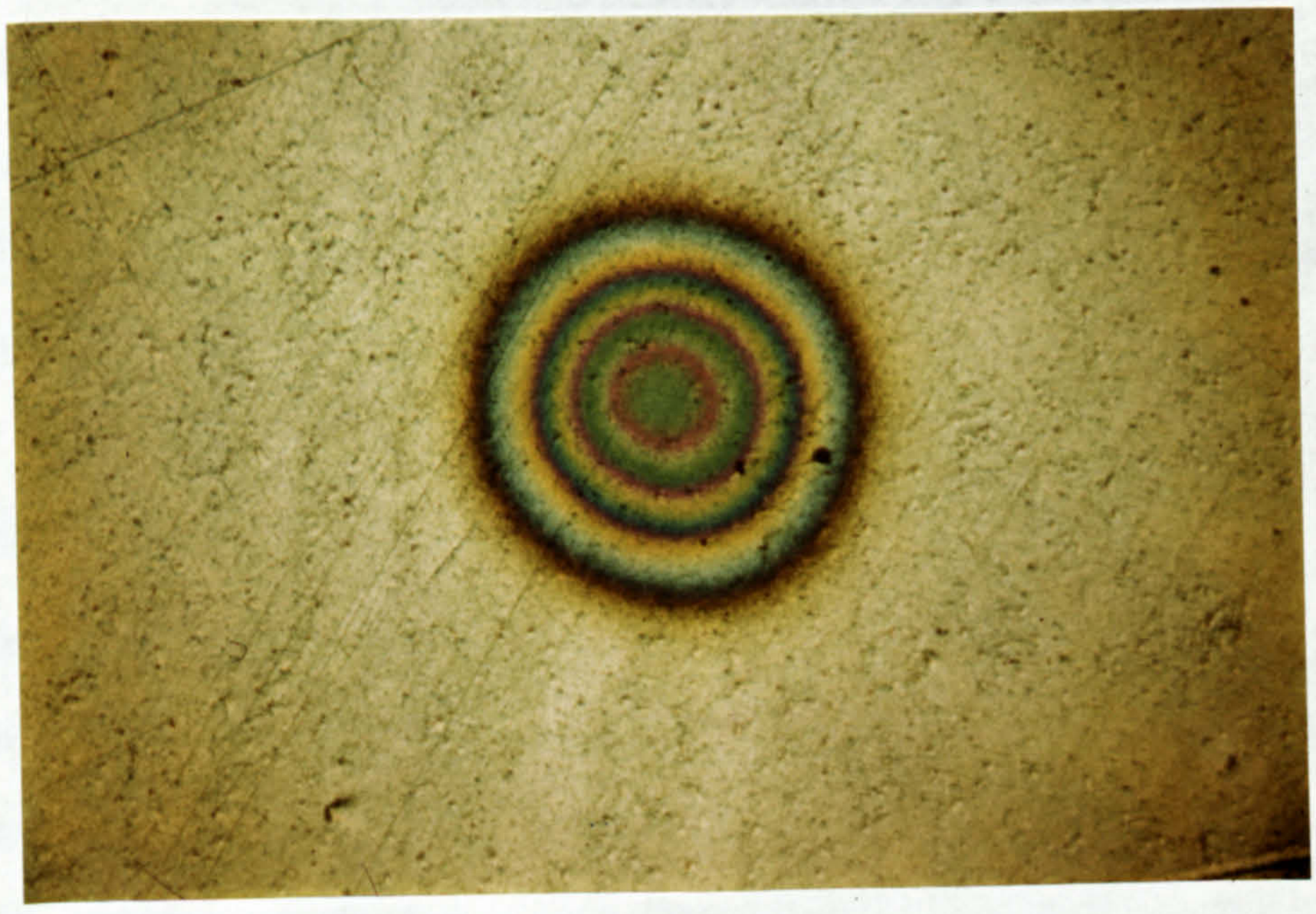
The Schmidt number for the system is calculated at 3.54 for film properties giving $Sc^{1/3} = 1.524$.

7.8 CoO Deposition Experimental Results

Results are tabulated including derived parameters in Appendix (4). Only the stagnation point values are recorded, a dimensionless radial mass transfer profile and a typical profile are given in this section. A typical deposit is shown in figs (7.11) and (7.12).



fig(7.11) INTERFERENCE FRINGES ON A TYPICAL CoO DEPOSIT ON COPPER × 9



fig(7.12) CENTRAL FRINGES FROM CoO DEPOSIT × 24

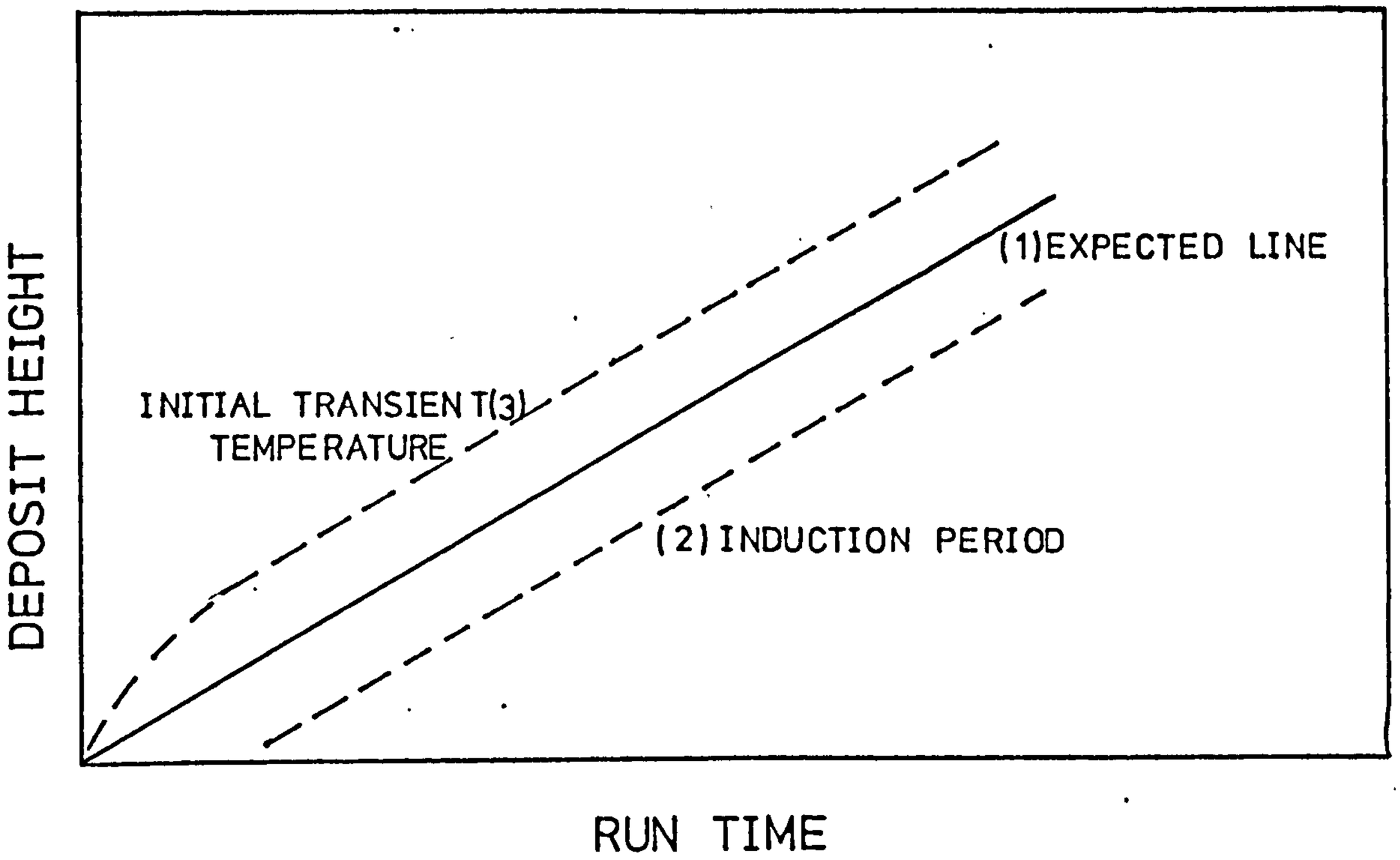
7.8.1 Temperature Conditions Under the Jet

A plot of amount of oxide deposited against time for constant experimental conditions would be expected to produce a straight line passing through the origin as with line (1) in fig (7.13). If the experimental line gives a negative intercept on the deposition axis this would imply an induction period was necessary to start the CoO deposition, as shown by line (2). More likely if the experimental line gives a positive intercept, line (3), this would imply an initial higher rate of transfer due to a higher initital surface temperature than the equilibrium value established later in the run. This would occur if the initial cooling of the surface by moving the substrate under the cooler jet is not balanced by fast conduction of heat in the copper substrate. This transient heat transfer condition would not have to be very long to affect the results of runs of the duration of those in the present work. Thermal effects will be most critical in a region of chemical control where the reaction rate as discussed in chapter five is highly temperature sensitive. The sensitivity is less in the mass transfer region but still critical. As the effects of reaction products may be important also in the chemical control region the two experimental plots made to investigate these effects are from what will be shown to be the mass transfer region. Two plots are shown in fig (7.14) for two different Reynolds numbers.

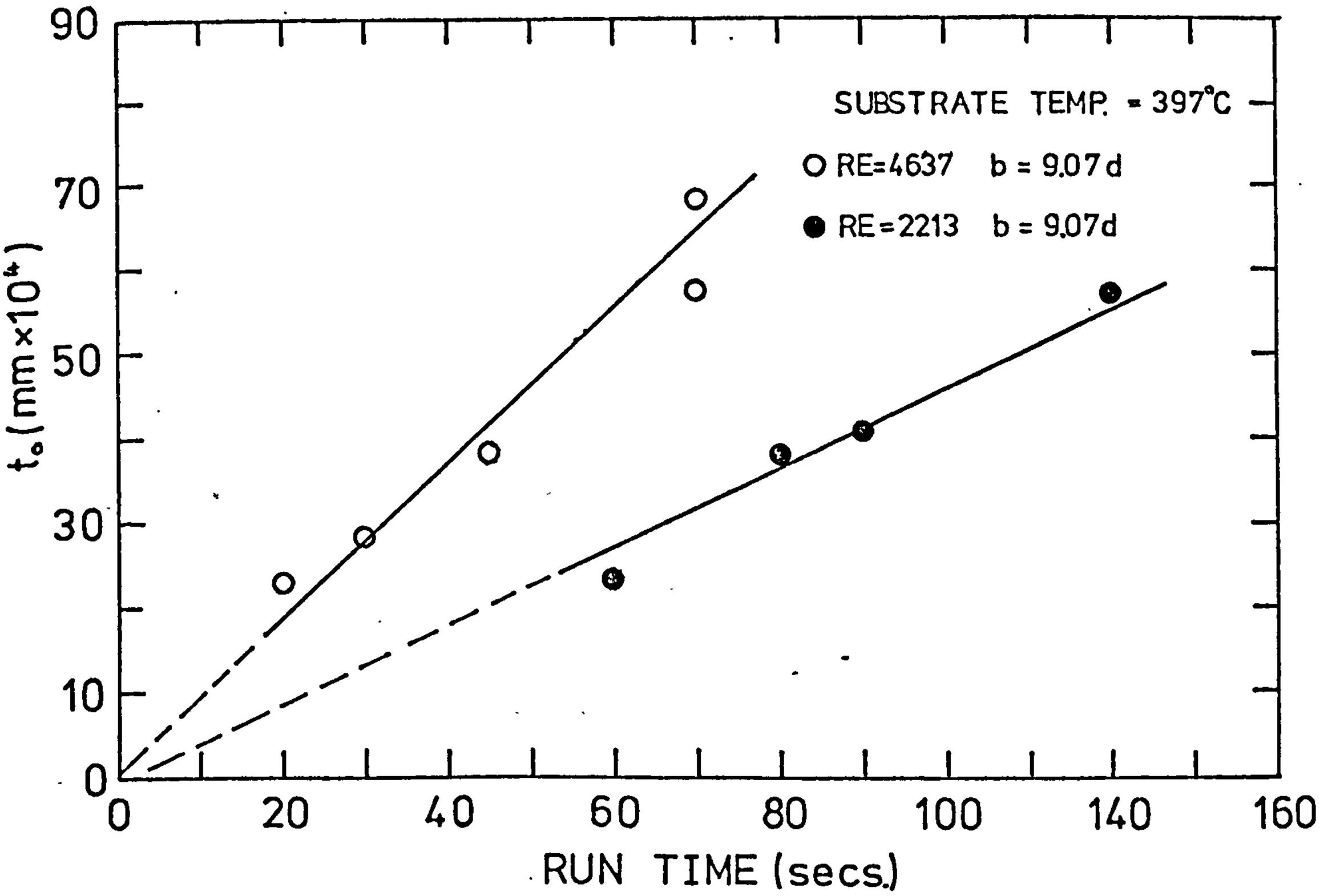
7.8.2 Arhenius Plot for CoO Deposition

Experiments were performed using the highest Reynolds number to be used in the series of experiments of 4637 over a range of temperatures from 221 to 425^{o}C at constant jet plate distance of 9.07d. A plot of log deposition rate versus inverse deposition temperature was made to identify the mass transfer and chemical control regions, fig (7.15). The reproducability of the experiments can be judged from the two experiments at 397^{o}C. The

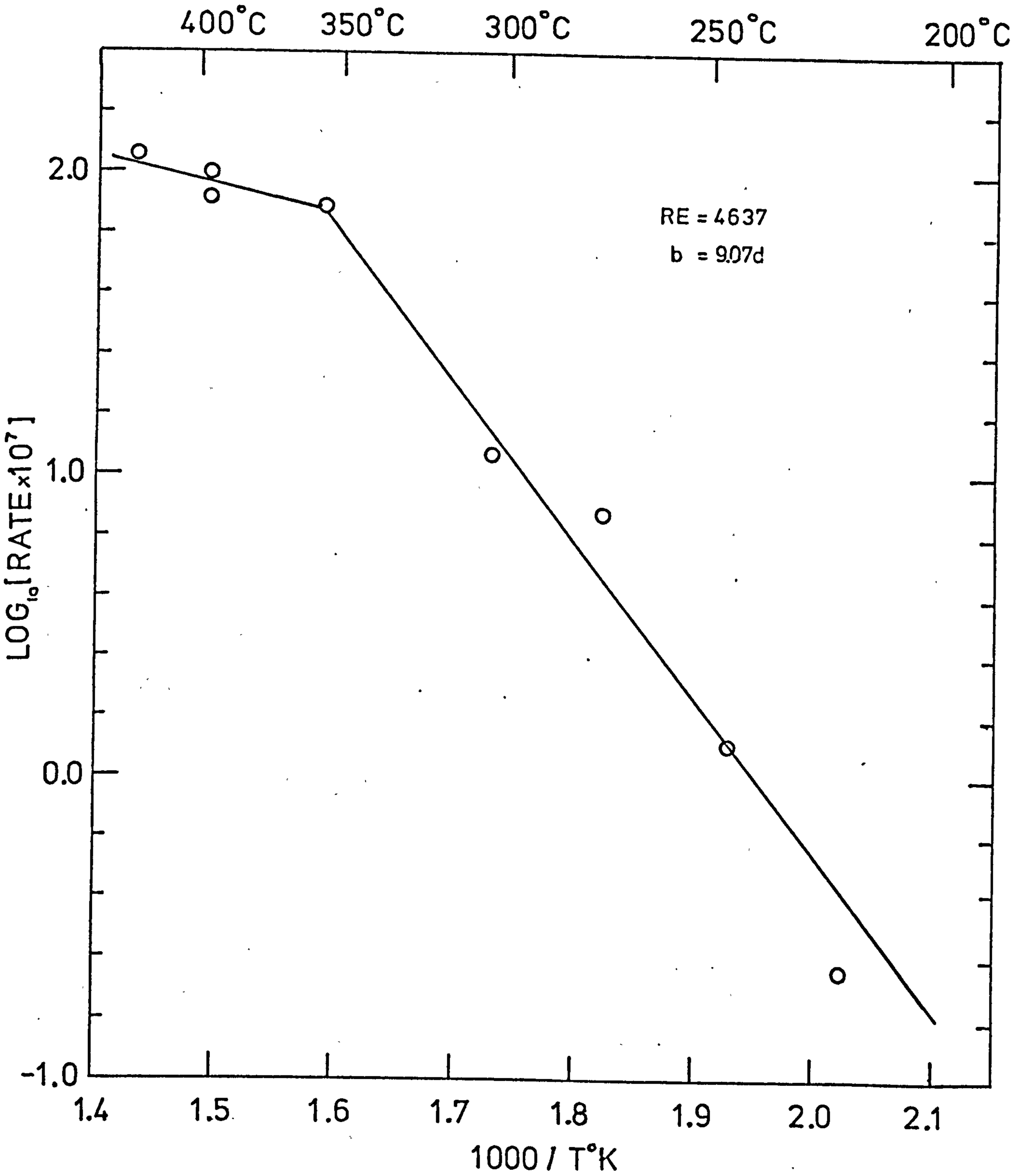
fig(7.13)



TEMPERATURE CONDITIONS UNDER THE JET



fig(7.14)



fig(7.15) ARHENIUS PLOT FOR CoO DEPOSITION

two deposition thicknesses were within 17% of each other. Scatter at lower temperatures was higher.

7.8.3 Reynolds Number Effect in High Temperature Region

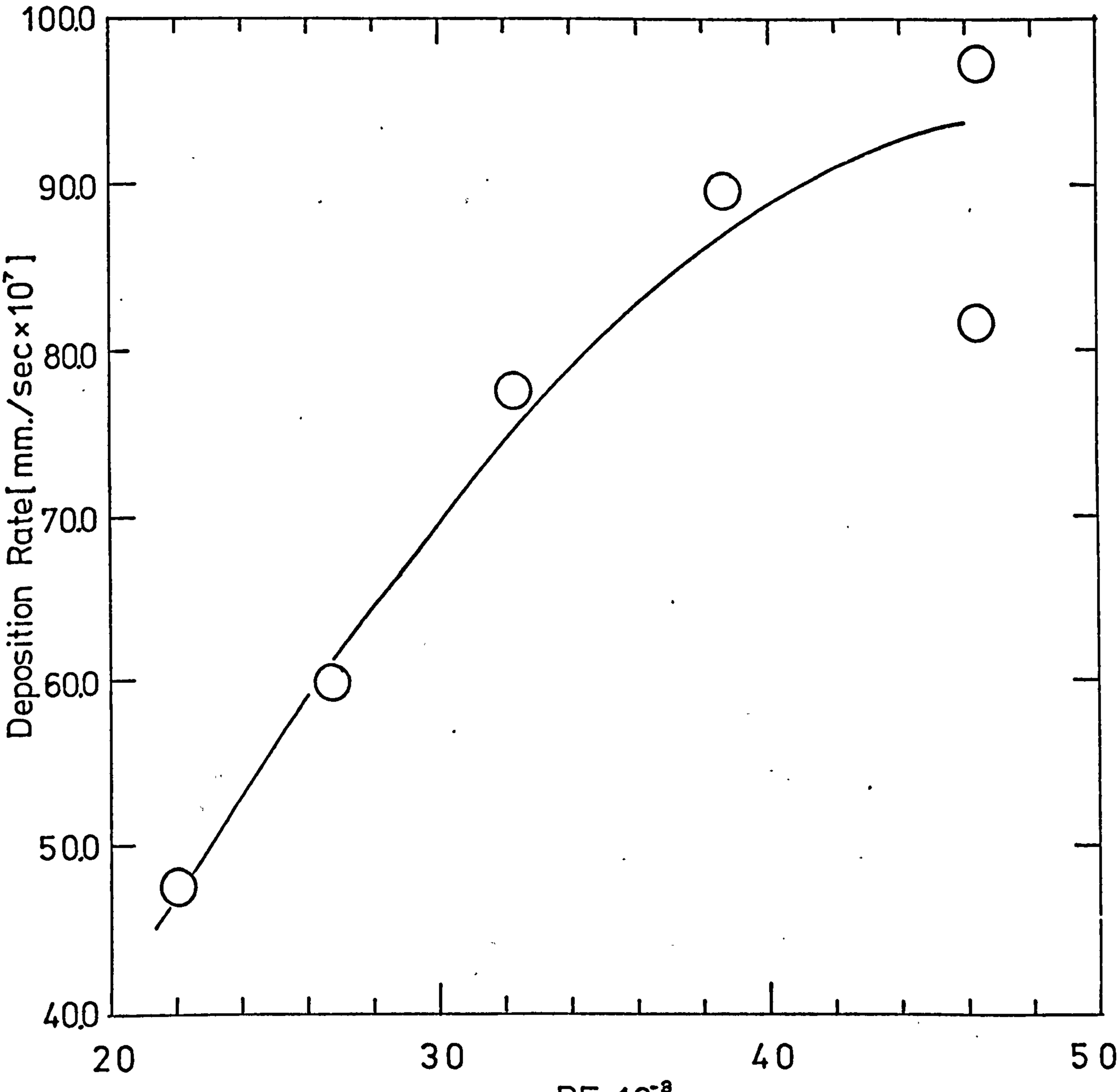
For depositions made at 397°C varying the Reynolds number for otherwise constant experimental conditions was found to vary the deposition rate markedly as shown in fig (7.16). This type of dependence would be expected in a mass transfer region.

7.8.4 Effect of Varying Jet Plate Distance in the High Temperature Region

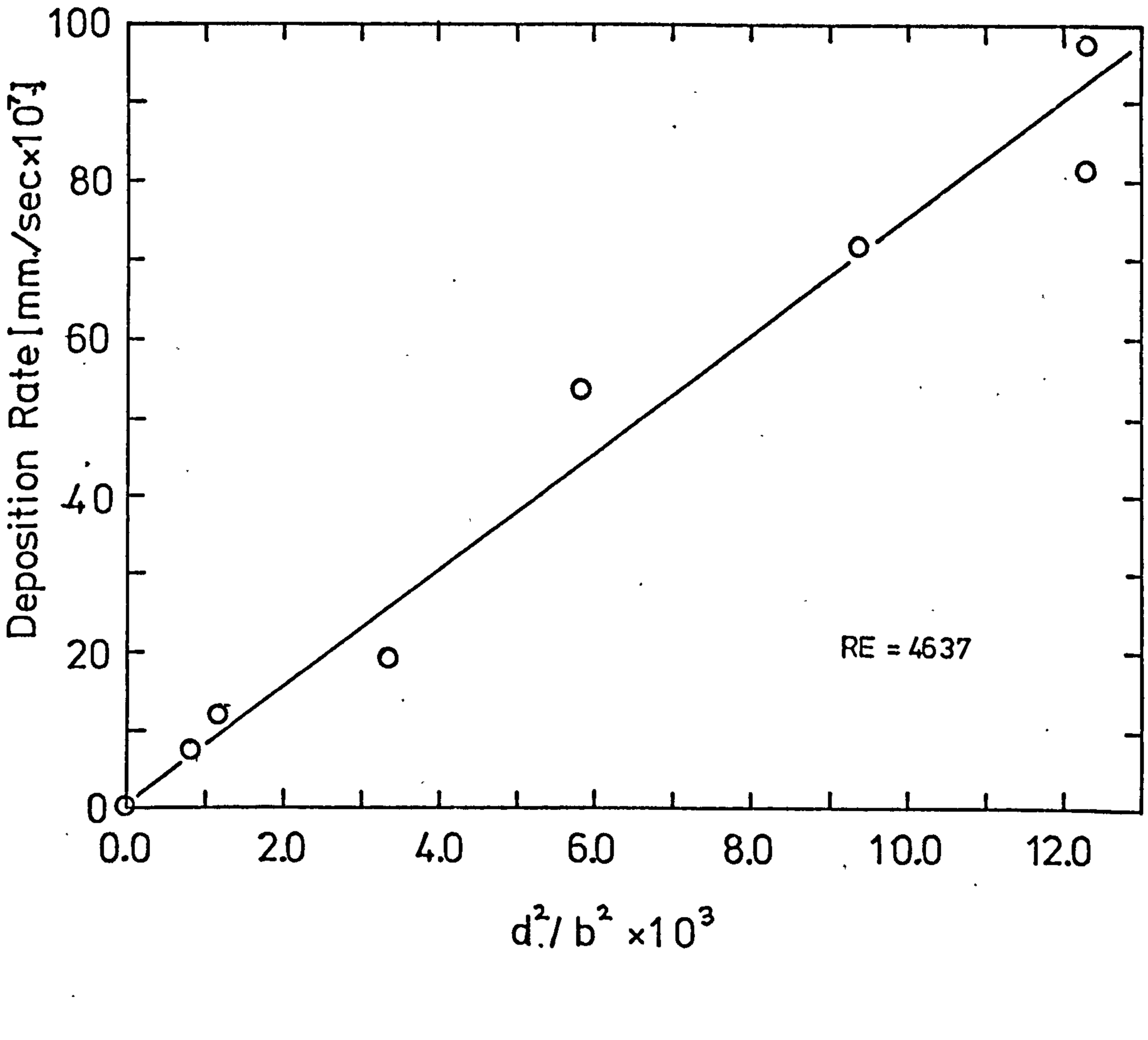
Varying the $d/_b$ ratio on runs performed at 397°C with a Reynolds number of 4637 produced a varying deposition rate as would be expected from a mass transfer control region as predicted by the stagnation point mass transfer theories. The variation is however a function of $d^2/_{b^2}$ fig (7.17) because of the concentration dilution effect from entrainment as discussed in Appendix (2).

7.8.5 Radial Deposition Profile

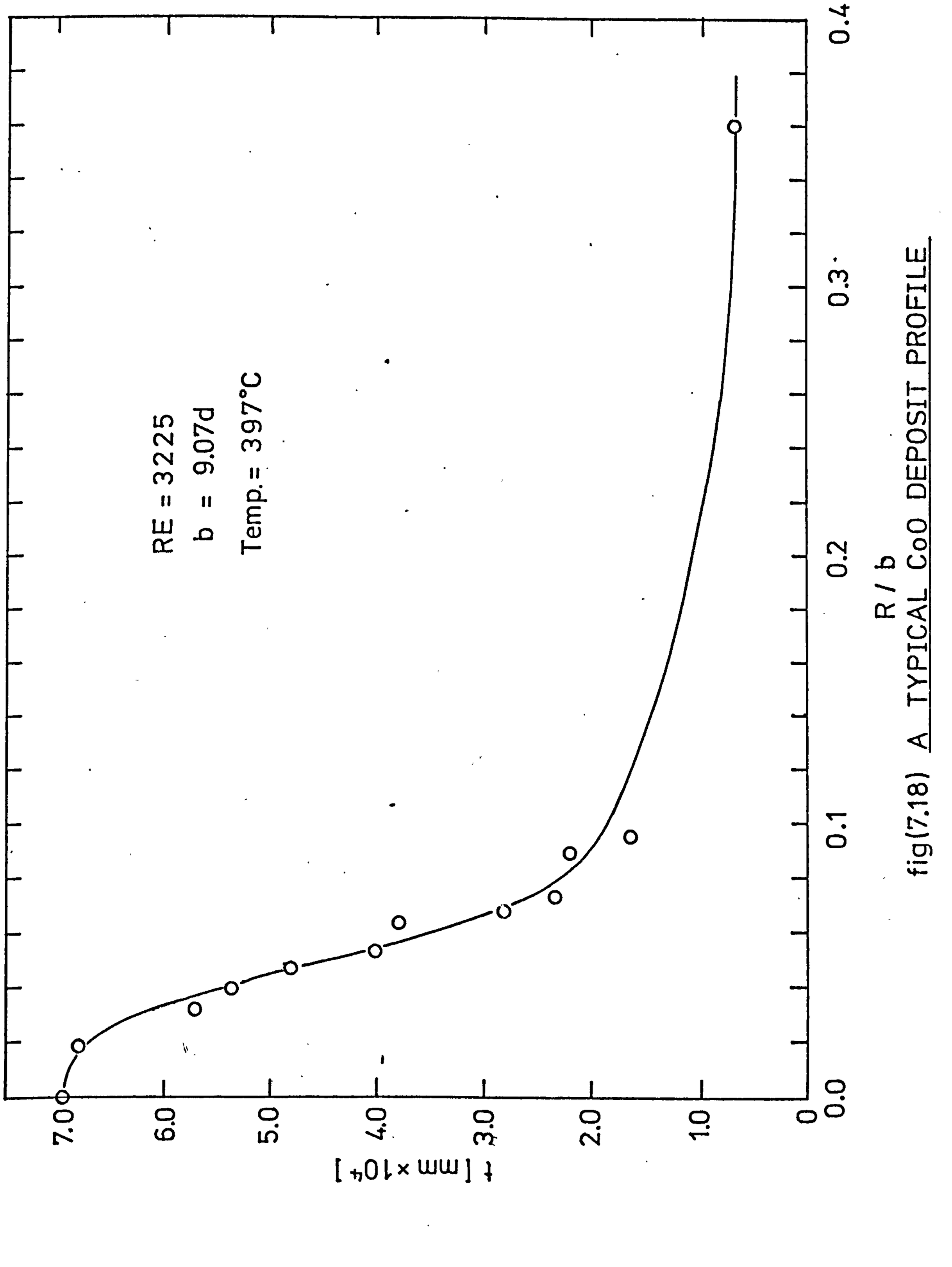
A typical deposit profile, in fact that for the deposit in figs (7.11) and (7.12), is given in fig (7.18). The fairly flat zone around the stagnation point drops away sharply to give a high central peak. Outside a radius of R/b = 0.1 the deposit thicknesses change very slowly. The profiles for all the experiments whose stagnation point values are tabulated in Appendix (4) were calculated to give fig (7.19). This is a scatter diagram in dimensionless form of Sh/Sh_o versus R/b. In calculating the radial Sherwood position the driving force is assumed to be that of the stagnation point concentration difference so the profiles are also of dimensionless physical deposit thicknesses. Also plotted is the theoretical profile derived in chapter six and tabulated in table (6.1). The dimensionless



fig(7.16) REYNOLDS NUMBER DEPENDENCE OF CoO DEPOSITION RATE AT 397°C



fig(7.17) DEPENDENCE OF DEPOSITION RATE ON JET TO PLATE DISTANCE AT 397°C



fig(7.18) A TYPICAL CoO DEPOSIT PROFILE

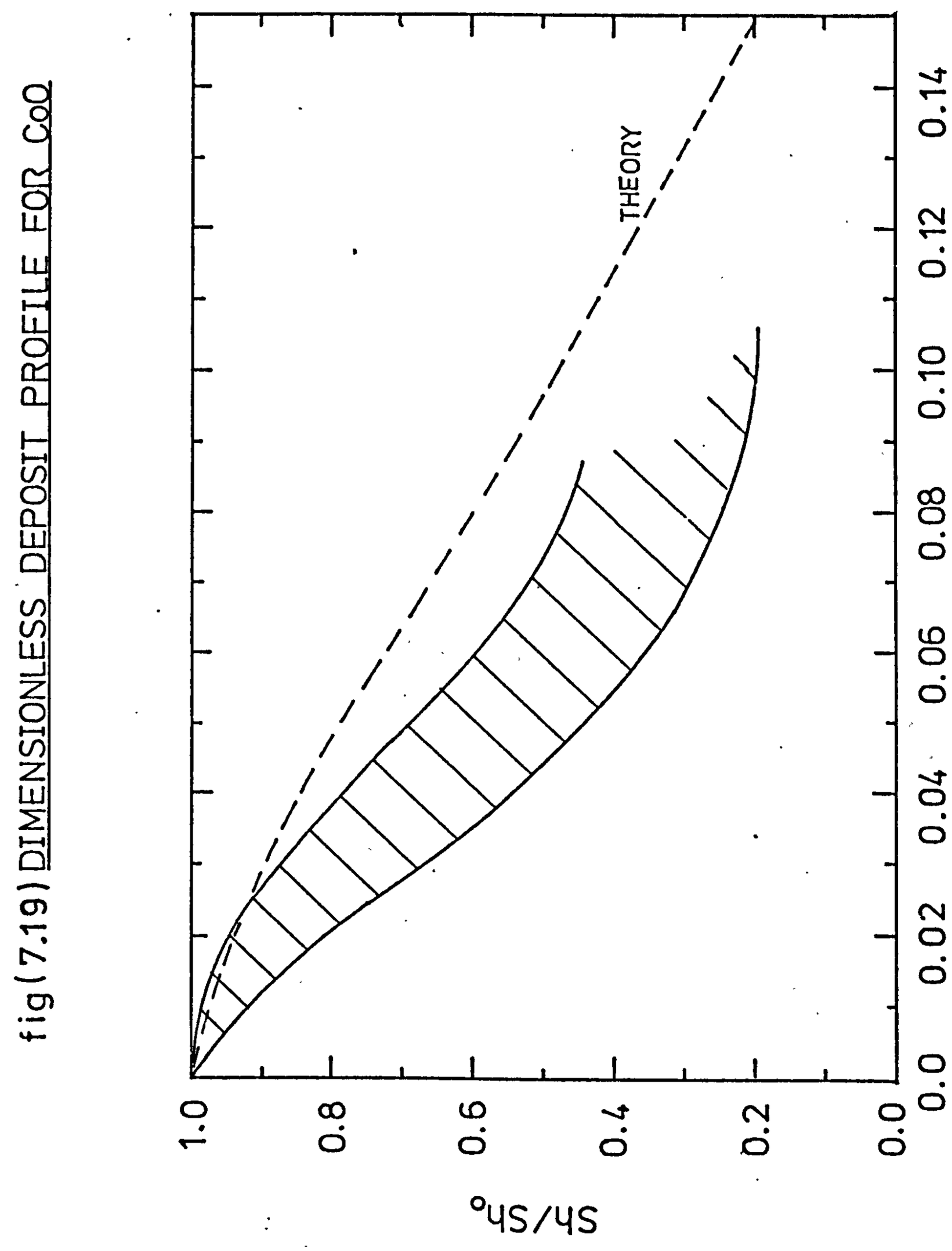
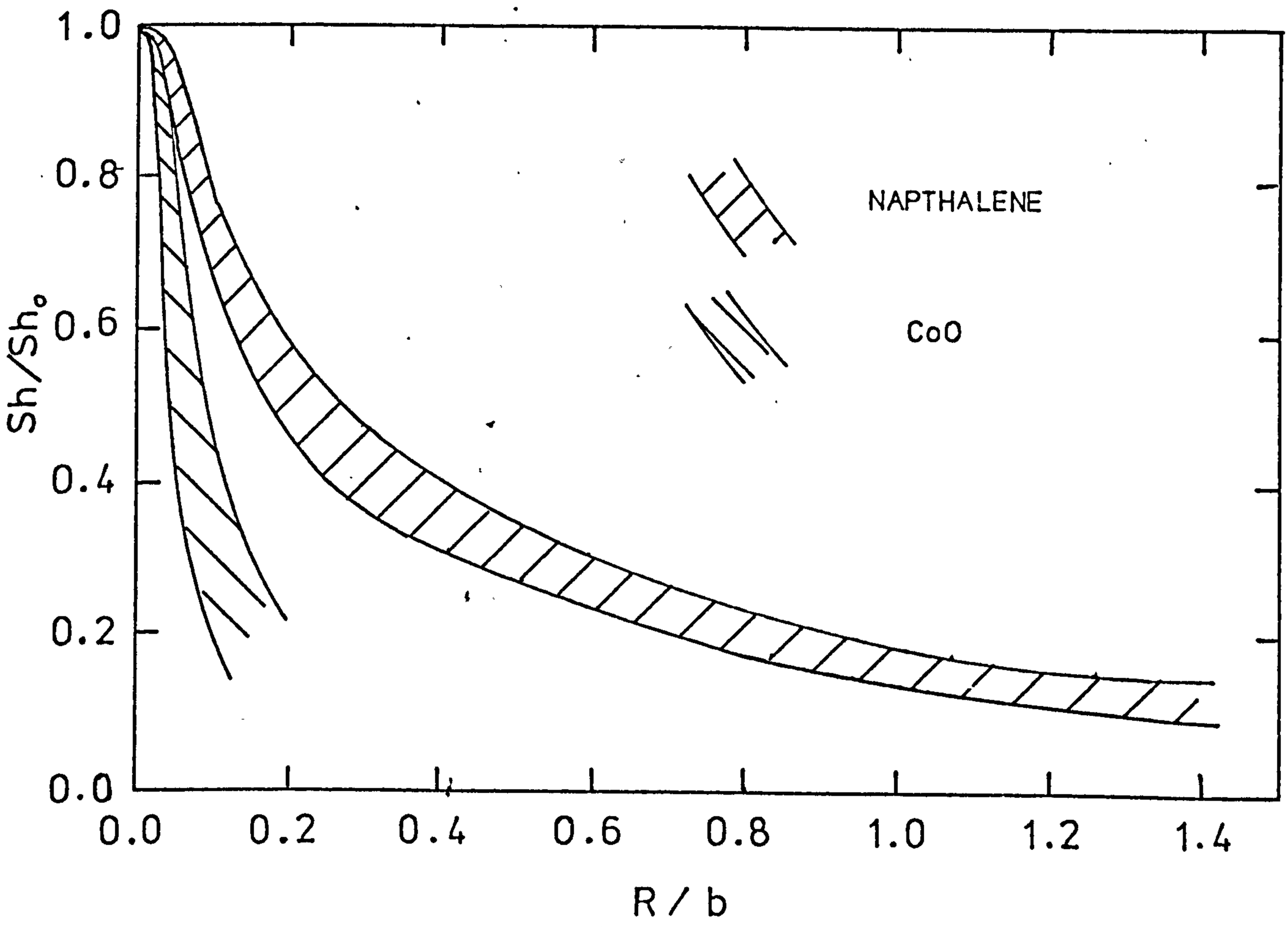


fig (7.19) DIMENSIONLESS DEPOSIT PROFILE FOR CoO



fig(7.20) DIMENSIONLESS PROFILES FOR NAPTHALENE AND CoO

profile is replotted in fig (7.20) to compare it with the profile from the napthalene work in fig (4.19).

7.8.6 Scanning Electron Microscopy Results

Various deposits made on thin copper substrates laid on top of the main substrate were examined on a Cambridge Mk2A Stereoscan. The deposits made on pyrex glass slips were also examined. The latter had to be pre-silvered to make the target conducting. The deposits were scanned along a diameter and the nature of their surfaces compared with the substrate surface. Very few surface features could be seen on the deposits (the microscope could resolve at best a step height of 3.10^{-5} mm) as shown in figs (7.21) and 7.23). The surface roughness that could be resolved was similar to that on the substrate materials shown in figs (7.22) and (7.24). The deposits appeared continuous and coherent and the lack of marked surface features indicated the absence of preferential crystal growth.

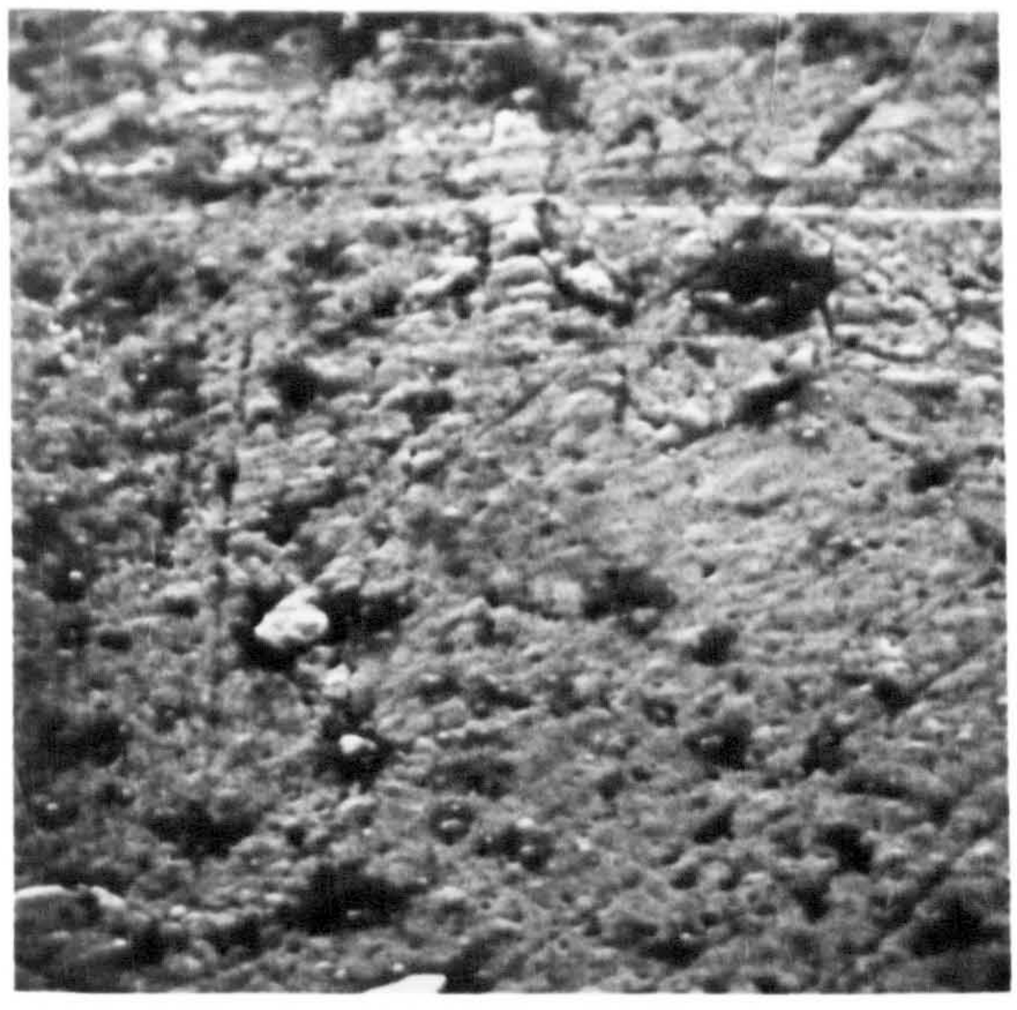
7.9 Discussion of Experimental Results

7.9.1 The Chemical and Mass Transfer Control Regions

The Arhenius plot in fig (7.15) suggests a chemically controlled region for CoO deposition between 221 and 350°C and a mass transfer controlled region above 350°C. The deposition rate in the higher temperature region has been shown to be a function of the fluid dynamics of the system, the jet Reynolds number, fig (7.16) and the jet plate distance, fig (7.17). This is what would be expected in a mass transfer controlled region. The deposit profile shape has also been qualitatively predicted by the simple mass transfer approach of chapter six. The correlation of mass transfer theory for the variation with Reynolds number is left to chapter nine. The smooth surface of the deposits in figs (7.21) and (7.23) indicate that crystallographic effects can be ignored.



fig(7.21) CoO DEPOSIT ON COPPER × 4900



fig(7.22) COPPER SUBSTRATE × 2500



fig(7.23) CoO DEPOSIT ON GLASS × 2100



fig(7.24) GLASS SUBSTRATE × 2100

7.9.2 Temperature Conditions Under the Jet

The scatter in the results plotted in fig (7.14) is sufficient to mask any significant thermal effects and lines passing through the origin can be drawn through both sets of data. There is almost certainly no induction period effect and any initial temperature drop can be ignored for the longer experiments.

7.9.3 The Effect of Jet Plate Distance

The results in fig (7.17) tend to confirm the assumption made in Appendix (2) that the quantity of recycled CoAcAt is negligible and that the deposition rate in the mass transfer zone is a function of $d^2/_{b2}$.

7.9.4 The Nature of the Deposit

The interference profiling method shows that the deposits were typified by a high central mound. The electron microscope photographs show that the surface is smooth in relation to the substrate material. One point not mentioned previously arose as a result of the attempted microprobe analysis mentioned in section (7.1). Occasionally on the radial traverse of the deposit high readings, denoting the presence of copper were noted, suggesting faults in the CoO film. No evidence of this could be seen in the microscopy results, although microcracks due to differential cooling of the oxide deposit and metal substrate could conceivably have been produced.

7.9.5 The Deposit Profile

The theoretical profile derived in chapter six by ignoring depletion of reactant due to chemical reaction predicts as might be expected higher values for the radial mass transfer rates than those measured (fig(7.19)).

The inclusion of the depletion effect would bring the theoretical line much closer to the practical scatter diagram. It will be noted that this could also be accomplished by using Prandtl's turbulence model in the free jet as the model predicts a much sharper concentration profile in the free jet.

7.9.6 Experimental Errors

The reproducibility figure quoted in section (7.8.2) of 17% is high. Errors will come mainly from timing because of the short run durations, and, more especially, from temperature control. A difference of $1^{o}C$ in the chemical control region can double the reaction rate and although the effect in the mass transfer zone is much less it is still considered to be the major source of error. The interference technique of measurement, although sensitive away from the stagnation point, where the position of a fringe is noted, is not so sensitive at the stagnation point where the true deposit height can lie between those corresponding to two fringes. In this case the slight irregularities in the area will produce a mixture of the two colours, with probably one of the lines dominating the area because of its higher intensity. For a deposit producing three orders of interference fringes the error at the stagnation point can be as much as 20%. This is most critical in calculating the dimensionless profile.

7.10 Conclusions

(1) It has been demonstrated that the deposition of CoO from the hydrogen reduction of CoAcAt in the presence of free oxygen and water vapour is controlled by a chemical reaction rate up to a temperature of $350^{o}C$ in the impinging jet system and using the particular concentration of CoAcAt employed. Above $350^{o}C$ the rate controlling step is the diffusion process bringing reactant to the surface.

(2) The impinging jet system in the mass transfer control zone produces a sharp profile deposit in vapour deposition systems.

C H A P T E R E I G H T

NICKEL DEPOSITION FROM THE TETRACARBONYL

8.0 NICKEL DEPOSITION FROM THE TETRACARBONYL

Nickel carbonyl undergoes thermal decomposition to nickel and carbon monoxide as for the equation:

$$Ni(CO)_4 = Ni + 4CO$$

The reaction forms the basis of the Mond nickel purification process after its discovery by Mond (1891) in the nineteenth century.

Heats of reaction for the decomposition given in the literature vary from -32 to -45.7 k cals. per mole. Work on direct determination by International Nickel gave a value of -34.5 k cals. Indirect values are, from Sykes and Townshend (1955) - 36.5 k cals, from Fisher et al (1957), from Spice et al (1955) - 39.1 k cals., and from Sykes (1958) - 38.8 k cals. The equilibrium conversion of the carbonyl has been calculated by Carlton and Oxley (1967), using the free energy of formation data of Spice et al (1955) of $\Delta G_{298} = 5.5$ k cal and $\partial \Delta G/\partial T = -87.9$ cal/^{o}K, to show that the carbonyl can be considered totally converted to nickel and carbon monoxide above 35^{o}C for a total pressure of 0.01 atmospheres and above 80^{o}C for 0.1 atmospheres.

Non-equilibrium data from a commercial plant, reported by Gabe (1968) from the data of Tseidler (1964), gives higher conversion levels at pressures of greater than one atmosphere than those indicated by the equilibrium calculations.

Activation energies from the literature vary from 6.9 k cals. per mole, from Kiprus et al (1966), to 12.0 k cals per mole, from Garnett et al (1934). Bawn (1935) gives a value of 10.2 and Goldberger (1961) 7.2 k cals. per mole.

Carlton and Oxley (1967) give a summary of previous kinetic work on nickel carbonyl decomposition and quote various authors as having found first order behaviour for the reaction rate. They themselves, in an extensive

analysis, find a second order two site mechanism to describe the reaction best.

At temperatures above 200°C the Boudouard reaction becomes important as CO dissociates partially into carbon as for:

$$2\,CO = C + CO_2$$

The CO_2 formed can also produce an oxidising condition with the CO because of the equilibrium:

$$2\,CO + O_2 = 2\,CO_2$$

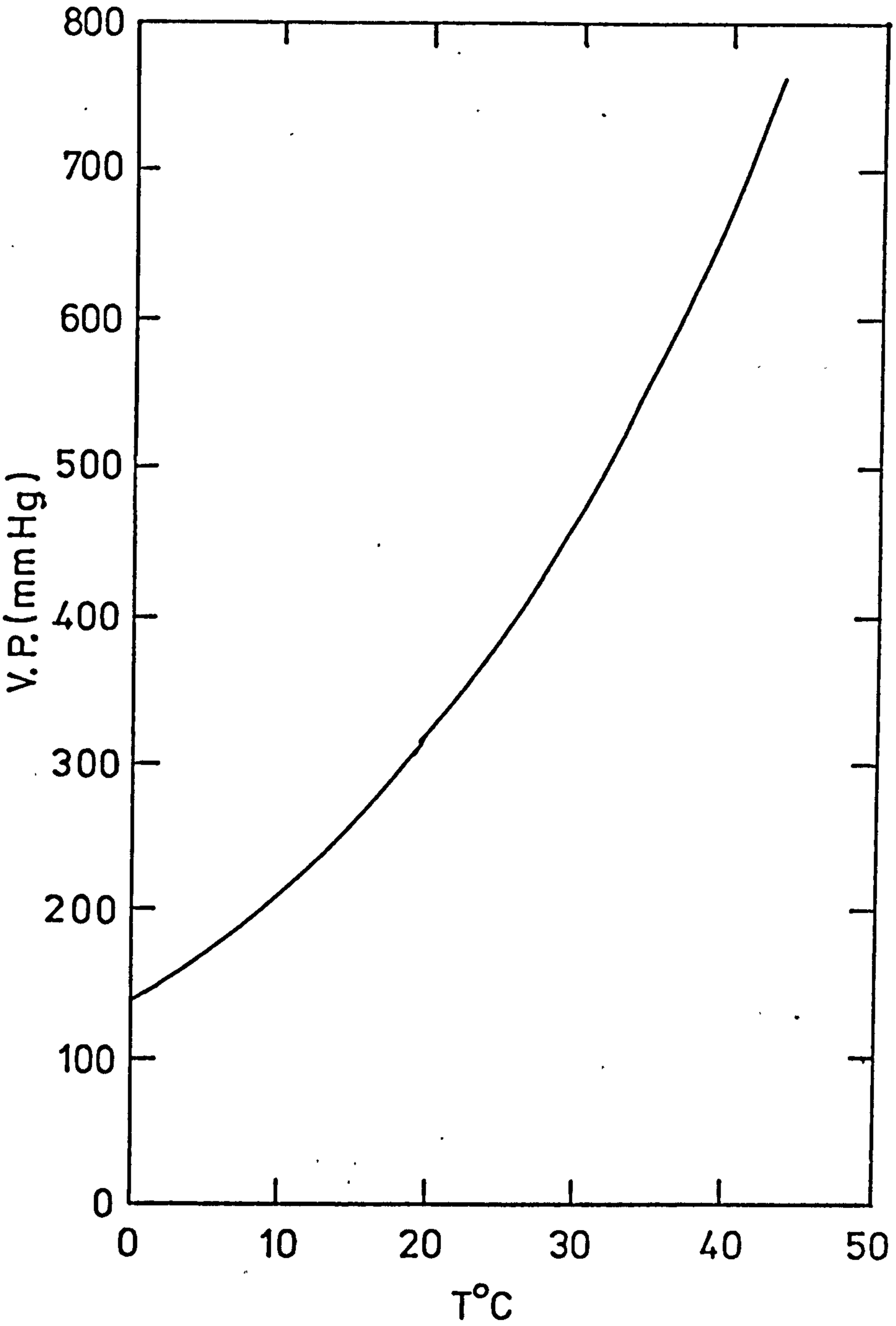
Measured diffusion coefficients for carbonyl are not available and values were calculated in Appendix (1).

Nickel Carbonyl, a colourless liquid, boils at 43.2°C and has a very high vapour pressure,(fig (8.1), data from International Nickel Co.) It is highly inflammable and liable to self-ignition if the residue formed from the slow decomposition of the carbonyl is exposed to atmosphere. The vapour is highly toxic, the maximum concentration that can be safely inhaled for long periods has now been fixed at one part per billion. Because of the hazards inherent in working with this compound, stringent safety precautions are necessary and these are summarised in section (8.1.4).

Nickel carbonyl is produced commercially by the action of carbon monoxide on nickel under pressure. The chemical used in the present series of experiments was supplied free by International Nickel Limited in cylinders pressurised to four atmospheres with carbon monoxide.

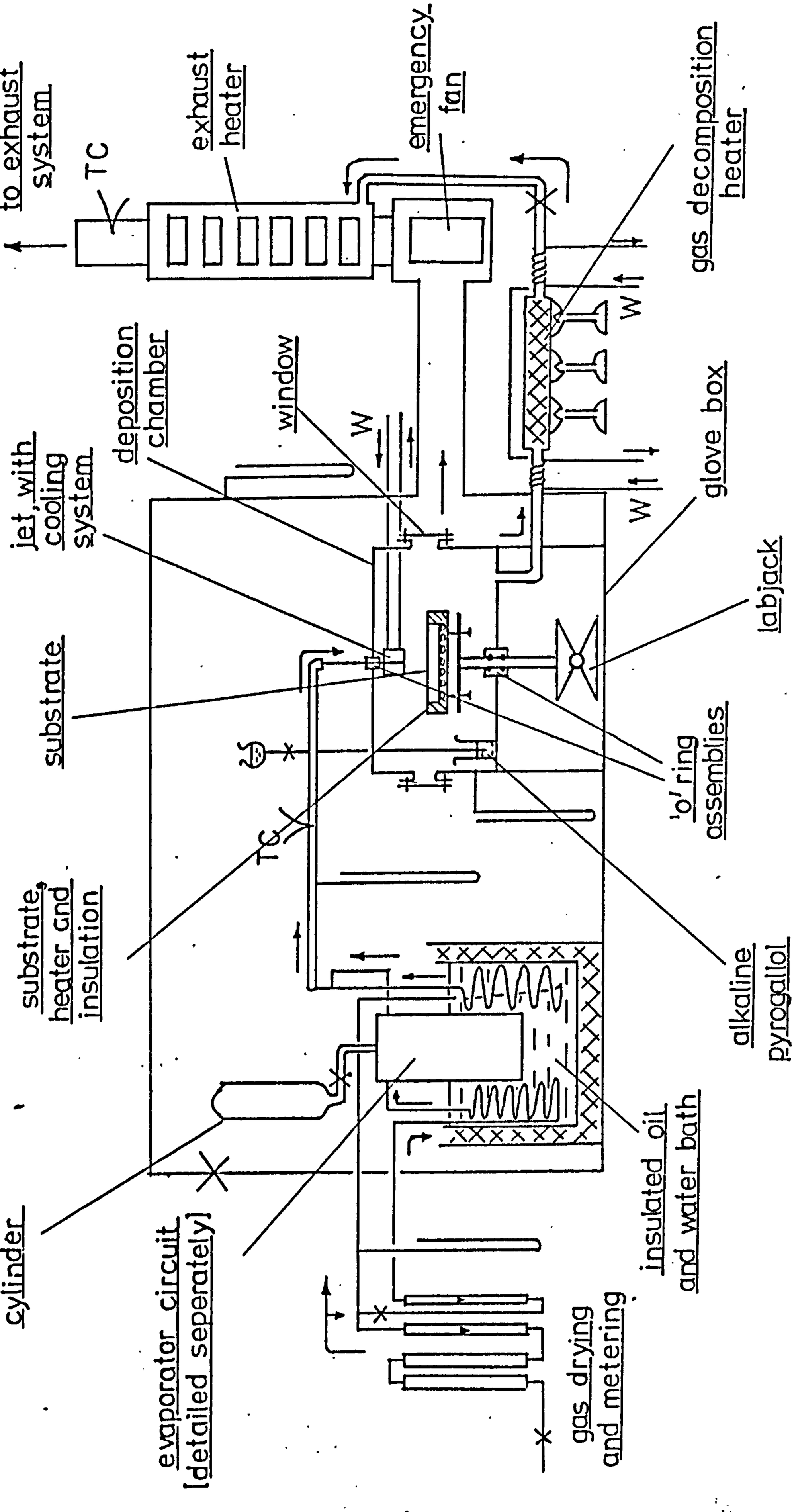
8.1 Experimental Apparatus and Method

The apparatus for nickel deposition is essentially similar to that for cobalt oxide and is shown sceratically in figs (8.2) and (8.3). A general view of the apparatus is given by fig (8.4) and close-ups of the

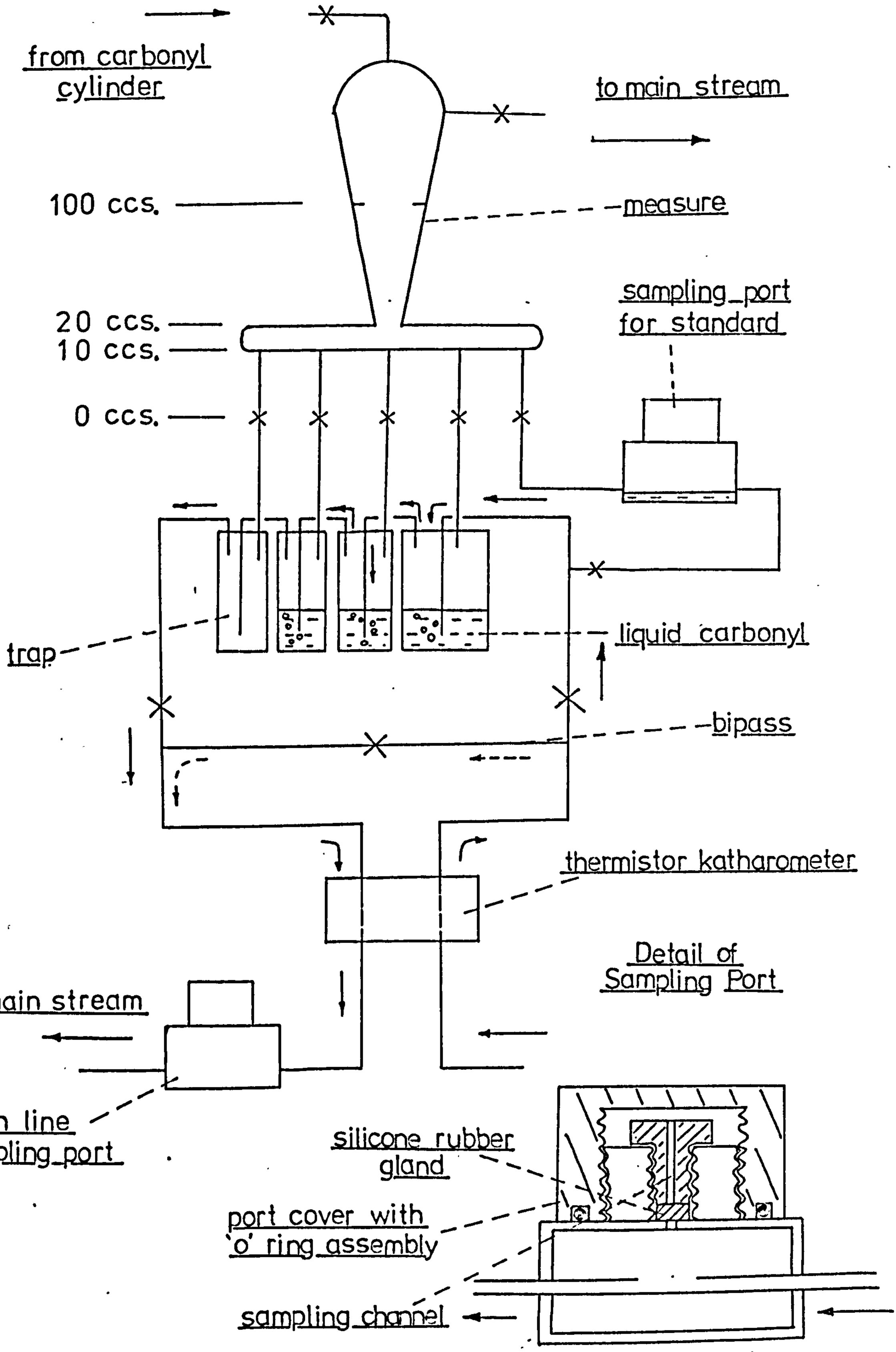


fig(8.1) VAPOUR PRESSURE OF NICKEL CARBONYL AS A FUNCTION OF TEMPERATURE

fig(8.2) SCHEMATIC DIAGRAM OF NICKEL DEPOSITION APPARATUS



fig(8.3) EVAPORATOR CIRCUIT



main apparatus in figs (8.5) and (8.6).

Nitrogen carrier gas was dried in silica gel columns and metered through a calibrated rotameter. The bulk of the flow passed through a temperature stabalising coil, immersed in an insulated bath containing water and paraffin oil, into a copper pipe delivering the carrier gas to the same jet as that used in the previous CoO deposition experiments.

The remainder of the flow was metered into the evaporator circuit, fig (8.3), which was contained in the oil and water bath. After passing through a temperature stabilising coil, the evaporator flow passed through one arm of a thermistor detector and into the evaporator. The latter consisted of four closed copper cylinders which could each be filled from the top with liquid carbonyl. The flow passed to each in turn, bubbling through the liquid carbonyl. The last cylinder was left empty to act as a trap for any entrained droplets. The nitrogen, with the carbonyl vapour, passed through the second arm of the thermistor detector and rejoined the main flow via a sampling port. Provision was made for the evaporator to be isolated completely or partially by the operation of a bipass. The individual cylinders in the evaporator were filled with carbonyl from a calibrated glass measure. This measure was connected to the carbonyl cylinder and had a pressure equalising tap connecting it to the main stream. A fifth tapping from the measure connected with a sampling port which was used to provide a standard in the concentration analysis. All taps connected to the evaporator were of the 'Speedivalve' vacuum type. The taps in the glass measure were of the P.T.F.E. 'Rotaflow' design. Both types exhibited excellent leak tightness properties.

The combined evaporator and main flows were then passed through the jet to impinge on the same copper substrate and assembly as used before. Shielding was considered insufficient thermal insulation for the jet, because

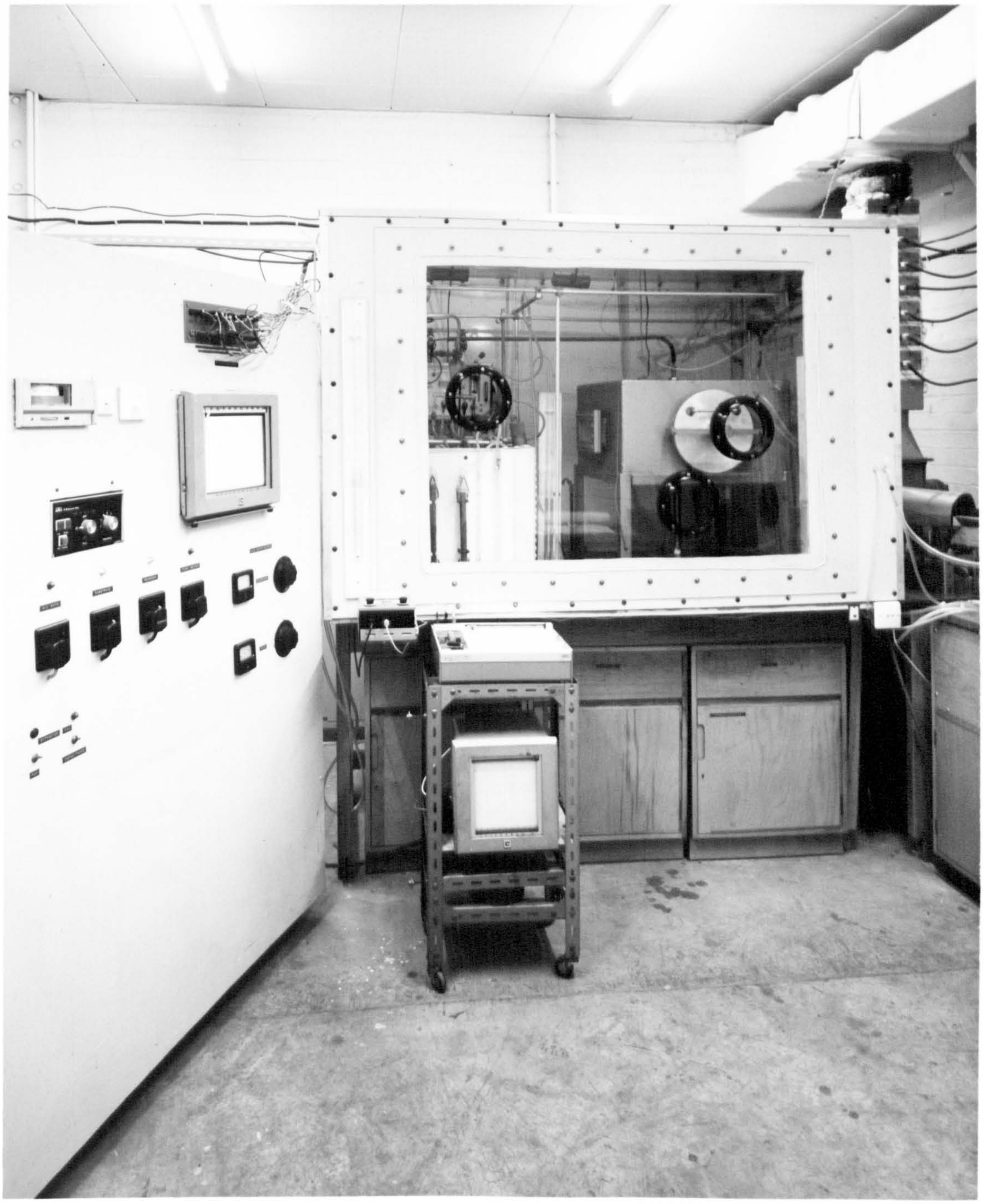


Fig (8.4) NICKEL DEPOSITION APPARATUS



Fig (8.4) NICKEL DEPOSITION APPARATUS

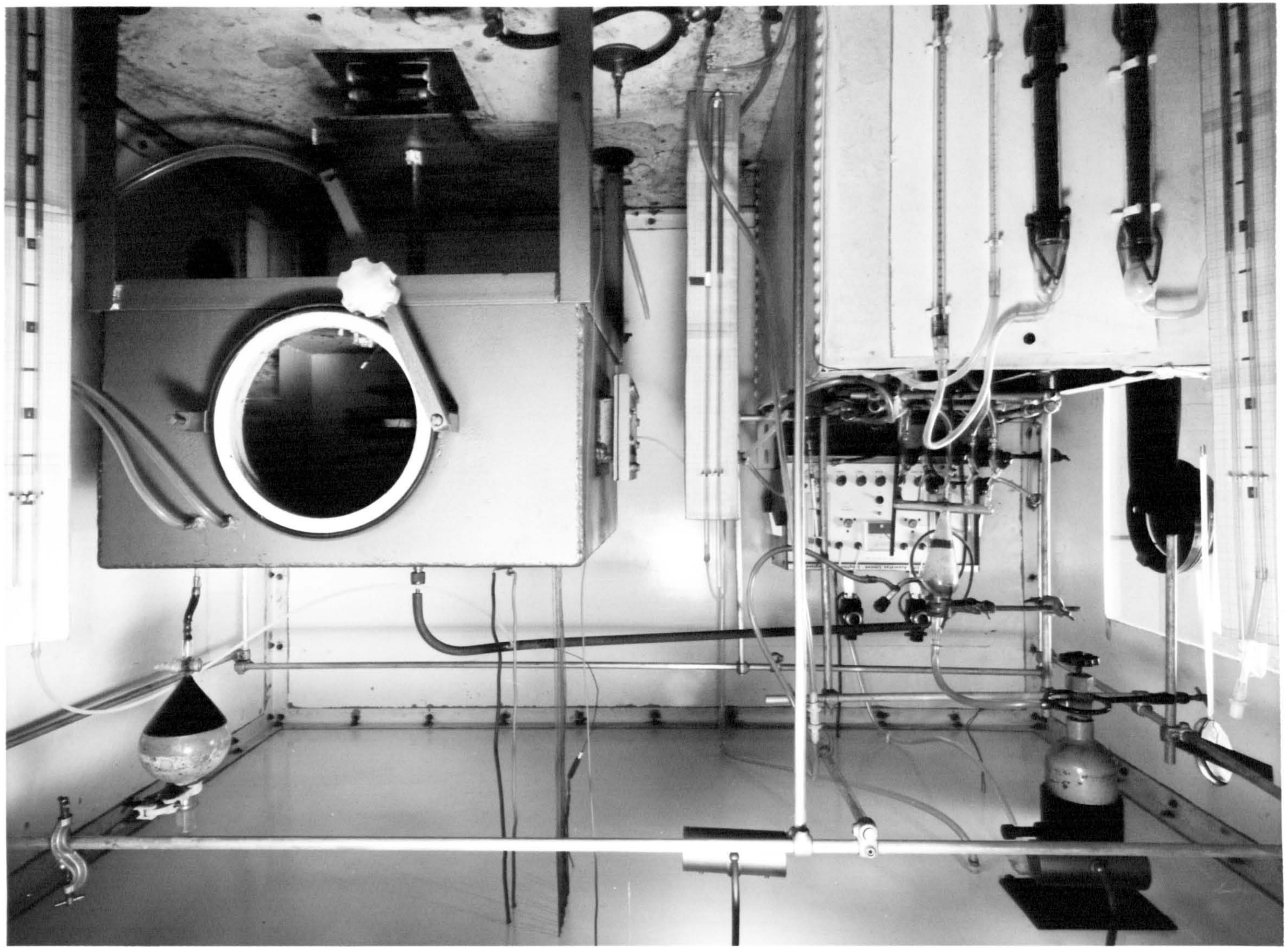




Fig (8.5) GLOVE BOX INTERIOR

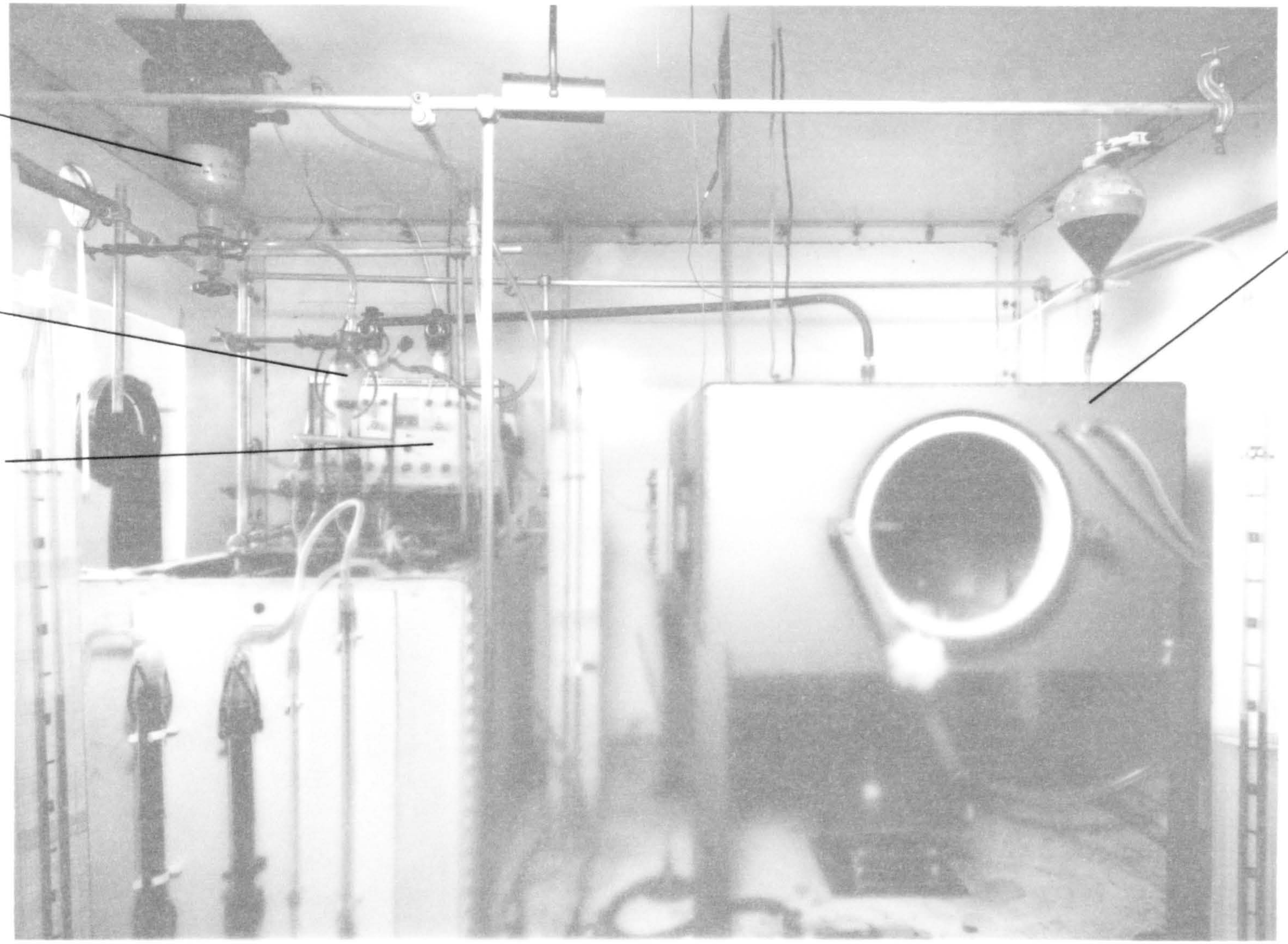


Fig (8.5) GLOVE BOX INTERIOR

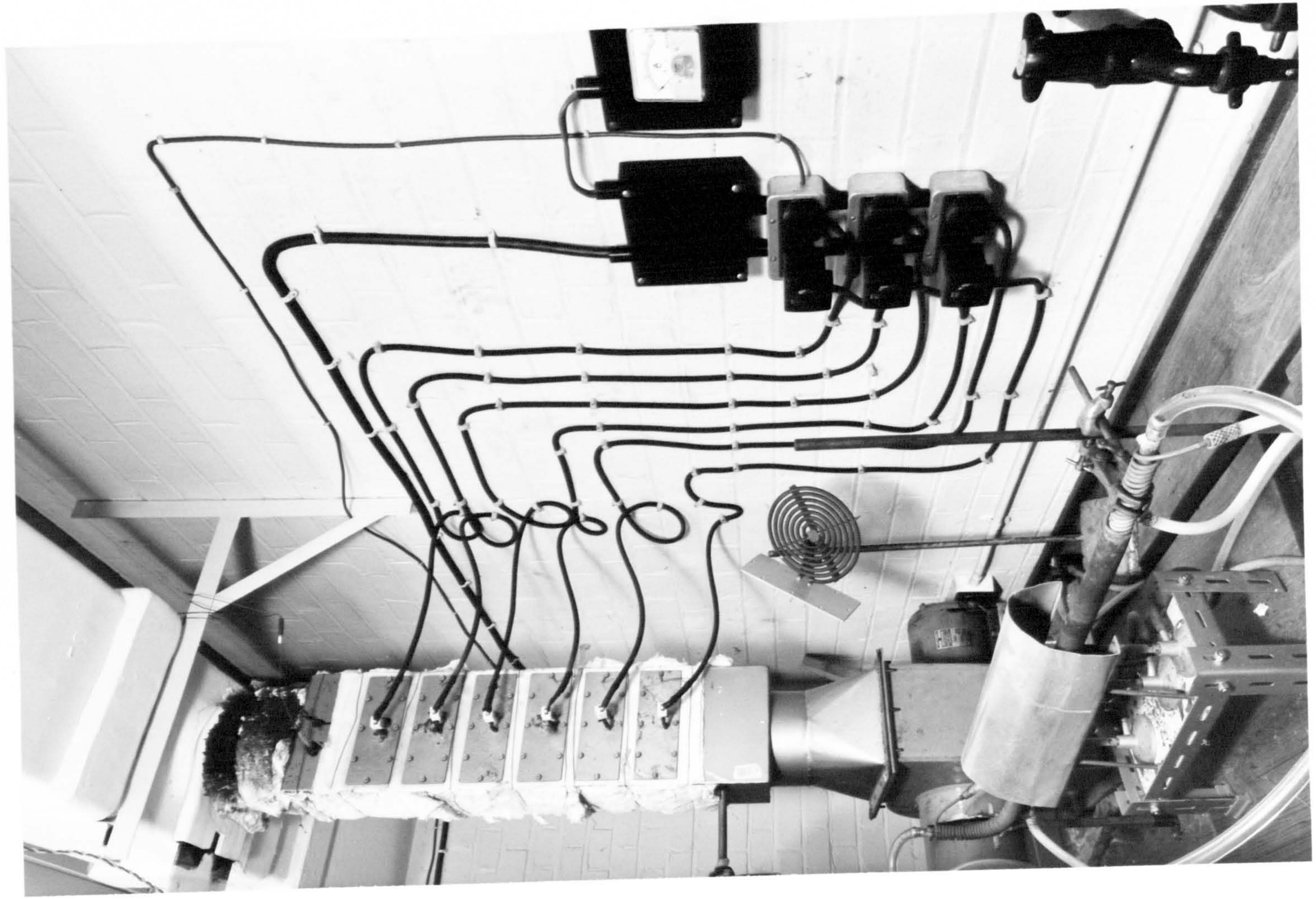


Fig (8.6) EXHAUST HEATER AND GAS DECOMPOSITION HEATER

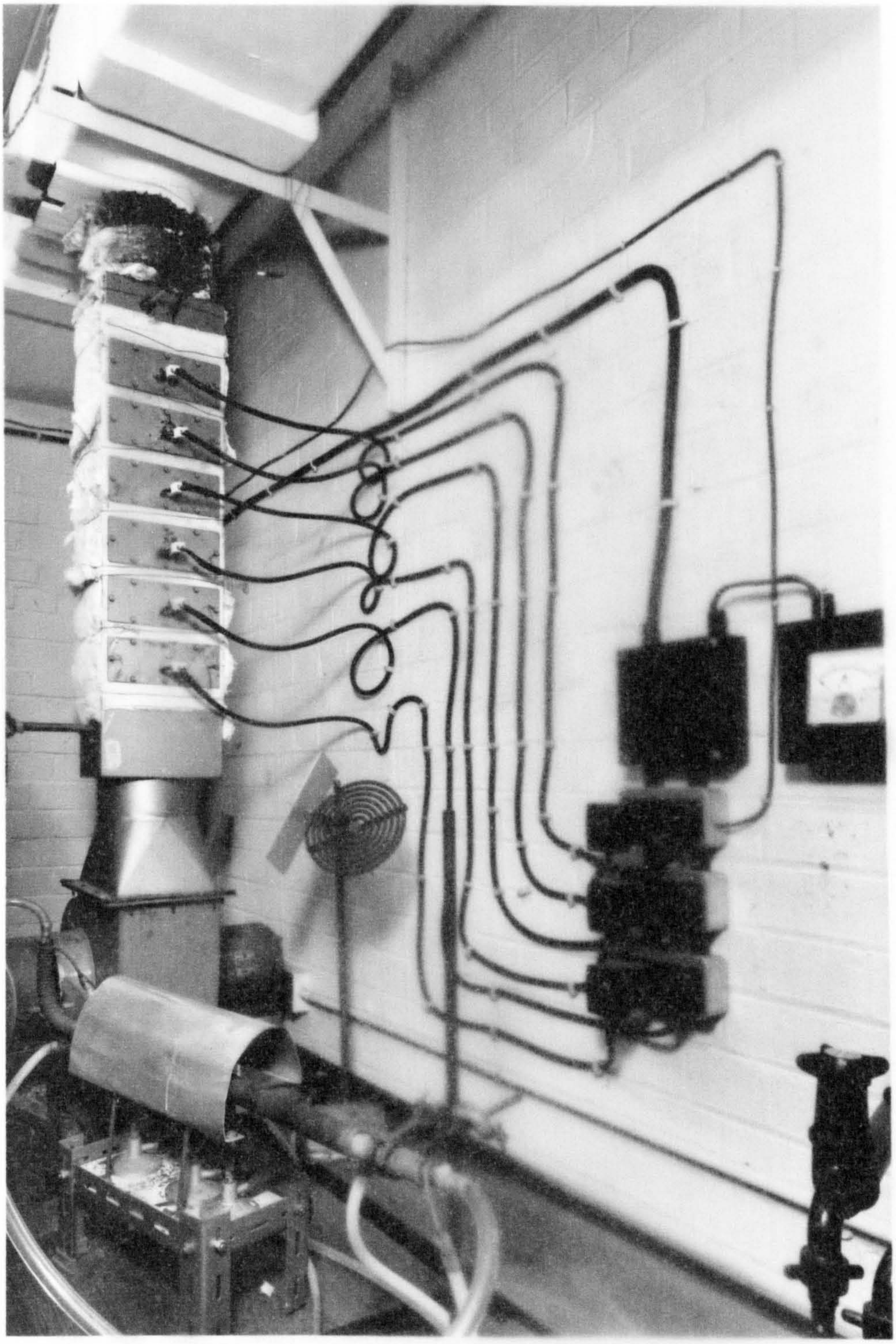


Fig (8.6) EXHAUST HEATER AND GAS DECOMPOSITION HEATER

of the smaller chamber size, and a water cooled jacket was fitted instead.

The substrate assembly could be raised and lowered as before and the jet was again positioned away from the substrate axis to allow a number of deposits to be made on one substrate block. Temperature control and monitoring, the purging of the apparatus, measurement of jet/plate distance also remained the same. The substrate was again prepared by grinding, polishing and chemical cleaning and any surface oxide was reduced by hydrogen at 300°C.

The deposition chamber for these experiments was redesigned with a completely double welded structure of 8.35 mm mild steel. Two side pyrex windows were incorporated allowing limited sight of the substrate and jet assemblies. Easier access to the inside of the chamber than before was effected via a circular flanged port with an 'O' ring assembly, fig (3.5), onto which an aluminium cover could be screwed down to seal the chamber.

A large, insulated oil and water bath was used to contain the evaporator circuit, bar the glass measure, to provide good temperature stability during an experiment in the gas and evaporator, as the ambient temperature inside the glove box containing the apparatus rose during an experiment. The bath also served to provide a visual check on the leak tightness of the breakable joints. Paraffin oil, although expensive, had to be used in conjunction with water in the bath, as the water set up a galvanic cell within the bath attacking the apparatus and clouding the water.

Most of the apparatus was contained inside a large glove box measuring 1.83 m x 1.22 m x 1.22 m high. The box was constructed of 12.7 mm thick block board bolted onto an angle iron frame and sealed with 'Selastic', a non-drying compound. The front panel was cut away and a 1.07 m x 1.52 m perspex sheet, 6.35 mm thick, was screwed onto the wood surrounds and sealed by a stranded P.T.F.E. gasket. Three glove ports were incorporated into this

front panel. Another smaller window with one other glove port was made at the carbonyl cylinder end of the glove box. A removable panel allowed the movement of material into and out of the box.

The glove box was connected to the extraction system of the laboratory via an electric heater. A pressure drop of between 2.5 and 5.0 mm of water was maintained across the box walls by the extraction system to ensure that no carbonyl accidentally allowed into the glove box could escape into the laboratory. The pressure drop was controlled by a damper above the electric heater and two valves in the far end of the glove box.

The exhaust heater, fig (8.6), was constructed of thin mild steel sheet with fibre lagging. Six 2.1 kW 'radiant rings' provided the heat, three were operated by 'Simmerstat' controllers working on a bimetal strip principle. A replacement heater is shown in fig (8.6). The heater was packed with wire wool to increase the heat transfer rates. The air flow through the system was adjusted to give an acceptable negative pressure in the glove box and the heater controlled to give a measured exit temperature from the heater of above 200°C. An emergency fan was incorporated in the base of the heater should the extraction system have failed.

The exhaust from the deposition chamber contained a dangerous level of carbonyl vapour. This was decomposed in the decomposition heater constructed from a 25.4 mm diameter copper tube filled with copper gauze and heated by three bunsen burners fitted with flame spreaders. The ends of the burner tube were water cooled. The burner heated the chamber exhaust gases to over 250°C at all the flow rates used. The exit gas was then passed into the base of the electric exhaust heater via a jet, in case carbon monoxide levels produced by the carbonyl decomposition rose above the explosion limits.

The presence of very low levels of carbonyl concentration can be detected with a clear naked flame, which is supposed to become tinged with

yellow if carbonyl is present. Experiments on a towns gas microburner, left permanently lit, inside the glove box, did not produce a yellow colouration, rather the flame turned a grey-white.

Experiments were performed to identify the mass transfer and chemical control regions at a Reynolds number of 6734, a carbonyl concentration in nitrogen of 1.38 mole %, and a jet/plate distance of 15.1d. The effect of jet/plate distance and varying the Reynolds number between 2510 and 7380 in the mass transfer region was studied. The apparent order of reaction of the carbonyl decomposition in the chemical control zone and in the range of carbonyl concentration of 0.276 to 2.07 mole % was also investigated. The upper value for the Reynolds number was limited by the safety precaution of limiting the excess pressure inside the apparatus to half an atmosphere. Experimental times were mainly between two and ten minutes but much longer runs were necessary for the slower chemically controlled depositions.

Reynolds numbers were calculated from jet properties and other variables using film properties.

Some proving runs were made with thin copper sheets over the thicker substrate as these could be removed without dismantling the substrate assembly. Some of the deposits produced in this manner were examined with the scanning electron microscope.

During all experiments involving carbonyl a complete breathing apparatus was worn. A list of other safety precautions follows in section (8.1.4). and other precautions and remedial actions in the event of an accident can be found in a booklet supplied and published by International Nickel Limited.

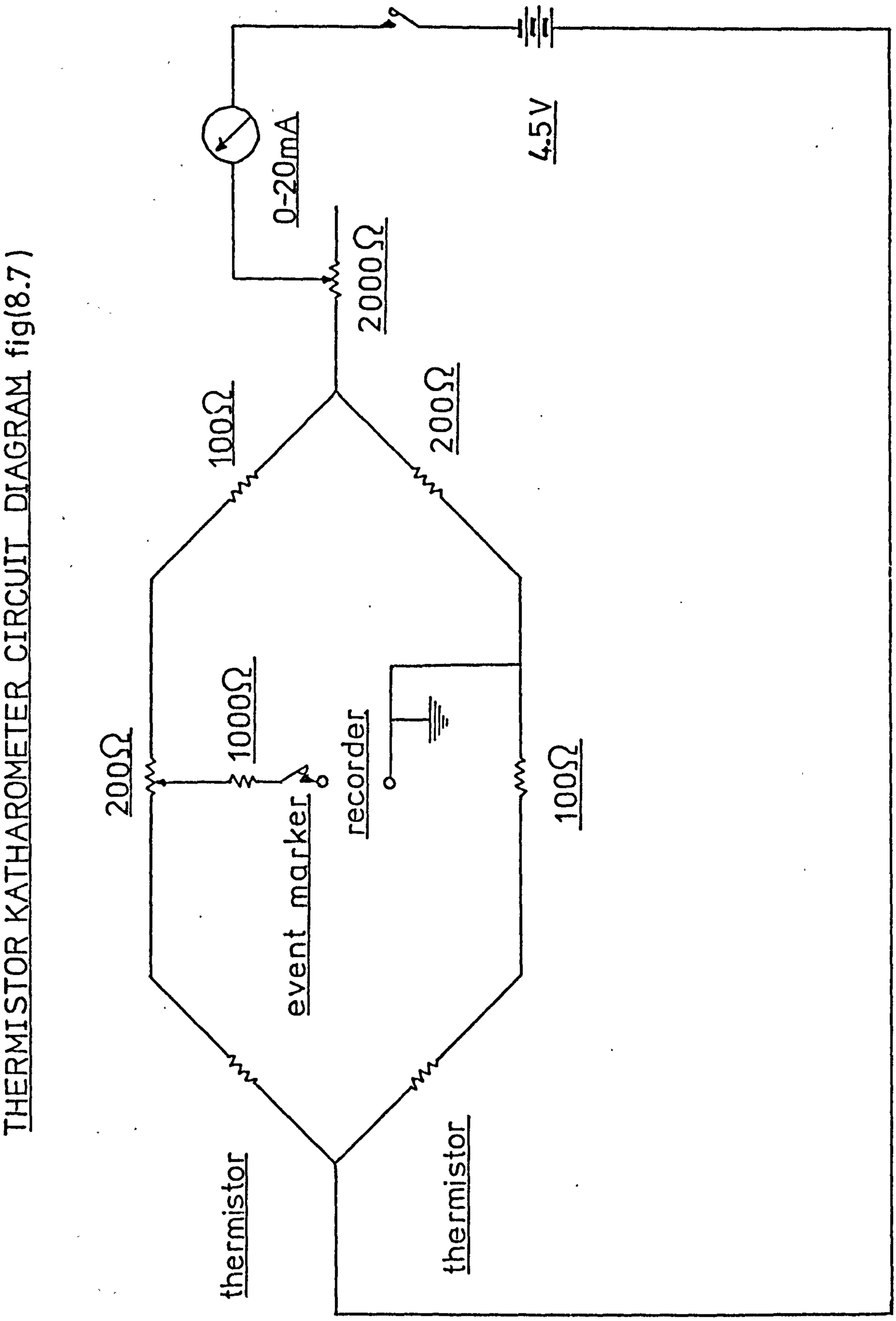
8.1.1 Calibration of the Evaporator and Analysis of the Carbonyl Concentration

The inclusion of a thermistor katharometer detector in the evaporator circuit was an effort to continuously monitor the concentration of carbonyl

in the evaporator exit flow. The principle of operation is to have two electrically matched thermistors as part of a Wheatstone bridge and for the difference in the thermal properties of the flows passing each thermistor to outbalance the bridge in proportion to the difference in composition of the two flows. The thermistors are oxide particles, supported on platinum leads, whose electrical resistance is a fast moving function of temperature. They constitute two arms of the balanced Wheatstone bridge circuit shown in fig (8.7). The circuit is an adaption of one recommended by the manufacturers to give a high impedence output and an event marker to mark an event on the potentiometric recorder used to display the bridge output.

The current passing through the bridge circuit acts in a second capacity to heat the thermistors. The thermistors lose this heat to the gas passing them and the rate of heat loss depends on the heat transfer coefficient between the oxide and the gas. This rate is a function of, amongst other things, the molecular properties of the gas, so, different species, in removing heat at different rates, will vary the equilibrium temperature of the thermistor and therefore its resistance. When the same gas is flowing at identical rates and temperatures passed each thermistor the bridge is in balance, the introduction of another species passed one thermistor causes an imbalance in the bridge producing a voltage output change that can be read on the recorder.

The optimum operating temperature for the thermistors used in the detector was, unfortunately, too high, in that some carbonyl decomposed on one thermistor altering its characteristics permanently and rendering the device unservicable. The detector was, however, useful in calibrating the evaporator, in preliminary experiments, using acetone as the evaporated species. The rate of concentration build up in the system, as a function of evaporator flow rate, was investigated, as only when a constant composition was obtained from the evaporator could a significant experiment be performed.



THERMISTOR KATHAROMETER CIRCUIT DIAGRAM fig(8.7)

Although the detector gave a qualitative measure of concentration build up, it needed calibration to give a quantitative value. This was done by taking samples from the sampling port on the exit side of the evaporator with a 1 ml. hypodermic syringe and comparing these samples with standards on a Fisons Mini 1 Gas Chromatagraph, contained incidentally in the glove box. The chromatagraph, as supplied, is intended for the analysis of mixtures of small molecular species, and the larger acetone and carbonyl molecules could not pass through the columns standard in that model. As nitrogen was the carrier gas used in the deposition experiments, using nitrogen as the carrier gas in the chromatagraph as well, meant that the chromatagraph detector would only sense the evaporated component in the injected samples and no separation of more than one species would be necessary. This meant that the column packing could be dispensed with and an empty column used instead.

Standards, for comparison with the samples, were obtained by sampling saturated compositions of evaporate species in the carrier gas, by taking 1 ml. samples from the port connected to the graduated measure in fig (8.3). A quantity of evaporate was kept permanently in this port. The concentration of evaporate in the gas phase was assumed to be given by the vapour pressure at the temperature of the port.

Knowing the characteristics of the evaporator from the acetone experiments, a check on the concentration of carbonyl was made by injecting samples into the chromatagraph at various times during the experiment. The concentration was found to rise quickly to saturation values at all flowrates used. The length of time to reach saturation increased with decreasing evaporator flow but never exceeded fifteen minutes. This delay was due to the large volume of piping in the evaporator circuit.

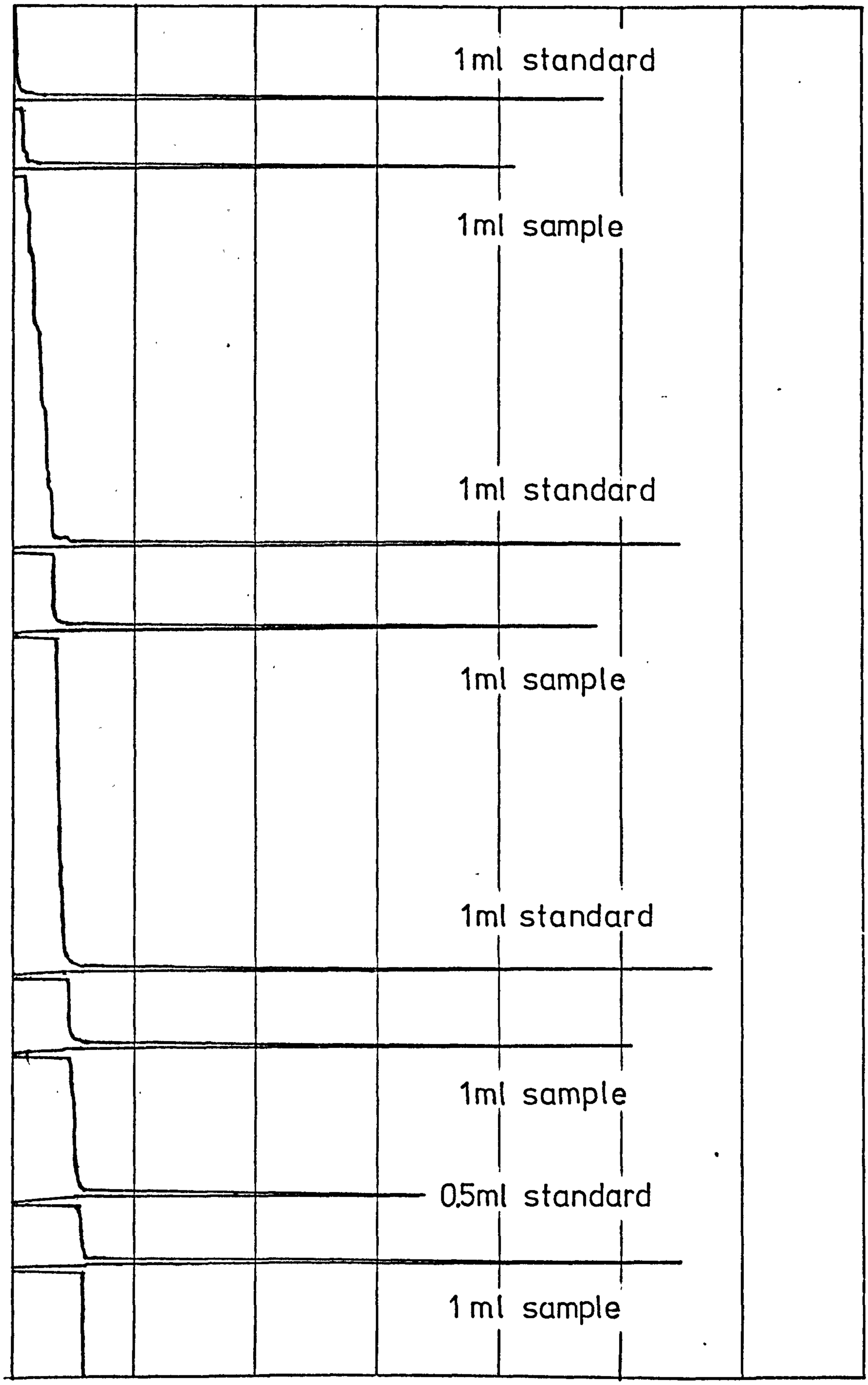
The chromatagraph was run using a lower bridge current and a higher carrier gas flow rate than for the recommended optimum values, to lower the

operating temperature of the thermistors in the detector, and avoid the possible decomposition of carbonyl in the detector.

The sensitivity of the chromatagraph dropped with experimental time due partly to the slight rise in temperature within the glove box and also as a function of the total quantity of carbonyl injected. An example of the chromatagrams produced is given in fig (8.8), showing the gradual fall off in sensitivity over just twelve minutes. The difference in peak heights between the sample and standard is due to the difference in temperature between the standard and evaporator gas giving a higher concentration of carbonyl in the former.

8.1.2 Analysis of the Deposit Shape

It had been hoped to profile the nickel deposits with a mechanical gauge to measure, not only the stagnation point deposition rate, but also the effect on deposit shape of varying experimental conditions, so that the nickel deposits could be better compared with the cobalt oxide deposits previously produced. Unfortunately, the deposits produced in the area of special interest, the mass transfer zone, were friable and powdery, any mechanical contact changed their shape appreciably. The only successful method that could be applied was microscopy, whereby a travelling microscope was focussed on the centre of the deposit and refocussed, using a calibrated, graduated height adjustment, away from the centre. As the deposit was highly localised, as in the CoO depositions, the error introduced by ignoring the deposition well away from the stagnation point is negligible, compared with the reproducability of the method itself. The latter was averaged for one particular deposit to give an estimated error of $\pm$ 2% on large deposits but much more on the smaller deposits produced in the chemical control zone.



fig(8.8) CHROMATAGRAM FOR CARBONYL ANALYSIS DURING AN EXPERIMENT

8.1.3 Calculation of the Sherwood Number

The Sherwood number is calculated in the same manner as previously from the definition:

$$Sh_o = \frac{t_o \text{ (Density of Ni) } d}{s \text{ (Conc. of Ni in gas at jet) } D_{Ni(CO)_4/N_2}} \quad \ldots\ldots (8.1)$$

Allowance is made in the concentration term for the increase of gas temperature from jet to substrate and, as before, a film temperature is taken as the significant value. The diffusion coefficient is calculated in Appendix (1). Equation (8.1) by substituting relevant values becomes:

$$Sh_o = \frac{t_o}{s} \; 262.2 \quad \ldots\ldots\ldots (8.2)$$

with no allowance for concentration depletion due to entrainment. Using a value for the recirculated concentration of 0.4 jet exit value produces a factor of 0.576 calculated in Appendix (2) for a jet/plate distance of 15.1d which was that used for the mass transfer correlation. Tabulated data and data derived using these parameters is contained in Appendix (4).

The Schmidt number calculated for the system from film temperature data was 2.1.5.

8.1.4 Summary of Safety Precautions

(1) All apparatus containing carbonyl liquid or vapour was contained in an extracted glove box. The box could be isolated completely. A manometer indicated the running of the extraction system and a emergency fan was installed in case of the failure of the system.

(2) All exit gas from the glove box was heated to a temperature well above the decomposition temperature for carbonyl.

(3) Exit gases from the deposition chamber were similarly heated.

(4) Detection flames were left burning inside and outside the glove box, always near the ground as carbonyl vapour is much heavier than air.

(5) Safety notices and a warning light were used to keep all but those immediately concerned with the apparatus from the room containing it.

(6) Gas and electric heaters were deliberately used in case of the failure of one or other service.

(7) A complete compressed air breathing apparatus was worn at all times during the operation of the apparatus.

(8) An oxygen cylinder was kept in the room as a first measure should any vapour have been inhaled.

(9) Supplies of tablets to counteract the effects of carbonyl poisoning were kept in the college medical centre.

(10) Bromine water and liquid bromine were used extensively to destroy any possible leaks of carbonyl into the environment.

8.2 Experimental Results

Tabulated results in terms of the stagnation point values are contained in Appendix (4).

8.2.1 The Boudouard Reaction

Deposits made at 250°C and 300°C were analysed for carbon content, by X-ray analysis for the presence of a carbide, and chemical analysis for the presence of primary or combined carbon, by ignition and testing for CO_2. No carbon was detected and its effects were therefore ignored in future work.

8.2.2 Arhenius Plot

Deposits were made and analysed in the range 113°C to 225°C. The rate of change of reaction rate as the temperature varied was very large between 113°C and 175°C, fig (8.9), but this tailed off markedly above 175°C. The 'activation energy' calculated for the first region was 14 k cal per mole. The deposits made above 175°C were increasingly powdery in nature and results at temperatures above 225°C were not recorded because the open sponge-like structure of the deposits greatly increased the apparent thickness of nickel deposited.

Reproducability between two deposits at 200°C was 6.1% but the scatter increased markedly in the lower temperature depositions as temperature measurement and control became critical.

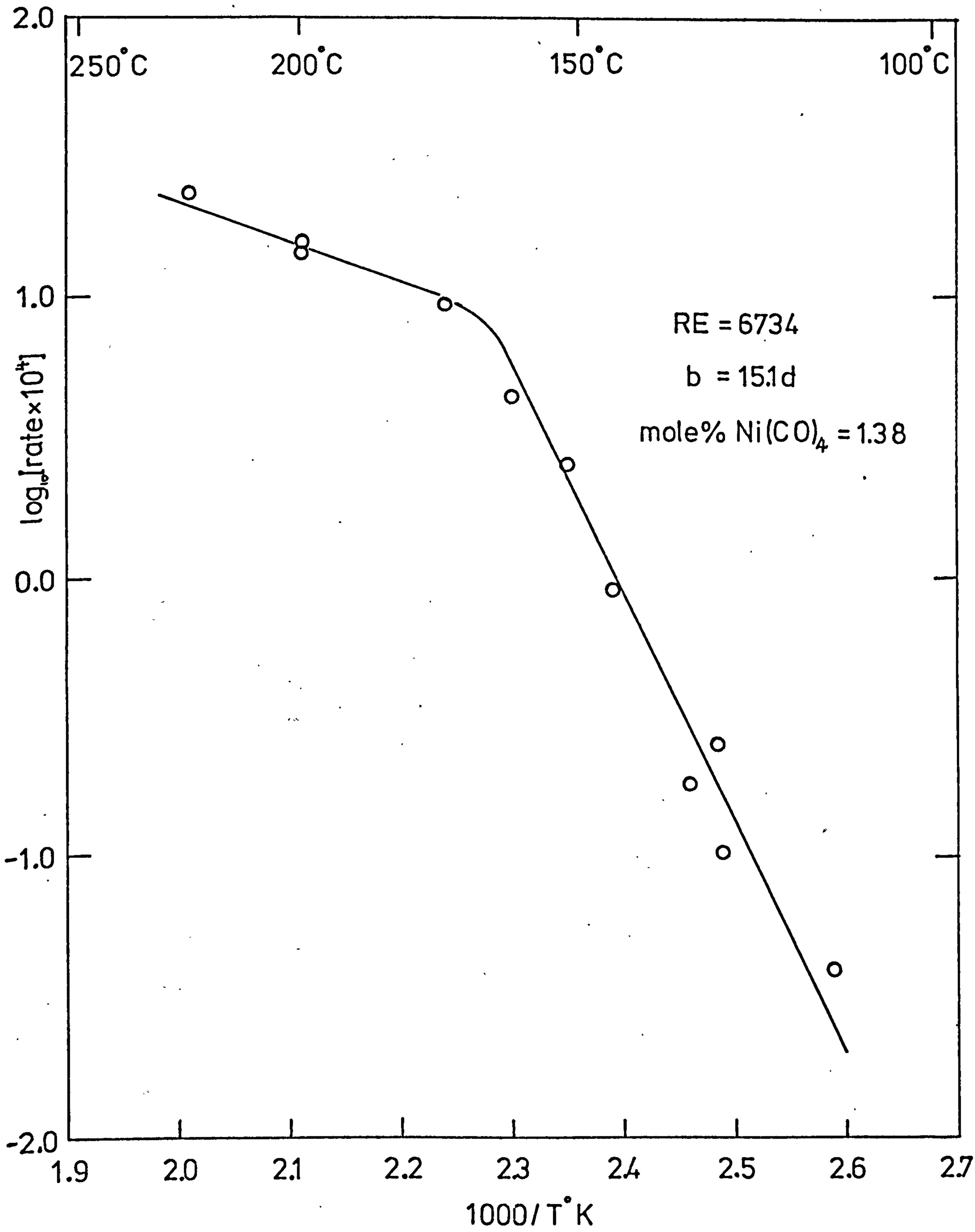
The calculation of an 'activation energy' for the higher temperature depositions was not attempted as the slope of -0.75 predicted in chapter 5 is only indicative of the order of magnitude expected. The experimental line is also subject to a large error because of the open structures produced in this region. It can be seen, however, that the reaction rate is comparatively insensitive to temperature above 175°C.

8.2.3 Order of Reaction

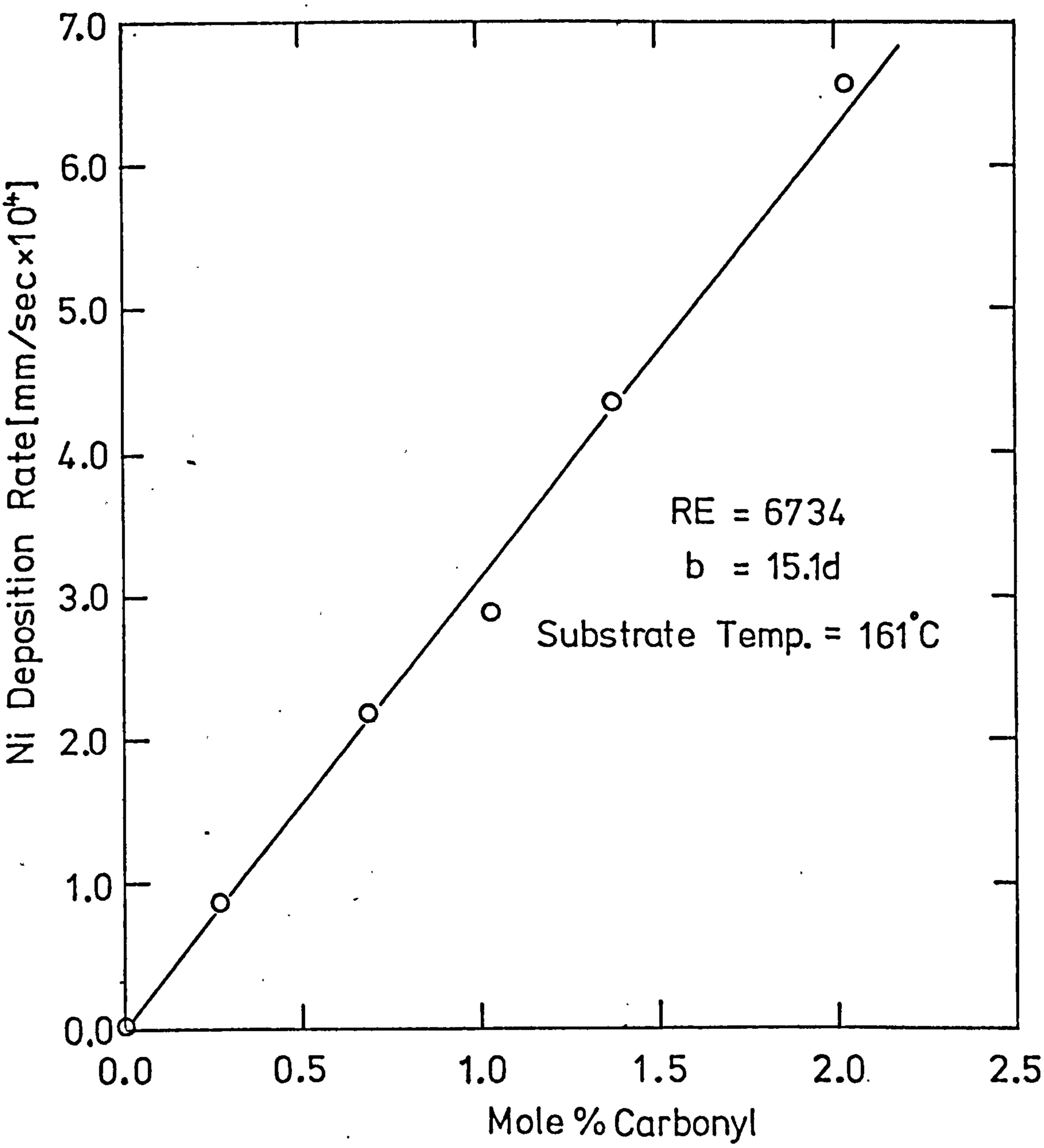
Altering the carbonyl concentration for constant Re and d/b at 161°C produced a linear relationship, fig (8.10), with reaction rate suggesting a first order type reaction in this region. The effect of recycled carbonyl is ignored as it will be similar for each experiment.

8.2.4 Effect of Reynolds Number Variation

For depositions made at 200°C, increasing the Reynolds number was found to significantly increase the mass transfer rate. No such corresponding



fig(8.9) ARHENIUS PLOT FOR NICKEL CARBONYL DECOMPOSITION



fig(8.10) RATE OF NICKEL DEPOSITION FOR VARYING CARBONYL CONCENTRATION

effect was found in depositions made at 161°C. Results are plotted in fig (8.11).

8.2.5 Fall off in Reaction Rate with Time

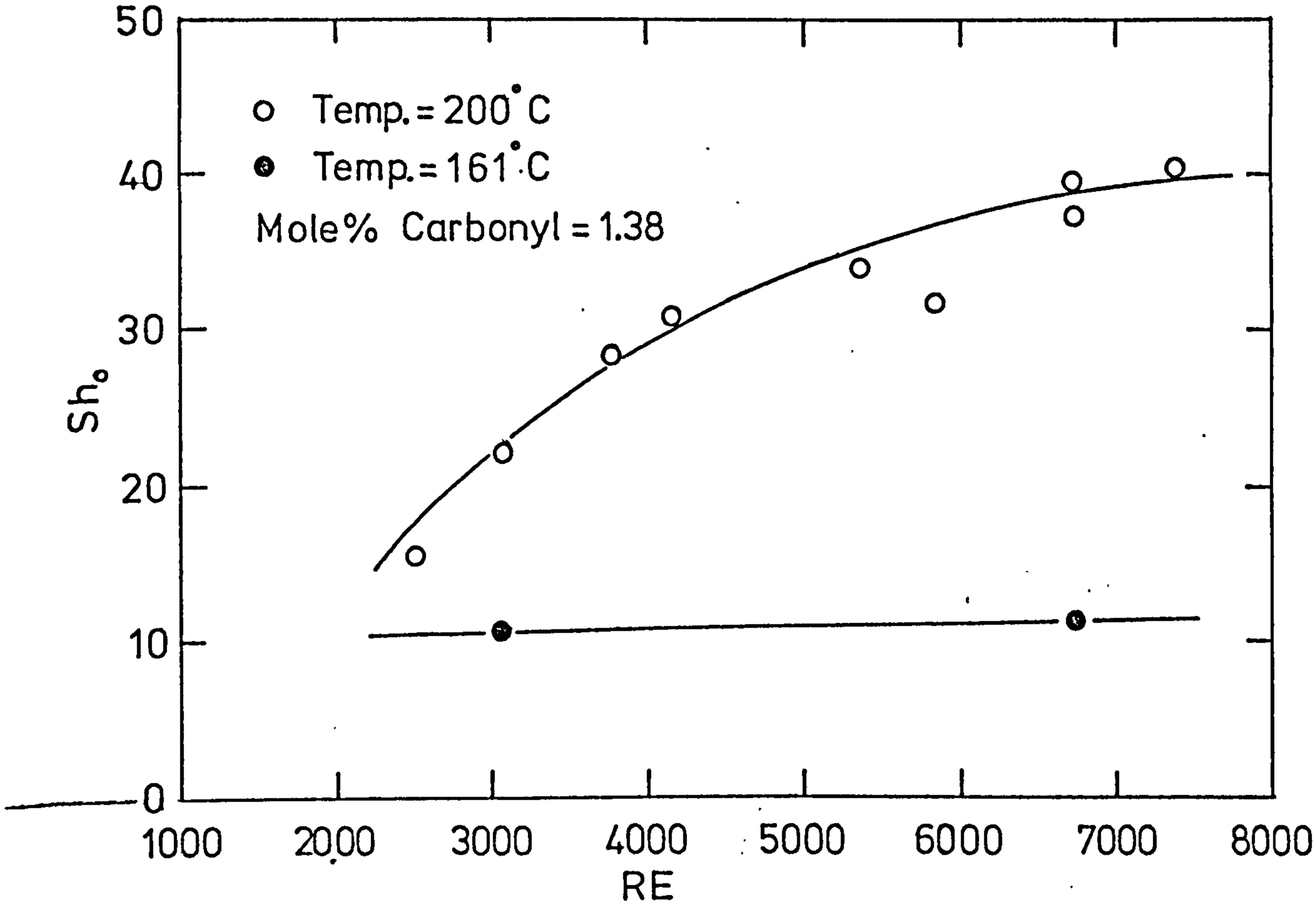
Fig (8.12) shows how at 161°C depositions made at constant experimental conditions showed a marked decline in deposition rate with total experimental time. Such an effect was not noted in depositions at 200°C.

8.2.6 Effect of Jet/Plate Distance

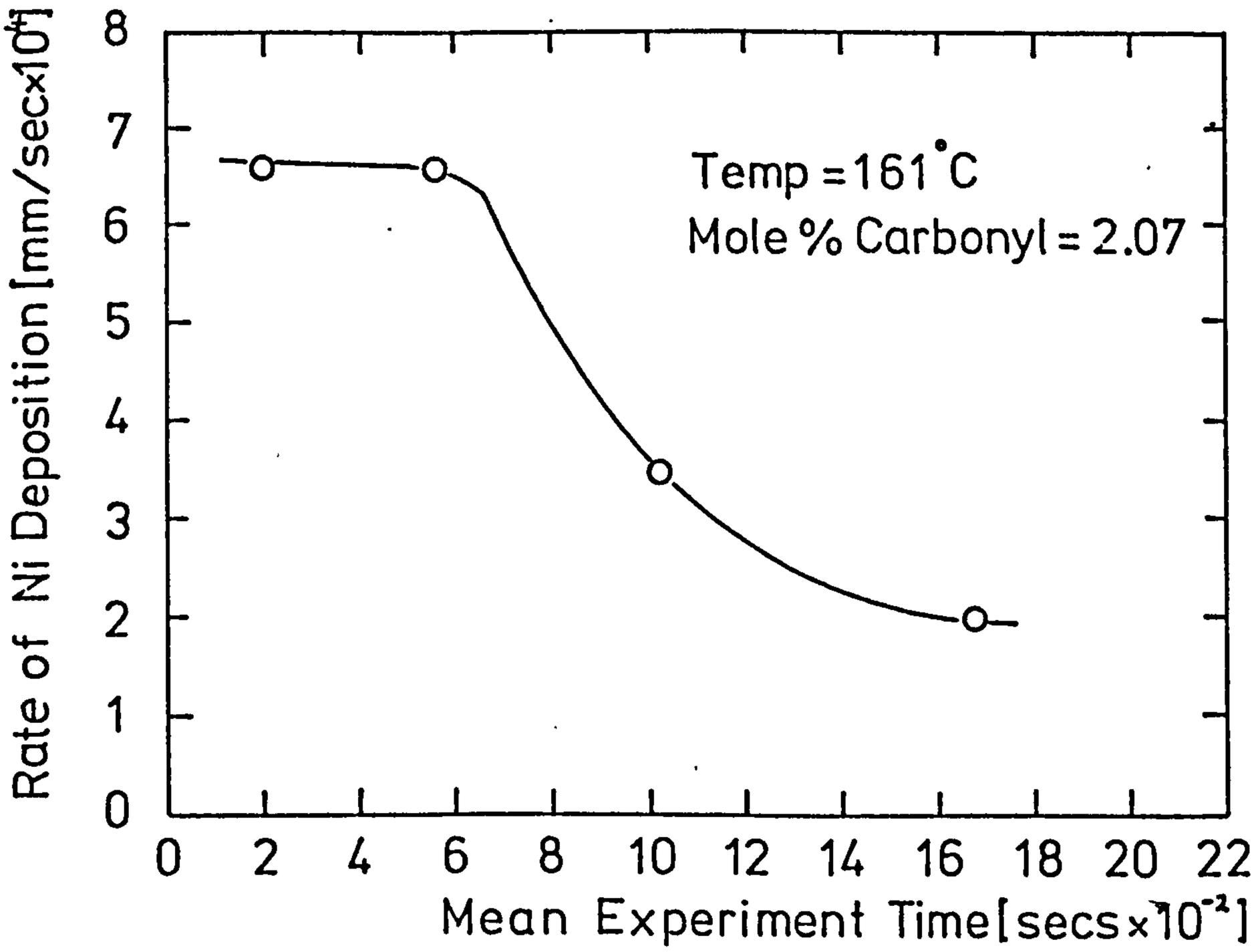
Varying the d/b ratio in runs at 200°C produced a marked effect on deposition rate. The variation produced does not follow a simple relationship, fig (8.13), of Sh $\propto$ d/b, or d^2/b^2, as in the CoO deposition experiments. The effect is discussed in Appendix (2) of the jet entraining a carbonyl containing gas of lower concentration than that in the nozzle exit. Assuming an environment concentration of 40% jet exit value a theoretical line is drawn in fig (8.13) through the mid-point of the two experimental results at d/b = 6.62×10^{-2}. For comparison, the line for a Sh $\propto$ d/b relationship is included.

8.2.7 Thermal Effects

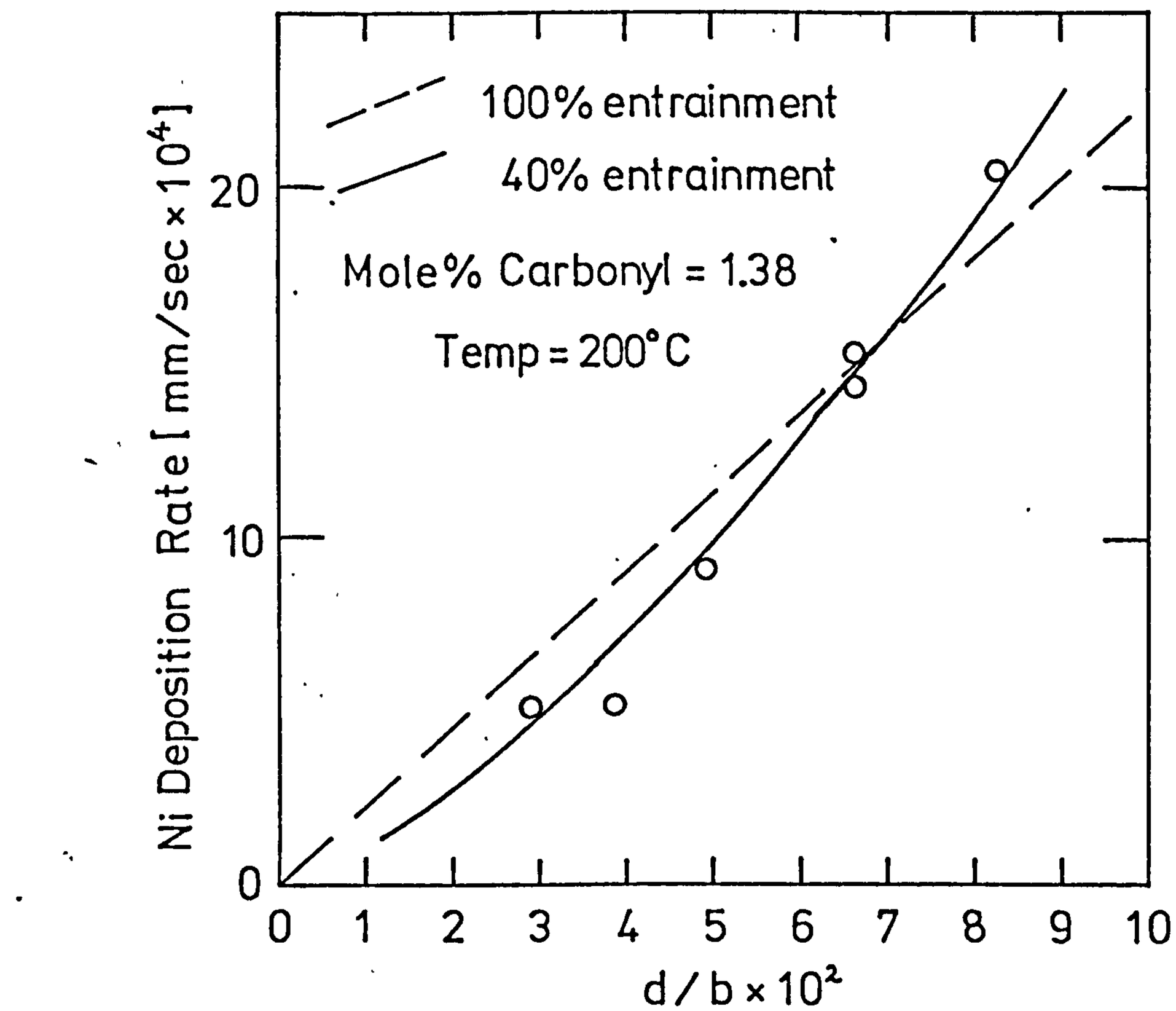
Following the analysis of possible thermal effects on initial deposition rate for the CoO deposition, which found negligible effects with deposit times of the order of seconds, no similar analysis was thought necessary for Nickel deposition experiments which were of the order of minutes. However, at a substrate temperature of 151°C, deposits made at a Reynolds number of 6734 and b/d = 9.1 exhibited a different shape to those mounds produced at higher b/d ratios. The deposit for the former runs exhibited a dip in the centre.



fig(8.11) EFFECT OF REYNOLDS NUMBER ON DEPOSITION RATE



fig(8.12) DECAY IN REACTION RATE WITH TIME



fig(8.13) EFFECT OF JET/PLATE DISTANCE ON DEPOSITION RATE

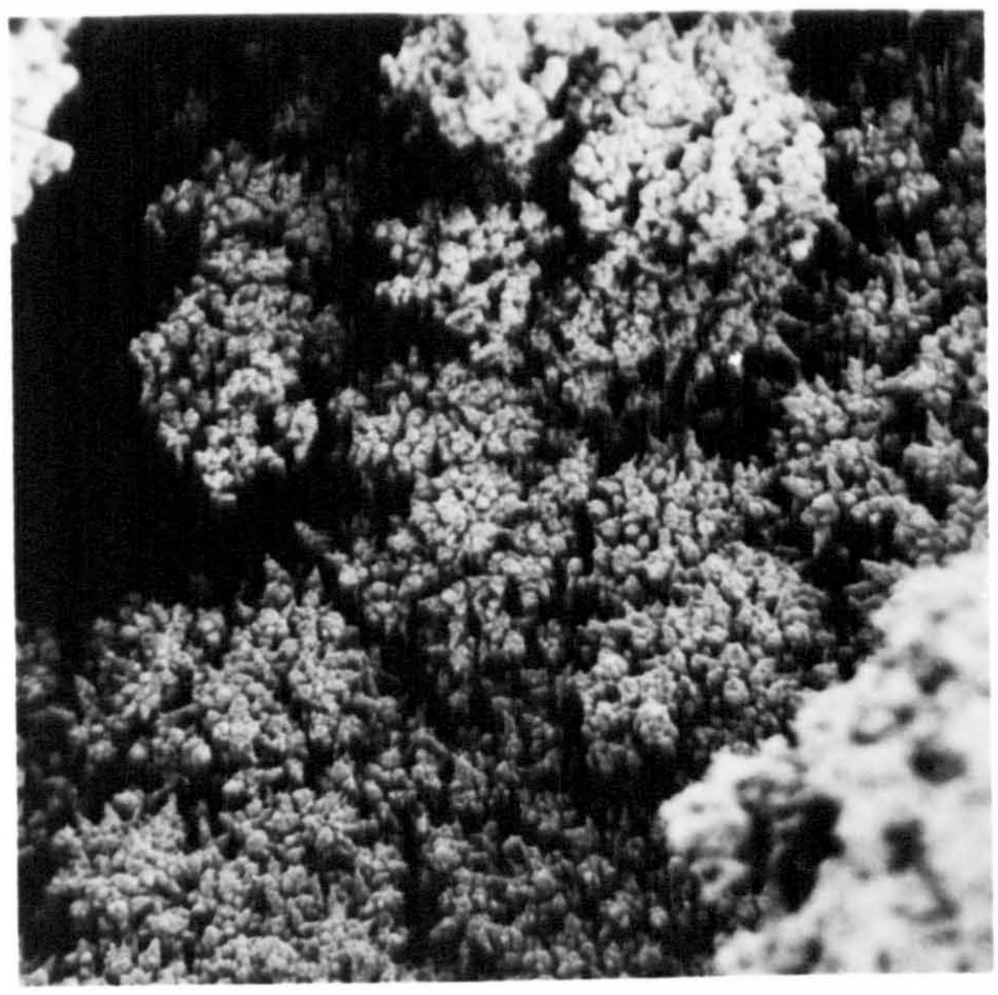
8.2.8 The Nature of the Deposits

At no substrate temperature employed in the present series of experiments was a completely shiny nickel deposit produced. At the lowest temperatures ($< 130^{o}C$) investigated the nickel deposited away from the stagnation point was bright but the centres were always more uneven and dull in colour, although at these temperatures the deposits were fully adherent to the copper substrate and would take a mechanical polish. The central dull region grew relatively larger the higher the substrate temperature until above $160^{o}C$ the deposits became much less adherent to the substrate and much more open in microstructure. Above $175^{o}C$, the deposits consisted of a friable blackish powdery deposit, until at temperatures in excess of $250^{o}C$ a sponge like deposit was formed.

The chemical environment inside the chamber was varied in an attempt to suppress the powdery nature of the high temperature deposits. High water vapour content of the chamber atmosphere, CO_2 and H_2 additions to the carrier gas had no effect on the nature of the deposits. The structure was found to be insensitive to anything but temperature variation.

Scanning electron microscope pictures of deposits typical of different temperature ranges are shown in figs (8.14) to (8.18). These deposits were, of necessity, made on thin copper discs laid on top of the thicker copper substrate. Because of this the relevant deposition temperatures are not precisely known. Examination under an optical microscope enabled a rough classification to be made by comparison with experiments made on the thicker substrate whose deposition temperature was then known. Samples of powder from depositions at 200^{o} and $250^{o}C$ were removed from the thicker substrate and examined.

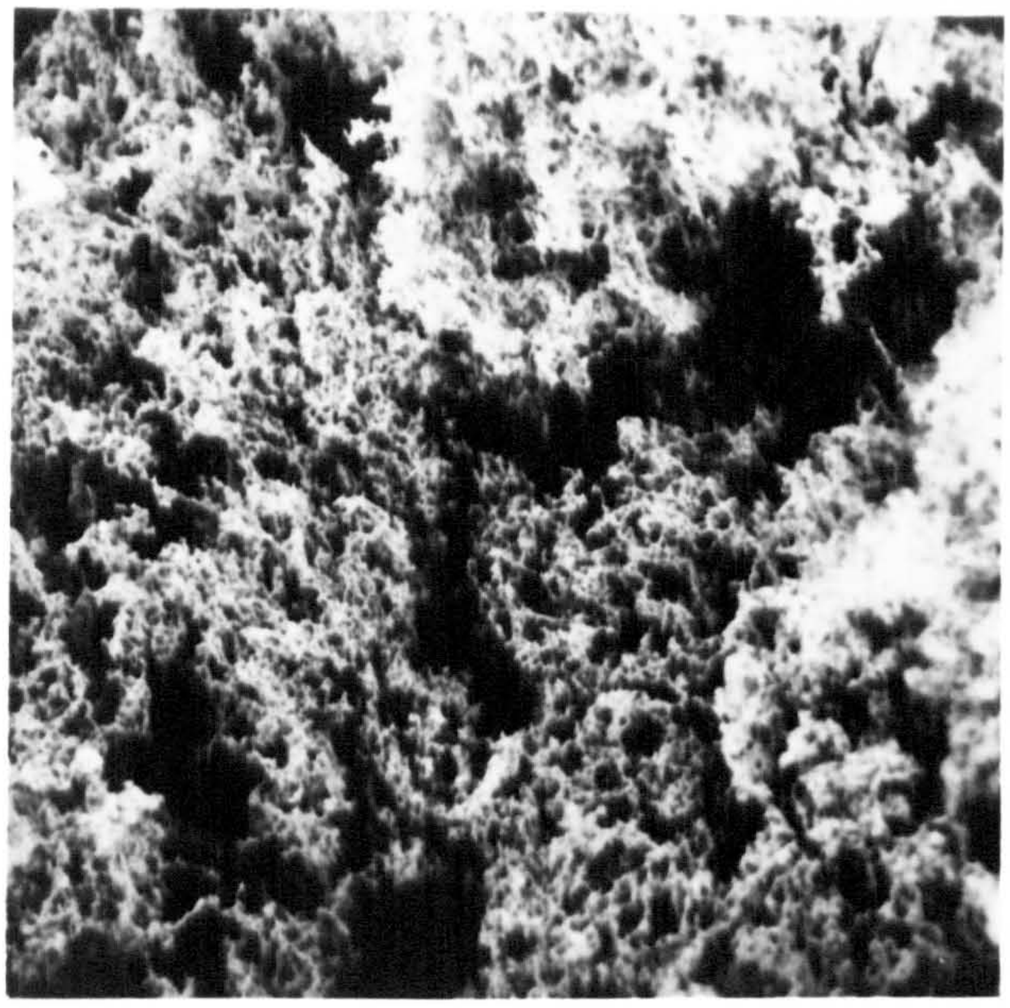
The photography shows the open, often markedly crystalline, growths that are typical of the high temperature regions, 200 - $250^{o}C$, figs (8.14), (8.15) and how this structure becomes even more open at higher temperatures, fig (8.16).



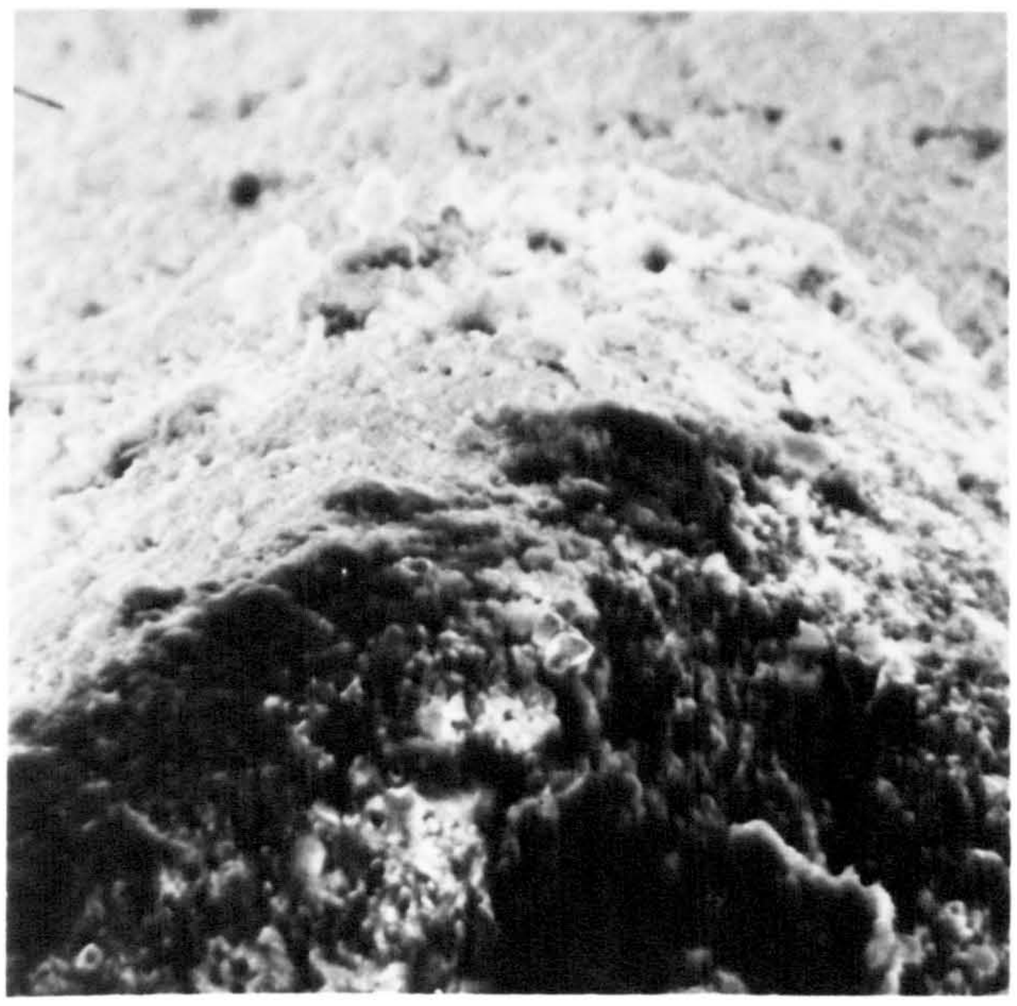
fig(8.14) TYPICAL NICKEL STRUCTURE OF DEPOSITS FROM 200-250°C × 2200

fig(8.15) DETAIL OF NICKEL DEPOSIT 200-250°C × 22000

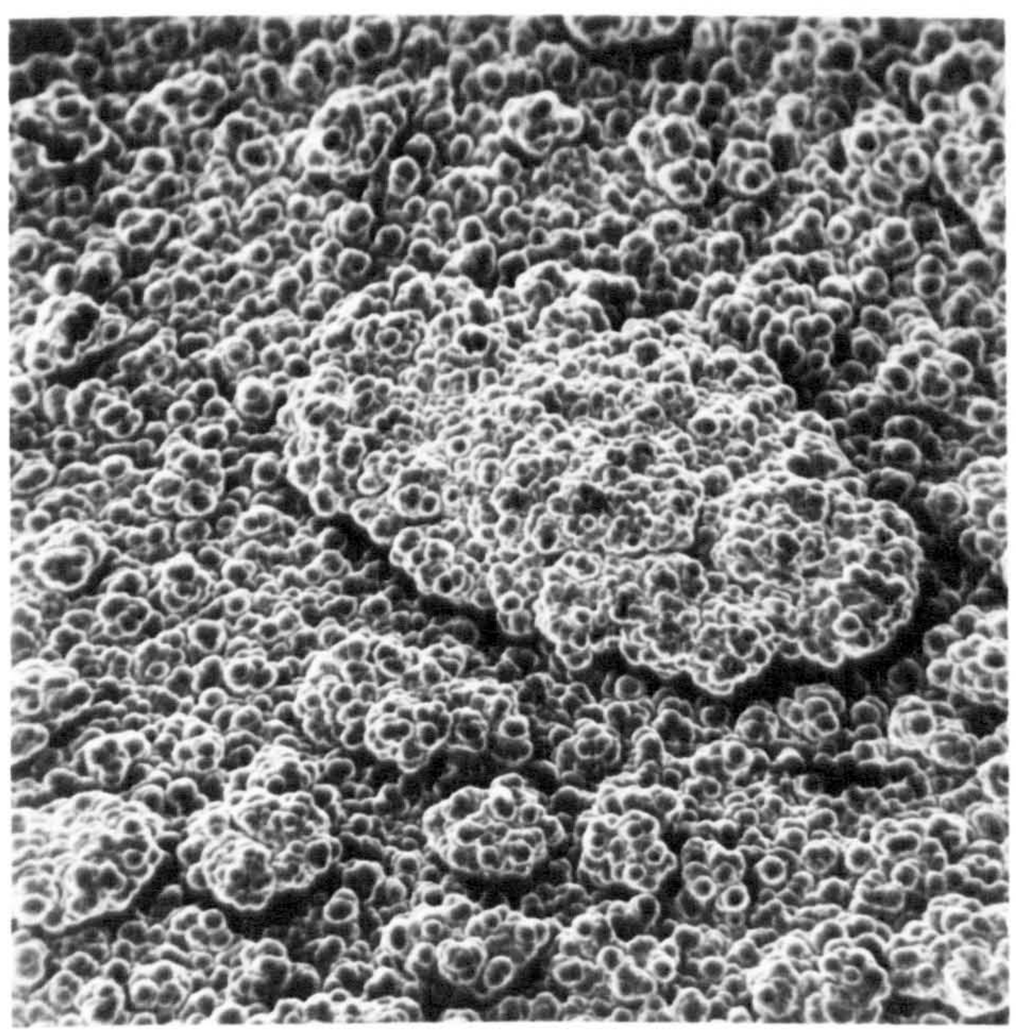




fig(8.16) TYPICAL NICKEL STRUCTURE OF DEPOSITS FROM 250 - 300°C x 2550



fig(8.17) CENTRAL PEAK OF A NICKEL DEPOSIT IN THE UPPER CHEMICAL CONTROL REGION 150-170°C x 890



fig(8.18) BRIGHT NICKEL DEPOSIT FROM THE LOWER CHEMICAL CONTROL REGION < 130°C x 450

A highly localised deposit from the region 150° - 170°C is shown in fig (8.17), and a deposit which appears shiny to the eye from the lowest temperatures used in fig (8.18). Even in the latter case the surface relief is considerably greater than that found in the cobalt oxide deposits.

A sample of nickel was stripped from the thicker substrate and mounted and sectioned to examine any visible microstructures. No structure or significant voids could be seen in the unetched state and etching with recommended reagents including HNO_3 - Acetic and Ferric Chloride did not reveal any microstructure. Electroetching in dilute HNO_3 - Acetic was similarly unsuccessful. Nickel is, however, a difficult substance to etch especially when pure.

As discussed in section (8.1.2), the depositions, in the region of most interst, could not be profiled. Visual examination showed that the deposits were similarly localised as in the CoO depositions.

8.3 Discussion of Experimental Results

8.3.1 Chemical and Mass Transfer Control Regions

The Arhenius, log Rate versus 1/T curve, fig (8.9), suggests a chemically controlled region for carbonyl decomposition, in this system, up to about 175°C, with a mass transfer control zone above this temperature. As the deposits in the proposed mass transfer zone are not well produced, being powdery and highly crystalline as shown by figs (8.14) and (8.15), more evidence was produced in this series of experiments to identify the two regions than in the CoO depositions. The temperature dependence of the depositions above 175°C is slightly higher than that expected, but this is explained by the assumption in the measuring technique of 100% density of the nickel deposits. The structure of these deposits was very open and

increasing the temperature produced successively more open structures as shown in fig (8.16).

The deposition rate in the high temperature region is a significant function of the fluid mechanics of the system, the Reynolds number, fig (8.11), and the jet/plate distance, fig (8.13). The deposition rate in the proposed chemical region is not a function of Reynolds number. This is what would be expected from mass transfer and chemical control regions respectively. In the lower temperature region, the reaction rate falls off with time as shown by fig (8.12), this is not found in the higher temperature region. Carlton and Oxley (1967) have demonstrated the effect of CO concentration on Nickel deposition rates at temperatures above those affected by thermodynamic restraints, and it is the entrainment of CO, produced in the carbonyl decomposition and recycled inside the deposition chamber, by the jet that is thought to account for the effect in fig (8.12). This is a chemical effect and would only be expected to affect a chemical control region.

The chemical control region is further identified from the activation energy calculated at 14 k cals per mole which is in the same range as the published data. Mass transfer theoretical correlation with the data in fig (8.11) is given in chapter nine, where the rate is shown to be predicted by mass transfer theory.

All this evidence leads to the postulation of a mass transfer control region above 175^{o}C and a chemical region below this temperature. As the order of reaction is shown in fig (8.10) to be first order, the system will behave as predicted by the relevant section in chapter five.

8.3.2 Order of Reaction

For the variation of carbonyl concentration investigated during these experiments a first order reaction mechanism best describes the decomposition

reaction. This agrees with many of the workers cited by Carlton and Oxley (1967) but is not necessarily at variance with the latter's second order model because of the relatively narrow range of compositions studied in this series of experiments.

8.3.3 Thermal Effects

The deposition rate is highly sensitive to temperature in the chemical control region. This not only gives problems in controlling the reproducability of experiments but it is also instrumental in producing a difference in shape in deposits performed where the rate of conduction of heat within the substrate is too slow to even out a small temperature profile in the substrate. When deposits are made producing a considerable thickness of nickel, the nickel acts as its own substrate and, as this metal has a thermal conductivity only one fifth that of copper, thermal effects can be critical. The effect is not noted in the cobalt oxide experiments. Although the conductivity of CoO, estimated from values of similar oxides, is about 2% that of nickel, the deposit thicknesses are of a totally different order. Cobalt oxide deposit thicknesses range up to 6×10^{-4} mm but nickel deposits are about 1 mm thick.

The thermal load on the substrate will follow the heat transfer profile under the impinging jet, tending to counteract the mass transfer profile, to flatten the deposit, or, as in the particular experiments discussed, to produce a dip at the deposit centre instead of a peak.

8.3.4 Nature of the Deposits

The powdery deposits produced in the mass transfer zone are of little use for plating purposes. A very low substrate temperature is needed to produce a useful film. The structure in the wall jet region was better, producing good films of nickel, and this points to the possibility that the

nature of the structure depends on the deposition rate rather than the rate controlling mechanism itself. The concentration of carbonyl could not be altered controllably to check on this. Very low concentrations might be expected to produce good films at any temperature.

8.3.5 Prediction of Varying the System

As the deposition rate was found to follow a first order reaction type in the chemical control zone, concentration variation will not alter the temperature, for a given Reynolds number, at which the mass transfer process becomes rate limiting. There is the possibility that the rate could change to second order at higher concentrations, which would lower the changeover temperature at higher concentrations. Data derived from the present experiments can then be applied to any impinging jet system, at the stagnation point, with the reservations on a possible order of reaction change and any thermal effects similar to those discussed in section (8.3.3).

Application to a system of different geometry is more complex and depends on any comparison that can be made of the fluid mechanics. Carlton and Oxley (1967) found a similar change over temperature of about 175°C for their work on deposition onto heated wires in cross flow.

8.4 Conclusions

(1) Nickel deposition from the tetracarbonyl in the impinging jet system is chemically controlled up to a temperature of 175°C for Reynolds numbers up to 6734. Above this temperature, the rate controlling step is mass transfer.

(2) The chemical reaction:

$$Ni(CO)_4 = Ni + 4CO$$

procedes as a first order reaction, with respect to the concentration

of carbonyl, for concentrations of carbonyl between 0.276 and 2.07 mole per cent in a nitrogen carrier gas. The activation energy for the reaction is about 14 k cals per gram mole.

(3) The impinging jet system is not suitable for the deposition of bright coherent nickel films from the carbonyl in the range of carbonyl concentrations studied, excepting depositions at low temperatures in the range 110° to 130°C which may even then need further polishing.

CHAPTER NINE

CORRELATION OF MASS TRANSFER EFFECTS

9.0 CORRELATION OF MASS TRANSFER EFFECTS

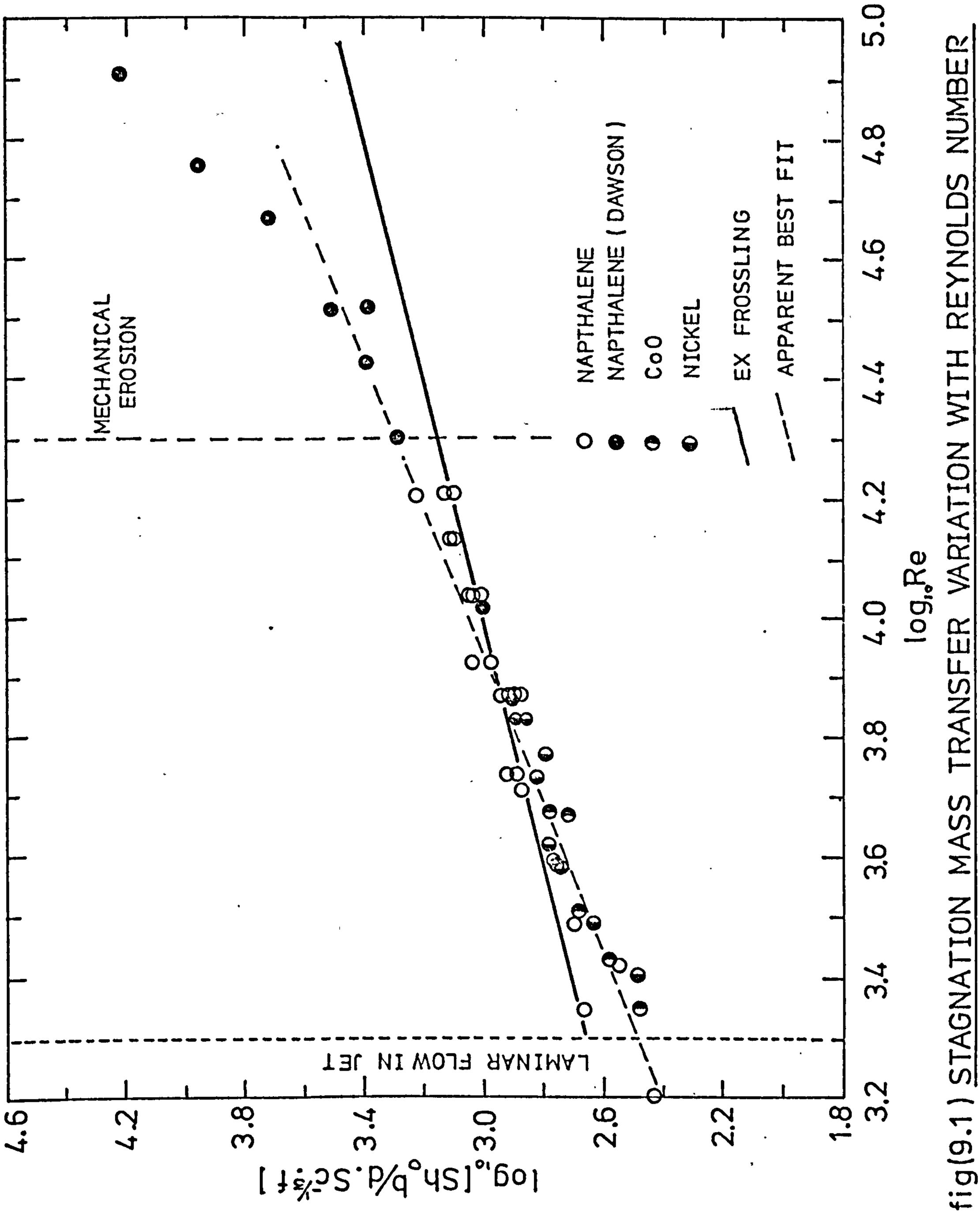
In this concluding chapter the relevant mass transfer work from chapters four, seven and eight is compared and the contributions of the present work to the understanding of mass transfer in the impinging jet are summarised.

9.1 Stagnation Point Mass Transfer

The three systems are most usefully compared by the stagnation point mass transfer rates. Fig (4.2.1) correlated the stagnation point mass transfer for napthalene erosion by an air jet for the present work and included the data of Dawson and Trass (1966). The data in this figure is reproduced in fig (9.1) together with the data for cobalt oxide and nickel deposition in the regions identified as being mass transfer rate controlling. The theoretical line from the most successful stagnation point model, that from the extension of Frossling's laminar solution is also shown. Allowance is made in the correlation of the vapour deposition data for the fall in reactant concentration due to entrainment by the inclusion of the factor f as discussed in Appendix (2). This is equal to b/d for the CoO experiments.

The data from the vapour deposition experiments correlates well with that for napthalene, tending to give slightly lower mass transfer rates. The difference can be explained by the error in calculating the diffusion coefficient. The two methods used to calculate the diffusion coefficient of CoAcAt in hydrogen give values 15% either side of their mean. The methods in themselves are not highly accurate and the data from which the calculation was made probably contain considerable error. In all, an estimated error for the diffusion coefficient of $\pm$ 30% is envisaged.

For a given system, the x axis group in figure (9.1) is given by an equation which depends on D_{AB} for other variables held constant as for:



fig(9.1) STAGNATION MASS TRANSFER VARIATION WITH REYNOLDS NUMBER

$$x = A\, D_{AB}^{2/3} \qquad \ldots\ldots\ldots (9.1)$$

where A is a constant. Differentiating:

$$\delta x = 2/3\, D_{AB}^{-1/3}\ A\ D_{AB} \qquad \ldots\ldots\ldots (9.2)$$

If δD_{AB}, the error in D_{AB}, is $\pm$ 30% D_{AB}:

$$\delta D_{AB} = 0.30\, D_{AB} \qquad \ldots\ldots\ldots (9.3)$$

Substituting:

$$\delta x = \pm 2/3\, D_{AB}^{2/3}\, 0.3A \qquad \ldots\ldots\ldots (9.4)$$

or,

$$\delta x = \pm 0.2\, A\, D_{AB}^{2/3} \qquad \ldots\ldots\ldots (9.5)$$

Therefore:

$$x = D_{AB}^{2/3}\, A \pm 0.2\, D_{AB}^{2/3} \qquad \ldots\ldots\ldots (9.6)$$

Giving the two cases:

$$x = 1.2\, D_{AB}^{2/3}\, A \text{ or } 0.8\, D_{AB}^{2/3}\, A \qquad \ldots\ldots\ldots (9.7)$$

Taking logs:

$$\log x = \log 1.2 + \log D_{AB}^{2/3}\, A \qquad \ldots\ldots\ldots (9.8)$$

$$\text{or } \log 0.8 + \log D_{AB}^{2/3}\, A$$

giving errors on the x axis log scale of +0.08 or -0.1. This type of scatter can bring the data onto the same line of best fit.

It has already been discussed in chapter four how a gradual decay in mass transfer would be expected near the laminar-turbulent transition region in the pipe jet. The vapour deposition data does tend to decay at a higher Reynolds number than that of the napthalene. This is understandable as the

critical Reynolds number in pipe flow is not a well defined constant, laminar flow can persist to much higher Reynolds numbers than the 2,100 value assumed earlier. The actual critical value will depend a lot on the roughness in the pipe, and whether the jet was subject to any vibration. The critical value will then dominate the level of turbulence in the free jet. This, it was argued in chapter three, can be the dominant effect on mass transfer rates.

The theory from the extension of Frossling's laminar solution predicts the mass transfer rates acceptably in the range $4,000 \leqslant Re \leqslant 16,000$ and the success of the analysis in this region indicates that the stagnation point region is dominated by laminar effects. It must be acknowledged that the data in fig (9.1) would be better fitted by a line of higher slope, like the one suggested which corresponds to:

$$Sh_o \, {}^{b}/_{d} \, f = 5.7 \, Re^{0.52} \, Sc^{1/3} \quad \ldots\ldots\ldots\ldots (9.9)$$

It is felt, however, that the fall off below Re = 4,000 is predictable from the flow conditions in the jet and that the higher Reynolds number mass transfer rates are elevated by the effects of supersonic or underexpanded jets and, in the case of the napthalene work, mechanical erosion. The equation (2.39) is then recommended for $Re \geqslant 4,000$ in pipe jets:

$$Sh_o \, {}^{b}/_{d} \, f = 10.0 \, Re^{0.5} \, Sc^{1/3} \quad \ldots\ldots\ldots\ldots (9.10)$$

and the equation (9.9) for $2,100 \leqslant Re \leqslant 4,000$ to accommodate the effect of transition flow.

The relevant equations in the literature tend on the whole to give higher exponents than 0.5 on the Reynolds number for stagnation point mass or heat transfer. Only Gardon and Cobonpue's (1961) data indicates this type of dependency. Rao and Trass (1964) found an exponent as high as 1.0 fitted their cinnamic acid erosion data, but these experiments were subject to a high contribution from the effects of mechanical erosion.

9.2 The Radial Mass Transfer Profile

The possibility that a convenient dimensionless mass transfer radial profile could be found for the impinging jet system has been discussed at

various stages in the preceding chapters. A similar scatter diagram to that obtained for heat transfer by Gardon and Cobonpue (1961) was produced for the napthalene work and compared with this heat transfer profile in fig (4.19). The mid-point of the mass transfer profile was used with moderate success in chapter seven to predict the radial profile for a vapour deposition system, in fig (7.19), demonstrating its use despite the considerable scatter. The scatter in a correlation of Sh/Sh_o vs. R/b can be understood by examining the governing equations for the stagnation point and the wall jet mass transfer rates. At the stagnation point, equation (9.10) has been found to describe the rate with an expression of the type:

$$Sh_o = K_1 Re^{0.5} d/_b \quad \ldots\ldots\ldots\ldots (9.11)$$

In the wall jet equations of the type:

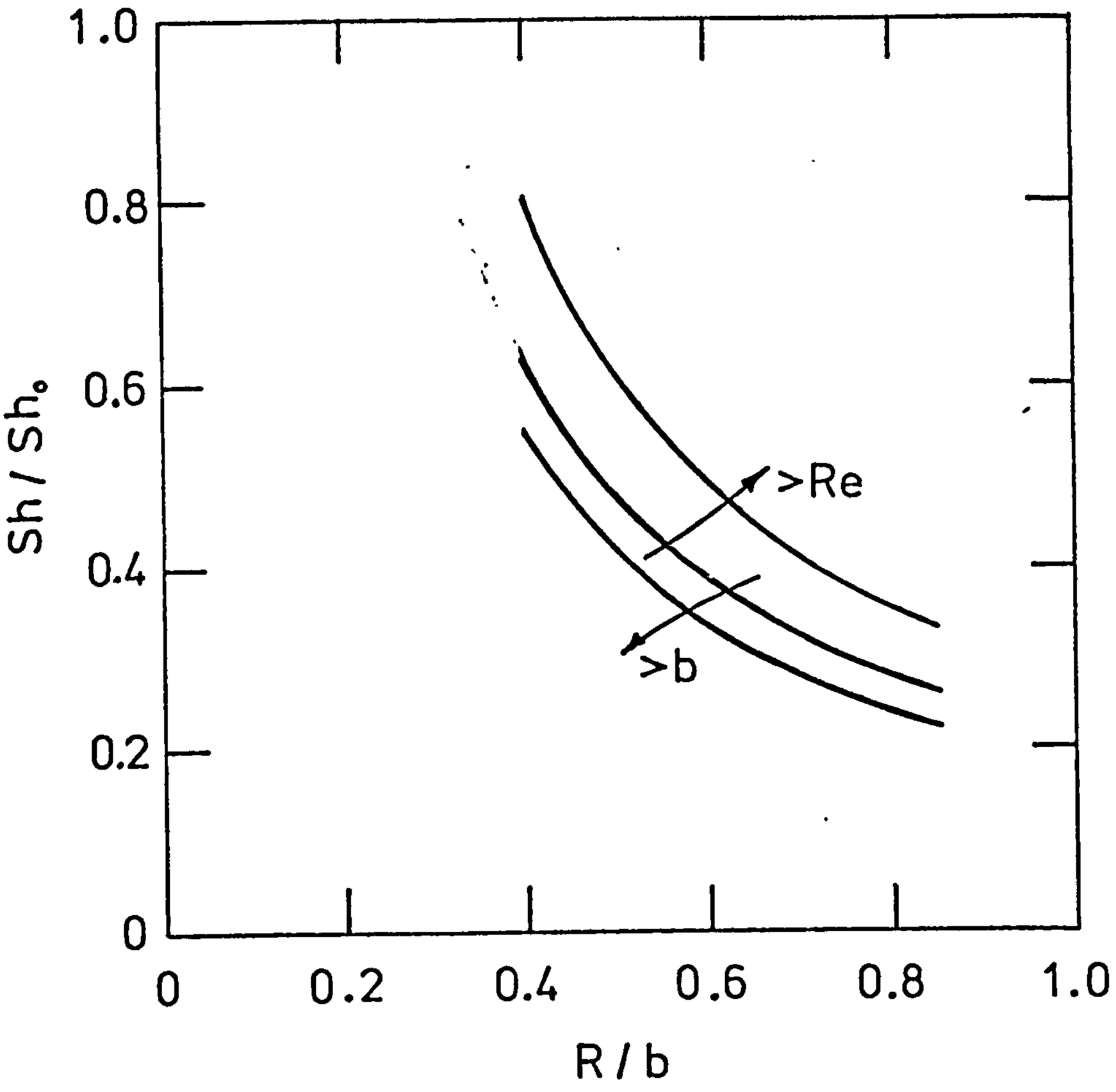
$$Sh = K_2 Re^{0.8} (d/_R)^{1.17} \quad \ldots\ldots\ldots (9.12)$$

describe the rate, giving an expression for the type of profile plotted in fig (4.19) of the form:

$$\frac{Sh}{Sh_o} = K_3 Re^{0.3} \frac{b}{R} \left(\frac{d}{R}\right)^{0.17} \quad \ldots\ldots (9.13)$$

with the two terms, $Re^{0.3}$ and $(d/_R)^{0.17}$ marring the correlation.

The effect of doubling the Reynolds number and the jet plate distance is shown in fig (9.2) indicating how the scatter can occur. For a rough calculation of the local radial heat or mass transfer rates the dimensionless profiles of fig (4.19) are useful, but precise calculations must be made from the wall jet equation (3.107). Work on the fluid mechanics of the system indicates that the wall jet can be considered to start at about R/b = 0.3. The mass transfer correlations predict the wall jet mass transfer data further away from the stagnation point from about R/b = 0.4 and it is from this position that equation (3.107) is recommended. The Dawson and Trass relationship



fig(9.2) ANALYSIS OF SCATTER IN THE DIMENSIONLESS MASS TRANSFER PROFILE

derived for the air/napthalene system, equation (3.108), is directly comparable with equation (3.107) apart from the complex constant term which is highly dependent on the boundary layer profile exponent, x, and the more complex Reynolds number relationship with the Sherwood number. Rewriting equation (3.107) in terms of Sh:

$$Sh = 0.0524 \frac{\rho}{\rho - \rho_{Ao}} \left[\frac{(x+1)(x+2)}{x}\right]^{0.846} \int\Delta \, Re^{0.846} \, Sc^{-1} \, \frac{d}{R}^{1.172} \quad \ldots (9.14)$$

The $\frac{\rho}{\rho - \rho_{Ao}}$ term disapears for very small concentrations of diffusing species and the laminar Schmidt number is only included to balance the diffusion coefficient in the Sherwood number and the kinematic viscosity used to compound other terms into a Reynolds number. $\int\Delta$ is given by equation (3.57) and has a value of 0.862 for x = 14 from the computer program listed in Appendix (3).

APPENDIX ONE

Calculation of Diffusion Coefficients

Bird, Stewart and Lightfoot (1960) quote the Chapman Einskog formula for the estimation of diffusion coefficients as:

$$D_{AB} = 0.0018583 \sqrt{\frac{T_K^{o3} \left[\frac{1}{M_A} + \frac{1}{M_B}\right]}{P \sigma_{AB}^2 \Omega_{AB}}}$$

where σ_{AB} and Ω_{AB}, the Lennard Jones parameter and the Lennard Jones function must be estimated from firstly:

$$\sigma_{AB} = \tfrac{1}{2} (\sigma_A + \sigma_B)$$

where σ_A and σ_B are the atomic volumes of A and B and for Ω_{AB} from ε_{AB}, the other Lennard Jones parameter, given by:

$$\varepsilon_{AB} = \sqrt{\varepsilon_A \varepsilon_B}$$

Ω_{AB} is found from tables of KT/ε_{AB}. The individual ε and σ values are given from the following approximations.

$\varepsilon/K = 0.77\ T_c$ - c - critical temperature

$= 1.15\ T_b$ - b - boiling point

$= 1.92\ T_M$ - M - melting point

and,

$\sigma = 0.841\ \tilde{V}_c^{1/3}$

$= 2.44 \left[\frac{T_c}{P_c}\right]^{1/3}$

$= 1.166\ \tilde{V}_{b\ liq}^{1/3}$

$= 1.222\ \tilde{V}_{m\ sol}^{1/3}$

The relevant temperature T is taken as the film temperature or numerical average of the substrate and jet exit temperatures to compensate for the heating effect of the substrate..

CoAcAt in Hydrogen

There is no data on the melting point of CoAcAt. It sublimes at 120°C at 0.2 mm but decomposition is reported as low as 100°C by Berg and Truemper (1965). The same authors give data on other divalent acetylacetonates, Beryllium is the only one of these to melt prior to decomposition (108°C). Data on trivalent compounds is more extensive, Co III (213°C), Al (194°C, 112°C), Fe (184°C, 179°C), Cr (216°C), Mn (184°C). The other values included are those from Hoene et al (1958). The small scatter in the literature values and the similarity of the range of melting point values makes the choice of 200°C appropriate for the melting point of CoAcAt.

The density of CoAcAt was measuredusing a density bottle displacement method. The displaced fluid used was a saturated solution of CoAcAt in acetone, which was found to wet the fine powder successfully. The calculated density was 1.40 g/cc.

Ignoring any increase in volume to the melting point, this gives a value of σ at 6.946 Angstron units and a value for ε/K from the melting point of 384.0. From known data for hydrogen, $\sigma_{AB} = 4.931$ and $\varepsilon_{AB} = 120.8$ K. For the film temperature of 518°K, Ω_{AB} is found from the tables in Bird, Stewart and Lightfoot to be 0.9594.

Substituting the relevant variables into the Chapman Einskog formula produces a value for D_{AB} of 0.664×10^2 mm^2/sec.

Because of the approximations used, it is worth also considering the relationship of Gilliland (1934).

$$D_{AB} = \frac{0.0043\ T^{3/2}}{P\ (V_A^{1/3} + V_B^{1/3})^2} \sqrt{\frac{1}{M_A} + \frac{1}{M_B}}$$

Using the recommended method of calculating the molecular volumes of CoAcAt by the number of different bond lengths, a value of 226.8 is calculated for V_{CoAcAt}. Substituting the appropriate values into Gillilands expression gives a value of D_{AB} of 0.493×10^2 mm^2/sec. The mean of the two values is used in the preceding chapters for the diffusion coefficient of CoAcAt in Hydrogen and is equal to 0.578×10^2 mm^2/sec.

$Ni(CO)_4$ in Nitrogen

Properties of Nickel Carbonyl are better known than those for CoAcAt. The liquid boils at 43.2°C and melts at -18.9°C, data from International Nickel. Its density at 17°C is 1.32 g/cm^3.

Two estimates of ε/K can be made giving values of 363.6 and 487.9. The mean of 425.7 is used. The density is used at both melting and boiling pcints to give two values for σ of 6.18 and 5.90, giving an average of 6.04 Angstrom units.

Using established data for Nitrogen, σ_{AB} is calculated as 4.86 and ε_{AB}/K as 197.4 giving a value of Ω_{AB} of 1.05. Substituting the relevant variables into the Chapman Einskog formula gives a value for the diffusion coefficient of Nickel tetracarbonyl in nitrogen at a film temperature of 423°K of 0.133×10^2 mm^2/sec.

APPENDIX TWO

Decay of Reactant Concentration due to Entrainment

Abramovich (1963), using Taylor's (1932) theory of turbulence (which, as Abramovich shows, gives a good fit to the free jet data of Stark (1953), Ruden (1933) and Syrkin and Lyakhovsky (1936) derives the following expressions for free jets:

$$\frac{\rho_{Ao} - \rho_{Ab}}{\rho_{Ae} - \rho_{Ab}} = \frac{0.7}{\frac{2as}{d} + 0.29}$$

$$\frac{U_{ho}}{U_{he}} = \frac{0.96}{\frac{2as}{d} + 0.29}$$

where a and s are two constants.

Combining these expressions gives:

$$\frac{\rho_{Ao} - \rho_{Ab}}{\rho_{Ae} - \rho_{Ab}} = 0.73 \frac{U_{ho}}{U_{he}}$$

The centre line velocity U_{ho} decays as a function of d/b as for:

$$\frac{U_{ho}}{U_{he}} = k \frac{d}{b}$$

where, as discussed in chapter one, there is some dispute as to the value of k, a value of 6.1 being taken in the present work.

Combining the last two equations:

$$\frac{\rho_{Ao} - \rho_{Ab}}{\rho_{Ae} - \rho_{Ab}} = 4.45 \frac{d}{b}$$

where the environment concentration of A ρ_{Ab} is a fixed fraction of the jet exit value ρ_{Ae} as for:

$$\rho_{Ab} = F \rho_{Ae}$$

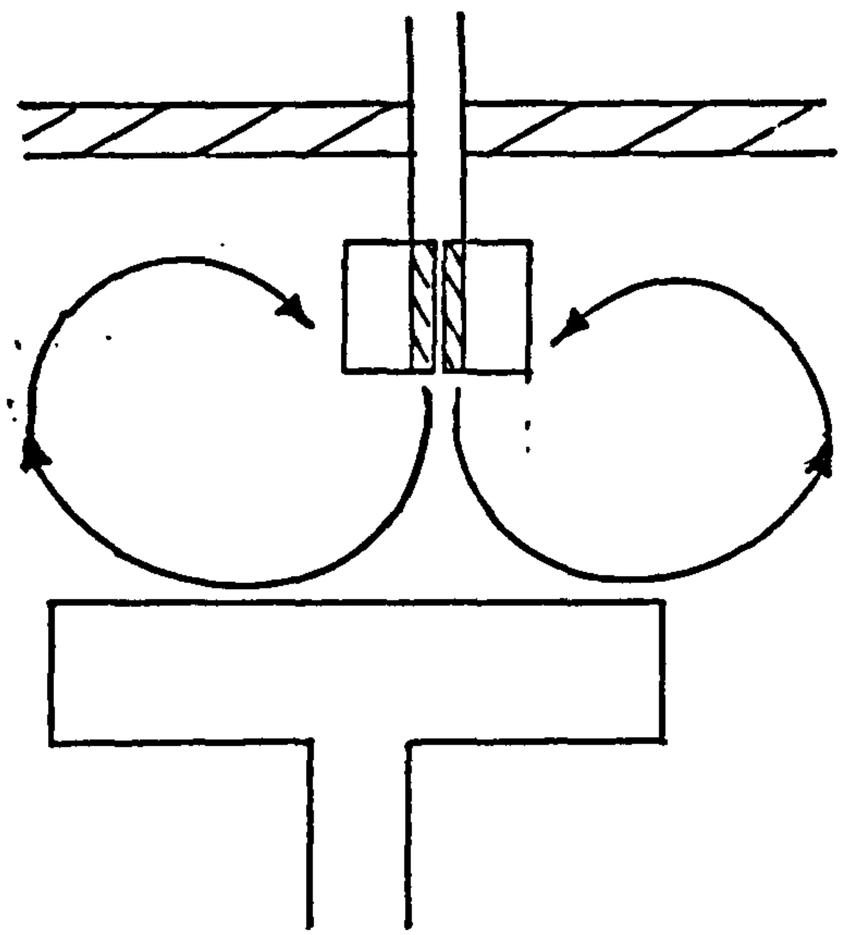
The last expression becomes:

$$\rho_{Ao} = F \rho_{Ae} + \rho_{Ae} (1 - F) 4.45 \frac{d}{b}$$

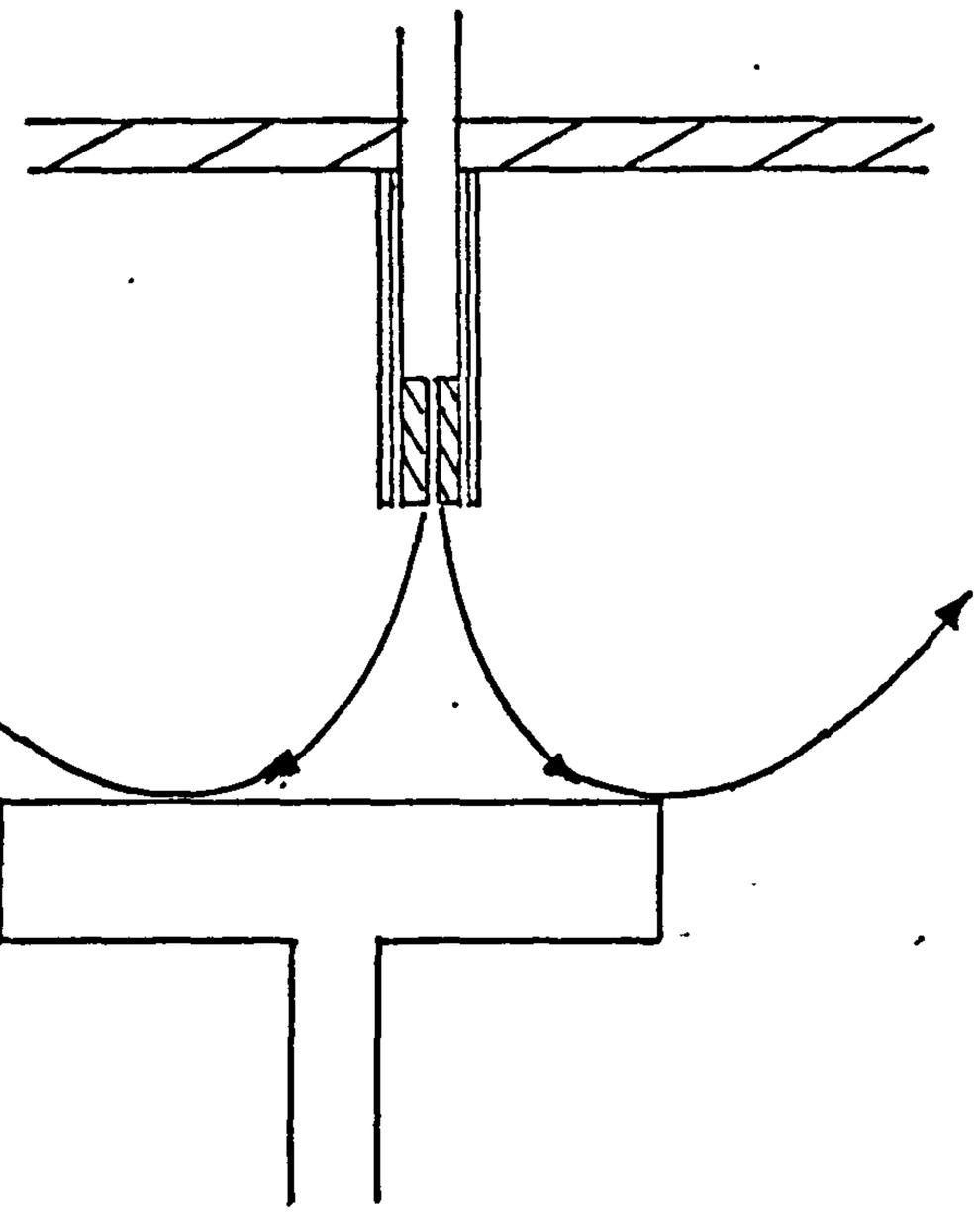
Estimation of the environment concentration is necessary in both vapour deposition systems as direct measurement is impractical because of the low concentrations and the practical dangers.

The flow patterns in each system are unfortunately dissimilar, in that, although the substrate temperatures are comparable, the gap between the substrate and the top of the deposition chamber in the carbonyl system was about half that in the acetylacetonate system. A water cooled jet is also used in the carbonyl system and this, it is thought, could, together with the proximity of the chamber top, promote a significant closed convective cycle within the chamber, returning unreacted carbonyl to be entrained in the jet. The simpler shielded jet in the acetylacetonate experiments would not produce such a recirculation, giving an insignificant recycling effect. A diagram illustrating the two cases is given overleaf.

Conversion rates of carbonyl were estimated by removing deposited nickel and weighing giving values of about 10%, fixing the highest possible recirculation level at 90% jet exit concentration. An attempt was made to sample the flue gas issuing from the deposition chamber and extrapolate the measured values to a maximum. This method gave values of about 20% of jet exit values. The actual entrained concentration lies between these two values and is estimated at 40% of jet exit values.



Ni Deposition



CoO Deposition

POSTULATED CONVECTIVE CYCLING IN THE DEPOSITION CHAMBER

The entrained concentration could conceivably increase during an experiment but no evidence of this was found.

For the acetylacetonate system, a much lower recirculation value is envisaged because of the more open flow pattern. Only traces of cobalt were detected in the acid stripper after the deposition chamber at the end of the whole series of experiments. In this case, the true Sherwood number is found by multiplying the apparent value based on a jet exit concentration calculation by b/d.

For the value of $\rho_{Ab} = 0.4\ \rho_{Ae}$ in the carbonyl system the following table is calculated:

b/d	$1/f$
12.1	0.620
15.1	0.576
20.2	0.513
25.75	0.504
34.0	0.408

where f is the multiplying factor for the Sherwood number.

APPENDIX THREE

Computer Program

The program consists of a series of loops calculating the predicted Sherwood numbers at varying positions across the plate. The integral in the wall jet model is determined by a Simpson's Rule method, subroutine which uses a successively smaller step length until the required accuracy is achieved.

The following is a schematic representation of the program, a full flow chart is not included.

```
$EXECUTE        PUFFT
$IBFTC GJD1
C*****************************************************************************
C
C                                NOMENCLATURE
C
C*****************************************************************************
C     R=RADIAL DISTANCE
C     C=R/B
C     RK=MASS TRANSFER COEFF.
C     SH=SHERWOOD NUMBER
C     SH1=SH FROM GARDON AND COBONPUE MODEL
C     SH2=SH FROM PERRY MODEL
C     DR=R/D
C     RD=R/D
C     XPO=PROFILE LAW EXPONENT
C     F=FUNCTION INTEGRATED IN SIMPSON INTEGRATION
C     VISC=GAS VISCOSITY
C     VISG=GAS VISCOSITY
C     RO=GAS DENSITY
C     DENG=GAS DENSITY
C     D=JET DIAMETER
C     B=JET PLATE DISTANCE
C     RE=JET REYNOLDS NUMBER
C     SC=SCHMIDT NUMBER
C     PR=PRANDTL NUMBER
C     DB=D/B
C     A=LOWER LIMIT OF INTEGRATION
C     BLIM=UPPER LIMIT OF INTEGRATION
C     S=VALUE OF INTEGRAL
C     DAB=DIFFUSION COEFFICIENT
C     UEX=JET EXIT VELOCITY
C     ROAO=REACTANT BULK CONCENTRATION
C     DSH=SH FROM DAWSON FORMULA
C     SHO=STAGNATION SH FROM SNEDEKER DONALDSON
C     IER=ERROR MESSAGE = 0 FOR NO ERRORS
C

      DIMENSION DR(100),R(100),C(100),RK(100),SH(100),SH1(100)
      DIMENSION SH2(100),DSH(100),RD(100)
      COMMON XPO
      EXTERNAL F
      EQUIVALENCE (VISC,VISG)
      EQUIVALENCE  (RO,DENG)
      XPO=14
    1 READ(5,4242)RE,D,B
      IF(RE.EQ.0.0)GO TO 2
 4242 FORMAT(3F10.0)
      SC=2.45
      PR=0.74
      DB=D/B
      I=0
      BO=1.
   31 DO 40 JK=1,9
      I=I+1
      C(I)=0.01*BO*FLOAT(I)
C*****************************************************************************
C
C    HEAT  TRANSFER  ANALOGY  BASED  ON  GARDON  AND  COBONPUE
```

```
C
C*************************************************************************
      SH1(I)=13.*SQRT(RE)*D*SC**0.33*(1.002-2.115*C(I)-1.546*C(I)
     1**2+15.617*C(I)**3-24.153*C(I)**4+11.743*C(I)**5)/(B*PR**0.333)
C*************************************************************************
C
C     HEAT   TRANSFER   ANALOGY   BASED   ON   PERRY
C
C*************************************************************************
      SH2(I)=7.830*RE**0.7*SC**(1./3.)*D/(B*EXP(3.48*C(I)))
      DR(I)=C(I)*B/D
   40 CONTINUE
      BO=BO*10.
      IF(BO.GT.11.)GO TO 32
      GO TO 31
   32 CONTINUE
      WRITE(6,3333)
 3333 FORMAT(1H1)
 4323 FORMAT(10X,11HSH FROM G C,4X,11HSH FROM P S,8X,3HR/B,12X,3HR/D/)
      WRITE(6,4323)
      WRITE(6,4321)(SH1(I),SH2(I),C(I),DR(I),I=1,10)
 4321 FORMAT(6X,4E15.4)
C*************************************************************************
C
C  WALL JET MODEL BASED ON GAUNTNER ET AL VELOCITY CORRELATION
C  AND BRADSHAW AND GEE SHEAR STRESS CORRELATION
C
C*************************************************************************
      A=0
      BLIM=1.
      CALL DMPSN(F,A,B,DEL,IMAX,SI1,S,N,IER,BLIM)
      WRITE(6,4040)IER
4040 FORMAT(//40X,3HIER/41X,I1//)
      FUNCT1=S
      WRITE(6,5050) S
5050 FORMAT(40X,1HS/33X,E15.4//)
      DAB=0.0611
      VISG=  181./10.**6
      DENG=0.001218
      UEX=RE*VISG/(DENG*D)
      CR=B/D
      RO=DENG
      ROAO=2.3/10.**7
      CONC=RO/(RO-ROAO)
      SC=2.45
      DO 99N=1,25
      RD(N)=FLOAT(N*4)/10.0
      RK(N)=0.0065*CONC*UEX*FUNCT1*(((XPO+1.)*(XPO+2.)/XPO)**0.846)/(RE*
     1*0.154*RD(N)**1.172 )
      R(N)=RD(N)*D
      C(N)=R(N)/B
C*************************************************************************
C
C        DAWSON   AND   TRASS   FORMULA
C
C*************************************************************************
      DSH(N)=0.044*RE**0.877/RD(N)
   99 SH(N)=RK(N)*D/DAB
      WRITE(6,3737)
```

```
 3737 FORMAT(7X,2HRK,12X,1HR,12X,3HR/D,10X,3HDSH,10X,2HSH)
      WRITE(6,3838)(RK(N),R(N),RD(N),DSH(N),SH(N),N=1,25)
 3838 FORMAT(1X,5E13.4)
      WRITE(6,3939)D,UEX,RE,CR,XPO
 3939 FORMAT(//9X,1HD,10X,3HUEX,10X,2HRE,11X,3HR/D,10X,3HXPO/1X,5E13.4//
     1)
C*****************************************************************
C
C   HEAT TRANSFER AT THE STAGNATION POINT FROM RESHOTKO AND COHEN
C                  SNEDEKER AND DONALDSON
C
C*****************************************************************
      SHO=10.95*SQRT(RE)*SC**(1./3.)*(0.35*PR+0.41)*D/(B*PR**(1./3.))
      WRITE(6,9751)SHO
 9751 FORMAT(20X,40HRESHOTKO AND COHEN SNEDEKER AND DONALSON/;8X,
     144HSTAGNATION POINT SHERWOOD NUMBER CORRELATION//35X,F10.4)
      GO TO 1
    2 STOP
      END
```

```
$IBFTC UNCT
      FUNCTION F(X)
      DIMENSION DR(100),R(100),C(100),RK(100),SH(100),SH1(100)
      DIMENSION SH2(100),DSH(100),RD(100)
      COMMON XPO
      F=(X-X**2)**(1.0/XPO)
      RETURN
      END
```

```
$IBFTC INTG
      SUBROUTINE DMPSN(F,A,B,DEL,IMAX,SI1,S,N,IER,BLIM)
      DIMENSION DR(100),R(100),C(100),RK(100),SH(100),SH1(100)
      DIMENSION SH2(100),DSH(100),RD(100)
      COMMON XPO
      DEL=0.01
      IMAX=20
      SI1=.0
      S=.0
      N=0
      BA=BLIM-A
      IF (BA)20,19,20
   19 IER=1
      RETURN
   20 IF(DEL)22,22,23
   22 IER=2
      RETURN
   23 IF(IMAX-1)24,24,25
   24 IER=3
      RETURN
C     COMPUTE SIGMA(1)
   25 X=BA/2.+A
      NHALF=1
      SUMK=F(X)*BA*2./3.
      S=SUMK+(F(A)+F(BLIM))*BA/6.
C     DIVIDE (A,B) INTO 2,4,...,2**I INTERVALS,
C     COMPUTE SIGMA(2),SIGMA(4),...,SIGMA(I)
      DO 28 J=2,IMAX
      SI1=S
      S=(S-SUMK/2.)/2.
      NHALF=NHALF*2
      ANHLF=NHALF
      FRSTX=A+(BA/ANHLF)/2.
      SUMK=F(FRSTX)
      XK=FRSTX
      KLAST=NHALF-1
      FINC=BA/ANHLF
      DO 26 K=1,KLAST
      XK=XK+FINC
   26 SUMK=SUMK+F(XK)
      SUMK=SUMK*2.*BA/(3.*ANHLF)
      S=S+SUMK
C     COMPARES THE I-TH AND(I-1)ST RESULTS
   27 IF( ABS(S-SI1)- ABS(DEL*S)) 29,28,28
   28 CONTINUE
      IER=4
      GO TO 30
   29 IER=0
   30 N=2*NHALF
      RETURN
      END
```

SH FROM G C	SH FROM P S	R/B	R/D
0.1361E 03	0.4354E 03	0.1000E-01	0.1200E 00
0.1331E 03	0.4205E 03	0.2000E-01	0.2400E 00
0.1301E 03	0.4061E 03	0.3000E-01	0.3600E 00
0.1271E 03	0.3922E 03	0.4000E-01	0.4800E 00
0.1241E 03	0.3788E 03	0.5000E-01	0.6000E 00
0.1211E 03	0.3658E 03	0.6000E-01	0.7200E 00
0.1181E 03	0.3533E 03	0.7000E-01	0.8400E 00
0.1151E 03	0.3412E 03	0.8000E-01	0.9600E 00
0.1122E 03	0.3296E 03	0.9000E-01	0.1080E 01
0.7603E 02	0.1389E 02	0.1000E 01	0.1200E 02

IER
0

S
0.8619E 00

RK	R	R/D	DSH	SH
0.1599E 03	0.1270E 00	0.4000E 00	0.2730E 03	0.8311E 03
0.7099E 02	0.2540E 00	0.8000E 00	0.1365E 03	0.3689E 03
0.4414E 02	0.3810E 00	0.1200E 01	0.9101E 02	0.2293E 03
0.3150E 02	0.5080E 00	0.1600E 01	0.6826E 02	0.1637E 03
0.2425E 02	0.6350E 00	0.2000E 01	0.5460E 02	0.1260E 03
0.1950E 02	0.7620E 00	0.2400E 01	0.4550E 02	0.1018E 03
0.1635E 02	0.8890E 00	0.2800E 01	0.3900E 02	0.8496E 02
0.1398E 02	0.1016E 01	0.3200E 01	0.3413E 02	0.7265E 02
0.1218E 02	0.1143E 01	0.3600E 01	0.3034E 02	0.6329E 02
0.1076E 02	0.1270E 01	0.4000E 01	0.2730E 02	0.5593E 02
0.9626E 01	0.1397E 01	0.4400E 01	0.2482E 02	0.5002E 02
0.8693E 01	0.1524E 01	0.4800E 01	0.2275E 02	0.4517E 02
0.7915E 01	0.1651E 01	0.5200E 01	0.2100E 02	0.4113E 02
0.7256E 01	0.1778E 01	0.5600E 01	0.1950E 02	0.3771E 02
0.6693E 01	0.1905E 01	0.6000E 01	0.1820E 02	0.3478E 02
0.6205E 01	0.2032E 01	0.6400E 01	0.1706E 02	0.3224E 02
0.5779E 01	0.2159E 01	0.6800E 01	0.1606E 02	0.3003E 02
0.5405E 01	0.2286E 01	0.7200E 01	0.1517E 02	0.2809E 02
0.5073E 01	0.2413E 01	0.7600E 01	0.1437E 02	0.2636E 02
0.4777E 01	0.2540E 01	0.8000E 01	0.1365E 02	0.2482E 02
0.4512E 01	0.2667E 01	0.8400E 01	0.1300E 02	0.2344E 02
0.4272E 01	0.2794E 01	0.8800E 01	0.1241E 02	0.2220E 02
0.4055E 01	0.2921E 01	0.9200E 01	0.1187E 02	0.2107E 02
0.3858E 01	0.3048E 01	0.9600E 01	0.1138E 02	0.2005E 02
0.3678E 01	0.3175E 01	0.1000E 02	0.1092E 02	0.1911E 02

D	UEX	RE	B/D	XPC
0.3175E 00	0.3477E 04	0.7429E 04	0.1200E 02	0.1400E 02

RESHOTKO AND COHEN SNEDEKER AND DONALSCN
STAGNATION POINT SHERWOOD NUMBER CORRELATION

78.4216

APPENDIX FOUR

Tabulated Data

Experimental data and derived values are tabulated in the following pages. Runs are coded A for napthalene erosion, C for CoO deposition and N for Nickel deposition. The first data shown is for the napthalene erosion profiles. The final tables contain the data relevant to stagnation point mass transfer.

Table (1)	-	Napthalene Erosion
Tables (2) and (3)	-	CoO Deposition
Tables (4) and (5)	-	Nickel Deposition

Run A1

$R/_d$	tav.(mm)	Sh
0.0	0.275	96.2
0.787	0.227	79.4
1.58	0.164	57.4
2.36	0.124	43.4
3.15	0.111	38.8
3.94	0.112	39.2
4.72	0.109	38.1
5.51	0.084	29.4
6.30	0.055	19.2
7.09	0.060	21.0
7.87	0.049	17.1
10.2	0.041	14.3
11.8	0.034	11.9

Run A1B

$R/_d$	tav.(mm)	Sh
0.0	0.697	89.8
0.315	0.642	82.7
0.630	0.607	78.2
0.945	0.556	71.6
1.26	0.533	68.6
1.57	0.466	60.0
1.89	0.404	52.0
2.2	0.384	49.5
2.83	0.331	42.6
3.46	0.300	38.6
4.09	0.279	35.9
5.20	0.260	33.5
5.98	0.238	30.7
6.77	0.202	26.0
7.56	0.19	24.5
8.35	0.174	22.4
9.92	0.146	18.8
11.5	0.118	15.2
13.9	0.102	13.1
18.6	0.081	10.4

Run A2

$R/_d$	tav.(mm)	Sh
0.0	0.600	120.0
0.315	0.565	113.0
0.63	0.527	106.0
0.945	0.457	91.6
1.26	0.415	83.1
1.57	0.388	77.7
1.90	0.339	67.9
2.52	0.292	58.5
3.15	0.269	53.9
3.94	0.257	51.5
4.72	0.230	46.1
6.30	0.192	38.5
7.87	0.164	32.9
9.45	0.119	23.8
11.0	0.103	20.6
13.4	0.093	18.6

Run A3

$R/_d$	tav.(mm)	Sh
0.0	0.605	121.2
0.315	0.505	101.2
0.630	0.497	99.6
0.945	0.448	89.7
1.26	0.405	81.1
1.57	0.354	70.9
1.89	0.291	58.3
2.2	0.276	55.3
2.83	0.242	48.5
3.46	0.229	45.9
4.09	0.220	44.1
5.67	0.180	36.1
6.46	0.171	34.3
8.03	0.118	23.6
8.8	0.121	24.2
10.4	0.111	22.2
14.3	0.066	13.2
15.9	0.060	12.0

Run A4

$R/_d$	tav.(mm)	Sh
0.0	0.666	145.2
0.315	0.635	144.6
0.630	0.627	136.7
0.945	0.553	120.5
1.26	0.528	115.1
1.57	0.468	102.0
1.89	0.401	87.4
2.20	0.392	85.4
2.83	0.294	64.1
3.15	0.309	67.3
3.78	0.307	66.9
4.57	0.278	60.6
5.35	0.210	45.8
6.30	0.198	43.5
7.87	0.160	34.9
8.66	0.164	35.7
9.45	0.141	30.7
11.0	0.133	29.0
14.2	0.091	19.9

Run A5

$R/_d$	tav.(mm)	Sh
0.0	64.6	151.7
0.315	63.8	149.8
0.630	57.3	134.5
0.945	52.8	124.0
1.26	49.0	115.0
1.57	43.9	103.0
1.89	40.0	93.9
2.20	38.7	90.9
2.83	32.9	77.2
3.15	30.8	72.3
3.78	28.2	66.2
4.41	25.5	60.0
5.20	24.1	56.6
5.98	22.3	52.4
6.77	20.5	48.1
7.56	17.3	40.6
8.35	17.3	40.6
9.92	14.5	34.0
11.5	12.0	28.2
13.1	10.2	24.0

Run A6

$R/_d$	tav.(mm)	Sh
0.0	0.474	86.3
0.315	0.440	77.5
0.630	0.431	75.3
0.945	0.392	67.8
1.26	0.358	61.3
1.57	0.330	55.9
1.89	0.309	51.8
2.52	0.250	40.5
3.15	0.243	39.1
3.78	0.222	35.1
4.88	0.214	33.5
5.67	0.187	28.3
6.46	0.159	22.9
8.03	0.152	21.6
9.61	0.131	17.5
11.2	0.102	11.9
12.8	0.089	9.4

Run A7

$R/_d$	tav.(mm)	Sh
0.0	0.439	67.2
0.315	0.415	63.5
0.630	0.369	56.5
0.945	0.379	58.0
1.26	0.324	49.6
1.57	0.307	47.0
1.89	0.285	43.6
2.2	0.259	39.6
2.83	0.219	33.5
3.46	0.205	31.4
4.09	0.182	27.8
4.72	0.175	26.8
5.51	0.171	26.2
6.30	0.159	24.3
7.87	0.128	19.6
8.66	0.112	17.1
10.2	0.088	13.5
14.2	0.070	10.7

Run A9

$R/_d$	tav.(mm)	Sh
0.0	0.403	56.0
0.315	0.391	54.3
0.630	0.369	51.2
0.945	0.340	47.2
1.26	0.339	47.1
1.57	0.302	41.9
1.89	0.273	37.9
2.20	0.250	34.7
2.52	0.237	32.9
2.83	0.210	29.2
3.46	0.196	27.2
4.09	0.187	26.0
5.20	0.170	23.6
5.98	0.140	19.4
7.56	0.103	14.3
9.92	0.0705	9.81
12.30	0.047	6.50

Run A13

R/d	tav.(mm)	Sh
0.0	0.274	128.2
0.315	0.264	123.5
0.630	0.218	102.0
0.945	0.207	96.8
1.26	0.190	88.9
1.57	0.178	83.3
1.89	0.156	73.0
2.2	0.153	71.6
2.83	0.115	53.8
3.94	0.106	49.6
4.72	0.090	42.1
5.51	0.082	38.4
6.30	0.065	30.4
7.87	0.050	23.4
9.45	0.048	22.5
10.24	0.039	18.2

Run A14

$R/_d$	tav.(mm)	Sh
0.0	0.504	70.0
0.315	0.505	70.1
0.630	0.463	64.3
0.945	0.416	57.8
1.26	0.383	53.2
1.57	0.369	51.2
1.89	0.335	46.5
2.2	0.325	45.1
2.83	0.265	36.8
4.4	0.232	32.2
5.20	0.228	31.7
6.77	0.209	29.0
7.56	0.192	26.7
9.13	0.144	20.0
12.3	0.110	15.3
14.7	0.100	13.9
20.5	0.049	6.8

Run A15

$R/_d$	tav. (mm)	Sh
0.0	0.477	55.4
0.315	0.453	52.6
0.630	0.396	46.0
0.945	0.382	44.4
1.26	0.369	42.9
1.57	0.336	39.0
2.20	0.332	38.6
3.15	0.294	34.2
3.94	0.250	29.1
4.72	0.237	27.5
5.51	0.237	27.5
6.30	0.204	23.7
7.87	0.192	22.3
8.66	0.198	23.0
9.45	0.176	20.5
10.24	0.152	17.7
11.8	0.136	15.8
16.5	0.100	11.6

Run A1 6

$R/_d$	tav.(mm)	Sh
0.0	38.5	45.5
0.315	37.5	44.3
0.630	35.2	41.6
0.945	30.6	36.1
1.26	27.1	32.0
1.57	26.3	31.0
2.2	21.8	25.7
2.52	19.4	22.9
2.83	17.5	20.7
3.15	16.2	19.1
3.94	16.2	19.1
4.72	16.9	20.0
5.51	17.2	20.3
6.30	16.4	19.4
7.09	17.4	20.5
8.66	16.5	19.5
9.45	16.1	19.0
12.6	12.4	14.6
14.2	12.2	14.4
17.3	8.2	9.68
20.5	6.0	7.08

Table (1)

Run No.	Re	$^b/_d$	Temp ^oC	Time Secs	Sh_o	$Sh_o . {}^b/_d$	$Sh_o . {}^b/_d . Sc^{-1/3}$	$\log_{10} Sh_o . {}^b/_d . Sc^{-1/3}$	$\log_{10}$ Re
A1 (a)	7429	12	19.0	5400	96.2	1154	1856	2.9325	3.8709
A1 (b)	7429	12	21.0	12000	89.8	1078	800	2.9031	3.8709
A2 (a)	10950	12	19.5	9000	120.2	1442	1070	3.0294	4.0395
(b)	10950	12			115.2	1382.4	1026	3.0111	4.0395
(c)	10950	12			122.0	1464	1086	3.0359	4.0395
A3 (a)	8448	12	19.5	9000	105.2	1262	936.2	2.9714	3.9268
(b)	8448	12			121.2	1454	1079	3.0331	3.9268
A4 (a)	13600	12	19.0	7800	145.2	1742	1292	3.1113	4.1335
(b)	13600	12			143.8	1726	1280	3.1072	4.1335
A5 (a)	16245	12	20.1	7200	151.7	1820	1350	3.1303	4.2106
(b)	16245	12			142.5	1711	1269	3.1035	4.2106
(c)	16245	12			191.0	2287	1696	3.2295	4.2106
A6 (a)	5475	12	18.0	10800	86.3	1036	768.5	2.8857	3.7384
(b)	5475	12			94.0	1128	836.8	2.9227	3.7384

Table (1) cont.

Run No.	Re	$^{b}/_{d}$	Temp ^{o}C	Time Secs	Sh_o	$Sh_o . {}^{b}/_{d}$	$Sh_o . {}^{b}/_{d} . Sc^{-1}/3$	$\log_{10} Sh_o . {}^{b}/_{d} . Sc^{-1}/3$	$\log_{10}$ Re
A7	4749	12	17.4	14400	67.2	806.4	598.2	2.7769	3.6767
A8	5147	12			83.65	1004	744.8	2.8721	3.7116
A9	3095	12			56.0	672	498.5	2.6976	3.4907
A10	3930	12			65.7	788.4	584.9	2.7671	3.5944
A11	2190	8			79.0	632.3	469.1	2.6713	3.3404
A12	2651	8			69.1	475.5	352.7	2.5474	3.4234
A13	7429	8	15.2	6360	128.2	1025.1	760.5	2.8811	3.8709
A14	7429	16	16.0	18000	70.0	1195.5	886.9	2.9478	3.8709
A15	7429	20	17.2	19320	55.4	1108.7	822.5	2.9152	3.8709
A16	7429	24	15.0	25200	45.5	1091	809.3	2.9081	3.8709
A17	1600	8			45.5	363.7	270.0	2.4314	3.204

Table (2)

Re	b	d/b	T °C	T °A	$1/T°A \times 10^3$	Time Secs	tmm x 10^7	Rate mm/Sec x 10^7	log rate x 10^7	Run No
4637	9.07d	0.1103	397	670	1.493	70	5705	81.5	1.9112	C1
4637	9.07d	0.1103	397	670	1.493	70	6817	97.4	1.9886	C2
2213	9.07d	0.1103	397	670	1.493	120	5705	47.5	1.6771	C3
2677	9.07d	0.1103	397	670	1.493	90	5389	59.9		C4
3225	9.07d	0.1103	397	670	1.493	90	6968	77.4		C5
3858	9.07d	0.1103	397	670	1.493	45	4034	89.6		C6
4637	33.75d	0.0296	397	670	1.493	600	4466	7.44		C7
4637	29.4d	0.0340	397	670	1.493	240	2825	11.8		C8
4637	10.3d	0.09709	397	670	1.493	75	5389	71.9		C9
4637	13.1d	0.07634	397	670	1.493	100	5389	53.9		C10
4637	17.35d	0.0576	397	670	1.493	360	6968	19.4		C11
4637	9.07d	0.1103	425	698	1.433	60	6817	113.6	2.0554	C12

Table (2) cont.

Re	b	$^{d}/_{b}$	T °C	T °A	$^{1}/_{T°A} \times 10^{3}$	Time Secs	tmm x 10^{7}	Rate mm/Sec x 10^{7}	log rate x 10^{7}	Run No
4637	9.07d	0.1103	221	494	2.024	3000	693	0.231	-0.6364	C13
4637	9.07d	0.1103	246	519	1.927	600	3811	57.52	0.876	C14
4637	9.07d	0.1103	276	549	1.822	3000	3811	1.270	0.104	C15
4637	9.07d	0.1103	305	578	1.730	600	6968	11.61	1.065	C16
4637	9.07d	0.1103	356	629	1.590	70	5389	76.98	1.8864	C17
4637	9.07d	0.1103	397	670	1.493	45	3811			C18
4637	9.07d	0.1103	397	670	1.493	30	2825			C19
4637	9.07d	0.1103	397	670	1.493	20	2364			C20
2213	9.07d	0.1103	397	670	1.493	80	3811			C21
2213	9.07d	0.1103	397	670	1.493	90	4034			C22
2213	9.07d	0.1103	397	670	1.493	60	2364			C23

Table (3)

Sh_o	$Sh_o (b/d)^2 Sc^{-\frac{1}{3}}$	$\log_{10} Sh_o (b/d)^2 Sc^{-\frac{1}{3}}$	$\log_{10} Re$	Re	Run No.
9.73	525.2	2.720	3.666	4637	C1
11.63	627.8	2.798	3.666	4637	C2
5.68	306.6	2.487	3.345	2213	C3
7.15	386.0	2.587	3.428	2677	C4
9.24	499.0	2.698	3.5086	3225	C5
10.7	577.8	2.762	3.5860	3858	C6

Table (4)

Re	b	d/b x 10^2	T°C	T°K	$1/T^{o}$ x 10^3	Time Secs	t mm x 10^2	Rate mm/Sec x 10^4	log rate	$Ni(CO)_4$ conc mole %	Run No.
6734	15.1d	6.62	134	407	2.46	1800	3.2	0.178	-0.75	1.38	N1
6734	15.1d	6.62	152	425	2.35	1140	28.4	2.49	0.396	1.38	N2
6734	15.1d	6.62	175	448	2.24	600	53.8	8.97	0.953	1.38	N3
6734	15.1d	6.62	128	401	2.49	1800	1.8	0.10	-1.0	1.38	N4
6734	15.1d	6.62	113	386	2.59	2580	1.0	0.0388	-1.411	1.38	N5
6734	15.1d.	6.62	130	403	2.48	1800	2.8	0.156	-0.807	1.38	N6
6734	9.0d	11.1	150	423	Produced a hollow					1.38	N7
6734	15.1d	6.62	200	473	2.11	600	91.0	15.2	1.182	1.38	N8
6734	15.1d	6.62	200	473	2.11	300	42.8	14.3	1.155	1.38	N9
6734	15.1d	6.62	225	497	2.01	300	69.0	23.0	1.362	1.38	N10
6734	15.1d	6.62	250	523	1.91	600	Powdery and open structure			1.38	N11
6734	15.1d	6.62	161	434	2.30	600	26.0	4.33	0.637	1.38	N12
6734	15.1d	6.62	161	434		2400	20.2	0.842		0.276	N13
6734	15.1d	6.62	161	434		900	26.0	2.89		1.035	N14

Table (4) cont.

Re	b	$d/_b \times 10^2$	T°C	T°K	$1/_{T^\circ} \times 10^3$	Time Secs	t mm x 10^2	Rate mm/Sec x 10^4	log rate	Ni(C0)4 conc mole %	Run No.
6734	15.1d	6.62	161	434		900	19.6	2.18		0.69	N15
6734	15.1d	6.62	161	434		420	27.6	6.55		2.07	N16
6734	15.1d	6.62	161	434		300	19.6	6.53		2.07	N17
6734	15.1d	6.62	161	434		600	20.9	3.48		2.07	N18
6734	15.1d	6.62	161	434		720	14.3	1.99		2.07	N19
6734	12.1d	8.28	200	473		180	36.8	20.4		1.38	N20
6734	34.0d	2.94	200	473		300	15.0	5.00		1.38	N21
6734	20.2d	4.94	200	473		240	21.6	9.0		1.38	N22
6734	25.75d	3.90	200	473		420	21.2	5.05		1.38	N23
5850	15.1d	6.62	200	473		300	36.0	12.0		1.38	N24
5360	15.1d	6.62	200	473		300	38.8	12.9		1.38	N25
4160	15.1d	6.62	200	473		300	35.0	11.62		1.38	N26
3075	15.1d	6.62	200	473		360	30.2	7.78		1.38	N27
7380	15.1d	6.62	200	473		240	36.9	15.4		1.38	N28

Table (4) cont.

Re	b	$d/_b \times 10^2$	T°C	T°K	$1/_{T^o} \times 10^3$	Time Secs	t mm x 10^2	Rate mm/Sec x 10^4	log rate	$Ni(C0)_4$ conc mole %	Run No.
3770	15.1d	6.62	200	473		300	32.2	10.7		1.38	N29
2510	15.1d	6.62	200	473		420	24.8	5.9		1.38	N30
6734	15.1d	6.62	145	418	2.39	1800	0.160	0.889	-0.05	1.38	N31
3075	15.1d	6.62	161	434		600	24.2	4.03		1.38	N32

Table (5)

Sh_o	$Sh_o . {}^b/d$	$Sh_o . {}^b/d . f\, Sc^{-\frac{1}{3}}$	$\log_{10} Sh_o . {}^b/d . f\, Sc^{-\frac{1}{3}}$	$\log_{10}$ Re	Re	Run No.
31.46	475.1	628.7	2.7985	3.7672	5850	N24
33.9	512.0	677.5	2.8309	3.7292	5360	N25
30.65	462.8	612.4	2.8781	3.6191	4160	N26
21.9	332.0	439.5	2.6430	3.4878	3075	N27
40.31	608.7	805.5	2.9061	3.8681	7380	N28
28.1	424.9	562.3	2.7499	3.5763	3770	N29
15.48	233.8	309.3	2.4904	3.3997	2510	N30
39.76	600.4	794.5	2.9001	3.8283	6734	N8
37.4	564.8	747.4	2.8735	3.8280	6734	N9

APPENDIX FIVE

References

Ambramovich G.N. (1963) 'The Theory of Turbulent Jets' M.I.T. Press.

Bennet C.O.& Myers J.E. (1962) 'Momentum Heat and Mass Transfer' McGraw Hill Book Co. Inc.

Babich B.N., Kurganov G.V., Strogonov Yu.D. (1967) Russ. Metall. 1 p124.

Baker E. (1967) Ph.D. Thesis Univ. of London. Imperial Coll. Rep No. TWF/R/3.

Bakke P. (1957) J. of Fluid Mech. Vol 2 p467.

Bawn (1935) Trans. Far. Soc. 1935, 31 p440.

Berg E.W., Truemper J.T. (1965) Anal. Chim. Acta. 32 p245.

Bird R.B., Stewart W.E., Lightfoot E.N. (1961) 'Transport Phenomena' John Wiley & Sons Inc.

Blasius H. (1913) Forschungsarbeiten des Ver Deutsh Ing. no.131.

Boussinesq J. (1877) Mém. prés. Aca. Sci. XXIII, 46 Paris.

Bradshaw P., Love E.M. (1959) Aero Research Council Rep. No. 21, 268.

Bradshaw P., Gee M.T. (1962) R and M No. 3252.

Bullen G.J. (1959) Acta. Cryst. 12 p703.

Carlton C.F., Oxley J.H., Blocher J.M. (1966) 'Vapour Deposition' John Wiley & Sons Inc.

Carlton H.E., Oxley J.H. (1967) A.I.Ch.E. Journal p86.

Carlton H.E., Oxley J.H. (1967)b A.I.Ch.E. Journal, Vol 13, No.3, p571.

Chattopadhyay B., Measor J.C. (1969) J. Mat. Sci. 4 p457.

Chilton T.H., Colburn A.P. (1934) Ind. Eng. Chem. 26 p1183.

Clauser F.H. (1954) J. Aero. Sci. 21, 2, p91 - 108.

Cobalt Monograph (1960) Publ. Centre d'information du Cobalt.

Corrsin S. (1951) J. Aero. Sci. 18, p417 - 423.

Dawson D.A., Trass O. (1966) Can. J. Chem. Eng. June p121. see also:

Dawson D.A. (1965) M.A.Sc. Thesis, Dept. of Chem. Eng. Univ. Toronto.

Dickenson J. (1963) Comptes Rendus de l'Acad. Sci. 257, 6, p1218.

Elrod H.G. (1954) Amerc. Soc. Heating & Vent. Engrs. Jrnl. 26, 3, p149.

Escudier M.P. (1965) Imperial Coll. London, Mech. Eng. Dept. Rep. TWF/TN/1.

Fisher, Cotton & Wilkinson (1957) J.A.C.S. 79 p2044-6.

Gabe D.R. (1968) J. Metal Finishing. Dec. 1968, p393.

Garnett et al (1934) J. Chem. Soc. 1934 p1817.

Gardon R., Cobonpue J. (1961) 1961 Int. Heat Trans. Conf. Part II p 454 - 460.

Gardon R., Akfirat J.C. (1965) Int. J. Heat & Mass Trans.

Gauntner J.W., Livingwood J.N.B., Hrycak P. (1970) NASA TN D-5652.

Gilliland (1934) Ind. Eng. Chem. 26 p681.

Gilman J.J. (1960) J. Appl. Phys. 31 p2208.

Glauert M.P. (1956) J. of Fluid Mech. Vol 1, p625.

Goertler H. (1942) Z.A.M.M. 22 p244-254.

Goldberger (1961) Ph.D. Thesis, Polytech. Inst. Brooklin (1961).

Gostkowski V.J., Costello F.A. (1970) Int. J. H. & M. Trans. 13, 8, p1382.

Heskestad G. (1965) A.S.M.E. Trans. J. App. Mech. Paper No. 65 - APM - H.

Hinshelwood C.N., Williamson A.T. (1934) 'The Reaction between Hydrogen and Oxygen' Clarendon Press.

Hinze J.O., Zijnen B.G.van der Hegge (1949) Proc. 7th Int. Conf. for Appl. Mech. p286.

Hoene J. von., Charles R.G., Hickam W.M. (1958) J. Phys. Chem. 62 p1098.

Holdhusen J.S., Baines W.D. Trans. Americ. Soc. Civ. Engrs. 115 p665.

Hrycak P., Lee D.T., Gauntner J.W., Livingwood J.N.B. (1970) NASA TN D 5690.

Huang G.C. (1962) ASME Jrnl. Heat Trans. Aug. p237.

Jablonowski E.J. (1962) Cobalt 14, March.

Jakob M., Rose R.L., Spielman M. (1950) Trans. ASME 72 p859.

Jones W.P., Launder B.E. (1969) ASME 69 - HT - 13.

Kestin J. Maeder P.F. (1957) NACA TN 4018.

Kirpo et al (1966) Tr. Proekt Nauch-Issled Inst. Gipronikel 30 p50.

Kolmogorov A.N. (1942) Izv. Akad. Nauk. S.S.S.R. Ser. Phys. No. 1-2.

Kumada M., Mabuchi I (1970) J.S.M.E. Bull. 13 p55.

Leont'ev A.I. (1966) 'Advances in Heat Transfer' Vol 3, Academic Press p 92.

Mond L. (1891) U.S. Pats. 455227 - 455230.

Myers G.E., Shauer J.J., Eustis R.H. (1961) Stanford Univ. Mech. Eng. Dept. Tech. Rep. No.1.

Myers G.E., Shauer J.J., Eustis R.H. (1963) J. Basic Eng. 85, 1963.

Patanker S.V. (1967) Imp. Coll. Mech. Eng. Dept. Rep. No. T/F/E/S.

Perry K.P. (1954) Proc. Inst. Mech. Eng. Vol 168, p775.

Pohlhausen E.Z. (1921) Angew. Math. U. Mech 1, p115.

Poland R.A. (1967) M.Sc. Thesis, Imperial Coll. Univ. of London.

Poreh M., Cermak J.E. (1959) Proceedings of the Sixth Midwest Conf. on Fluid Mech. p198.

Poreh M., Tsuei Y.G., Cermak J.E. (1967) J. of App. Mech. June, p457.

Prandtl L. (1925) Z.A.M.M.5. p136

Prandtl L. (1945) 'Uber ein nues Formelsystem fur die ausgebildete Turbulenz, Nachrichten von der Akad. der Wissenschaften in Gottingen. p6-19. Van den Loeck & Ruprecht, Gottingen.

Rao V.V., Trass O (1964) Can. J. Chem. Eng. June p95.

Reichardt H. (1950) Reports of the Max Planck Inst. fur Stromungsforshung No. 3, p1-63.

Reshotko E., Cohen C.B. (1955) NACA TN 3513.

Ruden P. (1933) Turbulente Ausbreitungsvorgange im Frastrahl' Naturwiss 21 p375.

Sandell E.B. (1950) 'Colorimetric Determination of Traces of Metals' 2nd ed. Interscience Publ. Inc.

Schauer J.J., Eustis R.H. (1963) Stanford Univ. Mech. Eng. Dept. Tcch. Rep. No. 3.

Schlicting (1968) 'Boundary Layer Therory' 6th ed. McGraw Hill Book Co. Inc.

Scholtz M.T. (1963) A.I.Ch.E. Jrnl 94 p548.

Scholtz M.T., Trass O. (1970) A.I.Ch.E. Jrnl. Jan. p82.

Schwartz W.H., Cosart W.P. (1961) J. Fluid Mech. 10 p481.

Seban R.A., Back L.H. (1960) Int. J. of Heat & Mass Transf. 3 p255-265.

Seban R.A., Back L.H. (1961) J. Heat Transf. 84 p45-54.

Sherwood T.K. (1959) Chem. Eng. Prog. Symposium Series 55 25 p71.

Sigalla A. (1958) J. R. Aero. Soc. 62 p873.

Sitharamayya S., Subba Raju K. (1969) Can. J. Chem. Eng. 47 p365.

Smirnov V.A., Vererochkin G.E., Bridlick P.N. (1961) Int. J. Heat & Mass Trans. 2,1.

Snedeker R.S., Donaldson C.Du.P. (1964) ARAP Report No.63, Princeton N.J.

Spalding D.B. (1967) App. Mech. Reviews, Vol 20, No.8.

Spalding D.B. (1967)b Mech. Eng. Dept. Imperial Coll.London Univ. Rep TWF/TN/37 Section 3.3.

Spalding D.B., Patankar S.V. (1967) 'Heat & Mass Transfer in Boundary Layers' Morgan Grampian Press London.

Spice, Staveley & Harrow (1955) J. Chem. Soc. 1955 p100.

Stark S.B. (1953) 'Mixing of Gas Streams in a Flame' Zh. Tekhn. Fiz. 23, 10.

Syrkin A.N., Lyakhovsky D.N. (1936) 'Aerodynamics of an Elementary Flame' Soobshch Tsentr. Nauchn-Issled. Kotloturvinnyi Inst.

Sykes (1958) J. Chem. Soc. 1958 p2053-4.

Sykes & Townshend (1955) J. Chem. Soc. 1955 p2528-9.

Taylor G.I. (1932) Proc. Roy. Soc. (London) A 135 828 685.

Taylor G.I. (1935) Proc. Roy. Soc.(London) A 151 p421-478.

Tani I., Komatsu Y. (1966) Proc. 11th Int. Cong. App. Mech. 1964.

Tollmein W. (1926) ZAMM 6 p468-478.

Trass O. (1958) Sc.D. Thesis in Chem. Eng. M.I.T.

Trass O. (1970) Private Communication 3/3/1970.

Tseidler A.A. (1964) Metallurgy of Copper and Nickel Trans. for Russian I.P.S.T. (Jerusalem) 1964.

Valla O. (1971) Ph.D. Thesis (to be published) Imp. Coll. Univ. London.

Van Driest E.R. (1956) J. Aero. Sci. 23 p1007-1011 & 1036.

Vickers J.M.F. (1959) Ind. Eng. Chem. 518 p967.

Wakelin D.H. (1966) Ph.D. Thesis Imp. Coll. Univ. of London.

Wolfstein M. (1968) Ph.D. Thesis University of London.

Zerbe J., Solna J. (1946) NACA TM 1070.

APPENDIX SIX

Nomenclature

A list of the main symbols used in this work is given in this section. Certain symbols are used to describe more than one variable at various stages in the work, others, where used in isolated expressions are defined only in the text. The symbol K is used extensively to represent a constant term.

Dimensionless Numbers

$$Re = \frac{\rho u d}{\eta} \quad - \quad \text{Reynolds Number}$$

$$Nu = \frac{H d}{K} \quad - \quad \text{Nusselt Number}$$

$$Sh = \frac{k d}{D_{AB}} \quad - \quad \text{Sherwood Number}$$

$$Sc = \frac{\eta}{\rho D_{AB}} \quad - \quad \text{Schmidt Number}$$

$$Pr = \frac{Cp \eta}{K} \quad - \quad \text{Prandtl Number}$$

Letters

Symbol	Representing	Dimensions
A	Area or as a constant	L^2
a	Stagnation point velocity gradient	T^{-1}
B	Constant	None
b	Jet/Plate distance	L
C	Constant	None

Symbol	Representing	Dimensions
C_f	Friction factor	None
D_{AB}	Diffusion coefficient of A through B	L^2T^{-1}
d	Jet diameter	L
E	Activation energy	ML^2T^{-2}
F	Force	MLT^{-2}
f	Concentration factor	None
H	Heat transfer coefficient	$ML^2T^{-3}\theta^{-1}$
h	Vertical co-ordinate	L
j	Chilton Colburn factor	None
K	Thermal conductivity or constant	$MLT^{-3}\theta^{-1}$
k	Mass transfer coefficient or Prandtl mixing length constant	$MT^{-1}L^{-2}$
l	Prandtl mixing length	L
M	Molecular weight	M
m	Mass	M
N	Flux	$MT^{-1}L^{-2}$
n	Order of spectrum	None
P	Pressure	$ML^{-1}T^{-2}$
R	Radial co-ordinate or gas constant	L
s	Time for experiment	T
T	Temperature	θ
t	Thickness	T
U	Velocity	LT^{-1}
V	Velocity or volume	LT^{-1}, L^3
W	Velocity	LT^{-1}
x	Exponent in velocity profile	None
	Law or co-ordinate	L
y	Co-ordinate	L
z	Co-ordinate	L

Greek Letters

Symbol	Representing	Dimensions
α	Angular position of velocity	None
Δ	Dimensionless variable = h/δ	None
∇	Operator Del.	None
δ	Boundary layer height, specifically that for momentum	L
ε	Lennard Jones parameter	ML^2T^{-2}
η	Viscosity	$ML^{-1}T^{-1}$
λ	Prandtl mixing length constant	None
	or Wavelength of light	L
μ	Viscosity	$ML^{-1}T^{-1}$
	or Refractive index	None
ν	Kinematic viscosity	L^2T^{-1}
θ	Angular co-ordinate	None
π	3.142	
ρ	Ccncentration or density	ML^{-3}
σ	Lennard Jones parameter	L
τ	Shear stress	$ML^{-1}T^{-2}$
ϕ	Angular co-ordinate	None
Ω	The Lennard Jones function	None
	or symbol for ohms	
$\int\Delta$	Symbol used to denote integral in equation (3.57)	None

Subscripts

A	Value of species A
AB	For diffusion coefficient, to denote diffusion of A through B
b	Bulk or environment value

Symbols	Representing
e	Jet exit value
f	Property of film
h	In the h direction
K	Kelvin temperature scale
o	Centreline or maximum value
R	In the R direction
s	Surface value
t	Overall or averaged value
w	Local value
conc	Concentration, or mass transfer value
eff	Effective value
lam	Laminar component
th	Thermal, or heat transfer value
turb	Turbulent component
visc	Viscous component

Superscripts

*	Dimensionless variable
'	Fluctuating component
—	Time averaged
•	Derivative w.r.t. time
~	Molar quantity

ACKNOWLEDGEMENTS

The author is indebted to Mr. W.M. Steen for his supervision of this work and his genuine interest in all aspects of the project.

Sincere thanks are extended to members of staff and fellow students of Imperial College for their advice and assistance and especially to the scientific and workshop technicians whose proficiency and co-operation has done much to surmount many difficulties.

The author is above all most grateful to his wife for her moral support during the project, typing of this thesis and finally, for remaining married to a student of such limited means.

In conclusion, the author is grateful to International Nickel Limited for supplying the nickel carbonyl and much data, and to the Science Research Council for their financial support during the whole period of this work.